STRENGTH-STRUCTURE RELATIONSHIPS IN CARBON FIBRES

by
SIMON CHRISTOPHER BENNETT

SUBMITTED IN FULFILMENT OF THE REQUIREMENTS FOR THE DEGREE OF DOCTOR OF PHILOSOPHY

THE UNIVERSITY OF LEEDS
TEXTILE PHYSICS LABORATORY
DEPARTMENT OF TEXTILE INDUSTRIES

AUGUST 1976

"EDUCATION IS AN ADMIRABLE THING, BUT IT IS WELL TO REMEMBER FROM TIME TO TIME THAT NOTHING THAT IS WORTH KNOWING CAN BE TAUGHT"

OSCAR WILDE (1854-1900)

- THE CRITIC AS AN ARTIST, I.

ABSTRACT

The three-dimensional microstructure and macrostructure of various PAN-based carbon fibres has been characterized by bright- and dark-field transmission electron microscopy, and quantitative electron-diffraction analysis.

A skin-core heterogeneity was observed for all fibres heat treated to 2500°C, irrespective of type and time of stabilization cycle, the skin being variable in longitudinal extent and width, but typically, 0.1 μm in thickness - much smaller than the sheath zone attributable to oxidation, which has been observed in optical microscopy. At 1000°C and 1500°C, only a few layer planes at the fibre surface can be considered as forming a skin structure, and it is proposed that progressive growth inwards of a well-oriented skin structure occurs at heat-treatment temperatures in excess of 1800°C. The nature of the fibre surface so formed would suggest that the number of edge sites suited to bonding with a resin matrix in untreated fibre is inversely related to heat-treatment temperature. Examination of 'first-cut' sections suggests that the surfaces of the fibres are rippled, with, at 2500°C , the c-axes of skin crystallites being predominantly normal to the fibre surface; this is confirmed by scanning electron microscopy and examination of transverse sections.

In cross section, the sheath and core zones, first observed in optical microscopy, have been shown to possess no preferred transverse c-axis orientation, it being proposed that structural differences between the zones lie in a crosslinking mechanism during oxidative stabilization.

The origin of the intrinsic oriented structure of PAN-based carbon fibres has been traced, by quantitative electron-diffraction analysis, through heat treatment at 2500°C, 1500°C and 1000°C to the

important pyrolysis range 400 - 600°C. At this temperature it is proposed that a uniform angular spread of stacking size exists within the azimuthal spread of the (00ℓ) reflection. Heat treatment, particularly at 2500°C, causes the preferential growth of those crystallites aligned closest to the fibre axis, while the rôle of smaller crystallites oriented at high angles to the fibre axis is thought to be one of interlinking.

Surface and internal flaws, involving large crystallite misorientations, have been observed in type I fibres, and using the Reynolds - Sharp theory for fibre failure, estimates of mechanical properties for such fibres have been made which are encouragingly close to the observed values. In the absence of internal voids and the surface skin characteristic of these fibres, an intrinsic strength of 7 GNm^{-2} and strain-to-failure of 2% is predicted. Enhanced crystallization effects have not been observed in fibres heat treated to 1000°C or 1500°C, and the fracture of these fibres at strains below 2% is thought to be due to the presence of gross internal and surface voids, flaws and irregularities.

ACKNOWLEDGEMENTS

I would particularly like to thank Dr. D.J. Johnson for his continued interest and supervision throughout the course of this work, and I am most grateful to Professor C.S. Whewell for arranging the S.R.C. Research Studentship, and the Procurement Executive, Ministry of Defence, for assistance with consumables and travelling expenses. Additionally, I am indebted to Mr. W. Watt, F.R.S., and Mr. W. Johnson of the Royal Aircraft Establishment, Farnborough, Hampshire, for constructive criticism at our regular meetings, assistance with ultramicrotomy, and provision of all the specimens. Without their contribution much of this work would not have been possible.

In this laboratory my thanks go to Dr. J. Sikorski, who first interested me in the problems involved in the elucidation of fibre fine structure, to Mrs. P.E. Montague and Dr. B.P. Saville, who assisted in computational work, and to Dr. R. Murray, Dr. D. Crawford and Dr. M.G. Dobb for stimulating discussions concerning high-resolution electron microscopy. I am also grateful to Mr. T. Buckley for technical assistance and the provision of the scanning electron microscope images.

Thanks are also due to Mrs. Gertrud Uddin for both typing and proof-reading the manuscript, and to Miss Liz Brown for the duplication work.

Last, but not least, I would like to express my sincere gratitude to my wife, Jennifer, who has assisted and encouraged me throughout the last three years, but, more significantly, made considerable sacrifices in order that a successful completion of this thesis was possible.

Textile Physics Laboratory,
August, 1976.

CONTENTS

CHAPTER 1

THE PRODUCTION, PROPERTIES AND STRUCTURE OF CARBON FIBRES.

1.1 THE STRUCTURE OF GRAPHITES

1.1.1 Three-dimensionally crystalline graphite

The valence electrons of carbon permit trigonal bonding between each atom and its three nearest neighbours, resulting in the two-dimensional hexagonal lattice shown in Fig. 1. Debye and Scherrer[1] proposed that adjacent layers of this lattice are produced by normal and parallel translations along a bond by one bond length, successive translations being in the same direction. By this scheme the projection of atoms in every third layer is identical - ABCABCA.... stacking - the rhombohedral form (Fig. 2a.). The alternative ABABABA.... stacking (Fig. 2b.) first proposed by Hull[2] has since been confirmed by Bernal[3], but more recently[4,5,6] both forms have been shown to exist. The unit cell (Fig. 3) has the following dimensions:-

$$a=b=0.24614 \text{ nm}$$

$$c=0.6707 \text{ nm}$$

with $d_{100}=0.21316$ nm and $d_{110}=0.12307$ nm.

1.1.2 Polycrystalline graphites

In paracrystalline forms of carbon the individual layer planes vary in perfection and, in poorly-crystalline materials, are thought to be wrinkled and to contain vacant lattice sites. Although the layers in most structures are arranged parallel to one another, to form crystallites, the less-crystalline structures are thought to contain substantial fractions of disorganized carbon. The properties of a typical paracrystalline carbon have been found to depend upon:-

(i) the size of the crystallites

(ii) the orientation of the crystallites

(iii) the density

(iv) the microstructural organization.

The essential structural difference between paracrystalline

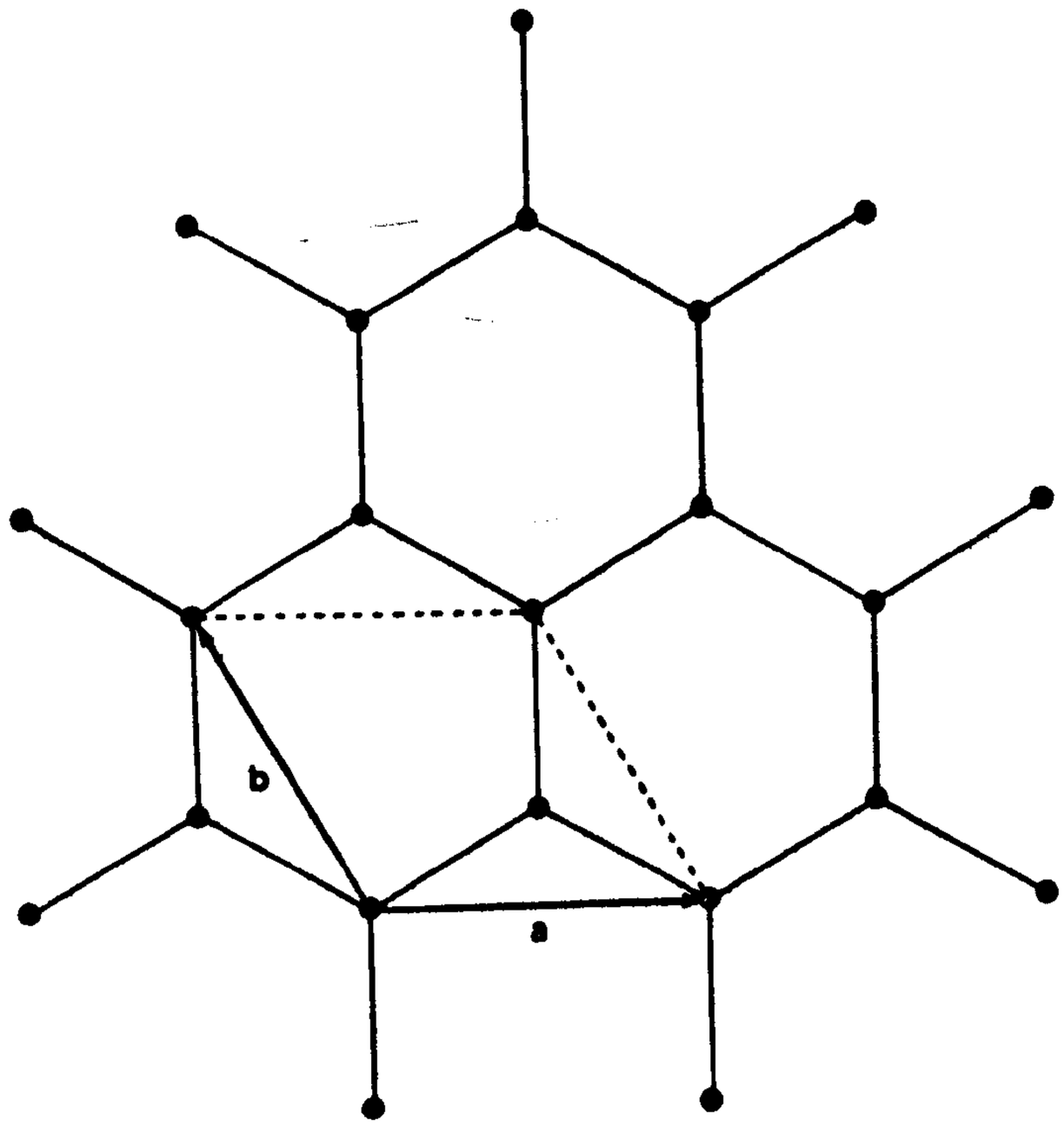

Fig. 1. The two-dimensional hexagonal arrangement of carbon atoms in a single graphite layer.

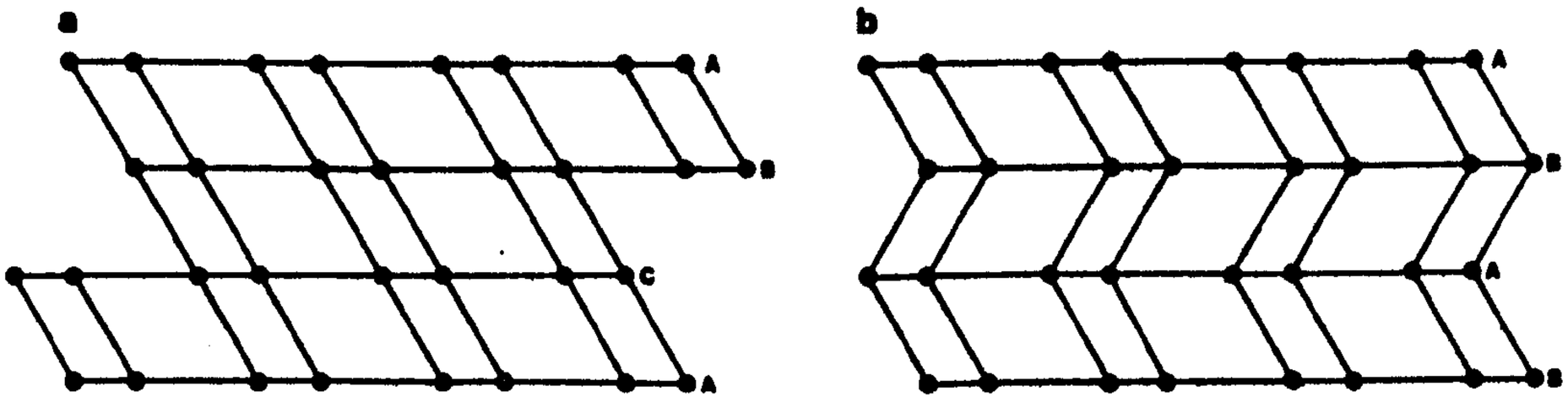

Fig. 2. Alternative stacking sequences of layer planes in graphite - (a) the rhombohedral form, and (b) the hexagonal form.

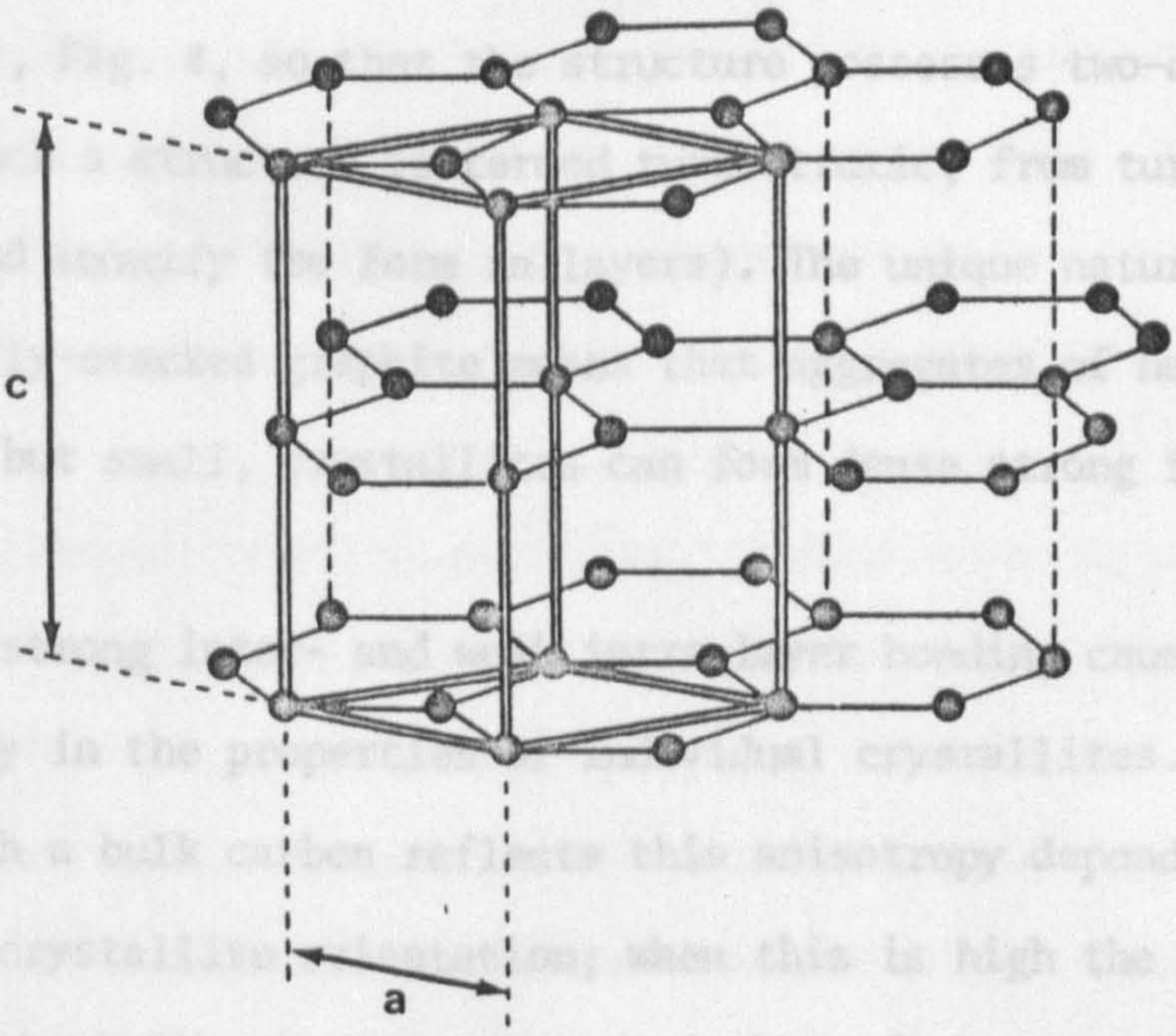

Fig. 3. The unit cell of graphite.

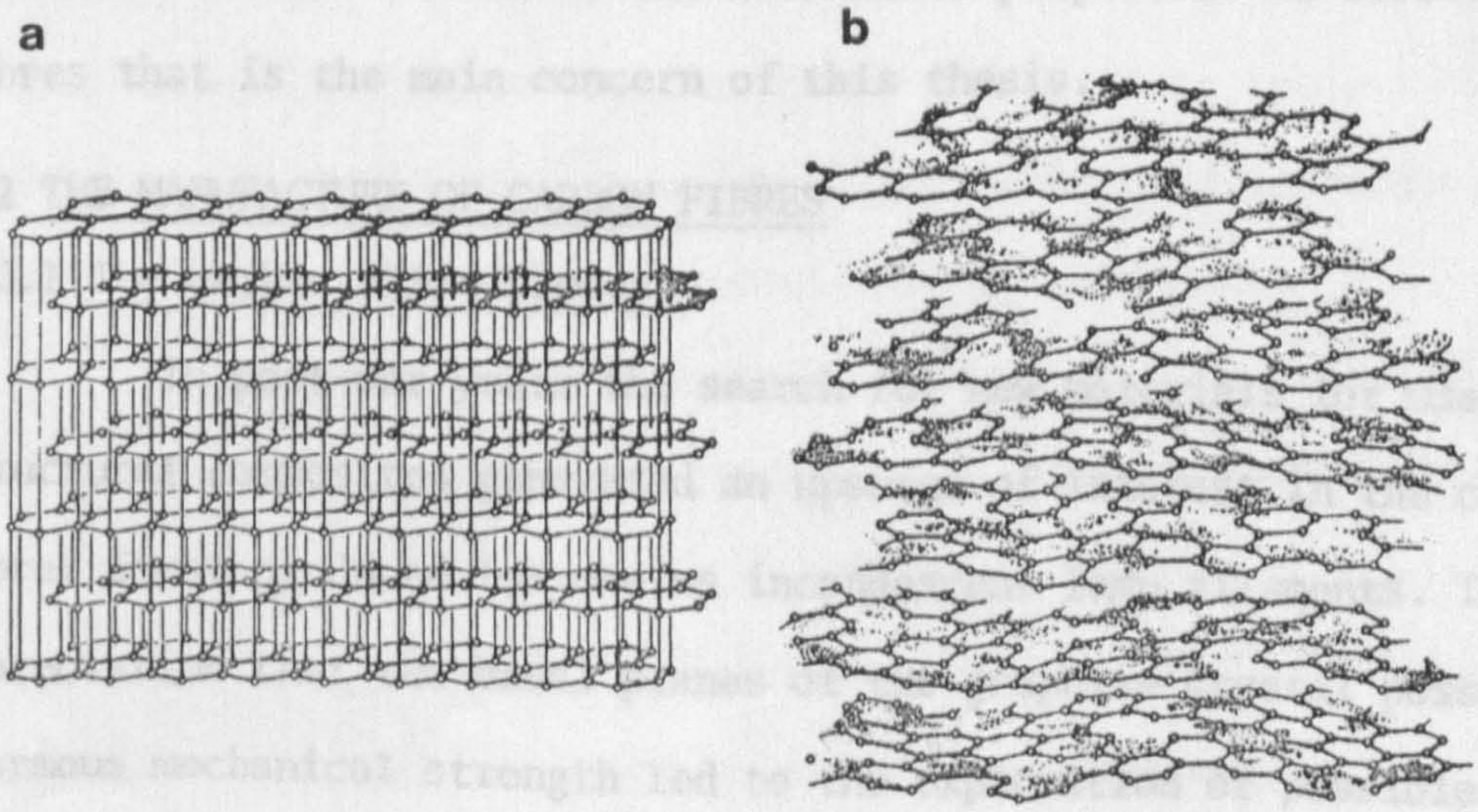

Fig. 4. (a) Three-dimensional stacking of layer planes, and (b) turbostratic stacking.

carbons and perfect three-dimensional graphite is that the adjacent sheets of hexagonally-arranged carbon are not ordered with respect to one another, Fig. 4, so that the structure possesses two-dimensional order only. Such a structure is termed turbostratic, from turbulent (disturbed) and stratify (to form in layers). The unique nature of turbostratically-stacked graphite means that aggregates of heavily cross-linked, but small, crystallites can form dense strong forms of carbon.

The strong inter- and weak intra-layer bonding causes high anisotropy in the properties of individual crystallites. The extent to which a bulk carbon reflects this anisotropy depends on the degree of crystallite orientation; when this is high the anisotropy of the bulk material approaches that of the constituent crystallites; when the crystallites are randomly oriented the anisotropy of the individual crystallites is perfectly averaged, so that the aggregate is isotropic. It is the study of the size, shape, orientation of, and crosslinking between the individual crystallites in relation to the mechanical properties of carbon fibres that is the main concern of this thesis.

1.2 THE MANUFACTURE OF CARBON FIBRES

1.2.1 The carbon fibre process

In post-war years the search for new materials for use in structural composites generated an upsurge of interest in the carbon fibres first produced for use as incandescent lamp filaments. The appreciation that the basal planes of the graphite crystal possess enormous mechanical strength led to the exploration of possible avenues of exploitation, with the result that relatively strong, flexible fibres were produced from pyrolyzed viscose rayon. Low-strength, low-modulus carbon yarns and fabrics were also made by the Union Carbide Corporation in the early 1960's, and these were used as

tape windings for rocket nose cones and heat shields.

In 1960 Bacon[7] had produced graphite whiskers, in the form of rolled scrolls, which had mechanical properties encouragingly close to the theoretical limits (in terms of crystal properties). Although impractical for industrial use, this discovery was important as it gave a direct experimental demonstration of the physical potential of carbon fibres.

A significant break-through in carbon-fibre technology occurred in the period 1960 - 1965, when it was discovered independently by Bacon et al.[8], Shindo[9,10,11], Watt et al.[12,13,14] and Standage and Prescott[15] that very high-strength carbon filaments could be obtained by subjecting a suitable precursor fibre to a continual tensile stress at some stage of the preoxidation or heat-treatment process. It is the high values of specific modulus and strength, due in part to a low density (about $2.10^3 kg.m^{-3}$) that made these new carbon fibres attractive materials as structural reinforcing agents; they form the basis of a new type of lightweight, stiff and strong material that promises to find extensive use in, for example, aerospace structures. Regrettably, carbon fibres have yet to realise their potential in these specialized fields, but recently high-strength fibres have found increasing use in a wide range of sporting and recreational equipment.

At present there are five main types of commercially available high-strength carbon fibre; these are derived from α-cellulose (e.g. Thornel), polyacrylonitrile (PAN) (e.g. Grafil, Modmor), pitch, lignin, and mesophase pitch. This thesis is concerned with the PAN-based materials, and the other types will not be considered in detail.

The manufacturing process of the commercial fibre varies in detail, depending on the precursor polymer and the heat-treatment cycle used. Typically the process involves the following basic steps;-

(i) preoxidation at a low temperature (200 - 300°C) to promote crosslinking, thereby stabilizing the precursor,

(ii) carbonization in an inert atmosphere at about 1000°C to produce type A fibres,

(iii) further heat treatment at 1500°C for type II (high-strength) fibres, or at 2500 - 3000°C for type I (high-modulus) fibres.

The rayon-based fibres are usually stressed at high heat-treatment temperatures, whereas the PAN-based fibres are stressed during the low-temperature oxidation step. Both precursors lose 50 - 80% of their initial weight during high-temperature heat treatment.

The outstanding mechanical properties of carbon fibres become of practical interest only if they can be efficiently translated into a usable structural form, such as a composite. Although the intrinsic tensile properties of carbon fibres appear to be directly related to the size and orientation of the graphitic subunits, the properties of a fibre-resin composite depend to a large extent on the nature of the fibre-matrix interface. In order to understand the mechanical properties of such a composite it is important to characterize the surface and bulk structure of the fibres at both a micro- and a macro-level.

1.2.2 The production of carbon fibres from PAN

A. Stabilization and pyrolysis

PAN fibres require a low-temperature air oxidation at 220°C in order to prevent degradation at higher temperatures. The important difference between Shindo's early work[10] and the Royal Aircraft Establishment (R.A.E.) process[12,13,14] is that in the latter case the fibres are prevented from shrinking during oxidation. This prevents the molecules within the stretched PAN fibres returning to

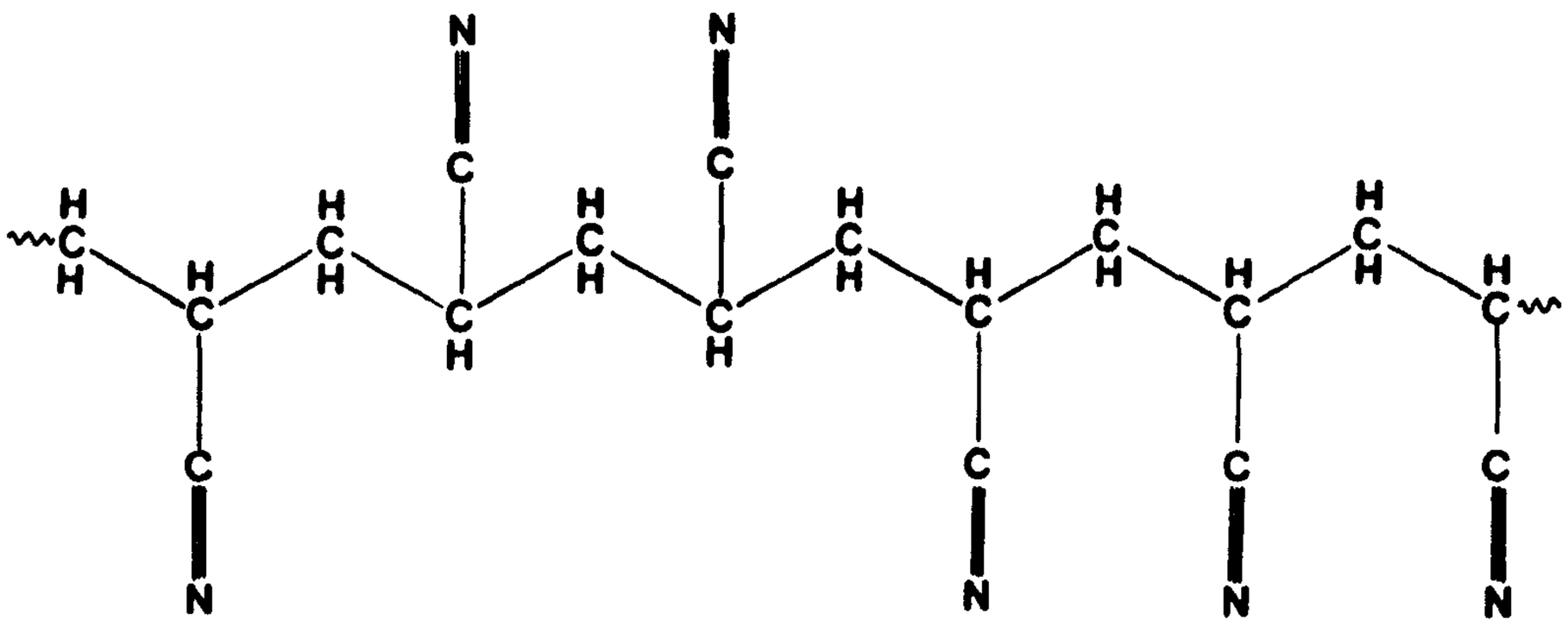

Fig. 5. The molecular structure of PAN.

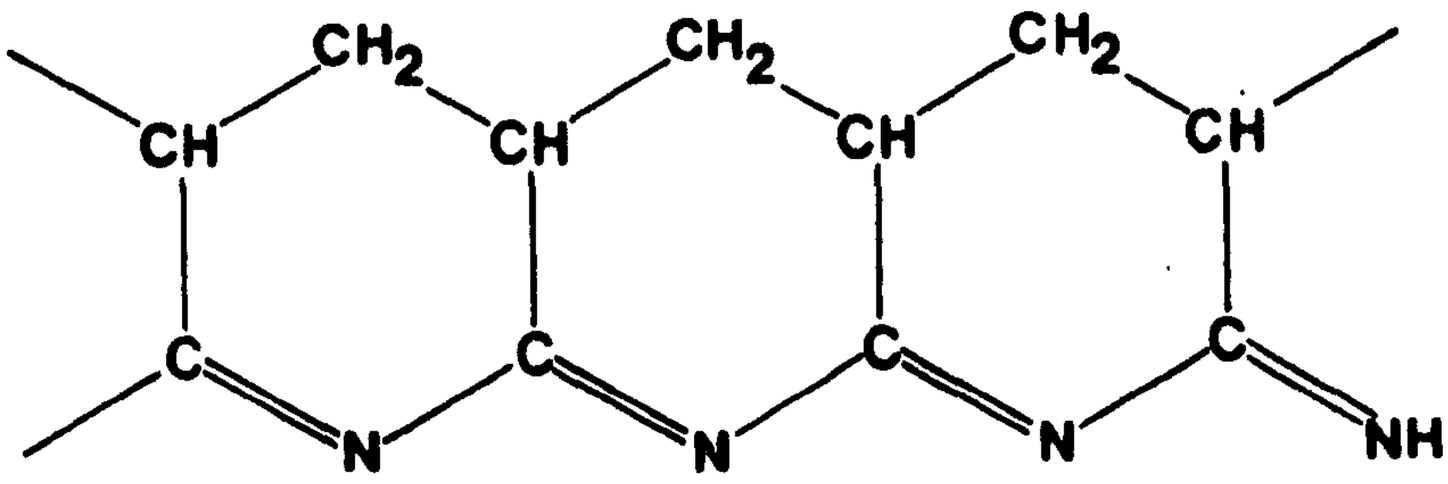

Fig. 6. The condensed naphthyridine ring structure of vacuum-stabilized PAN. After Grassie and Hay[16].

an amorphous state after heating above the second-order transition temperature (about 90 - 120°C). As the orientation of the graphite planes in carbon fibres is related to molecular orientation in the acrylic precursor, this is obviously an important consideration.

a. Chemistry of the low-temperature process - the theory of intra-molecular cyclization

It is widely accepted that PAN, which is a linear molecule carrying nitrile side-groups (Fig. 5), forms an oxidized ladder polymer, the exact structure of which is not clear, when heated in air. Grassie and Hay[16], however, have shown that when PAN is heated (without weight loss) in vacuum at 180 - 230°C a condensed naphthyridine ring structure (Fig. 6) is formed. Recently, Watt and Johnson[17] have shown that ladder-polymer formation is a prerequisite to oxidation, which would appear to be through a pyridone structure as proposed by Potter and Scott[18]. However, three of the four formulae proposed for oxidized ladder polymer[18,19,20,21] can be reconciled by tautomeric changes and different oxidation mechanisms (see Fig. 7). The lengths (n) of the conjugated sequences are considered to be of the order of 4 - 5 monomer units, and depend on termination effects. Goodhew et al.[22] propose that termination occurs when a nitrile group, adjacent to the growing end of the cyclized chain, fails to propagate due to steric hindrance[23]; this is characterized by the formation of ammonia[24,25]. Furthermore, it was proposed that the effect of the preoxidation treatment is to produce longer lengths of conjugated sequences (Fig. 8), as confirmed by increased HCN evolution[24,26]. Although there is considerable controversy regarding the type of bonding of the oxygen to the ladder polymer, there is little doubt that the methylene hydrogen atoms react during oxidation, and if the conditions are held for a sufficient length of time all

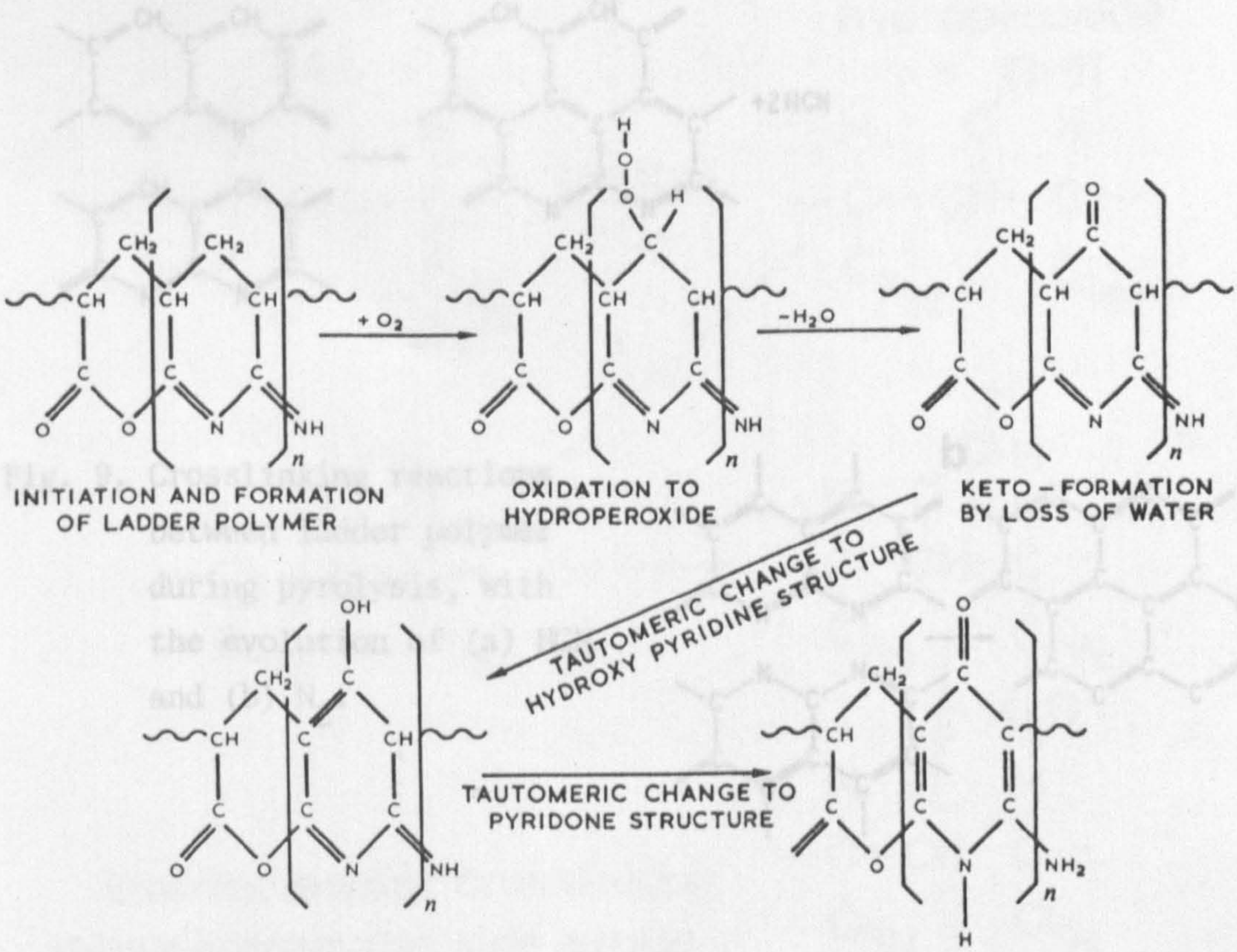

Fig. 7. Formulae for oxidized ladder polymer, showing tautomeric changes and different oxidation mechanisms. After Watt and Johnson[17].

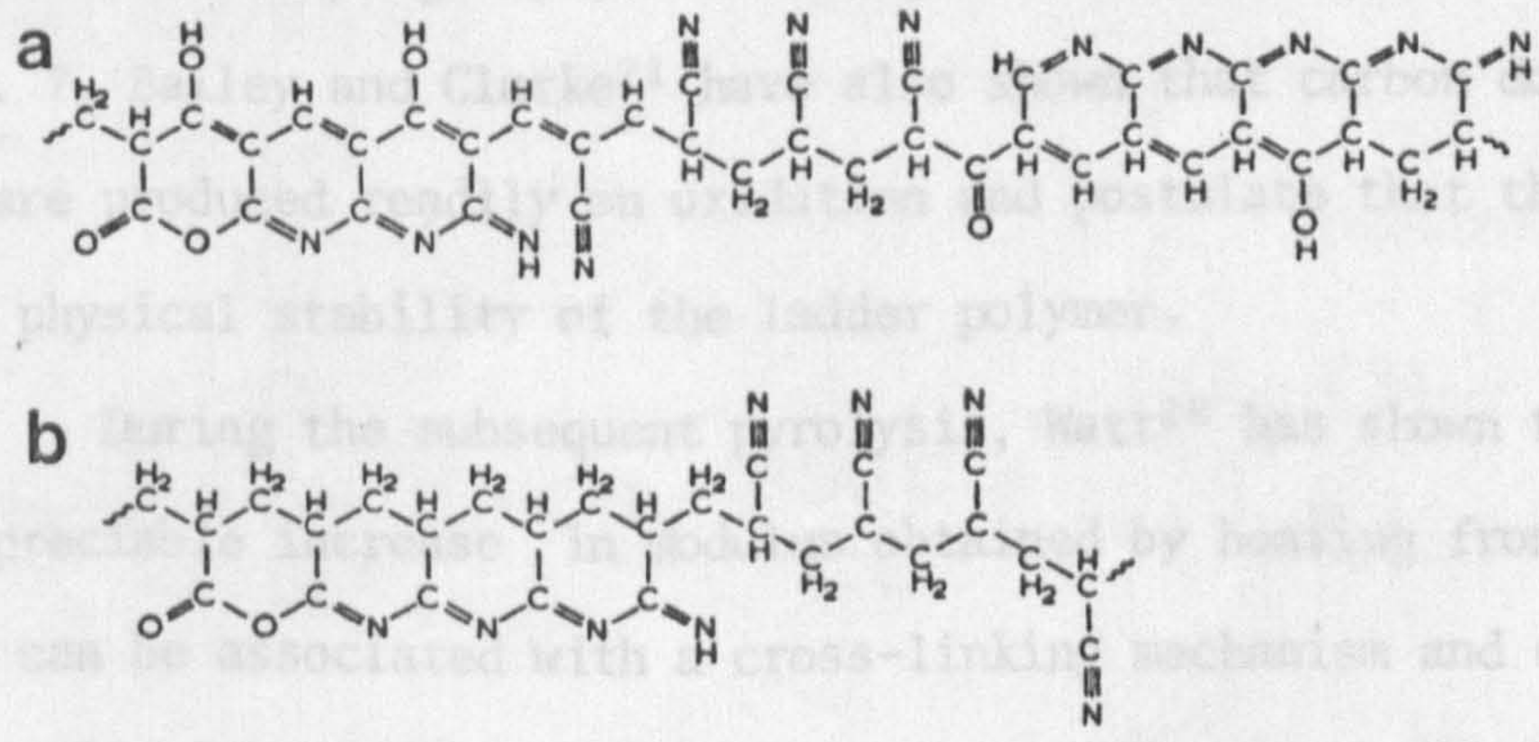

Fig. 8. Chemical formulae of (a) air-stabilized, and (b) vacuum-stabilized PAN. After Goodhew et al.[22].

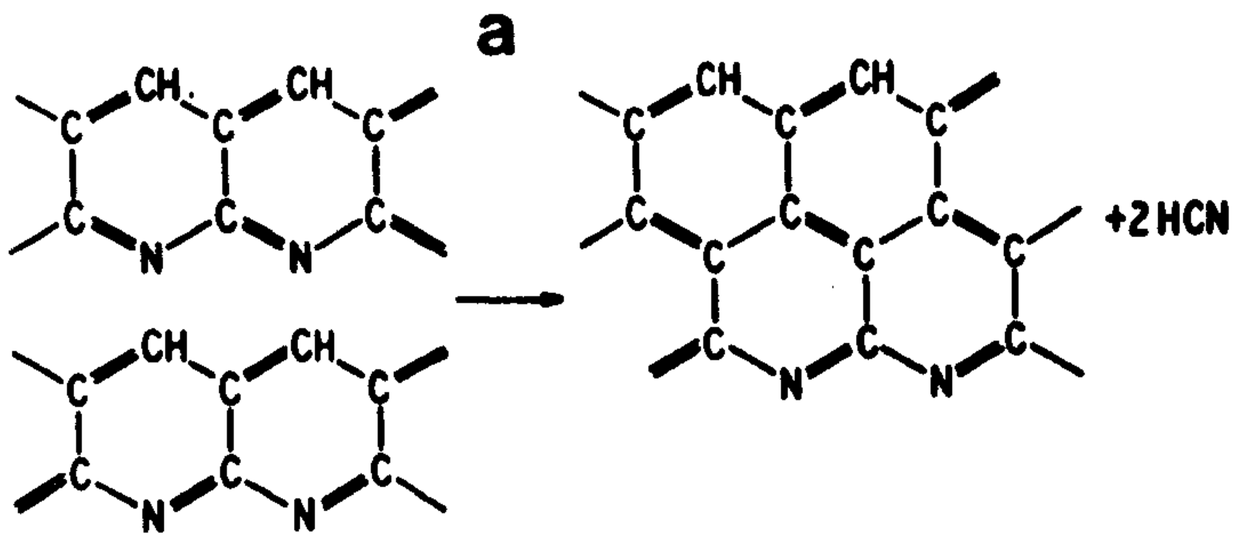

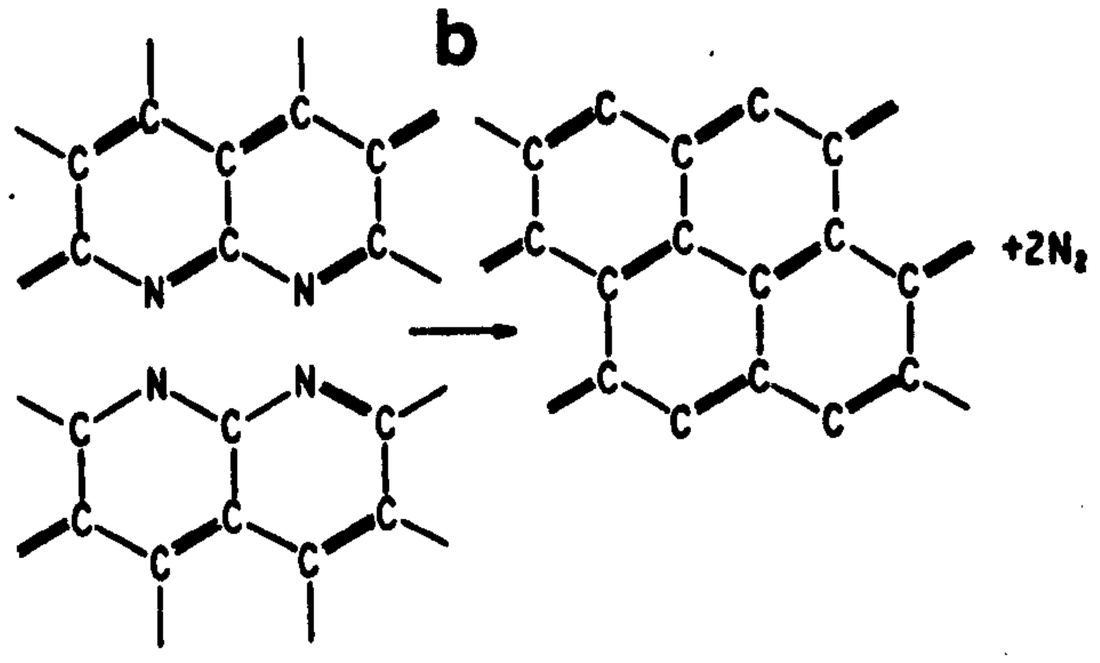

Fig. 9. Crosslinking reactions between ladder polymer during pyrolysis, with the evolution of (a) HCN and (b) N_2.

these hydrogen atoms disappear. At the same time, elemental analysis[27] indicates that only one third of the hydrogen atoms are removed, whilst infra-red spectroscopy shows the simultaneous development of hydrogen-bonded species, indicating the presence of hydroxyl groups. Additional infra-red evidence regarding the presence of carbonyl groups would seem to suggest that the main form of oxygen is in hydroxyl or carbonyl groups, confirming most of the models depicted in Fig. 7. Bailey and Clarke[21] have also shown that carbon double bonds are produced readily on oxidation and postulate that these add to the physical stability of the ladder polymer.

During the subsequent pyrolysis, Watt[28] has shown that the appreciable increase in modulus obtained by heating from 300 to 1000°C can be associated with a cross-linking mechanism and evolution of HCN (Fig. 9a.) and H_2O. Nitrogen evolution as elemental nitrogen starts at 600°C and reaches a maximum at about 900°C; consequently a cross-linking reaction between adjacent portions of ladder polymer was proposed (Fig. 9b.).

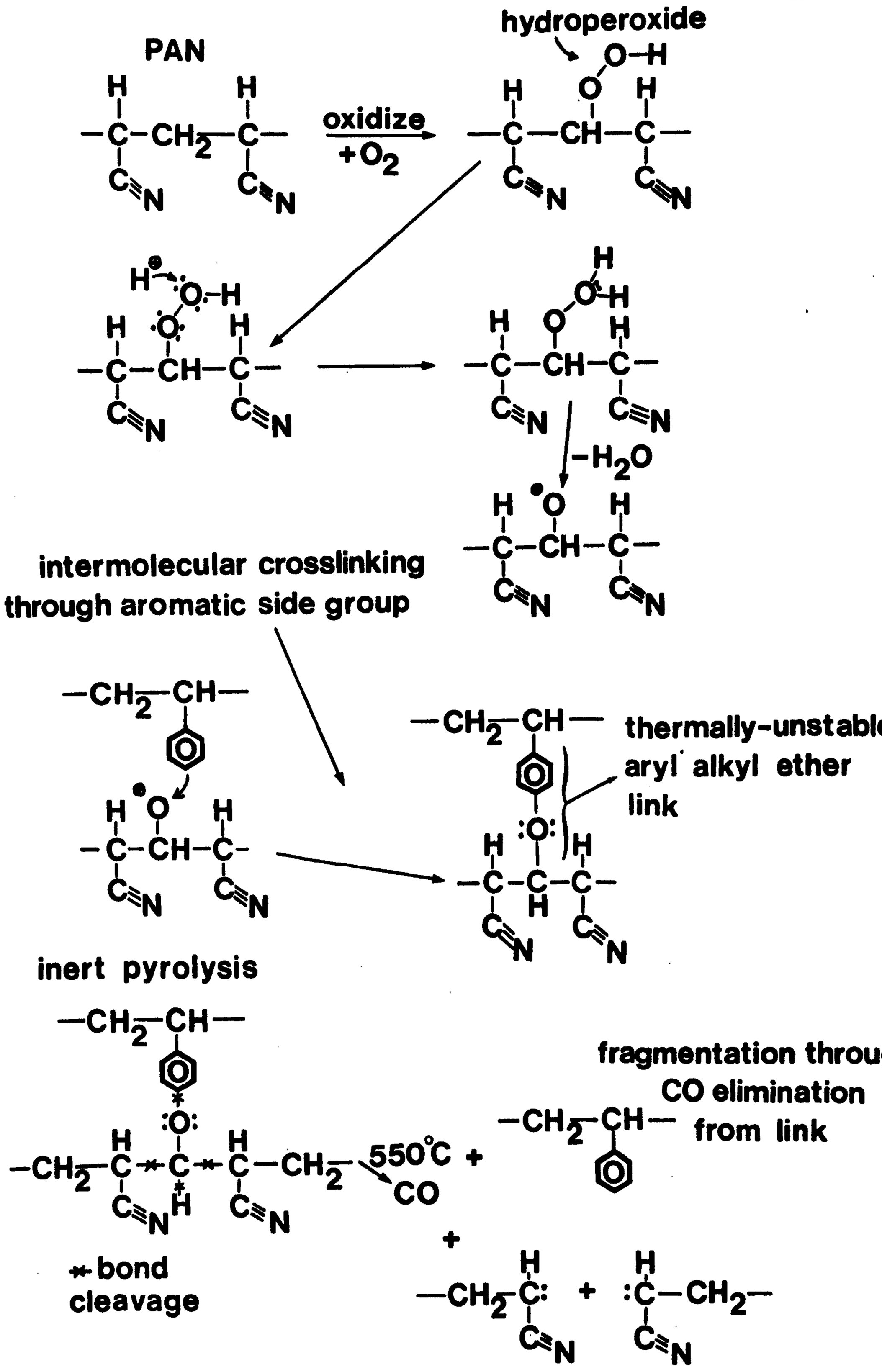

Fig. 10. Crosslinking through aryl ether link
(NB. The authors[30] do not specify the origin of the aromatic side group).

b. Chemistry of the low-temperature process - the alternative theory of fragmentation and intermolecular reactions

None of the conventional cyclization theories outlined above adequately explain the role of oxygen during the initial stages of pyrolysis, and all the proposed structures are highly idealized. Gaulin and McDonald[30] however, have interpreted the results obtained from elemental analysis in terms of intermolecular reactions previously unconsidered. They found that *intramolecular* cyclization to yield a linear ladder polymer is incompatible with experimental observations, which suggest that the reactions involve elimination, fragmentation, *intermolecular* crosslinking, and cyclization induced by dipole interactions between pendant nitrile groups.

Fig. 11. Intermolecular dipole attraction between pendant nitrile groups of PAN molecules. After Gaulin and McDonald[30].

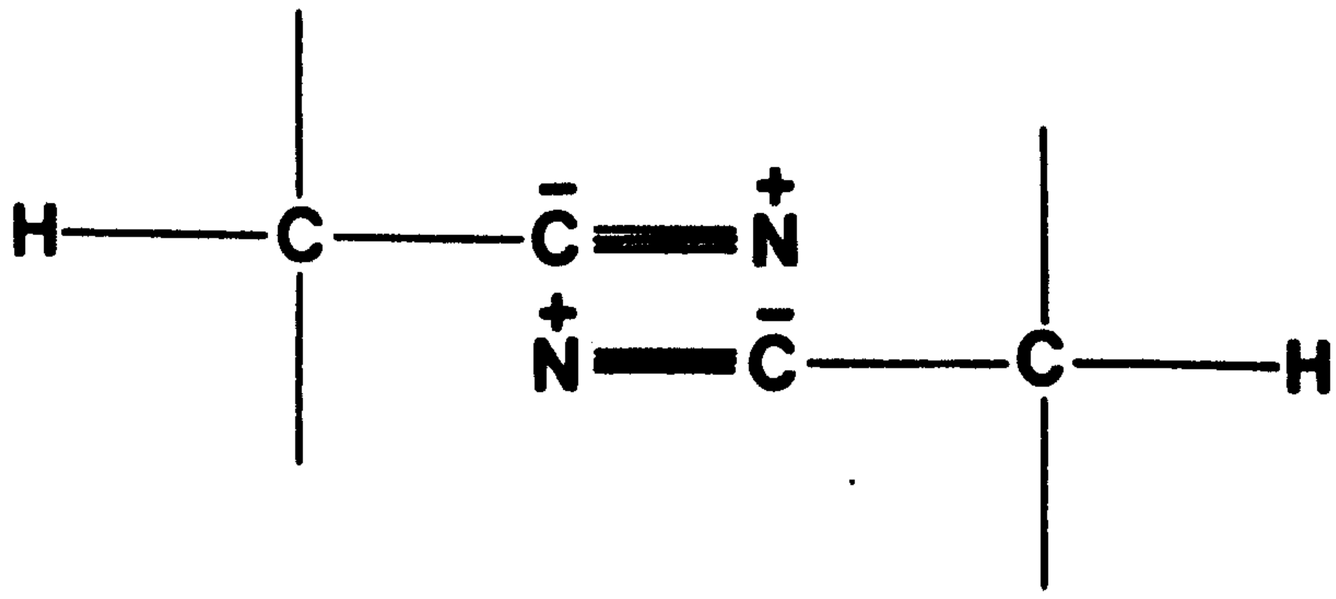

It was proposed that decomposition products derived both during heating PAN in vacuum at 260°C (where the characteristic exotherm was observed), and during subsequent pyrolysis, can be explained in terms of fragmentation reactions, while the higher temperature products (HCN and N_2) are derived by elimination reactions from the intermediate heterocyclic structures. However, after air oxidation, the degradation processes were shown to shift to higher temperatures, and the production of CO_2, H_2O, NH_3 and HCN during the preoxidation stage was considered as further evidence of extensive fragmentation. It was found that most of the carbon monoxide was evolved at 550°C, and it was claimed that this was attributable to aryl ether groups, inferring that appreciable cross-linking occurs during preoxidation through ether formation via elimination of water from hydroperoxides (Fig. 10).

Cyclization was proposed to be the result of elimination reactions induced by dipole interactions between the pendant nitrile groups. The conventional scheme of intramolecular cyclization requires considerable isotacticity, which is incompatible with conformation studies and the solution properties of PAN; the proposed syndiotacticity being in fact derived from the strong repulsive dipole effects between neighbouring nitrile groups[31]. It was further proposed that the presence of these strong dipoles leads not only to *intra*molecular repulsion, but also to *inter*molecular attraction (Fig. 11). In the light of these facts several structures amenable to ring closure are conceivable, and it was proposed that the actual mechanisms of both oxidative stabilization and subsequent thermal degradation of the 'cyclized' polymer are far more complex than previously supposed.

B. High-temperature heat treatment

Carbon fibres fall into the category of 'hard' or non-graphitizing materials, and as such retain a very imperfect structure

even after prolonged treatment at very high temperatures and ambient pressures. Complete graphitization would only be achieved under the influence of combined high pressure and high temperature - a technique not used in the conventional carbon-fibre process. In carbon fibres heat treated at 1500°C there is substantial, though imperfect, organization of the carbon into graphite-like layers; the purpose of further inert heat-treatment is to increase the crystallite size and improve the preferred orientation; this is accompanied by improvement in the perfection of the graphite layers, and a decrease in both inter-layer d-spacing and disorder. It should be stressed however that the structures produced at 2500°C are still essentially turbostratic, and use of the term 'graphitized' when referring to type I fibres is erroneous. Consequently, carbon fibres will be referred to in this thesis by the maximum heat-treatment temperature (HTT) that they have experienced.

Although type I fibres are potentially useful as structural-reinforcing materials (they have moduli close to the single crystal theoretical modulus) their use has declined recently due to the low strain-to-failure that they exhibit.

1.3 THE STRUCTURE AND MECHANICAL PROPERTIES OF CARBON FIBRES

1.3.1 Mechanical properties

A. Conventionally-produced fibres

The Young's modulus of a perfect single crystal of graphite parallel to the basal planes is close to 1000 GNm^{-2} (five times that of steel), yet that normal to the basal planes is less than 40 GNm^{-2} (one half that of aluminium)[32]. The modulus for basal plane shear is only about 4 GNm^{-2} for dislocation free graphite, and more than an order of magnitude lower than this value (equivalent to that of polyethylene) for graphite which contains dislocations. The theoretical

tensile strength parallel to the basal planes is at least 95 GNm^{-2} [33], and strengths as high as 20 GNm^{-2} have been measured in graphite whiskers[7]. By contrast, the shear strength between basal planes for dislocation-containing, but otherwise perfect, single-crystal graphite is only approximately 1 MNm^{-2} [34]. As will be shown later the amount and type of crystallite interlinking in carbon fibres, where in many cases the crystallites contain numerous dislocations and voids, is of great importance from a strength/shear point of view.

Carbon fibres with average tensile strength (σ_B) of 1.8 to 2.1 GNm^{-2} and Young's modulus (E) of about 420 GNm^{-2} were first reported[12,15] in 1966, although Shindo[10] had produced fibres of tensile strength about 0.7 GNm^{-2} and modulus about 150 GNm^{-2} as early as 1961. In 1967, Moreton et al.[13] published results showing that the choice of an optimum HTT of about 1500°C produced fibres of higher strength (about 3 GNm^{-2}) than those obtained by heat treatment at 2500°C (about 2.2 GNm^{-2}). However, where fibres of high modulus (greater than 350 GNm^{-2}) are required, it was shown that heat treatment at or above 2500°C is necessary. In one exceptional case a fibre heat treated at 1600°C exhibited a tensile strength of over 5 GNm^{-2} - one quarter of the maximum σ_B measured by Bacon[7] for graphite whiskers.

By 1968, Watt and Johnson[35] had examined the effect of heat treatment and precursor stretch ratio on Young's modulus. As expected, the modulus increased with increasing heat-treatment temperature, indicating that the preferred orientation of the turbostratic crystallites which constitute the fibre is improved by heat treatment. Similarly, the modulus of the final carbon fibre, whether it is heat treated at 1000, 1500 or 2500°C can be improved by stretching the precursor.

The tensile strength was shown to be highly dependent on the

tension maintained during oxidation, with length changes between 0 and +20% necessary to produce optimum strength in fibres prepared at heat-treatment temperatures of 1000, 1500 and 2500°C. In exceptional circumstances the strength fell by a factor of three when the fibres were allowed to contract 25% during oxidation. Apparently the oriented structure of all the carbon fibres studied is related to either the structure of the precursor, or the structure of the 'cyclized' polymer formed during oxidation.

Subsequent work at the Atomic Energy Research Establishment (A.E.R.E.)[36] showed that there was an appreciable increase of about 30% in the apparent modulus of both type I and II fibres when a tensile load is applied. It was found that this change of modulus is directly related to a change in the crystallite orientation, with the additional possibility that basal-plane dislocations play a significant rôle at low applied loads of less than 2.5×10^{-3} Kg. Both effects were found to be fully reversible with no evidence of hysteresis. In structural terms, these results indicate that the turbostratic graphite crystallites can be considered as linked in series through grain boundaries of small or moderate angles. Stress on the fibre reduces this angle appreciably before fracture occurs. Additionally it was proposed that the structure contains mobile dislocations which become pinned against grain boundaries at moderate stresses.

B. Modifications to the basic process and their effect on mechanical properties

Boron doping of type I fibres[37] showed dramatic increases in modulus (for example from 425 to 535 GNm^{-2}) and no significant change in strength at about 1.65 GNm^{-2}. As expected, the resistivity dropped considerably indicating higher perfection and orientation.

The necessary hot-stretching stage for carbon fibres made

from cellulosic precursors[38] led Johnson[39] to attempt the production of carbon fibres of higher than usual preferred orientation by stretching at temperatures high enough for plastic flow to take place. It was shown that the fibre modulus increases with extension, and that an extension of about 30% at 2800°C was capable of giving fibres with a mean modulus approaching 700 GNm^{-2}. However the tensile strength was found to be independent of extension, indicating that the defects which limit the strength are not annealed out by high-temperature stretching.

Moreton[40] was able to relate the tensile strength and modulus of carbon fibres heat treated to 2500°C directly to the strength and modulus of the precursor PAN. He found that the precursor could be spun satisfactorily at steam-stretch ratios up to x13, and that this subsequently gave the optimum mechanical properties in the high-temperature carbon fibres. It was claimed that improved orientation had been maintained during pyrolysis as a result of increasing the amount of extension. A similar dependence of tensile strength on stretch-ratio indicated that, although the strength of carbon fibres is highly flaw-sensitive[41,42,43], the presence of defects in the precursor fibre could be minimized by choosing a high steam-stretch ratio.

Later Moreton[44] was able to show that stretching the PAN fibres by x14 in glycerol at 150°C produced a 40% improvement in precursor tensile strength. Corresponding improvements in strength and modulus were found in the fibre carbonized at 1000°C, and the modulus was found to be higher in the carbon fibres heat treated at 2500°C. Again, however, the strengths of the type I fibres were no more than comparable with those normally found in high-modulus, PAN-based carbon fibres, further emphasizing the high dependence of tensile

strength on flaws and defects.

Recently[45], a patent has described similar methods of obtaining highly-oriented precursor PAN, and the effect that this orientation has on the mechanical properties of carbon fibres heat-treated in the range 1000 - 2600°C. Improvements in both modulus and strength were claimed.

C. Anomalous tensile strengths

Although, theoretically, the strength of a material should continue to rise as the modulus is increased, there was, in 1970, a well-documented (e.g. 13) maximum in the ultimate tensile strength against heat-treatment temperature curve for fibres of a circular cross section at about 1500°C. In an attempt to explain this anomaly LeMaistre and Diefendorf[46,47] have characterized the three-dimensional structure of circular and dog-bone cross-section carbon fibres. It was proposed that because of a circumferential crystallite orientation Mrozowski cracks result from the radial tensile stresses generated in circular cross-section fibres during cooling from high heat-treatment temperatures. In dog-bone shaped fibres, however, the basal planes, although thought to be aligned paralled to the fibre surface, are predominantly oriented along the large cross-sectional axis of the fibre, and the possibility of cleavage cracking is thus reduced. Jones and Duncan[48] have used this crack-formation mechanism to explain the dependence of tensile strengths on post heat-treatment cooling rate.

Moreton[41] has verified the existence of random flaws in his experiments concerning the effect of gauge length on ultimate tensile strength, and Thorne[43] and Johnson[42] have concluded from scanning electron-microscope (SEM) studies that impurities in the PAN precursors are the major cause of flaws in carbon fibres. Similarly, the voids seen in high-temperature fibres[49] have been interpreted

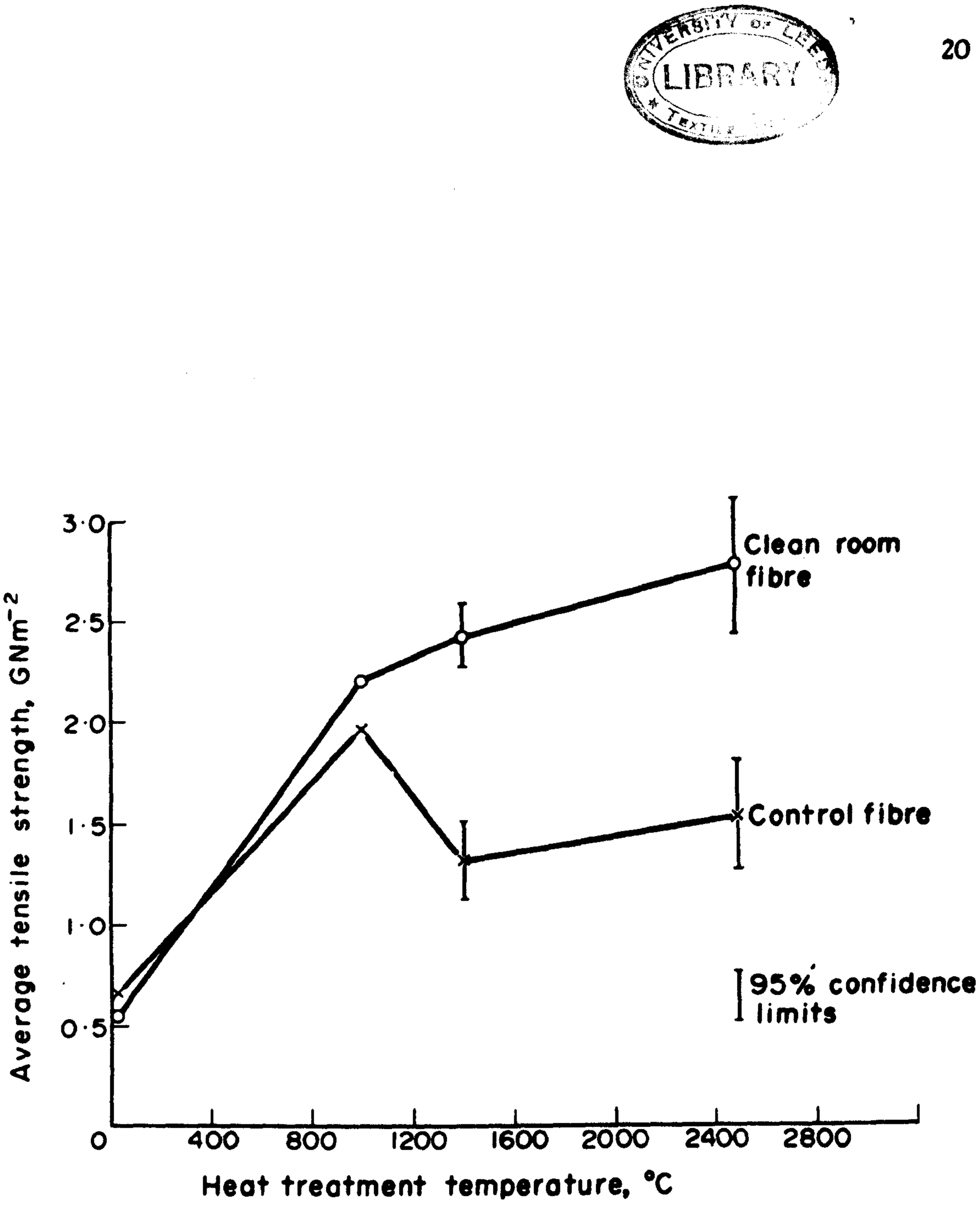

Fig. 12. The dependence of ultimate tensile strength on heat-treatment temperature for clean-room spun and control fibres. After Moreton and Watt[50,51,52].

as the main cause of the anomalous strength decrease observed after heat-treatment above the 1200 - 1600°C range.

Although contamination can occur at any stage of the carbon-fibre process it seems most likely that the highest risks involve either the presence of impurity particles in the PAN spinning solution, or the surface impurities picked up either during spinning and collection or during subsequent handling and conversion to carbon fibre. In order to minimize these effects Moreton and Watt[50,51,52] developed a dope-filtration and clean-room spinning technique capable of producing relatively high-strength type I carbon fibres. They found that not only did the tensile strength of clean-room spun fibres continue to rise after heat treatment above 1200°C and up to 2500°C (Fig. 12), but that the gauge-length effect was eliminated over the 10 - 50 mm range for fibres heat treated at 2500°C. They chose a break at below 2 GNm^{-2} as representative of a failure at a severe flaw, and calculated the average severe flaw separation to be about 200 mm.

Diefendorf and Tokarsky[53] have recently emphasized the need to know both the number and severity of flaws in order to understand the strength of carbon fibres, which should, theoretically, be 10 - 20% of the modulus, but are, at the time of writing, typically less than 1 - 2%. In a series of tensile and loop tests the strength was found to increase with shorter gauge lengths, as expected, since the number of flaws decreases. Using a weakest-link model for fibre failure, estimates of basic link strengths of 8 - 9 GNm^{-2} and lengths of about 20 μm were made for a type I fibre. Similarly, in other Courtelle-based fibres it was found that the higher the strength of the fibre the smaller the gauge-length effect. The flaw-free strength was estimated at approximately 12 GNm^{-2} corresponding to an acceptable 2 - 3% strain-at-failure. This clearly indicates that when all the flaws at this level have been removed

the intrinsic strength of the fibre will be directly related to the microcrystalline structure.

Thorne[54] has also confirmed that breaking strains of at least 3% are possible in effectively surface-treated carbon fibres heat-treated in the range 1000 - 1500°C. He showed that loop tests indicate breaking strains of around 5%, and that a significant number of fibres had breaking strains of greater than 3% in tensile tests of 10 mm gauge lengths. He concluded that the present shortfall in experimental values of breaking strain is partly explained by the persistence of some surface flaws, even after surface treatment, which cause failure at strains less than 1.5%.

1.3.2 The structure of carbon fibres

A. X-ray diffraction studies

Conventional wide-angle parameters such as Z, L_c, and c/2 have been reported by Badami et al.[55] for fibres heat treated at 2600°C, and Johnson et al.[56] have investigated the dependence of these parameters on stress graphitization. Similarly, Ruland has quantitatively assessed the correlation between modulus and orientation[57] (Fig. 13), and pore size and heat-treatment temperature[58]. These results have been confirmed by Johnson and Tyson[59,60] and Johnson et al.[61] who reported the increase in small-angle pore size over the heat-treatment range 1000 - 2800°C. Ergun[62] has attempted to measure a disorder parameter and fault-free stacking size from an analysis of the line widths of several orders of the 00ℓ reflections, but Fourdeux et al.[63] have shown this to be unsatisfactory because of the dependence of crystallite size on orientation.

Diefendorf and Tokarsky[64] in an extensive review have examined carbon fibres heat treated at various temperatures, and made from different precursor materials. They conclude that the fibres consist

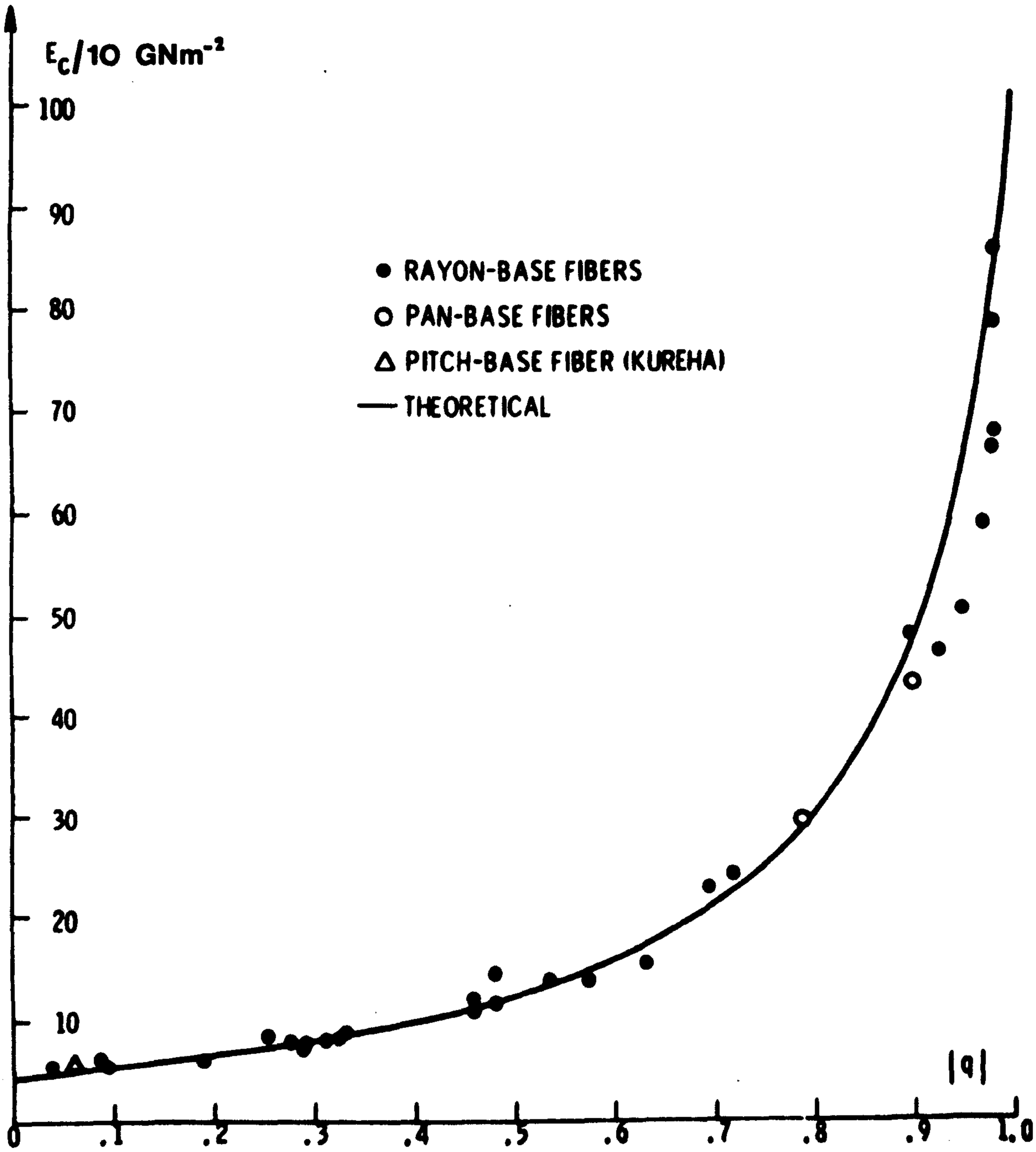

Fig. 13. The dependence of modulus (E_c) on crystallite orientation function (q). After Ruland[57].

of long undulating and twisting ribbons. For type A fibres a ribbon thickness of 1.5 - 2.0 nm and width about 2.0 nm was proposed, the ribbons being highly undulated and twisted to give an intertangled mass, providing tight coupling between ribbons. Fibres of higher modulus showed increased stacking size and higher preferred orientation as expected. In one exceptional carbon fibre, modulus greater than 700 GNm^{-2}, three-dimensional ordering was observed together with a preferred a-axis orientation compatible with that expected if the orientation of the carbon backbone of the PAN polymer was retained throughout processing (Fig. 14). Similar observations have been made by Ergun[65] on a highly-oriented PAN-based carbon fibre.

Stewart et al.[66] have quantitatively assessed the preferred a-axis orientation in carbon fibres heat-treated at 1000, 1500 and 2500^{o}C, and found that in all cases the fibres have mean a-axis orientations parallel to the fibre axis with a standard deviation in the range 24 - 28^{o}. They propose that when the basal planes are arranged with their a-axis parallel to the longer sides of the crystal sheets (Fig. 14) (in the case of carbon fibres this is the fibre axis) the minimum number of carbon atoms per unit length have an unsatisfied valence (that is, they are bonded to only two other carbon atoms instead of the usual three). Thus it was proposed that this configuration is preferentially formed as it has the lowest surface energy.

More recently, Rose[67] has reported a detailed study of the dependence of the interlayer d-spacing, c/2, and preferred orientation of crystallites, Z, on heat-treatment temperature. He showed that heat treatment in the temperature range 2000 - 3000^{o}C improves the c/2 parameter from about 0.345 nm to 0.340 nm. This is in direct conflict with the early work of Franklin[115] who proposed that only two interlayer

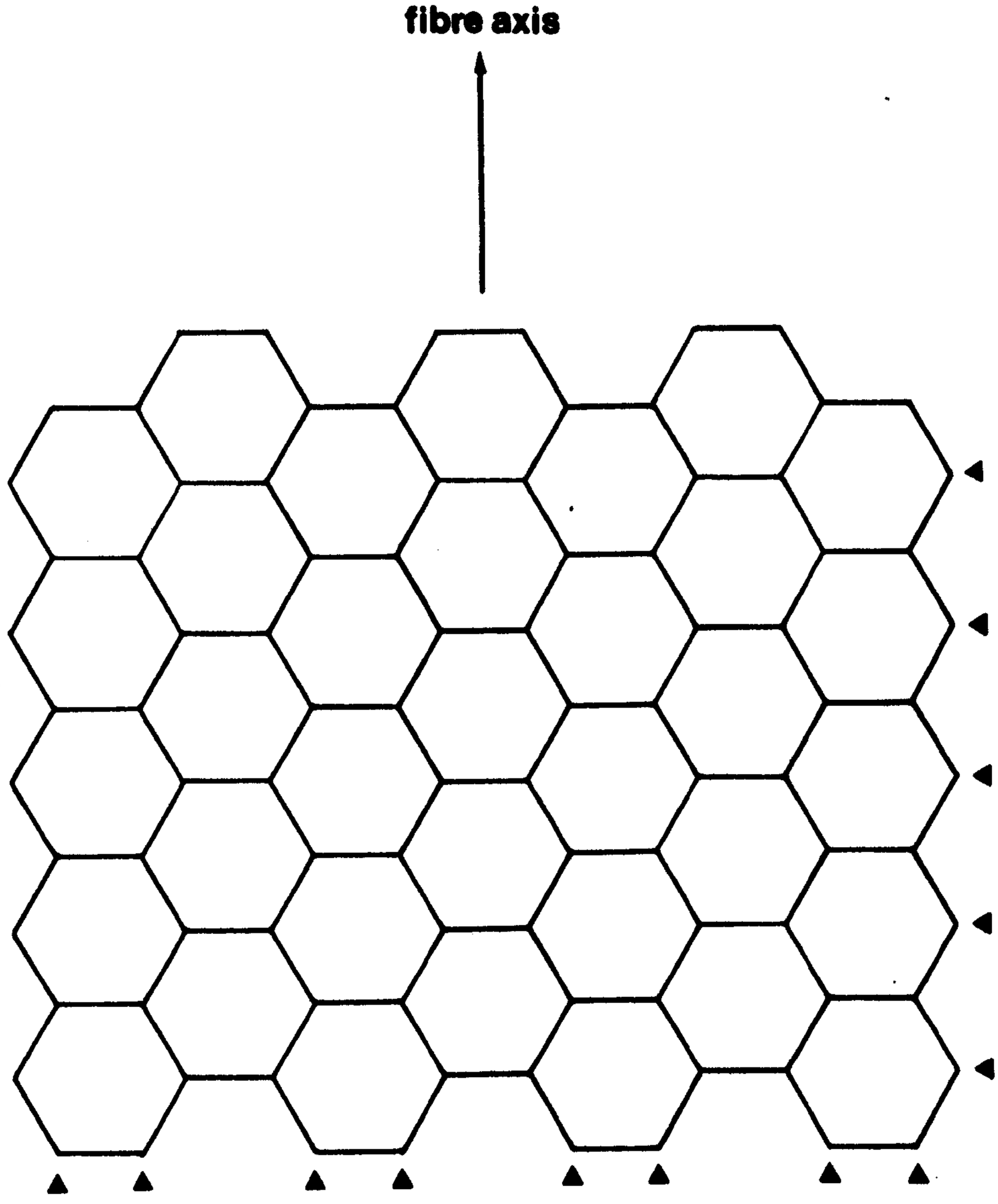

Fig. 14. a-axis orientation in carbon fibres. Carbon atoms having an unsatisfied valence are arrowed.

spacings were possible in graphite - 0.3345 nm for three-dimensionally stacked sheets, and 0.3440 nm for turbostratic stacking. Using the expression of Takahashi et al.[68], relating c/2 to L_a, Rose predicted a limiting value for L_a of about 20 nm for PAN-based fibres heat treated to 3000°C. It was claimed that this is directly related to the fibril diameter of 40 nm said to exist in the precursor fibres, as it was thought that this might reduce to about 20 nm because of lateral shrinkage during high-temperature heat treatment. Extrapolation of the c/2 against Z relationship to an orientation of Z=0° suggested an interlayer spacing very close to that of three-dimensional graphite. It was proposed that practical achievement of such orientation, for example by hot stretching, is precluded by the complex wrinkled nature of the elemental ribbons which, it was thought, constitute the basic fine structure of the fibre.

Structural development during the pyrolysis of PAN in the temperature range 320 - 1000°C has been studied by Oates and Johnson[69,70], who conclude that although the mean stacking size, L_c, does not alter appreciably throughout the range, the crystallite length along the fibre axis, $L_{a//}$, increases from 1.9 nm at 320°C to 2.5 nm at 1000°C. Of greater significance, the intensity of the (100) meridional reflection increases appreciably, indicating the development of longer, highly-imperfect, cyclized structures. However, the (100) equatorial reflection remains almost negligibly small up to a heat-treatment temperature of about 700°C, whereupon there is a significant increase. This indicates that there is no diffraction evidence for crosslinking of ladder polymer prependicular to the fibre axis until this temperature is reached.

In a low-angle x-ray scattering study, Tyson[71] has attempted to combine structural parameters with strength and failure-strain data in an elastic-plastic theory of failure (see section 1.3.5). He

characterized a disordered phase, which was claimed to contain nitrogen and carbon in highly-distorted, imperfectly-formed layers, in terms of density, volume and size. These x-ray parameters all increase more rapidly beyond about 1600°C, which was proposed to be the temperature above which buckling forms the means of fibre failure. At 1000°C it was proposed that the more isotropic nature of the fibre, and the stronger longitudinal boundaries prevent this type of failure.

B. The microstructure of carbon fibres

Johnson and Watt[72] first showed micrographs of thin, ultra-microtomed sections of carbon fibres; samples heat treated at 2500°C revealed an internal structure of long, narrow, axially-aligned units, 10 nm in width, and of indeterminate length. Specimens heat treated to 1000°C invariably ruptured along their length during sectioning, and opened to give a net-like structure of fibrillar units 80 - 100 nm in diameter, apparently running the entire length of the fibre. It was tentatively suggested that this structure may have been derived from the fibrillar nature of the precursor PAN. Support for the fibrillar fine structure of type I fibres was independently provided by Badami et al.[55], who measured stacking sizes of about 5 nm from low-resolution dark-field images. Although unappreciated at the time, this publication also presented the first evidence of structural heterogeneity in high-temperature fibres, when a 'skin' of high preferred orientation was observed at the edge of the sections. A transverse section of a high-modulus fibre was also depicted, but no comment regarding its structure was made. However, it was observed that the coarsely-fluted outer surface of the PAN fibres was retained throughout the manufacturing process.

From medium-resolution dark-field micrographs, Johnson and Tyson[59] were able to show that there is an almost normal distribution of stacking sizes in fibres heat treated at 2650°C. The mean size was

found to be 6.5 nm, close to the x-ray diffraction value of 6.0 nm, and that 99.7% of the crystallites have widths between 2 nm and 11 nm. Many small pores less than 1 nm in width were also observed, but it was appreciated that quantitative analysis of features of this size is invalidated by choice of an inappropriate level of objective-lens defocus (see Appendix 1). A three-dimensionally graphitic phase was also found in these preparations, and although it was suspected that this may have been a surface phenomenon this remained unsubstantiated after ion etching of the fibres. Consequently, it was proposed that the more perfect graphite phase is distributed throughout the fibre, and that it may cause the large scale intensity variations observed in longitudinal sections.

In a study of very highly-oriented rayon-based carbon fibres, Fourdeux et al.[73] were able to show that partial graphitization had occurred; subsequently the dependence of 'graphitization' on heat-treatment temperature and degree of stretch was examined by electron diffraction[74]. They observed hkℓ modulations in fibres heat-treated at 2900°C and stretched to give a Young's modulus of about 140 GNm^{-2}. Transmission electron-microscope evidence supported a fibrillar fine structure, with the main axis of the fibrils always parallel to the fibre axis. In fibres of low preferred orientation it was proposed that the fibrils were wrinkled, but became progressively straighter with increasing preferred orientation.

Although medium-resolution transmission electron microscopy had appeared successful in the characterization of the gross fibrillar texture of carbon fibres it could yield no information concerning the stacking of individual basal planes, and crystallite aggregation and interlinking. This however, became available in 1968, when, using the phase-contrast technique developed by Heidenreich et al.[75], lattice-

fringe images of the graphite layers were obtained. Measurements of stacking size seemed to correlate well with x-ray diffraction estimates, but the size of the layers in the direction of the fibre axis appeared to be considerably larger (several hundred nm) than previously supposed[94]. The layers however, exhibited straight and curved sequences; the straight parts being 10 - 30 nm long, and the curved sections 5 - 10 nm long. The angle between two consecutive straight crystallites was found to be within the angular spread of the 002 diffraction arc.

Similar phase-contrast techniques have been used to examine cellulose-based[76] and PAN-based[77] carbon fibres. Hugo et al.[76] observed thin regions at the surface of fluted fibres, and found that the layer planes are essentially continuous over long distances in the direction of the fibre axis, micropores being formed by changes in plane direction. The continuous, but imperfect nature of the basal planes has been confirmed by Johnson[77], who also proposed that the observed dark extinction bands arise where layer planes are distorted out of the diffraction condition. Longitudinal and transverse sections examined by Phillips et al.[78] indicated high preferred axial orientation, but no preferred orientation in the cross-section, where layer-plane packets showed considerable curvature and a random arrangement about the fibre axis. Moiré fringes suggested that the plane packets did not extend through the full thickness of the slice but formed a complex three-dimensional network, thus limiting the dimensions observable in any thin section.

In an attempt to correlate structural changes during pyrolysis with the chemistry of the process, colleagues in this laboratory[61,79], in collaboration with RAE[70], have examined fragmented PAN-based fibres heat-treated in the range 320 - 3000°C. They were unable to find any evidence of a fibrillar texture in the low heat-treatment range

(320 - 1000°C), and proposed instead complex and extensive crystallite interlinking. Qualitative examination of micrographs recorded at the appropriate level of defocus suggested developing order, length, and packing of the lattice planes. At 320°C fringes were visible over lengths of 1 - 1.5 nm, and it was proposed that these represented the ladder-polymer fragments present after that heat-treatment. At 410°C the length had grown to about 3.0 nm, at 800°C to 5.0 nm; at the highest heat-treatment temperature there was an improvement in lattice-fringe contrast thought to be due to the increase in $L_{a\perp}$ by crosslinking.

Fourdeux et al.[74] have predicted from high-resolution phase-contrast lattice-fringe images the length of the layer planes in high-modulus fibres of very high preferred orientation. Their results indicated that the planes were continuous over lengths of 1 - 10 μm, of the same order as the range of lengths of extended chains in medium to high molecular weight polymers. Analysis of (002) dark-field images enabled accurate crystallite width (stacking size, L_c) calculations, and the use of (100) dark-field techniques verified the turbostratic disorder present in the layer stacking. It was claimed that the micrographs were in good agreement with the 'wrinkled-ribbon' structural model.

This 'wrinkled-ribbon' model for fibre fine structure was reviewed in the light of more detailed structural studies in 1971[63]. Extinction bands in (002) dark-field images were attributed to a Moiré effect resulting from a superposition of two microfibrils with their layer planes in the (002) diffraction condition, but tilted by a small angle with respect to each other. The variations in spacing in the Moiré pattern along a given microfibril were presented as further evidence for the existence of smoothly curved regions as

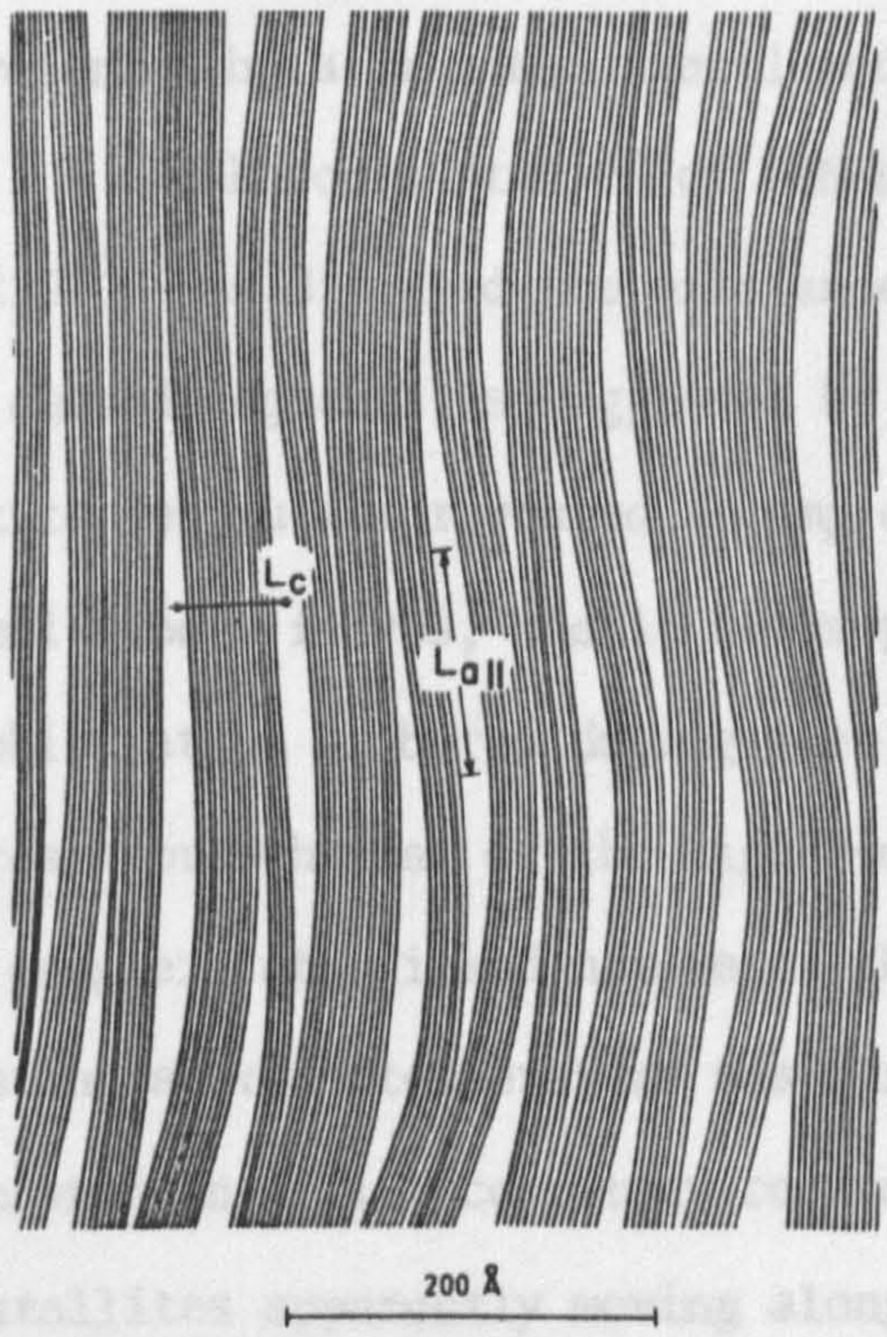

Fig. 15. The wrinkled-ribbon model of carbon fibre structure. After Fourdeux et al.[63].

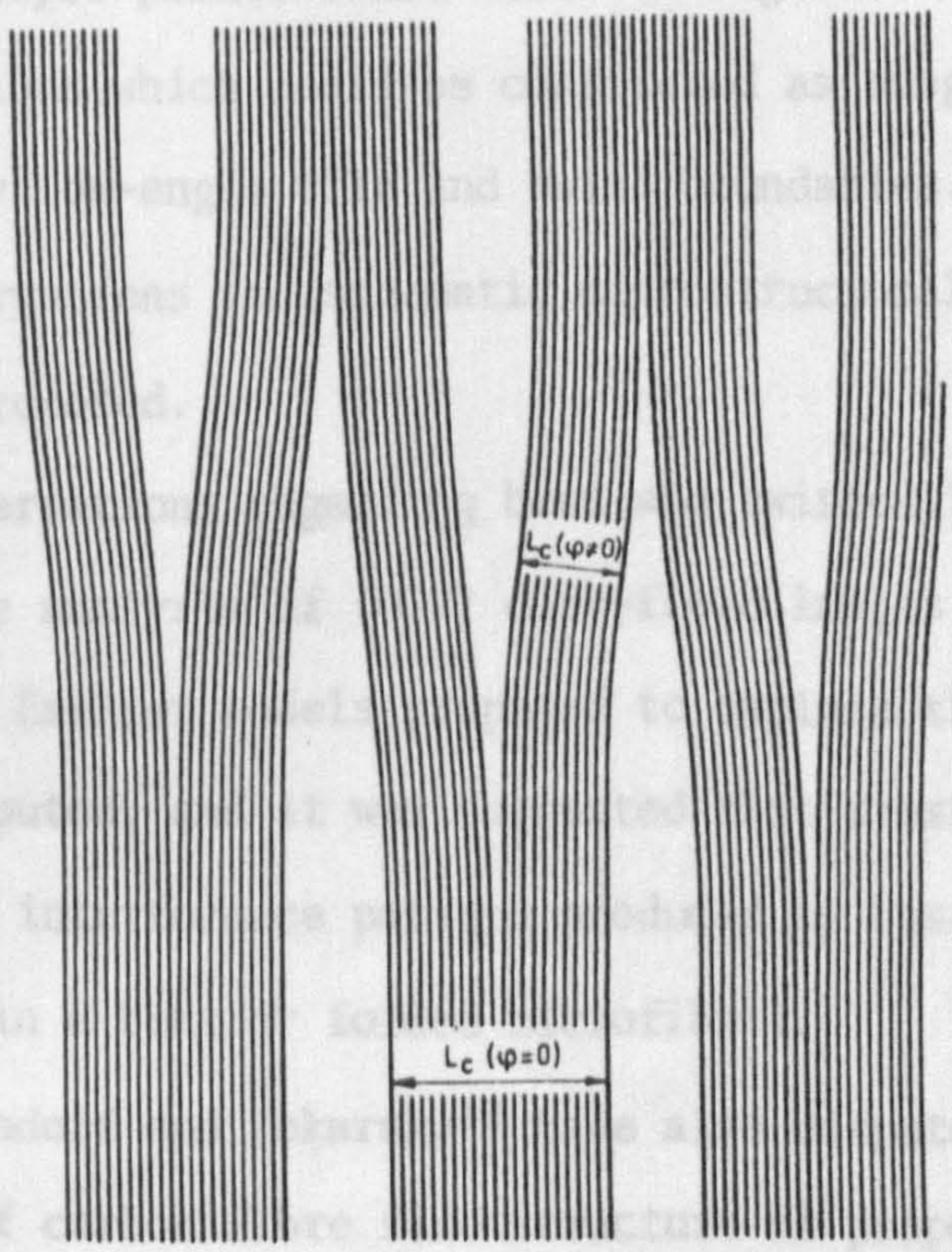

Fig. 16. The branched-fibril model explaining the dependence of stacking size on crystallite orientation. After Fourdeux et al.[63].

predicted by their model (Fig. 15). The dependence of stacking size on crystallite orientation, referred to in section 1.3.2.*A* above, was represented by a branched fibril model (Fig. 16).

Johnson's study[80] of PAN-based carbon fibres heat treated to 2500°C has disputed the existence of regular sequences of straight and curved segments as suggested by Ruland and his team. Direct lattice resolution revealed a complex three-dimensional structure in normal type I fibres, and it was proposed that only after stress graphitization or boron doping does the fine structure of PAN-based fibres approach that of the highly-oriented cellulose-based fibres. The complex interlinked nature of the turbostratic crystallites existing at this temperature was further confirmed by Crawford and Johnson[81] in 1971. Accurately controlled tilting experiments showed crystallites apparently moving along tilt axes without any sharp boundaries - indicating layer-plane continuity over a much greater length than envisaged in a single image. The existence of twist boundaries was supported by lattice-resolution pictures, and it was proposed that individual layer planes could well run together in small numbers through regions which could be considered as subgrains since they were related by low-angle tilt and twist boundaries. As a consequence of these observations the schematic microstructural model depicted in Fig. 17 was proposed.

Some of the observations regarding bent and twisted ribbons have been confirmed by the analysis of (002) dark-field images by Stewart and Feughelman[82]. Earlier models proposed to explain the dark extinction bands were disputed, and it was suggested that crossbanding could be attributed to an interference pattern produced by basal planes crossing over within a bent or folded microfibril.

Recently, Diefendorf and Tokarsky[53] have also disputed the 'wrinkled ribbon' model of carbon fibre fine structure as proposed by

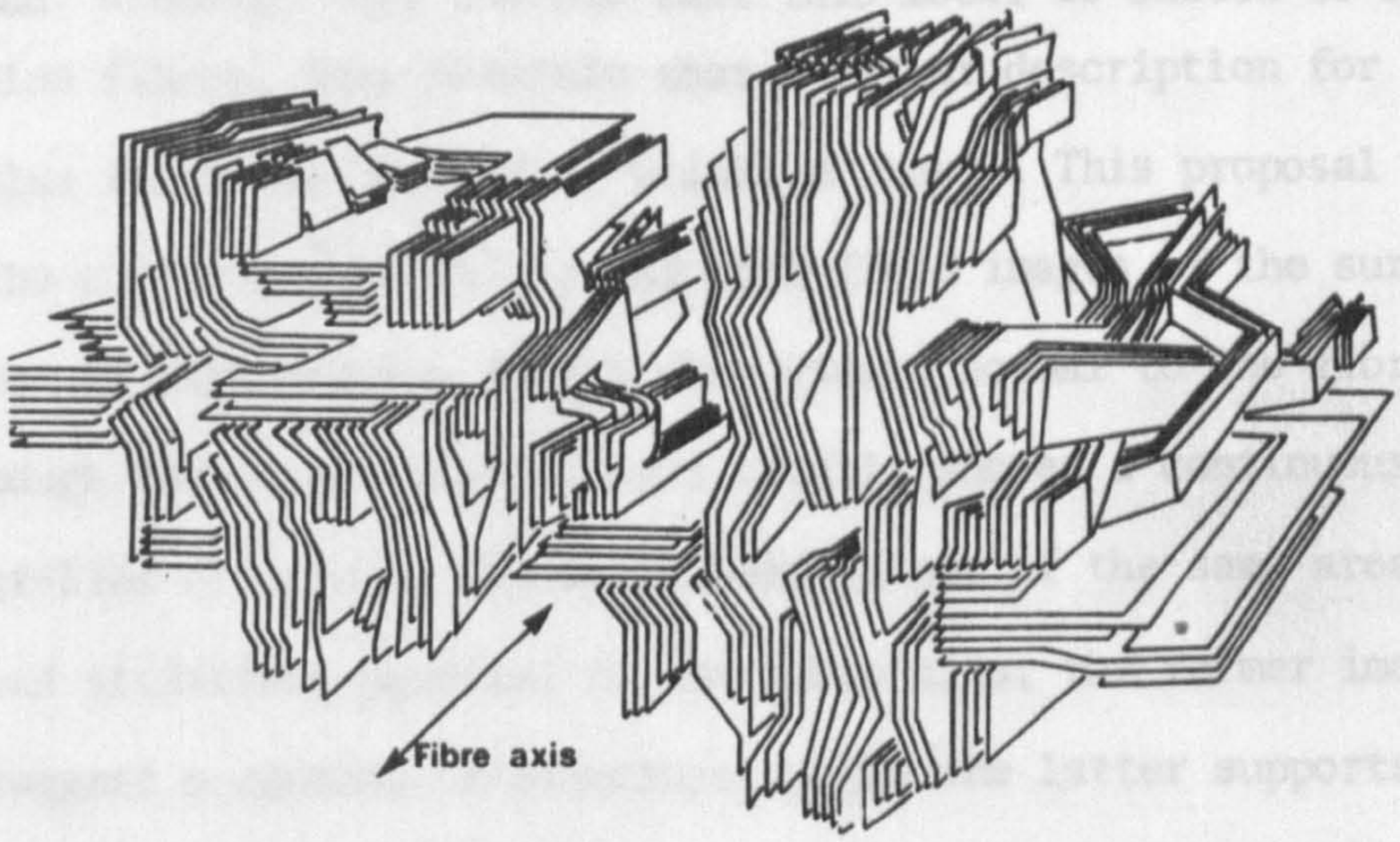

Fig. 17. Three-dimensional structural model of type I fibres. After Crawford and Johnson[81].

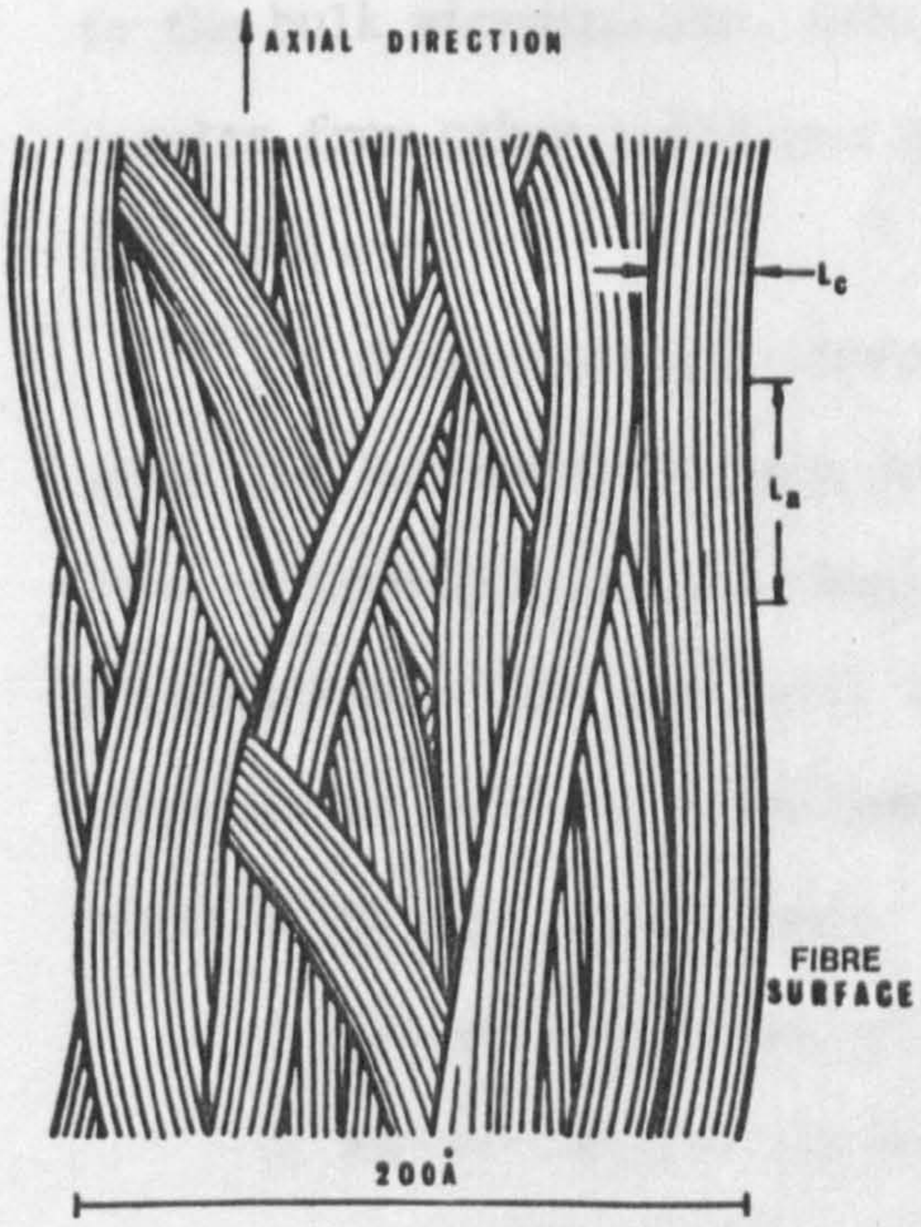

Fig. 18. Basket-weave structural model. After Diefendorf and Tokarsky[53].

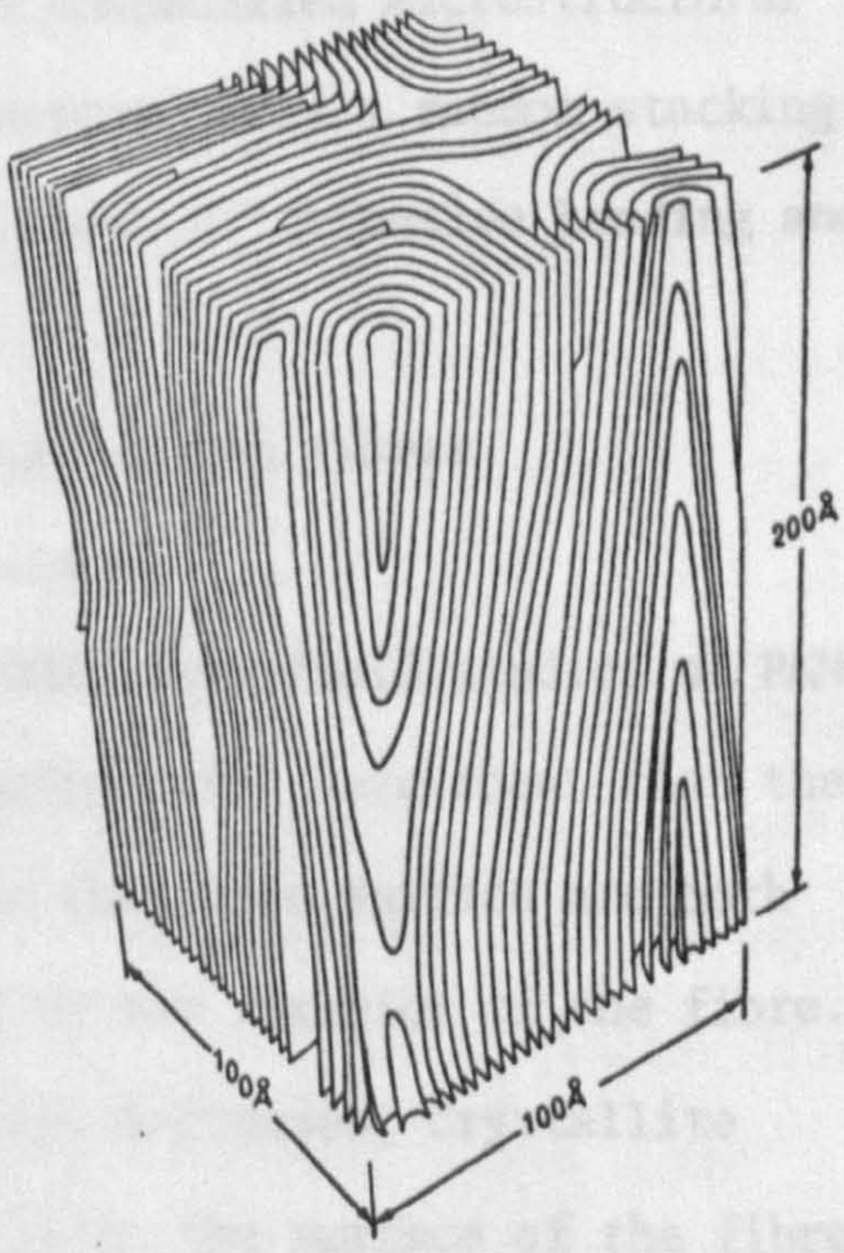

Fig. 19. The three-dimensional structural model of Wicks[98].

Ruland. Although they concede that this model is suited to low-modulus fibres, they maintain that a better description for higher-modulus fibres is that of a 'wrinkled sheet'. This proposal is based on the comparison of bright and dark-field images of the surface layers of high-modulus fibres when viewed normal to the fibre surface. Although the bright-field images clearly showed a continuous, rippled, sheet-like structure, the dark-field images of the same area merely showed striations parallel to the fibre axis; the former image tends to suggest a continuous structure, while the latter supports the fibrillar model. However, this technique of examination is limited to within a few tens of nanometres at the fibre surface, and should be questioned if attempts are made to relate the observed structure to the bulk microtexture. Indeed, the authors have interpreted their results from other techniques in terms of a 'basket-weave' model (Fig. 18).

A distinctly different three-dimensional structural model (Fig. 19) has recently been developed by Wicks[98], who used results from neutron irradiation coupled with unspecified microstructural observations. This new model is characterized by a random stacking sequence in transverse section, with zones of extensive bending and twisting of the layer planes.

C. The macrostructure of PAN-based carbon fibres

a. Fibres of circular cross-section

Electron-diffraction and (002) dark-field studies of PAN-based carbon fibres by Butler and Diefendorf[83] have shown that the turbostratic graphite crystallites at the fibre surface are both larger and more highly oriented than in the interior of the fibre. It was also proposed that as fibre modulus increases, crystallite alignment increases more significantly at the surface of the fibre

than in the core. The coexistence of two such phases has been confirmed by the dark-field study of Badami et al.[55], although they did not interpret their results in terms of a 'sheath-core' model.

The appreciation that such a bi-component structure existed in high-modulus carbon fibres led Watt and Johnson[84] to examine polished longitudinal sections of specimens heat treated at 2600°C. It was found that holes had formed as if from bubbles inside the fibre, but that their formation depended on the type of preoxidation treatment experienced by the precursor material. In particular, short stabilization times would generally lead to zone formation, and complete stabilization tended to give a homogeneous fibre. Following the discovery of holes in fibres heat treated to 2500°C the existence of compatible zones was found in the oxidized-only fibres. Both transverse and longitudinal polished sections of 3 denier PAN fibres heated in air for 2 hours at 220°C showed the presence of an outer zone or 'sheath' surrounding a darker inner zone or 'core', and it was considered that this inner core was unoxidized PAN which had polished differently from the outer zone of fully-oxidized material. Consequently, it was proposed that the rate of oxidation is a diffusion-controlled process, and this was verified by measuring zone thickness as a function of time of oxidation. It was found that the 'oxidized' zone thickness was directly proportional to the square root of the oxidation time.

Subsequent optical studies[53,64,85,86,87,88,89] have shown that in fully-stabilized PAN-based carbon fibres of a circular cross-section a *circumferential* crystallite orientation develops during high-temperature heat treatment (Fig. 20). If, however, similar fibres are under-stabilized a *radial* orientation develops in the under-oxidized core, while a *circumferential* texture is formed in the fully-oxidized sheath (Fig. 21). The thickness of the sheath was found to be

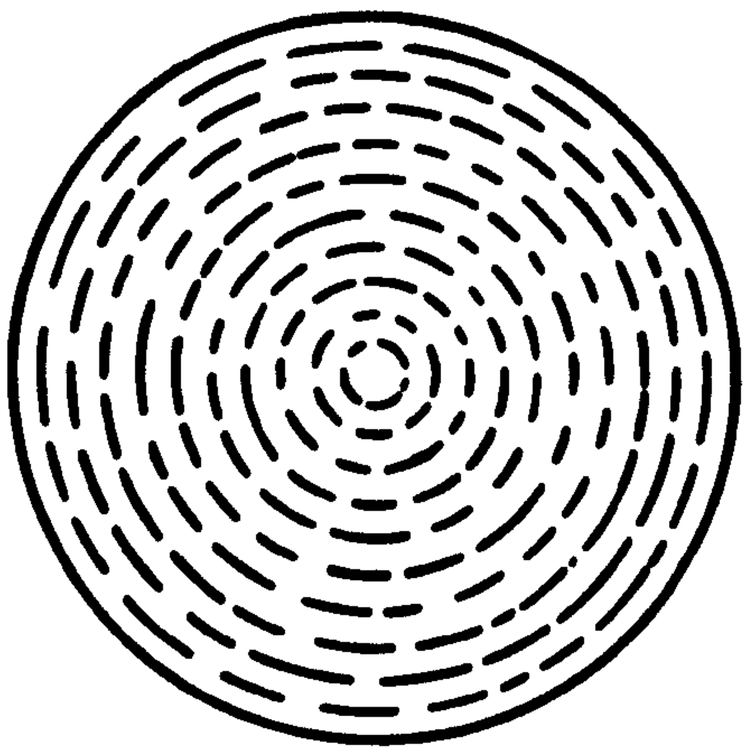

Fig. 20. Circumferential crystallite orientation of fully-stabilized circular cross section fibres.

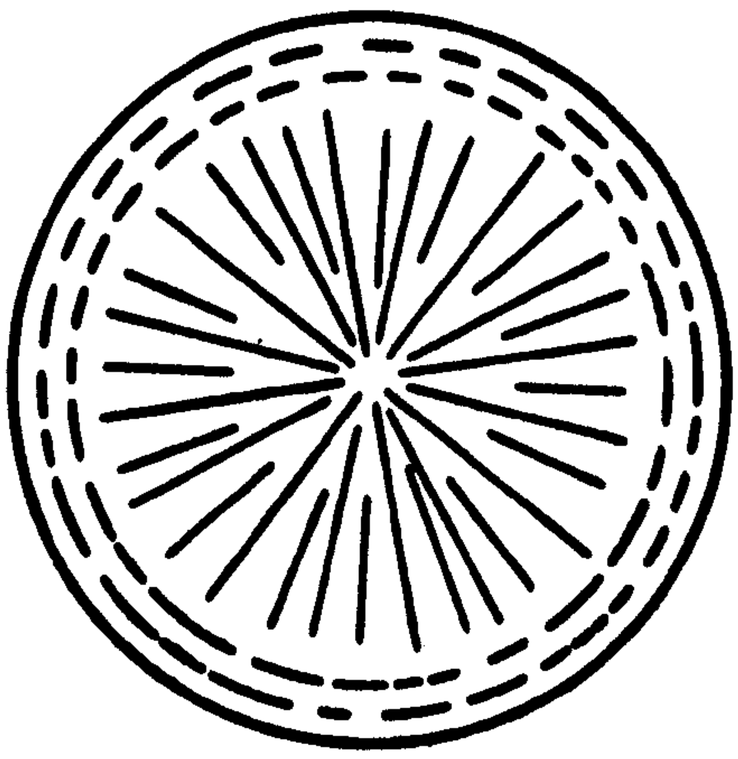

Fig. 21. Radial-circumferential crystallite orientation of partially-stabilized circular cross section fibres.

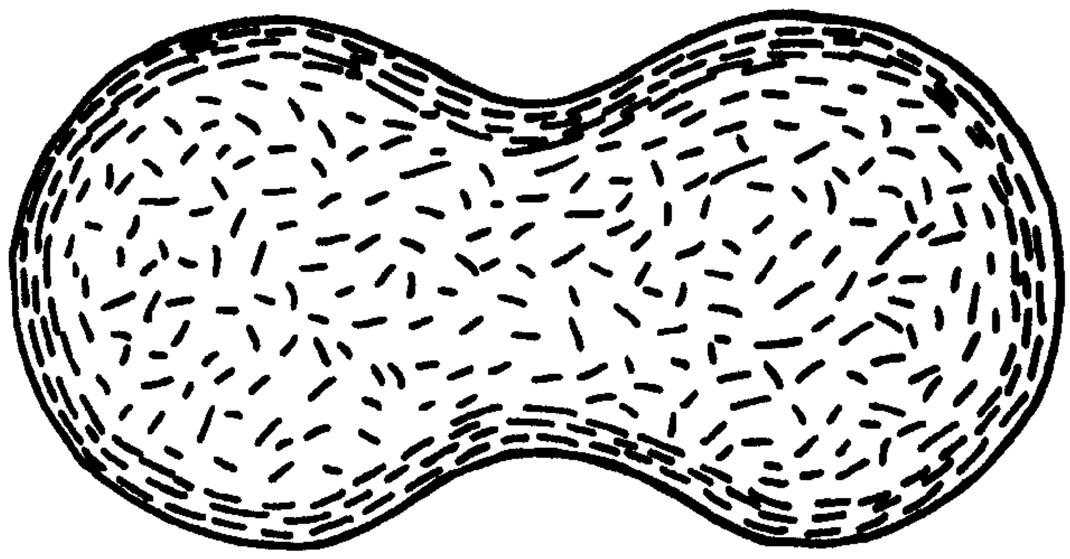

Fig. 22. Random crystallite orientation in the core of dog-bone cross section fibres.

a unique function of oxidation time, irrespective of fibre diameter, thus confirming the diffusion-controlled nature of the low-temperature stabilization process. Polarized-light microscopy[87a] suggested that in very thick fibres alternate circumferential and radial zones are formed; in nearly all cases a core, of varying dimensions, with no c-axis preferred orientation was observed. In the outer sheath, blocks of layer planes less than 500 nm in width were observed to follow the fibre surface.

The co-existence of at least two structurally different phases in type I fibres was first verified at lattice-resolution level by Johnson et al.[90] in 1973. This study indicated the presence of two distinct turbostratic graphite phases (T1 and T2) together with a small proportion of a third component (G) composed of more perfect three-dimensional graphite. T1 was designated as a well-oriented, highly-crystalline, but turbostratic graphite phase of preferred orientation about 15^{o}, T2 was a less well-oriented, less-crystalline, turbostratic phase of preferred orientation about 24^{o}, and G represented a three-dimensional graphitic phase of preferred orientation better than 5^{o}. In keeping with earlier work[47,83,91] it was proposed that the T1 phase originated from the highly-oriented sheath, and the T2 phase from the less well-oriented core; it was concluded that the presence of the T2 phase would lead to a reduction in Young's modulus, and also, because of the presence of many micro-voids, in tensile strength. The origin of the G phase was proposed to be due to collapse of an un-oxidized core on heat treatment to $2500^{o}C$ with the formation of highly graphitic lamellar sheets, as proposed by earlier workers[92,93], or that it had occurred as a surface artefact during heat treatment. Either mechanism was shown to be possible by the fact that there was no evidence for more than one phase in carbon

fibres heated at 1000°C only.

In a recent attempt to characterize the three-dimensional structure of circular carbon fibres ex-PAN heat treated at 1600, 1900 and 2500°C, Wicks and Coyle[87a] have used the technique of electron diffraction to study tapered fibres produced by flame polishing. Their results suggest that there is a trend of *increasing* alignment with respect to the fibre axis, and *decreasing* crystallite size from the centre to the surface of all the fibre types, although the effects are more pronounced in fibres heat treated at 2500°C. They conclude that in these latter fibres two distinct regions can be distinguished, viz:

(i) an inner region or core characterized by relatively low axial alignment and large crystallite size, and

(ii) an outer sleeve or sheath of material of high axial preferred orientation and low average crystallite size.

The proposed transition annulus between the two zones was found to be distinct with a thickness of about 1 μm, and separated a core approximately 3 μm in diameter from a sheath about 1.5 μm in thickness. (These zones were claimed to be the 'oxidation' zones first observed by Watt and Johnson[84]). An attempt was made to verify the observation of the trend of decreasing crystallite size from the centre to the surface of the fibre using single fibre x-ray analysis. Surface material was removed from the 2500°C fibres by oxidation, and the x-ray patterns compared with those obtained from unoxidized fibres. The results showed, significantly, that there is a trend of *increasing* stacking size from the centre to the surface of the fibre, although the data referring to orientation confirmed the earlier findings from the electron-diffraction analysis. Also, it is significant that for fibres heat-treated at 1600°C no variation in structure was discernible between thinned and un-oxidized fibres, and it was concluded that microstructural variations within these fibres are relatively minor,

and are only developed at higher heat-treatment temperatures.

Confirming the existence of two phases in circular cross-section PAN-based type I fibres, Larsen and Smith[87] were able to identify a circumferentially-oriented surface skin in transverse sections. However, their micrographs clearly show that the thickness of this sheath is incompatible with the observed 'oxidation-zone' thickness, and they were unable to produce evidence of the proposed radial orientation in the under-stabilized core.

b. Fibres of non-circular cross-section

With the exception of an outer sheath showing a crystallite orientation parallel to the fibre surface, fibres having a 'dog-bone' cross-sectional shape have been shown[85,88] to possess no preferred c-axis orientation in transverse section (Fig. 22). Recently, however, Watt and Johnson[17] have shown that under normal stabilization conditions such fibres do not develop oxidation zones; these are only observed after the fibres have been subjected to a vacuum heat-treatment at 220°C prior to oxidation. This suggests that, because of the different chemical composition of these fibres, a homogeneous macrotexture might be developed at higher heat-treatment temperatures.

1.3.3 Defect structure of carbon fibres

A. Internal flaws

High-voltage electron microscopy has proved useful in the study of macro internal defects in carbon fibres. Sharp and Burnay[49] have examined fibres of 8 μm diameter at 1MV and characterized the type, size and frequency of flaws found in PAN-based fibres heat treated in the temperature range 1000 - 3200°C. The defect characteristic of type I fibres was found to be a bubble or void elongated along the fibre axis, such flaws often occurring in groups joined together by narrow holes. Although defects up to 3 μm in diameter were observed

the most frequent size was found to be about 1 μm, present at a rate of about 1 per mm on average. Examination of fibres heat-treated between 1000 and 3200°C showed that this type of defect is only present after heat-treatment above 1800°C; fibres treated at low temperatures were found to contain only small inclusions up to 1 μm in diameter. Consequently, it was proposed that the flaws exhibited by type I fibres are caused by volatilization of inclusions seen in fibres heat treated at lower temperatures.

Later, Sharp et al.[95] were able to characterize the nature of flaws in both PAN and rayon-based carbon fibres, observing central cavities, diconical voids, irregular inclusions and needle-shaped cavities. It was found that these flaws tended to introduce mis-oriented crystallites into the fibre, the basal planes of which were often inclined at greater than average angles to the fibre axis. This would result in large concentrations of shear strain energy in these regions when the fibres are loaded in tension to typical breaking loads. These large localized concentrations can only be relieved by cracks normal to the basal planes - leading to fibre failure (see also section 1.3.5).

The work of Johnson[42] and Thorne[43] had proved that many flaw-causing impurities in carbon fibres could be identified using scanning electron microscopy, and the existence of voids in fracture surfaces of type I fibres has been verified by Johnson[89]. In a successful attempt to relate the fall-off in tensile strength at heat-treatment temperatures above 1500°C to the presence of internal voids, the RAE team developed a clean-room spinning technique[50,51,52]. Of twenty-four broken fibres examined in a scanning electron microscope no internal voids were found, and in all cases failure was initiated at a surface flaw. Additionally, it was found that fibres broken at

low strengths had large surface flaws and relatively smooth fracture surfaces, whereas high-strength fibres had small surface flaws and much rougher surfaces.

Thorne[54] has shown that high-quality optical microscopy is useful in the examination of fractured fibre ends. He was able to successfully locate fracture initiation points in type A fibres, both with and without a surface treatment.

It is well established that partial oxidation produces apparently different zones in precursor-PAN which are present throughout subsequent heat treatment. Johnson et al.[92], by using a short, high-temperature oxidation at 300°C and rapid carbonization rates, have produced fibres containing axially-aligned holes. A scanning electron-microscope study showed that heat-treatment at 2200 - 2600°C produced concentric lamellar graphite structures surrounding the central hole or cavity, and that the material around the outer surface of the fibre also appeared to form lamellae.

In an attempt to explain the anomalous tensile and compressive strengths of carbon fibres Barnet and Noor[99,100] have examined the effect of plasma-etching on embedded PAN-based fibres. The patterns resulting from this etching technique suggest to the authors that the fibres consist of a highly-crystalline surface sheath, a core section, and a number of connecting webs forming a radial continuum. It was proposed that random pockets of less-crystalline material were found between these webs, and that the macro-structure was characterized by large voids, internal cracks, highly-stressed regions, and surface flaws. These findings are summarized in Fig. 23. It was further claimed that this type of macrostructure is very similar to that found in acrylic fibres spun under high spin-draw ratios, and at high temperatures from a low-concentration spinning solution.

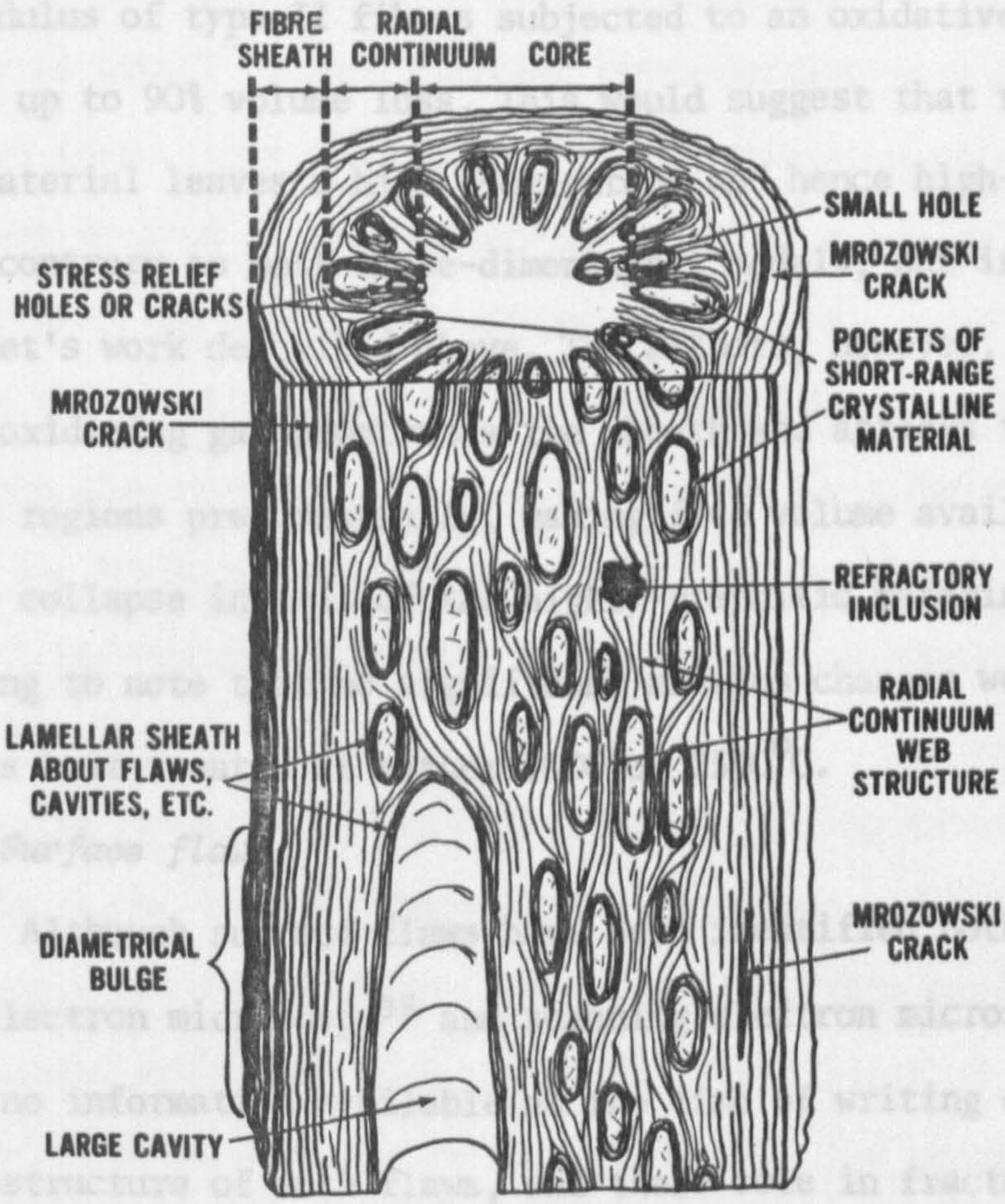

Fig. 23. The three-dimensional structural model of Barnet and Noor[99,100].

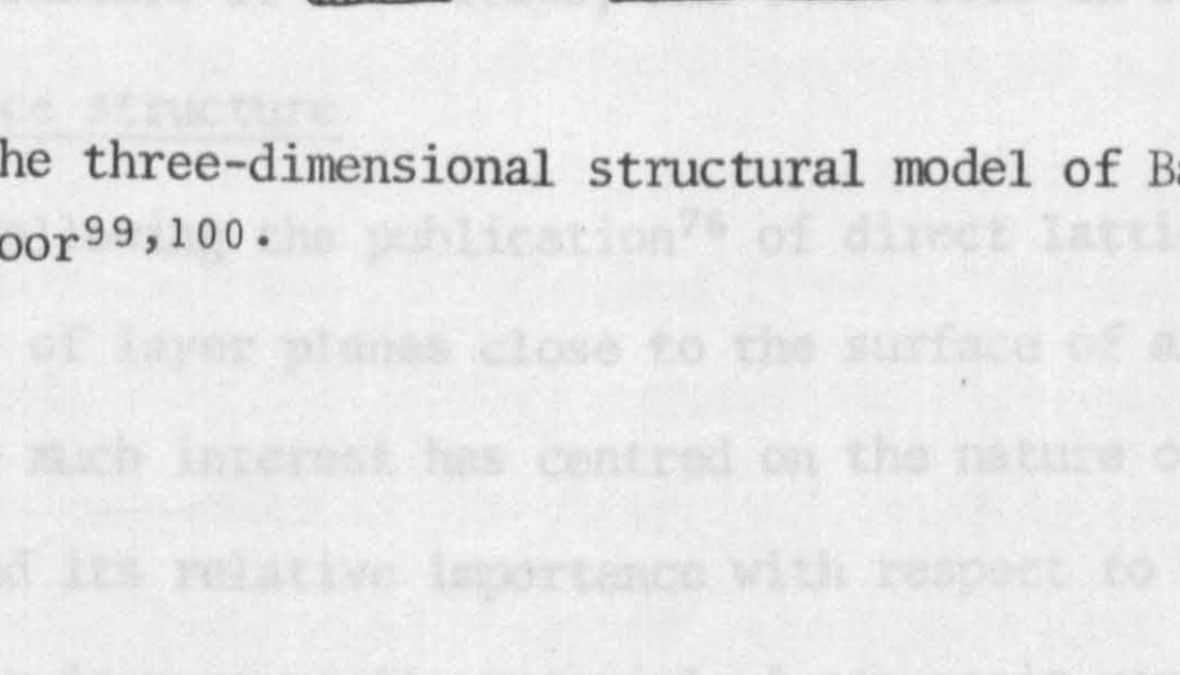

Fig. 24. Schematic representation of surface structure. After Roberts[76].

Hart and Pritchard[101,102] have reported substantial increases in the modulus of type II fibres subjected to an oxidative treatment producing up to 90% volume loss. This would suggest that removal of 'sheath' material leaves a highly-oriented, and hence high-modulus 'core' - contrary to most three-dimensional models, but in agreement with Barnet's work described above. The authors, however, proposed that the oxidizing gas penetrates the sheath and attacks the less graphitic regions preferentially, making free volume available for 'stepwise collapse inwards of the highly-graphitic material'. It is interesting to note that no significant modulus changes were reported for fibres heat-treated at either 1000 or 2500°C.

B. Surface flaws

Although surface flaws have been identified both by high-voltage electron microscopy[95] and scanning electron microscopy[89], there is no information available at the time of writing concerning the microstructure of such flaws, and their role in fracture mechanisms.

1.3.4 Surface structure

Following the publication[76] of direct lattice-resolution micrographs of layer planes close to the surface of a fluted rayon-based fibre much interest has centred on the nature of the fibre surface, and its relative importance with respect to bonding to the resin matrix in a composite material. A schematic representation of the model derived from a high-resolution study of rayon-based fibres is shown in Fig. 24 and this indicates an essentially basal-plane fibre surface.

The physical structure of carbon-fibre surfaces is of considerable importance in determining the interfacial area available for bonding between the fibre and the matrix in a composite structure.

Rayon-based fibres invariably exhibit regular, fluted cross-sections, with longitudinal grooves and striations, whereas, by contrast, PAN-based fibres usually show a circular cross-section with a relatively smooth and featureless topography. Scanning electron microscopy of fibres heat-treated at low temperatures indicated a highly-porous, rough surface, the effect of high-temperature heat treatment being to reduce the porosity open to the surface and anneal out much of the surface roughness[103]. The effect of oxidative treatments is to increase the surface area irrespective of heat-treatment temperature, with a corresponding significant increase in interlaminar shear strength[103,104,105].

The essentially basal-plane nature of *rayon*-based type I carbon fibres has recently been disputed by Bless and Lando[106]. The Raman spectra for carbon fibres is induced in a thin surface layer of the sample, due to the high extinction coefficient of graphite for the laser beam, and thus reflects primarily the properties of the surface layers. The results obtained suggest that a cellulose-based fibre of modulus 730 GNm^{-2} has an average surface crystallite diameter of 22 nm, whereas a PAN-based fibre of modulus 700 GNm^{-2} has an essentially infinite surface crystallite size, and hence a very low edge-concentration at the fibre surface. This indicates that the surface of very high-modulus carbon fibres made from an acrylic precursor is basal plane in nature.

1.3.5 The Relationship between Structure and Mechanical Properties

It is important to know the crystallographic orientation and perfection of the basal planes within the turbostratic graphite crystallites in carbon fibres, since these determine the strength and modulus of the fibre, and at the surface will determine the wetting and bonding characteristics of the resin to the fibre. Since the graphite

structure is strong in the two orthogonal directions of the layer plane, and weak in the third, perpendicular to the layer plane and parallel to the c-axis, any graphite layer plane slightly mis-oriented from the fibre axis will allow shear to become operative with a drastic lowering in fibre modulus. The fibre strength, however, will be a function not only of surface flaws and related effects, but of the axial and radial macrotextures. The strength of a carbon fibre-reinforced composite will depend largely on how efficiently the shear stress at and near the fibre/matrix interface can be transferred to the core of the fibre.

Ruland[57] has compared 'uniform strain', 'uniform stress', and 'elastic unwrinkling' models to explain the relationship between Young's modulus and preferred orientation. A subsequent study[107] of various higher modulus carbon fibres, however, has tended to indicate that the latter model is the only one consistent with experimental observations.

Reynolds, however, in measuring the orientation function for various single carbon fibres as a function of applied stress[108], has found that the experimental values of, for example, shear modulus, best fit the 'uniform stress' model. This leads to the idea that the graphite crystallites may be thought of as connected in series, and that individual carbon hexagon planes may extend over several crystallite diameters. This model is supported by the observed[36] non-Hookean behaviour of carbon fibres. The very high measured values of shear modulus (25 GNm^{-2} compared with theoretical predictions of 10 GNm^{-2}) would appear to cast doubt on the single fibrillar structures proposed by Ruland for type I fibres, as these fibrils would be expected to roll over each other as the fibre is twisted. However, Henrichsen and Fishbach[109] have recently stated that the torsional

behaviour of single carbon fibres is dominated by the structure and properties of the material at, or close to, the surface of the fibre, so interpretations of mechanical properties in terms of a homogeneous structure may well be erroneous.

Thorne[43] has shown that there is a linear relationship between ultimate tensile strength and modulus up to a heat-treatment temperature of 1000°C, with a constant breaking strain of about 1%. This relatively low value of strain-at-failure was found to be due to the operation of internal flaws which originate in the precursor PAN. For really high-strength fibres it was recommended that the concentration of such flaws should be less than 1 per 100 mm, and that the less well-defined surface flaws should be removed. Fibres fulfilling these conditions could be expected to have strengths around 5 GNm^{-2}, and breaking strains of 2 - 3%.

In the Griffith equation the size of basal cracks, c, is given by:-

$$c = \frac{\alpha}{\pi} \cdot \frac{2E}{\sigma^2} \qquad \text{.....(1)}$$

where α is the surface free energy, E is the modulus, and σ the ultimate tensile strength. From this relationship a strength against defect size plot can be made for any given surface free energy (Fig. 25).

Since carbon fibres fail in an apparently brittle manner, Whitney and Kimmel[110] have used a Griffith failure criterion to elucidate fracture mechanisms. For an ideally brittle material, α (from Eqn. 1) should correspond simply to the energy required to break primary chemical bonds, but since it is thought that large amounts of plastic work are done at the crack tip, the observed values of α are much higher than would otherwise be expected. A good agreement between calculated and observed crack dimensions was reported for a range of type I carbon fibres from various sources, and a comparison

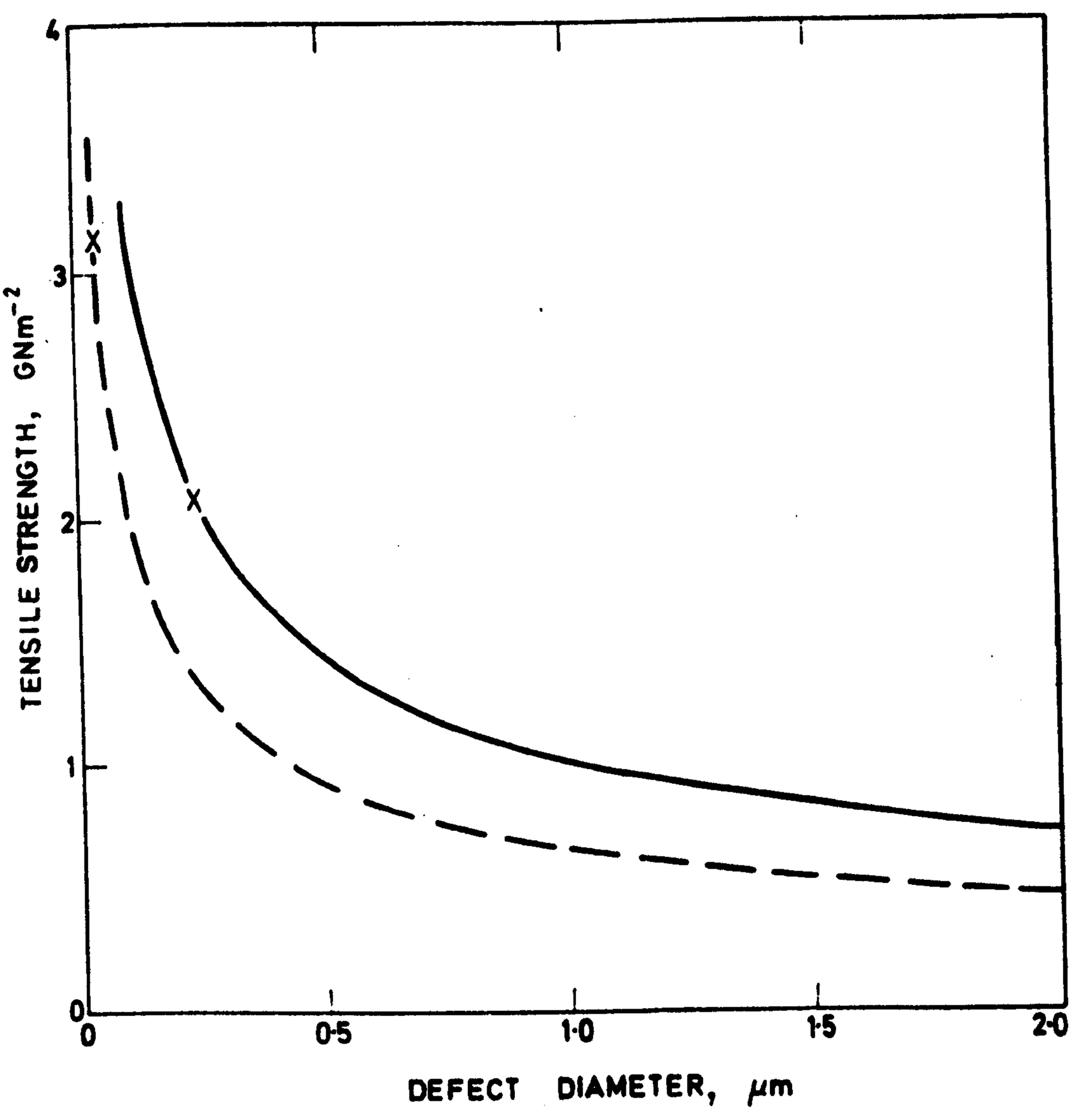

Fig. 25. Theoretical strength vs. defect size for type I (solid line) and type II (dashed line) fibres. After Reynolds[108].

between the calculated apparent surface energy and that predicted by theory suggested that substantial plastic work is occurring at the crack tip during fracture. Since plastic flow in graphite can only occur parallel to the basal planes it was proposed that the elongated micropores divert the crack propagation into a direction parallel to the fibre axis.

In a recent patent[111], the Griffith equation has been used to calculate the apparent fracture surface energy, α, of a range of carbon fibres. By measuring the stress, strain, Young's modulus and flaw size the surface energy was calculated to be in the range 14 - 42 Jm^{-2}, compared with the theoretical value of 4.2 Jm^{-2} calculated from single crystal compliances. It was proposed that this difference can be explained in terms of a plastic work term, and that α is an intrinsic property of the carbon fibre, and accordingly is microstructurally dependent. Means of increasing the surface free energy, by adjusting processing variables, were discussed in the patent.

Stewart and Feughelman[112] have claimed that both the strength and modulus of carbon fibres heat treated to above 1200°C are explicable in terms of fibre fine structure alone, provided that the contribution of bending to the unwrinkling of the ribbons is taken into account. The loss in strength, later attributed to the presence of internal flaws[50,51,52], which accompanies an increase in fibre modulus as the heat-treatment temperature is increased above 1500°C, was proposed to be a consequence of the increase in ribbon thickness. The effects of complex fibril interweaving and interlinking were not discussed in this model.

Reynolds and Sharp[113] have shown that, for a fibre whose Young's modulus is determined by the mean misorientation, $\bar{\phi}$, of hexagonal planes from the fibre axis, there is a large concentration

of shear stress in crystallites which are misoriented at angles greater than the mean. In a perfect single crystal containing no basal dislocations a shear strain-to-failure of 216% was predicted, but it was proposed that this is reduced to about 20% in the presence of very small crystal defects. This suggests that if a crystallite is misoriented by such an angle that it experiences a strain of greater than 20% then it will fail. Failure-strains of 1.3 - 1.5% were predicted for a range of carbon fibres heat treated at different temperatures, and estimates of critical flaw size in the range 26 - 48 nm were made. In view of the fact that in all cases these latter values are significantly greater than the average crystallite size it would seem that failure of a single crystallite of *average* size is not sufficient to lead to failure of the fibre. If, however, there is structural continuity with neighbouring crystallites which are themselves misoriented, then crack propagation might be expected.

Tyson[71] has recently used a modified elastic/plastic theory to explain the anomalous tensile strengths of fibres heat treated above 1000°C. The theory requires that a density fluctuation be present for crack nucleation and ultimate fracture, and that a critical strain exists over a region comparable to the spacing of the crack nuclei (this parameter having been obtained from low-angle x-ray diffraction). The pores and microvoids were proposed to be the plastic zones where, provided a critical strain is reached, crack nucleation begins. The density and weight-fraction of this disordered phase was shown to be particularly significant in limiting the strain-to-failure and strength of PAN-based carbon fibres heat treated in the temperature range 1000 - 2800°C.

CHAPTER 2

LONGITUDINAL STRUCTURE.

2.1 INTRODUCTION

The results obtained from polarized-light microscopy have suggested that a preferred c-axis orientation, dependent on stabilization conditions, exists in carbon fibres prepared at heat-treatment temperatures of 1000°C, 1500°C and, particularly, 2500°C. For example, circular cross-section fibres are thought to possess circumferential crystallite orientation when fully stabilized, and both radial (core) and circumferential (sheath) orientations when partially oxidized. If such a macrostructure exists then it should be revealed by examination of longitudinal sections. Figure 26(a) shows a schematic representation of the cut face at a depth of about r/2 into a fully-stabilized (circumferentially-oriented) fibre of radius r. An ultra-thin section cut from this face will have graphite sheets at A which are normal to the electron beam, and consequently (002) lattice-fringes and dark-field patterns will be absent from any recorded electron images. This would give an apparent 'sheath-core' heterogeneity even though the macrostructure is completely circumferentially oriented. However, if the cut face includes the axis, f, of the fibre a thin section cut from it will reveal an apparently homogeneous structure. When a 'radial-circumferential' texture develops, a 'sheath-core' macrostructure would be expected irrespective of the depth, δ, of the section into the fibre. Although the apparent core thickness, t_c, and sheath thickness, t_s, will be functions of δ, in all cases the value of t_s will be at least 1 μm for fibres of 6 - 8 μm diameter.

For fibres which have a dog-bone cross-sectional shape, many observed macrostructures would be expected depending on the direction of cutting with respect to the major and minor transverse axes. If a radial-circumferential model holds, cutting along the major axis (Fig. 27(a)) will show a sheath-core structure, while cutting along the minor axis

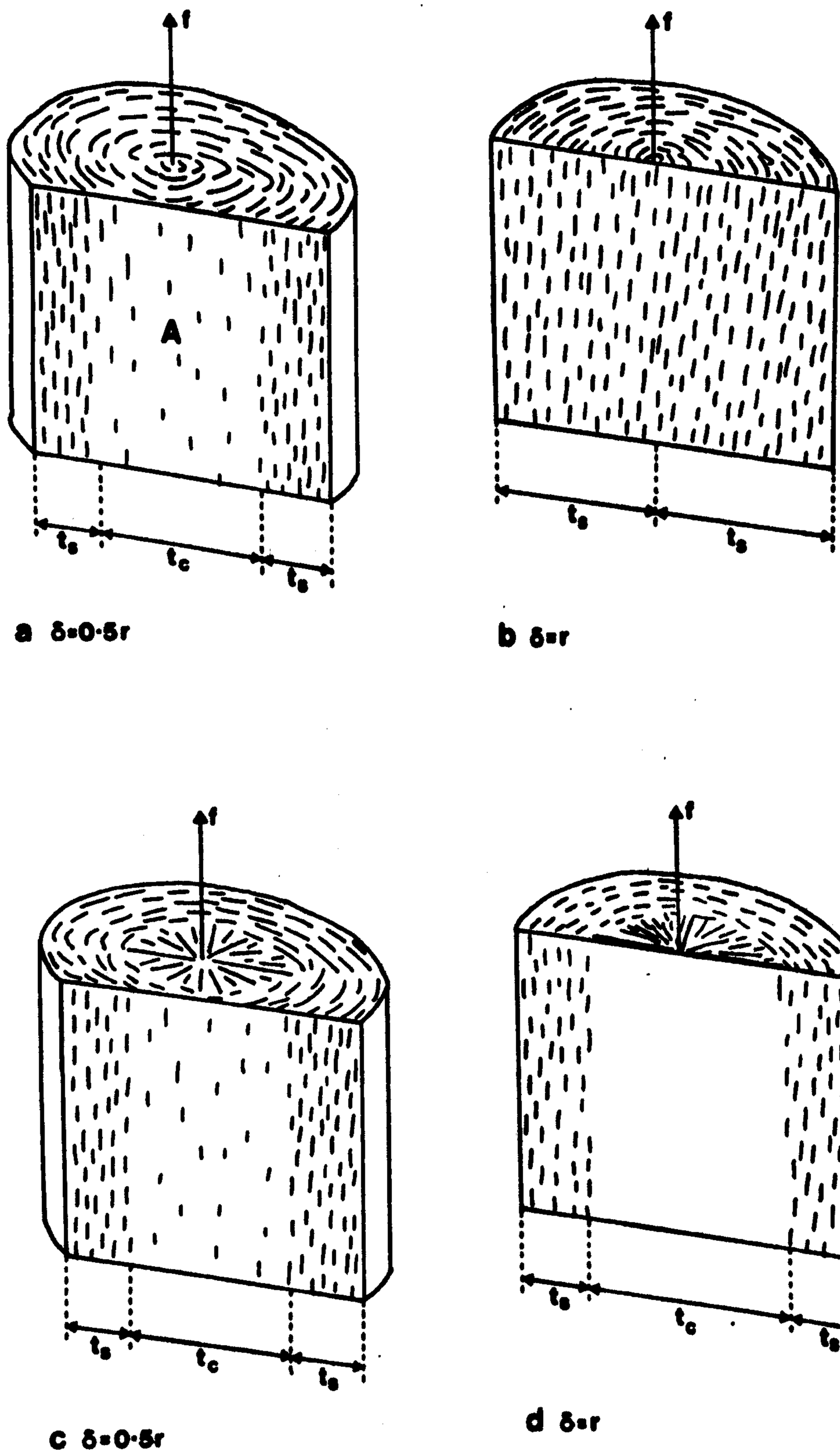

Fig. 26. Schematic representation of the cut faces expected from circular cross section fibres.

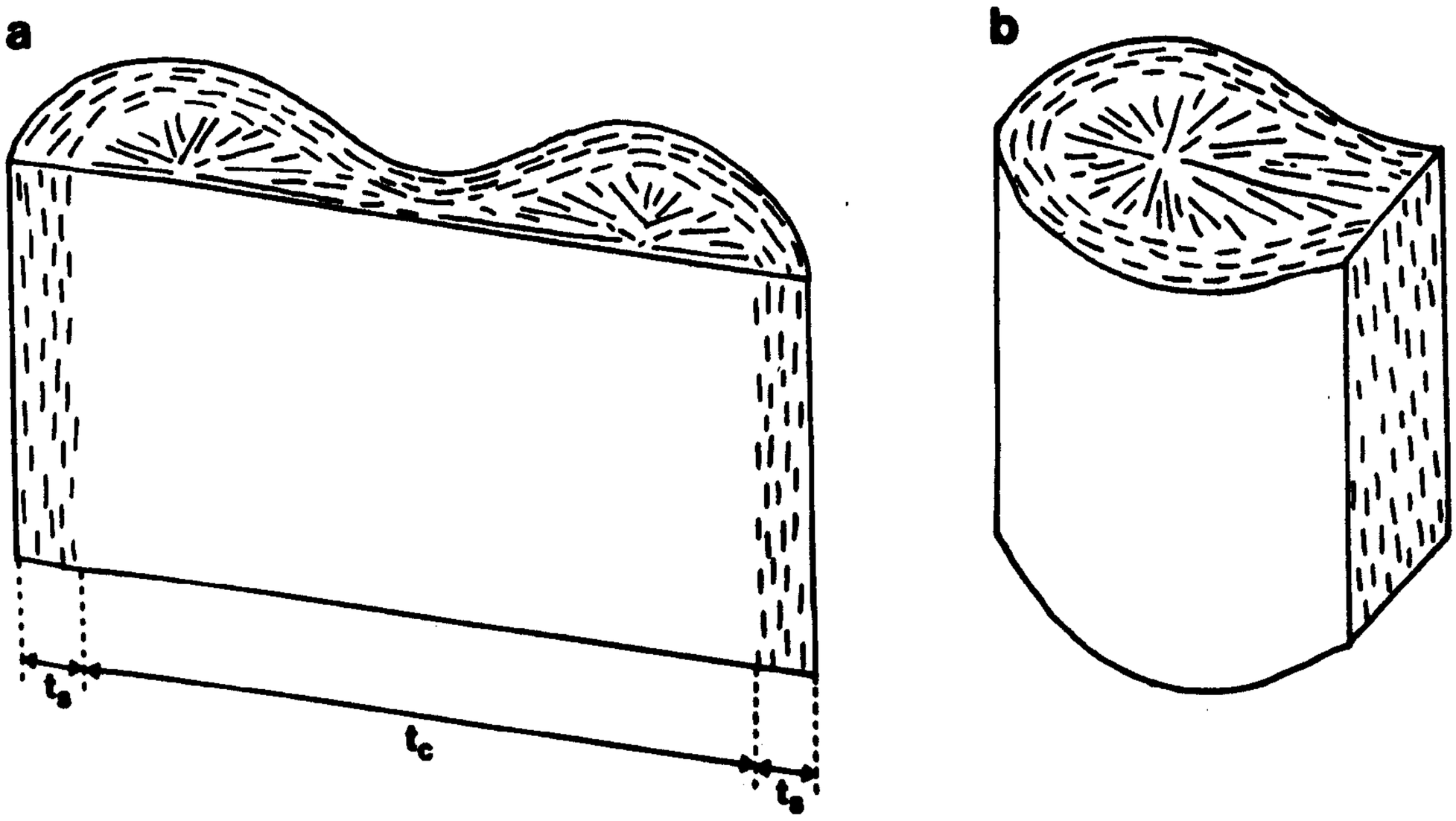

Fig. 27. Schematic representation of the cut faces expected from dog-bone cross section fibres.

(Fig. 27(b)) will reveal a homogeneous structure. If, however, with the exception of the surface layers, there is no preferred c-axis orientation in cross-section an apparently homogeneous structure would be expected irrespective of the direction of cutting (Fig. 27(c) and (d)).

2.2 EXPERIMENTAL PROCEDURE

The 39 specimens shown in Table 1 were embedded in a hard TAAB resin, and thin longitudinal sections prepared at RAE using an LKB Mk. 1 Ultra Microtome and a diamond knife as described by Johnson and Watt[72]. In all cases several thin sections from each specimen were obtained, and, where possible (i.e. before fibre pull-out), the entire fibre was sectioned and collected on Formvar-coated 400 mesh copper grids. Under exceptionally stable conditions it was possible to cut series of sections, nominally 30 nm thick, which appeared colourless in reflected light.

All specimens were examined in a Philips EM300 electron microscope operated at 100 kV with a liquid nitrogen anti-contamination trap, and fitted with a standard hairpin filament and a 0.3 mm diameter gun bias cap. Condenser apertures of 200 or 300 μm were used routinely throughout this study except where otherwise stated, and the following types of electron image obtained:-

(i) (002)-axial dark-field image at intermediate magnifications (50 000x - 100 000x). In this case the electron beam was tilted so that an equatorial section of the (002) diffracted arc coincided with the optical axis of the microscope; a small (less than 20 μm) centrally-aligned thin-foil objective aperture was then used to remove all other reflections. Crystallite size, and the extent of structural heterogeneities were measured directly from prints of know magnification.

(ii) Multibeam (i.e. no objective aperture), (000)-axial, phase-contrast

Table 1 Specimen Identification

PRECURSOR	VACUUM HEAT TREATMENT PRIOR TO OXIDATION	OXIDATION	HEAT-TREATMENT TEMPERATURE		
			1000°C	1500°C	2500°C
3 denier special Courtelle*	None	5h at 220°C	A1000	A1500	A2500
	None	10h at 220°C	-	-	B2500
	None	20h at 220°C	-	-	C2500
	None	40h at 220°C	D1000	D1500	D2500
1.5 denier special Courtelle*	None	1h at 220°C	E1000	E1500	E2500
	None	9h at 220°C	F1000	F1500	F2500
2 denier Dralon+	None	5h	G1000	G1500	G2500
	None	10h	H1000	H1500	H2500
1.5 denier special Courtelle*	None	2h at 230°C	J1000	J1500	J2500
	6h at 230°C	2h at 230°C	K1000	K1500	K2500
1.8 denier Orlon+	None	4h at 230°C	L1000	L1500	L2500
	6h at 230°C	1h at 230°C	M1000	M1500	M2500
Dralon+	None	3½h at 230°C	N1000	N1500	N2500
	6h at 230°C	½h at 230°C	P1000	P1500	P2500
1.5 denier special Courtelle*	Nominal	None	-	-	Q2500
3 denier special Courtelle*	None	2h at 220°C	-	-	R2500
	None	6h at 220°C	-	-	S2500

* - circular cross section, + dog-bone cross section

lattice-fringe image at an objective-lens defocus which gives enhancement of the 0.34 nm turbostratic graphite spacing. The focus for these images was always ascertained by using a TV monitor system (see Appendix 1), and the images usually recorded at a magnification in the range 350 000x - 500 000x. As in (i) above, crystallite and flaw size were measured directly from prints of known magnification.

(iii) Electron-diffraction patterns were always recorded at a condenser 2 (C2) setting of two coarse steps *over* focus (see Appendix 1), for times between 2 s and 10 minutes depending on selected-area aperture size, and the reflection of interest. For revealing structural differences between small areas a 10 μm diameter intermediate-lens (selector) aperture was usually used to select an area of diameter 0.4 μm at the specimen. Intensity traces of these electron-diffraction patterns were obtained using a Joyce-Loebl double-beam recording microdensitometer at a ratio-arm magnification of 50x, and with a short, narrow slit, and were digitized manually for input to an ICL 1906A computer. An Algol program used routinely in this laboratory for the resolution of overlapping x-ray diffraction peaks[116] (see Appendix 3) was adapted for use with the electron-diffraction data, traces being logarithmically corrected for saturation of the photographic emulsion[117] (see Appendix 2) and then resolved into the zero-order (000) peak, (00ℓ) peaks, (hk0) peaks where appropriate, and a polynomial background. The known asymmetry of the reflections was allowed for by fitting different functions to either side of each peak. The resolved widths (Δ s) at half-maximum peak intensity and/or integral breadths (the area under a reflection divided by its intensity) then gave values of apparent crystallite size (L) using the Scherrer equation:-

$$L = \frac{K}{\Delta s}$$

Text cut off in original

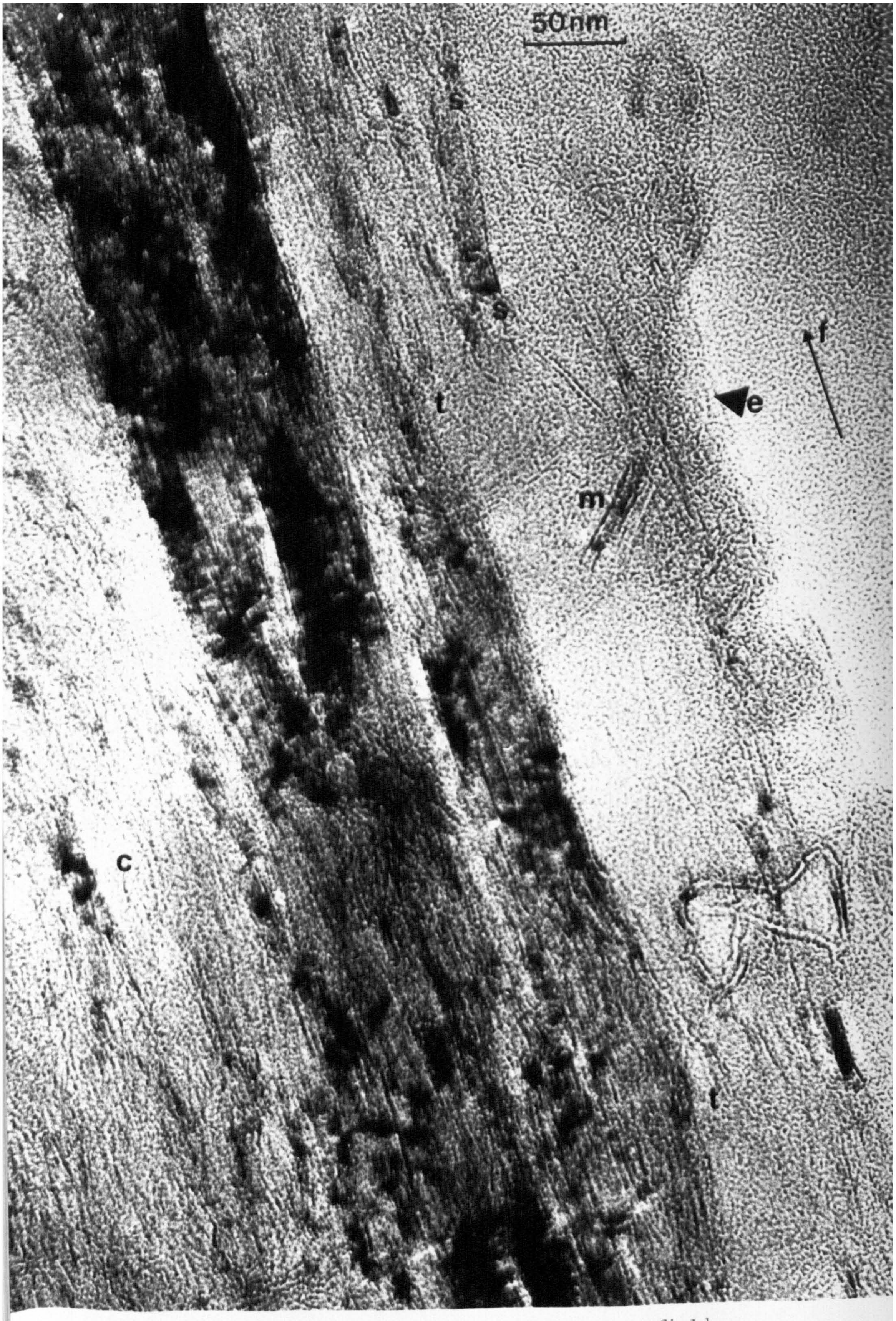

Plate I. Intermediate-magnification bright-field image of the skin structure of specimen

Plate II. Lattice-resolution image of the skin structure of specimen B2500.

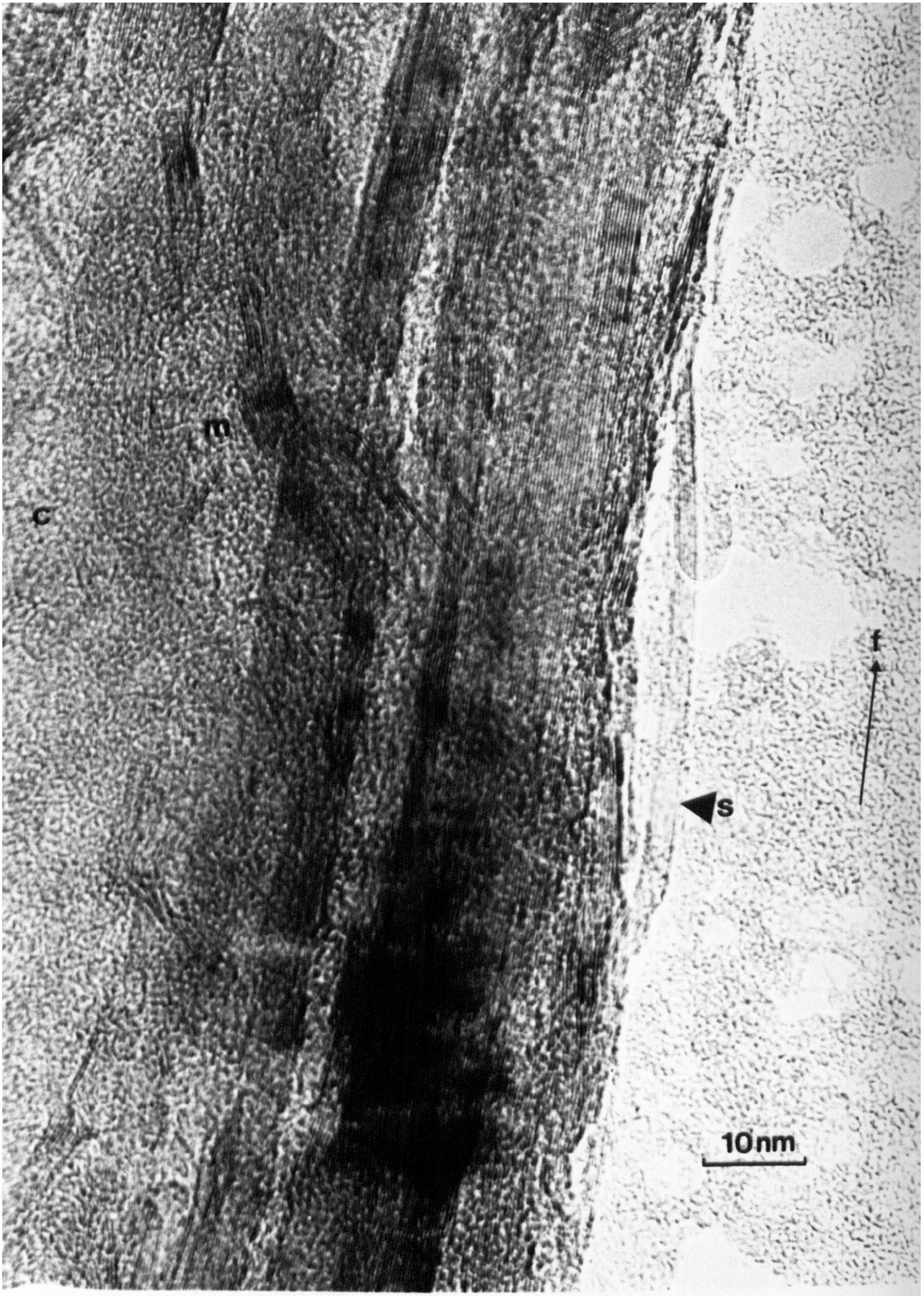

Plate III. Lattice-resolution image of the skin structure of specimen C2500.

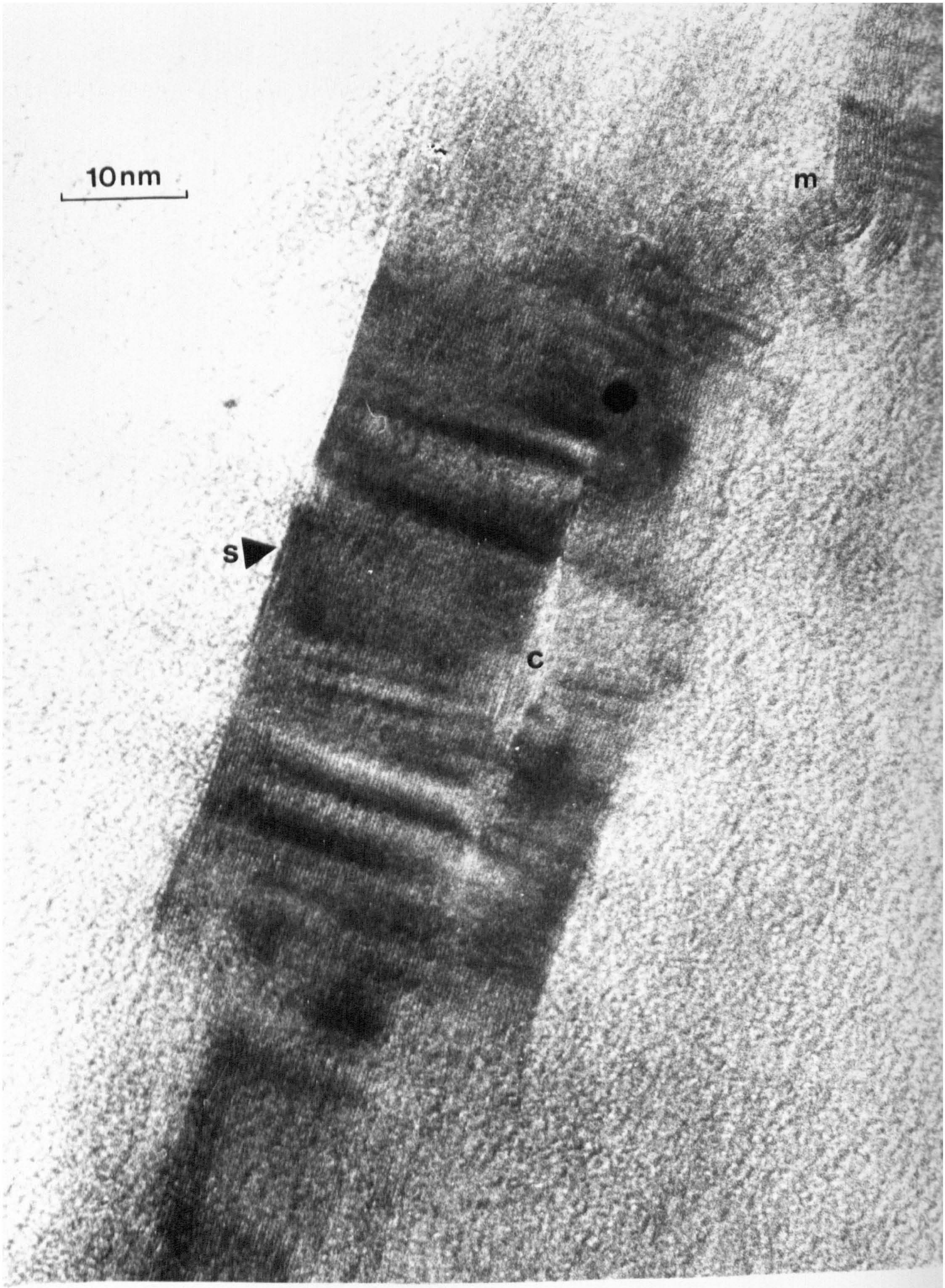

Plate IV. Lattice-resolution image of the skin structure of specimen D2500.

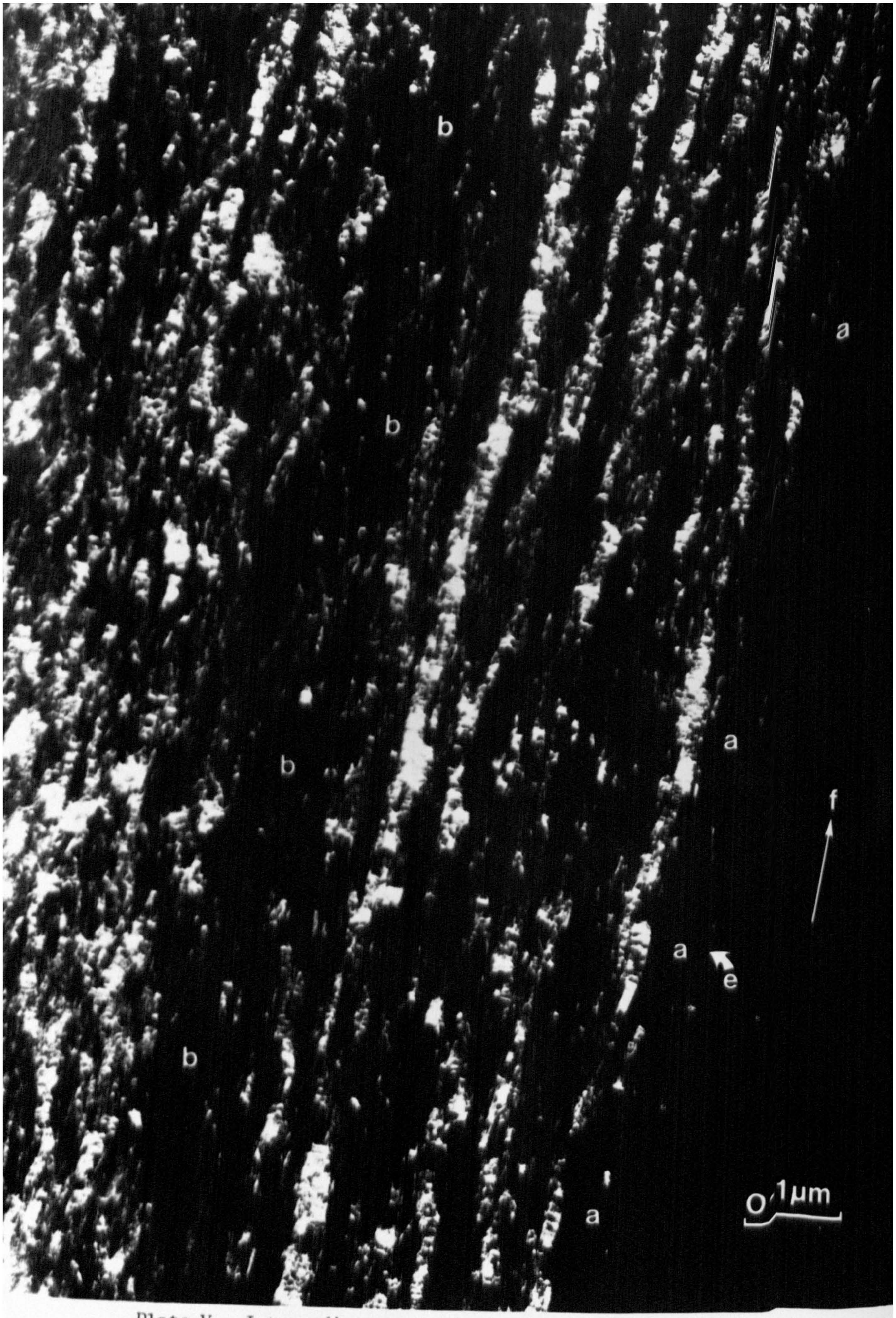

Plate V. Intermediate-magnification (002) dark-field image of the skin structure of specimen F2500.

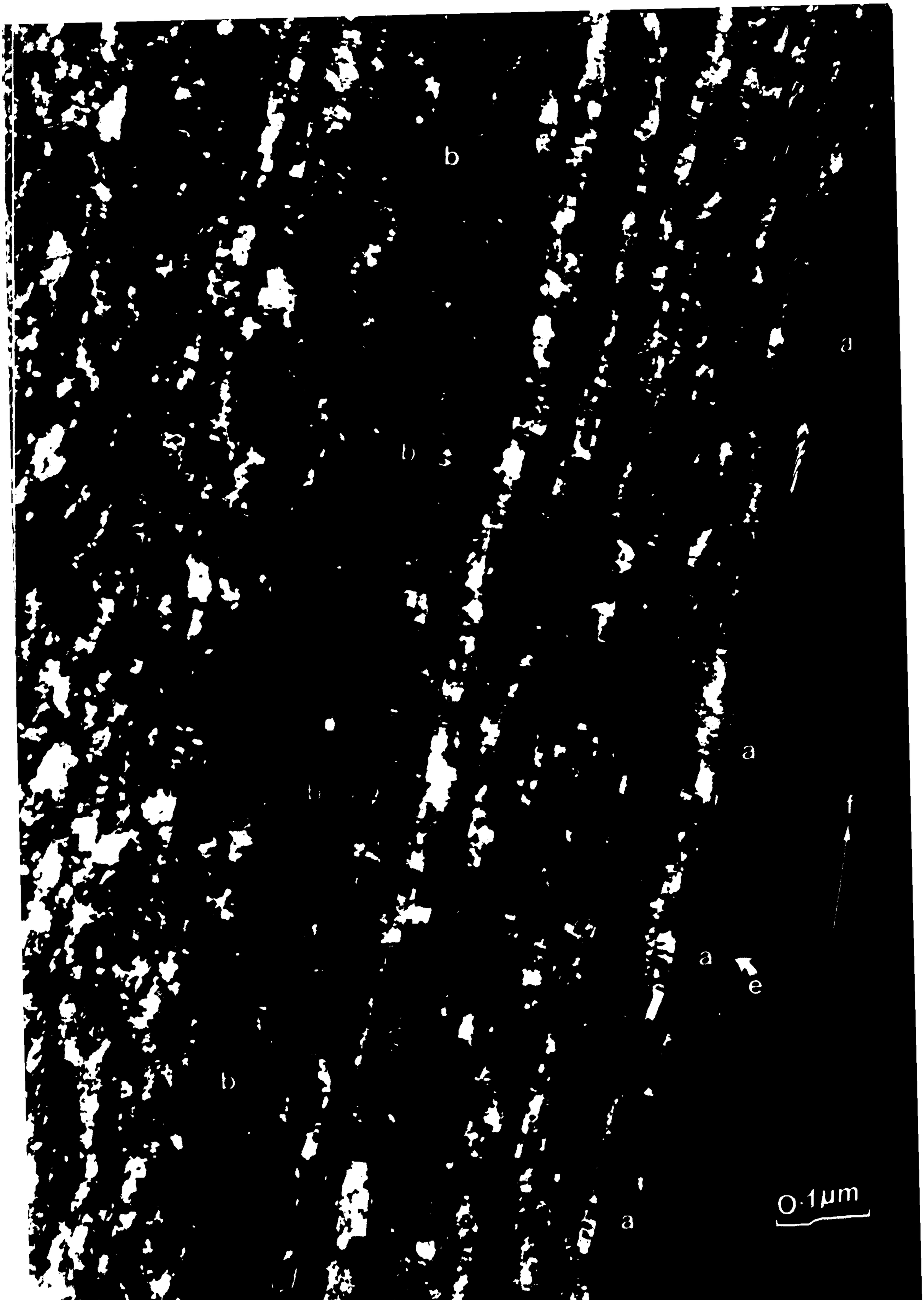

Plate V. Intermediate-magnification (002) dark-field image of the skin structure of specimen F2500.

The skin structure of specimen B2500 is seen at lattice resolution in Plate II. Large, highly-oriented crystallites, ranging in size up to a maximum of about 15 nm, can be seen linking together in a complex manner up to the edge, e, of the section. Irregular extinction bands at d indicate that the layer planes are highly distorted, and this is confirmed by extensive layer-plane bending at, for example, b. Crystallites of width between 8 nm and 14 nm can be seen to be misoriented at angles of at least 20^{o} to the direction, f, of the fibre axis at m, n, and r.

A somewhat different skin structure in specimen C2500 is seen at lattice resolution in Plate III. Although showing high preferred orientation, the crystallites within 40 nm of the fibre surface, s, are smaller, at about 6 - 10 nm, than normally observed. Significantly, there is again evidence of severe misorientation at m, where a crystallite of width 5 nm can be seen to be misoriented at 30 - 40^{o} to the direction, f, of the fibre axis. Apparently there is structural continuity between the skin region and the core, c, through this crystallite.

The variability in skin crystallite size is demonstrated in Plate IV, which shows a large, highly-graphitic surface crystallite of width 30 nm in specimen D2500. Although relatively perfect for carbon fibres this crystallite exhibits dark extinction bands due to lattice distortions, and a large crack has opened at c. Additionally, structural continuity with core crystallites is maintained through a misoriented crystallite at m, and the high degree of crystallite perfection means that the fibre surface, s, is basal plane in nature.

At lower magnification, and in the (002) dark-field mode of image formation, the extent of skin structure in specimen F2500 can be seen in Plate V. As in Plate I, a region, a, about 60 nm wide very close to the edge, e, of the section is characterized by a comparative absence

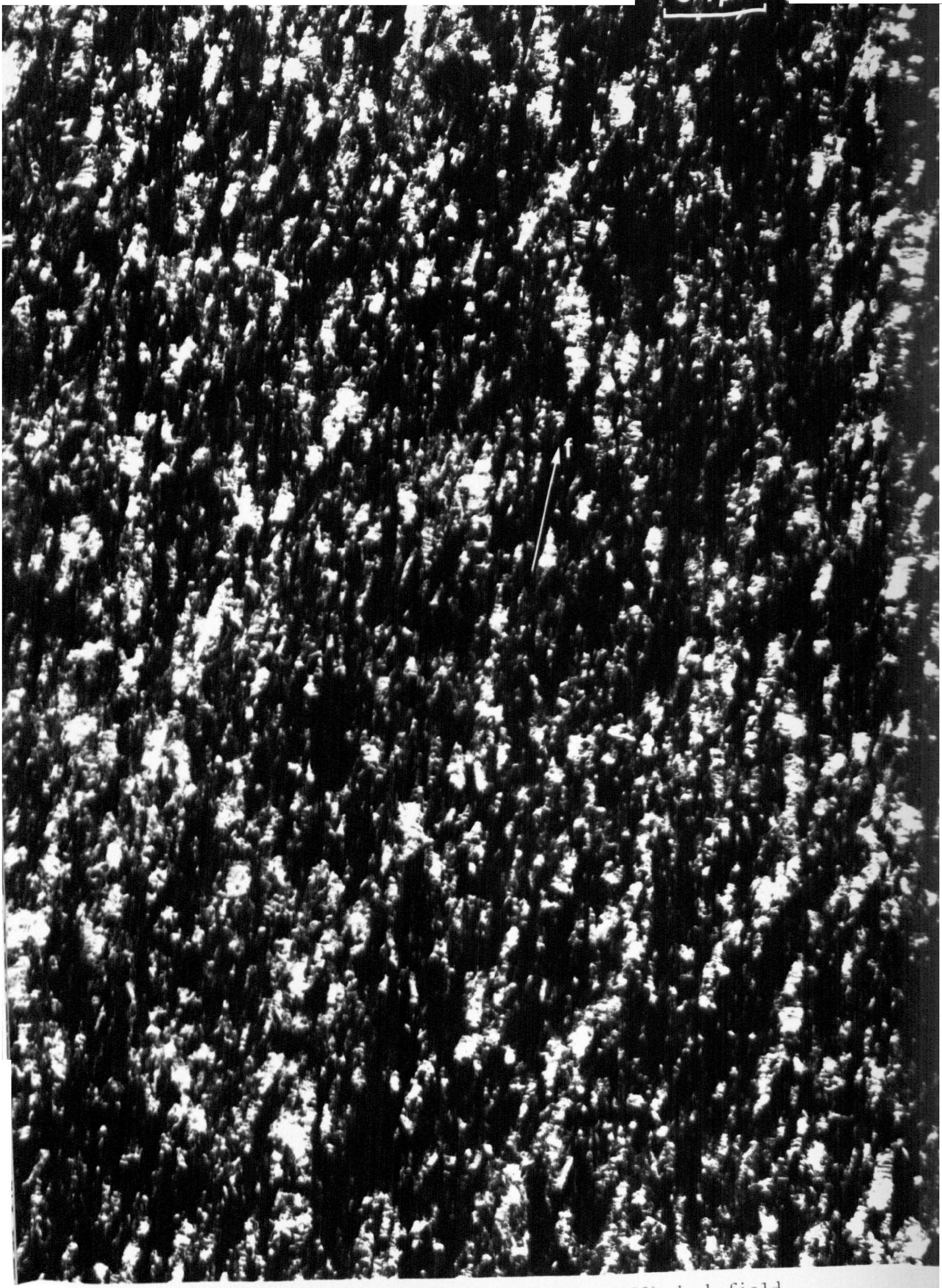

Plate VI. Intermediate-magnification (002) dark-field image of the core structure of specimen F2500.

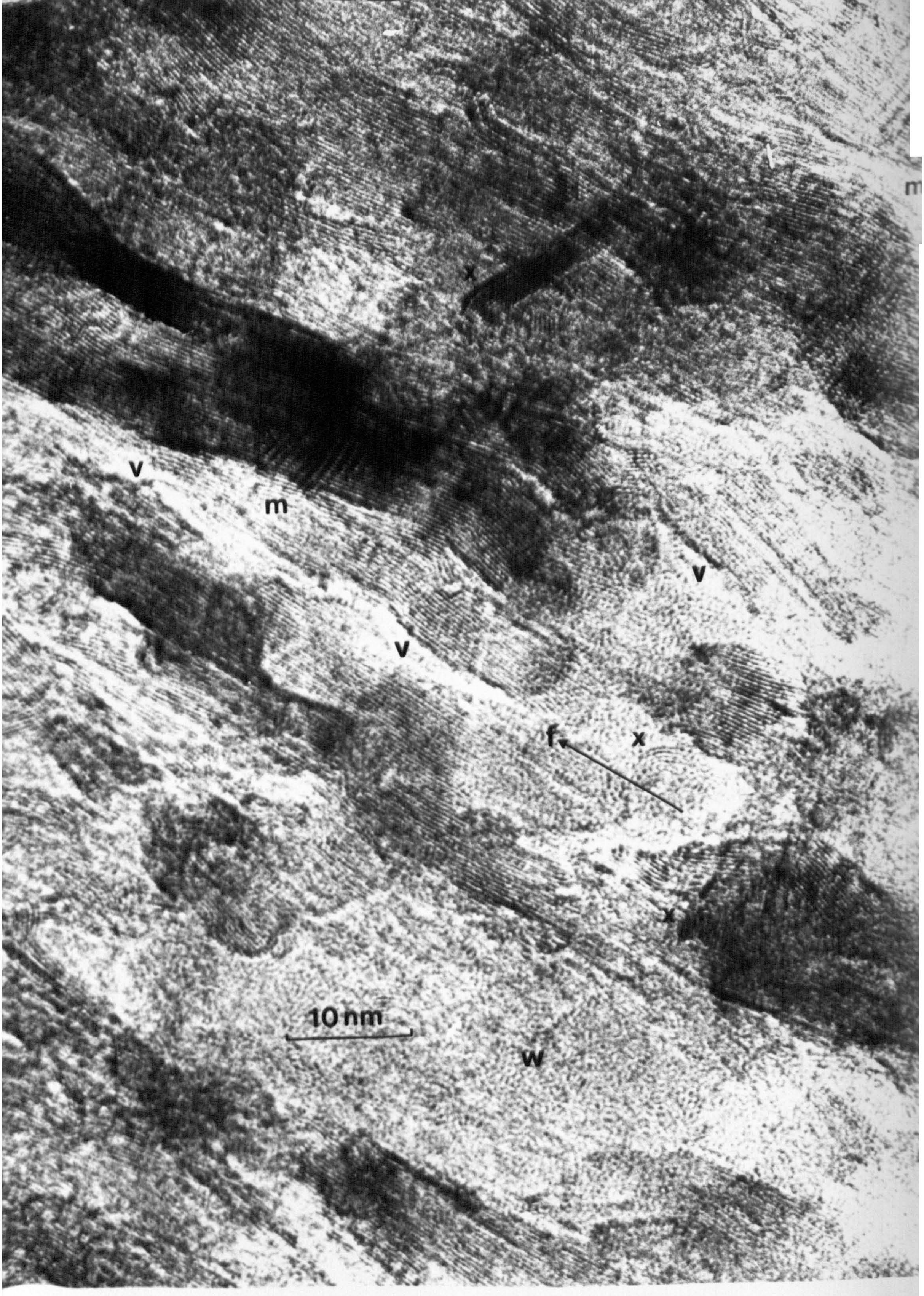

Plate VII. Lattice-resolution image of the core structure of specimen D2500.

of (002) diffracted intensity. The typical skin structure then extends inwards over 250 nm, but apparently there is a further region, b, of structural discontinuity before the core structure is reached. This region of apparently small crystallite size and low (002) diffracted intensity is about 80 nm wide. The skin zone is characterized by a large stacking size, high preferred orientation, and large crystallite lengths in the direction, f, of the fibre axis.

b. Core structure

A homogeneous core structure, irrespective of both time of preoxidation and fibre diameter, was exhibited by all the specimens examined. The extent of the skin region, which has a maximum thickness of about 500 nm, but is typically of the order 100 - 250 nm means that the core represents more than 90% of the fibre. Plate VI shows, in the (002) dark-field mode, the core structure of specimen F2500. Comparison with Plate V shows that the stacking size is smaller and the preferred orientation poorer in the core than in the skin. Additionally, the crystallites in the core are much more discontinuous in the direction, f, of the fibre axis than in the skin, and consequently one would expect lower values of $L_{a//}$, the ribbon length. The gross homogeneity is quite apparent from this image.

At lattice resolution, an essentially continuous, but in places highly misoriented structure is evident. Plate VII indicates crystallites with a range of stacking sizes up to about 13 nm linked together in a highly complex manner in specimen D2500. There is evidence of crystallite overlapping in Moiré patterns at m, while interlinking occurs through crystallites, x, inclined at angles of greater than 45^{o} to the direction, f, of the fibre axis. Apparent voids, v, are easily located between crystallites, and exceptionally a wide zone, w, shows no evidence of interference fringes presumably due to the absence of (002) planes in the diffraction condition.

Plate VIII. Lattice-resolution image of the core structure of specimen D2500.

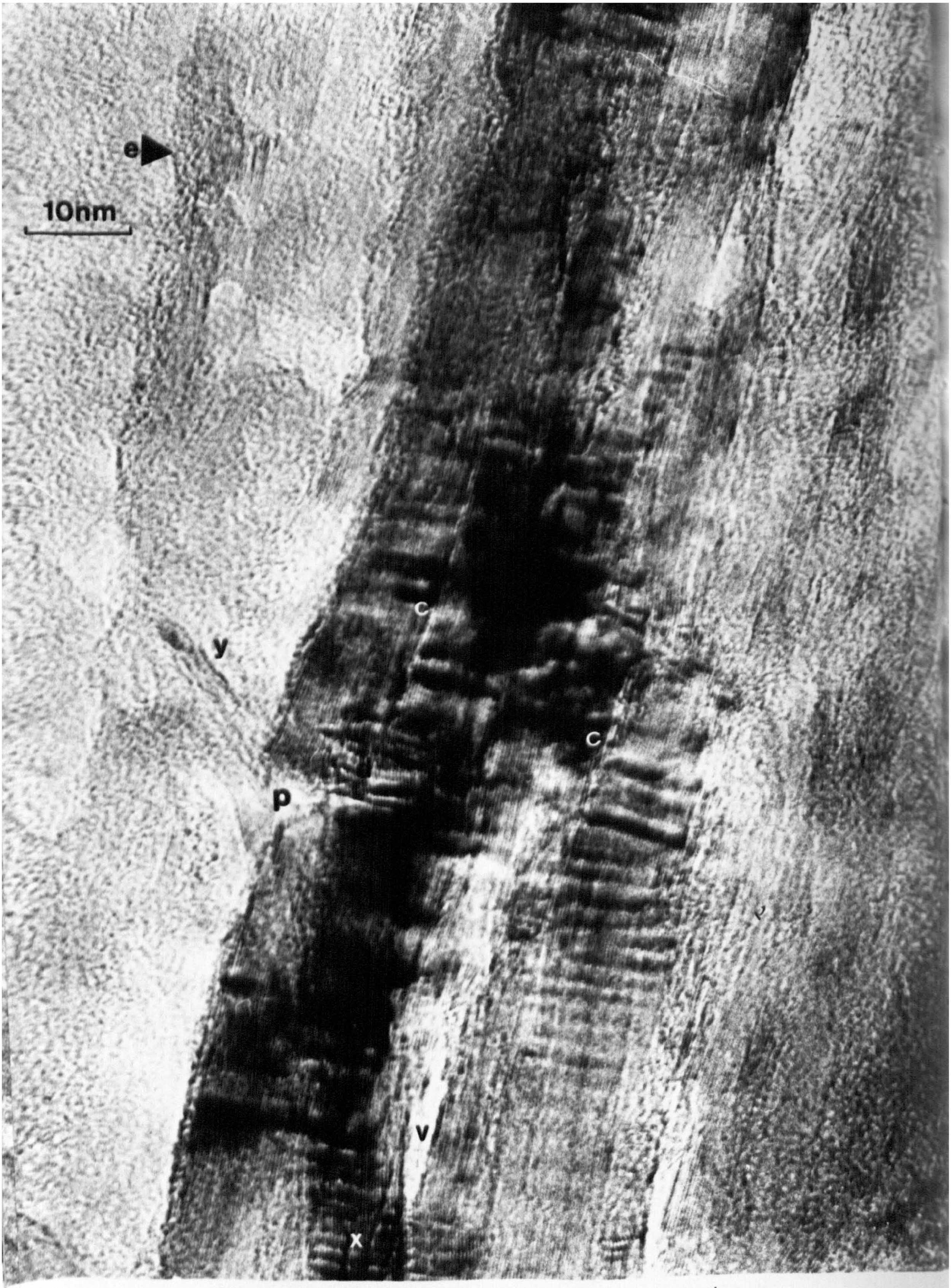

Plate IX. Lattice-resolution image of a flaw in the skin structure of specimen B2500.

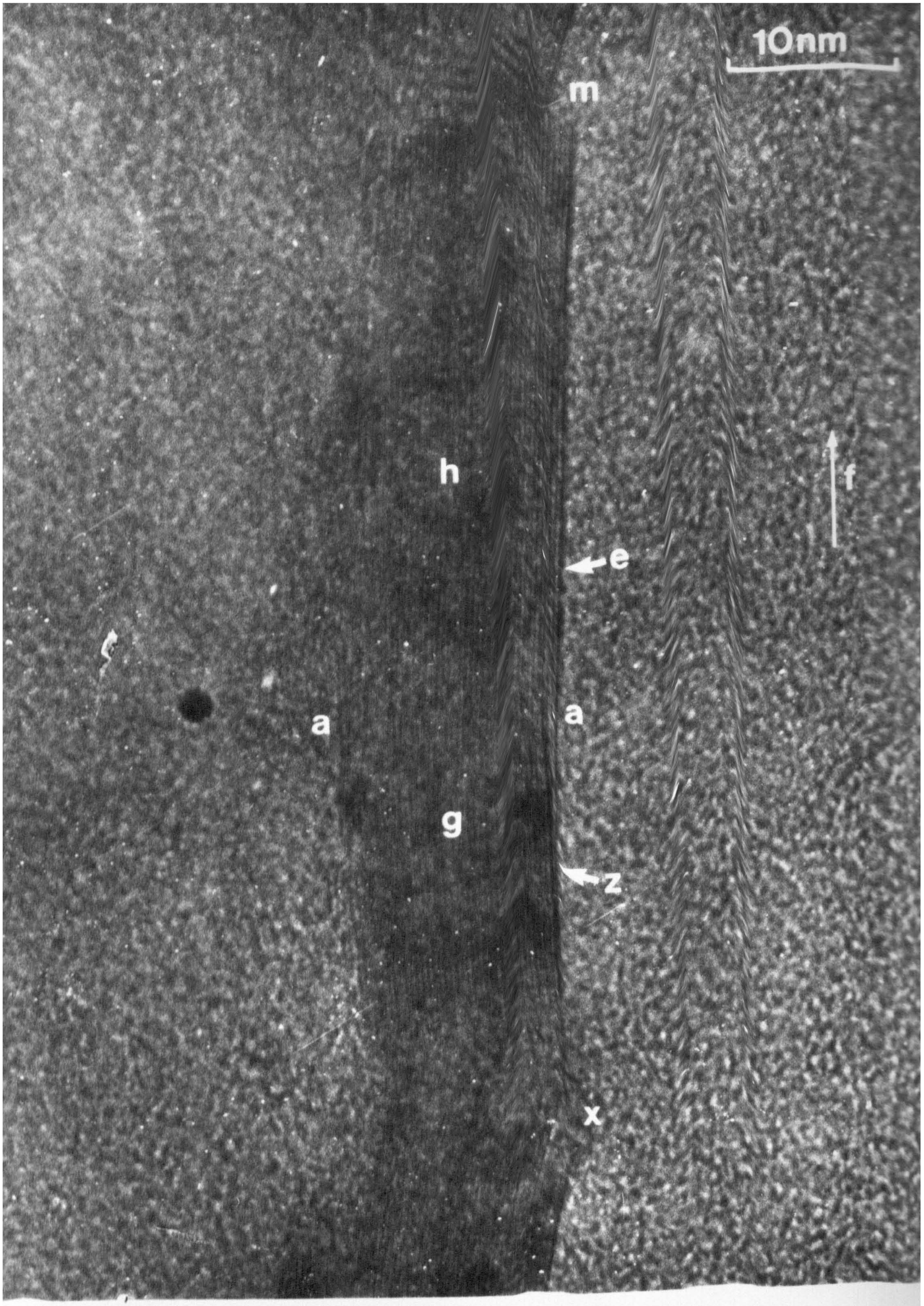

Plate X. Lattice-resolution image of flaws in the skin structure of specimen A2500.

Plate VIII shows a core structure, also from specimen D2500, which consists of highly-interlinked crystallites with a maximum stacking size of about 9 nm. Crystallites misoriented at angles of at least 45^{o} to the direction, f, of the fibre axis are apparent at m, and it is of significance that structural continuity is maintained through these crystallites.

c. Defect structure

In order to understand the strength of carbon fibres it is important to investigate any feature which may be considered as a flaw, characterizing its shape and size, and the crystallite orientation in its vicinity. Plate IX shows, at lattice resolution, the skin structure of specimen B2500. The bending and twisting of layer planes close to a highly-distorted region, d, has caused the formation of a flaw, p, while a misoriented crystallite of width 10 nm which starts at x apparently extends through this flawed region and terminates at y. An axially-aligned void, v, of width 2 nm and length at least 20 nm has opened between two of the almost perfectly-aligned edge crystallites, while cracks are in evidence at c. As in Plates I and V the large surface crystallites apparently do not extend fully to the edge, e, of the section, the outer zone of thickness between 15 and 30 nm being characterized by weak or no (002) interference fringes. A similar flaw to that at p in Plate IX is shown at the edge, e, of a section prepared from specimen A2500 in Plate X. The crystallite forming the surface of the fibre has twisted at x to give a flaw, and at m a misoriented crystallite overlaps with the other, larger surface crystallite to give a Moiré pattern. Layer-plane bending across a-a has resulted in a 6^{o} tilt of the edge crystallite at g with respect to that at h.

A striking surface flaw, from specimen B2500, is depicted in

Plate XI. Intermediate-magnification bright-field image of a gross flaw in the skin structure of specimen B2500.

Plate XII. Lattice-resolution image of a 'hair-pin' flaw in the skin structure of specimen C2500.

Plate XIII. Intermediate-magnification bright-field image of the surface structure of specimen C2500 showing the flaw depicted at lattice-resolution in Plate XII.

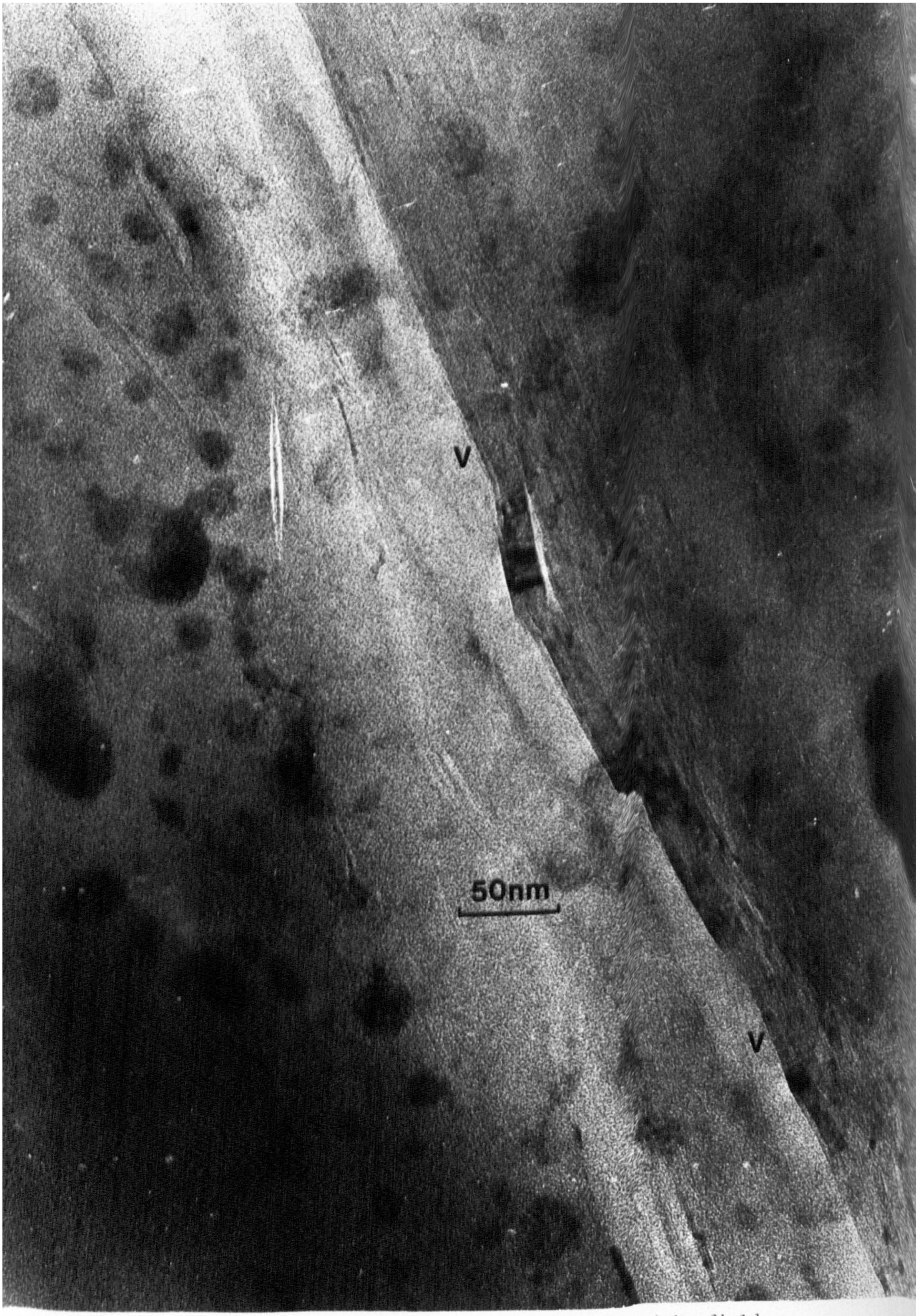

Plate XIV. Intermediate-magnification bright-field image of a misoriented crystallite in the skin structure of specimen D2500.

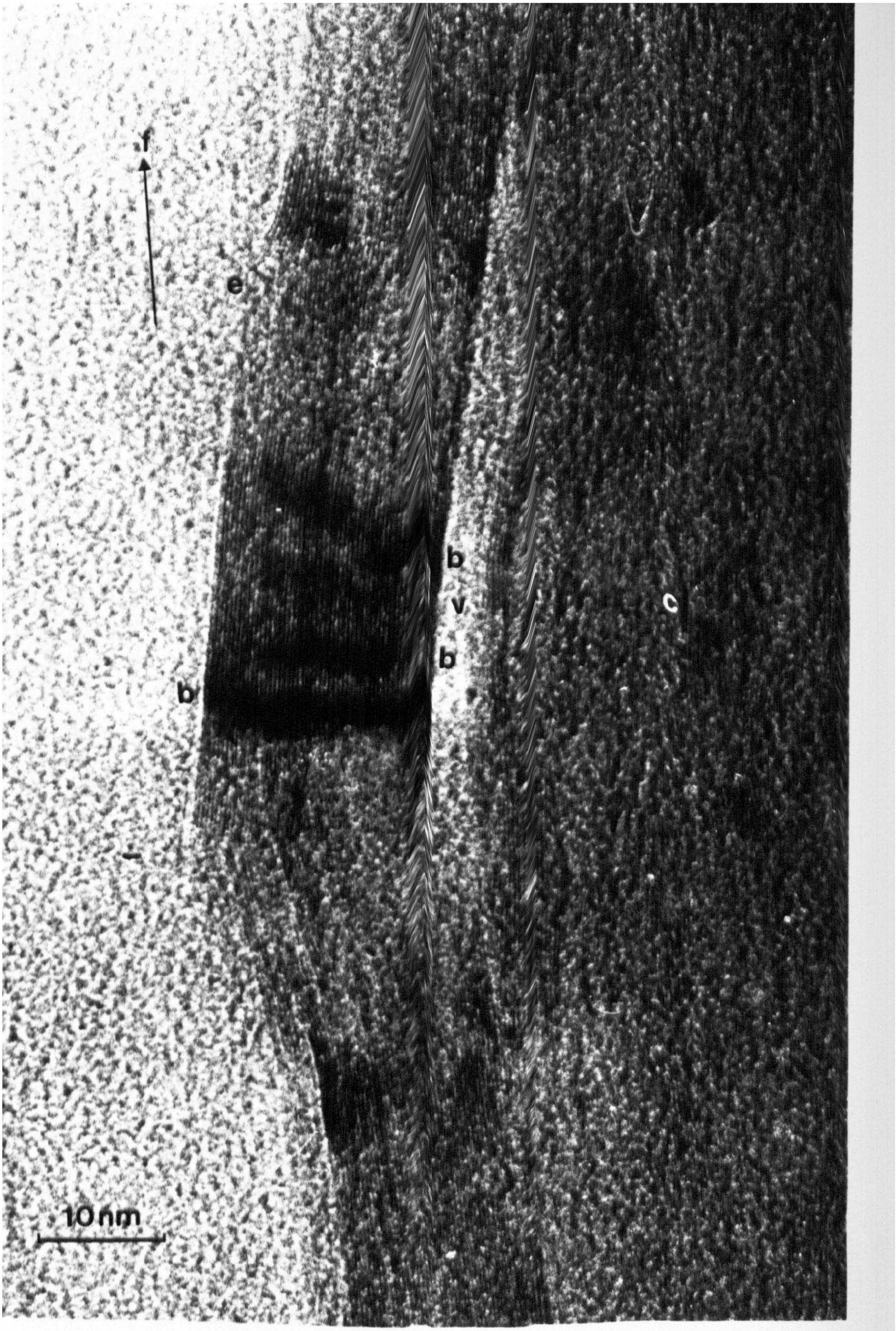

Plate XV. Lattice-resolution image of the misoriented surface crystallite depicted at lower magnification in Plate XIV.

Plate XVI. Lattice-resolution image of 'knee-shaped' flaw in the skin structure of specimen D2500.

the bright-field mode at intermediate magnification in Plate XI. A large surface crystallite, s, has pulled away from the core structure, c, along a-a, and fractured at x leaving a hole, h. It is proposed that the continuation of the surface crystallite has twisted out of the diffraction condition along w-w. It is possible that such extreme flaws *may* be due either to the disruptive effect of sectioning, or handling prior to embedding. In either case, a weakness must have existed in the fibre at that point in order for the flaw to be realized.

An 'inverted-hairpin' flaw in specimen C2500 is shown in Plate XII. Structural continuity of both ends of this misoriented crystallite is evident at x and y, and at lower magnification (Plate XIII) it is noticeable that it extends to a depth of at least 25 nm into the section at z. The general unevenness of the fibre surface is clearly shown in Plate XIII; the 'inverted hairpin' in fact forming a 40 nm deep step, s, while there is evidence of a smaller protuberance at x. Although the images in Plate XIII were recorded at lattice resolution they are reproduced at low magnification.

A 'blister' flaw in specimen D2500 is shown in bright-field at intermediate magnification in Plate XIV. The fibre surface is relatively smooth with the exception of the area v-v, where a 'bulge' of some 20 nm is evident. At lattice resolution (Plate XV) it is clear that the crystallite that forms the blister is about 17 nm wide, and is misoriented at about 15^{o} to the direction, f, of the fibre axis. The irregular dark extinction bands, b, are evidence of layer-plane distortion, and at e fracturing of layer planes has occurred. A void, v, of width 3 nm has opened between the misoriented surface crystallite and the core structure, c.

A very large surface crystallite of width about 35 nm in specimen D2500 is shown at lattice resolution in Plate XVI. This

Plate XVII. Lattice-resolution image of 'knee-shaped' flaw in the skin structure of specimen F2500.

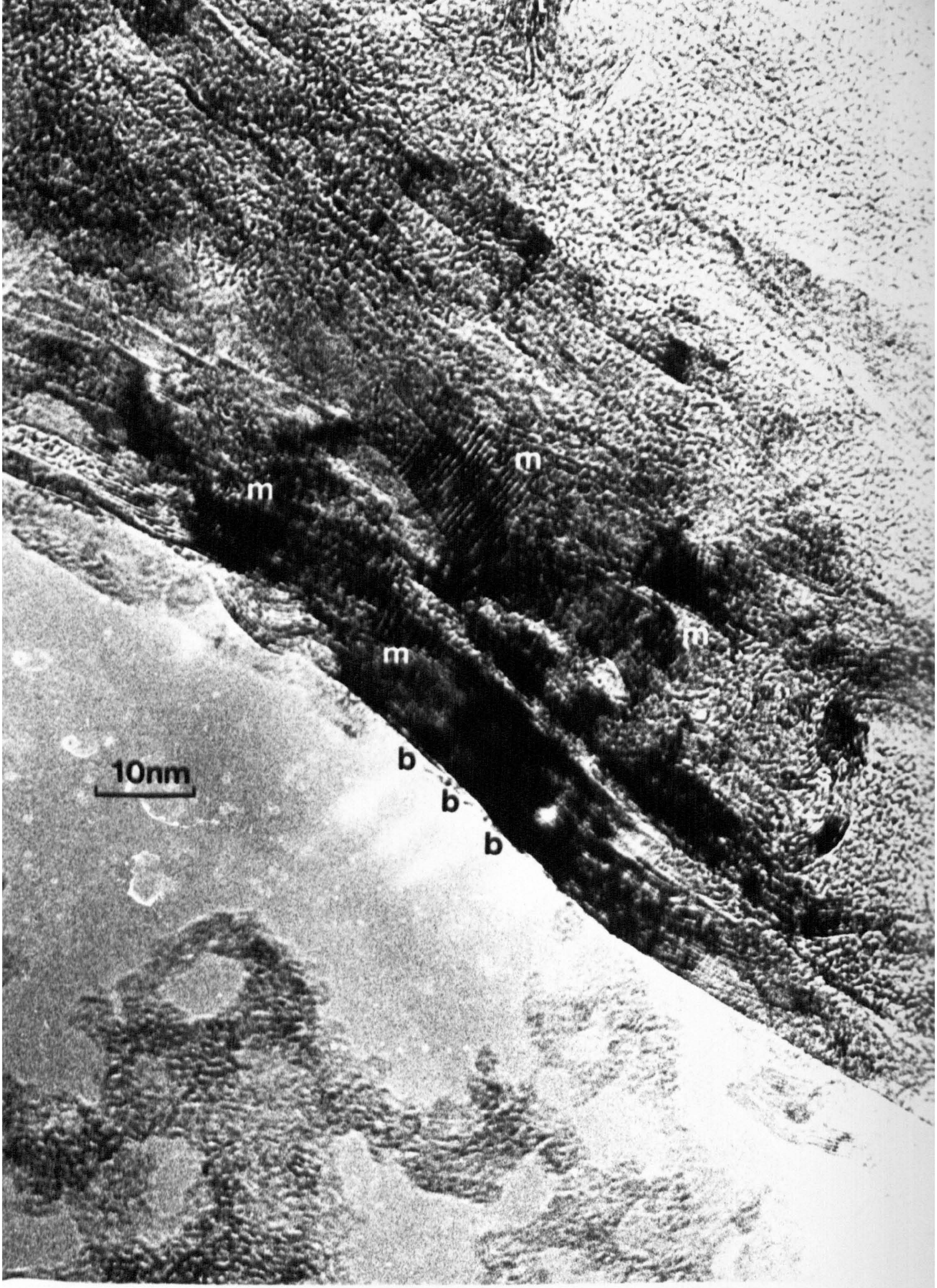

Plate XVIII. Lattice-resolution image of the skin structure of specimen F2500 showing misoriented, interlinked crystallites.

'knee-shaped' region consists of a highly graphitized crystallite bent through an angle of about 40^{o} along a-a. There is evidence of severe lattice disorder at d, and the layer planes have apparently twisted over out of the diffraction condition at g.

A similar 'knee-shaped' flaw in specimen F2500 is shown in Plate XVII. A crystallite of width 17 nm close to the edge, e, of the section is bent through an angle of about 20^{o} along a-a. Disruption of the lattice-fringe image in the form of extinction bands, b, cracks, c, and localized distortion, d, is indicative of the presence of severe dislocations,while structural continuity is maintained through interlinking at h. The direction, f, of the fibre axis is indicated.

A highly-graphitized and well-interlinked skin structure in specimen F2500 is depicted at lattice resolution in Plate XVIII. This skin, of total thickness 45 nm, consists of crystallites ranging in size up to about 10 nm, which are extensively interwoven in a complex three-dimensional manner. Regular Moiré-fringe patterns, m, result from crystallite overlapping, and dark extinction bands, b, particularly at the very edge of the section, are indicative of considerable lattice distortion. There is evidence of gross crystallite misorientation, not only in the skin at s, but also in the core at t. The structure of the surface crystallites signifies the essentially basal-plane nature of the fibre surface.

d. Quantitative electron diffraction

The techniques of analysis of electron-diffraction patterns outlined earlier were used to obtain quantitative measurements of size and distortion parameters for the skin and core regions in specimens A2500, B2500, C2500 and D2500. In all cases several (up to six) orders of the (00ℓ) reflection were observed in skin regions, while usually only the first two orders were seen in the electron-diffraction patterns of the core (Plate XIX). The limited extent of the skin necessitated

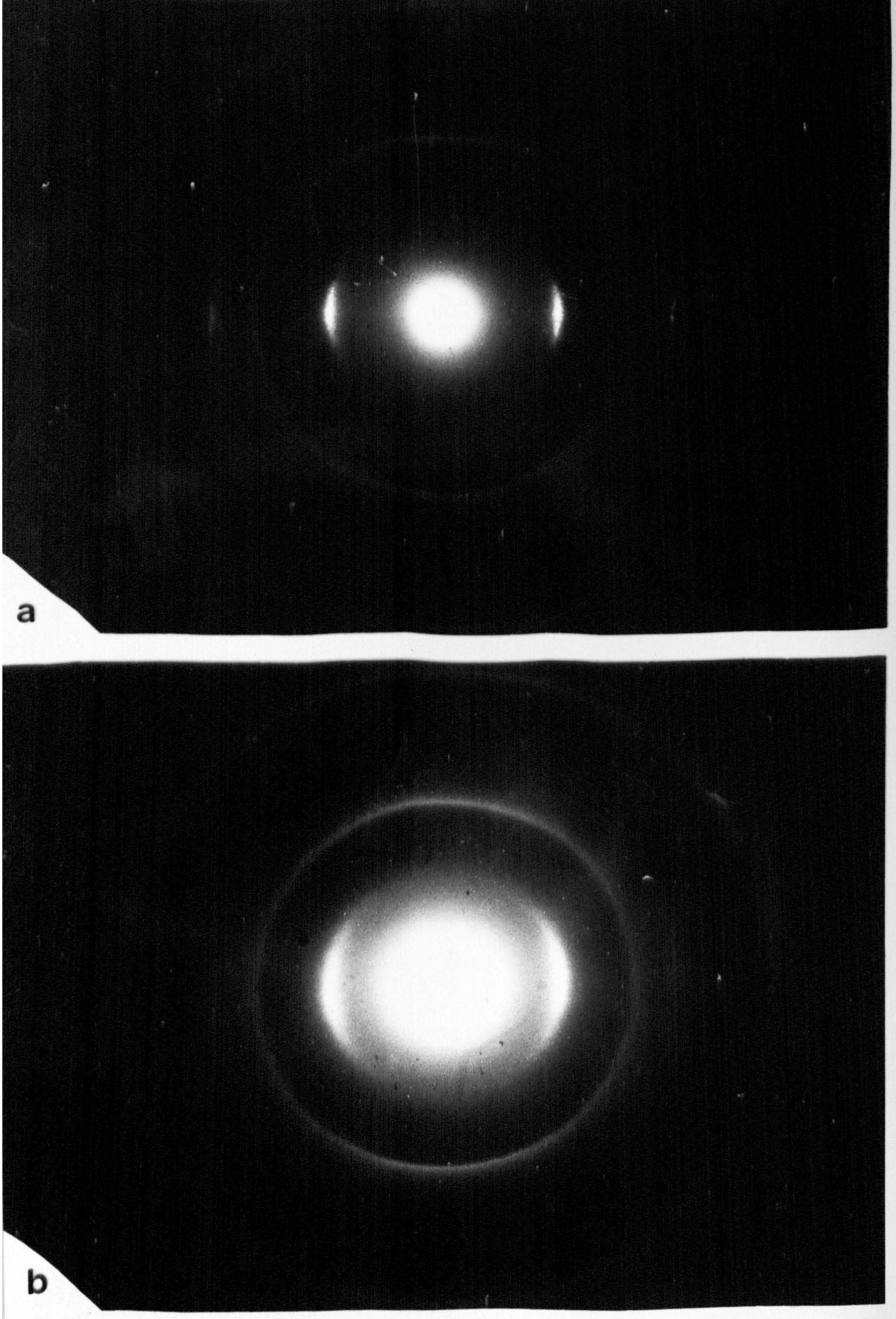

Plate XIX. Electron-diffraction patterns from (a) skin, and (b) core of specimen C2500.

the use of a 10 μm diameter intermediate-lens aperture, which selects an area of diameter 400 nm at the specimen, and the longitudinal variability of the skin meant that meaningful averaged electron-diffraction patterns could only be obtained by integration (recording the pattern of many different areas on the same plate). However, integration was unnecessary in the core because of its homogeneity.

Crystallite size and lattice distortion.

The computer program used in this study outputs the width in s at half maximum peak intensity, and using the Scherrer equation, with K=1, the apparent stacking size was obtained for each of the resolved (OOℓ) reflections. As the width, Δs, was found to increase linearly with ℓ^2 the technique first proposed by Ergun[118] and later adapted by Thrower and Nagle[119] was used to derive the 'mean defect-free distance', D_C, and lattice distortion parameter, σ. D_C is defined as the distance over which there is a probability e^{-1} of encountering a lattice defect, and σ is defined as a strain parameter such that a lattice distance r parallel to the c-axis is altered by $\pm\sigma$ r with a probability of 0.5.

A graph of Δs against ℓ^2 for specimens A2500, B2500, C2500 and D2500 is shown in Fig. 28. The marked difference between skin and core regions is apparent, but there is no evidence to suggest that different oxidation times have any significant effect on either crystallite size or perfection in either region. Figure 29 shows a successful resolution of the (002) reflection from (a) skin, and (b) core regions of specimen B2500, and the ability of the program to cope successfully with very asymmetric peaks is demonstrated in Fig. 30, where the (110) and (006) equatorial reflections of specimen B2500 (skin) are resolved.

The mean defect-free distance, D_C, and lattice distortion parameter, σ, are shown in Table 2 for skin and core regions of specimens

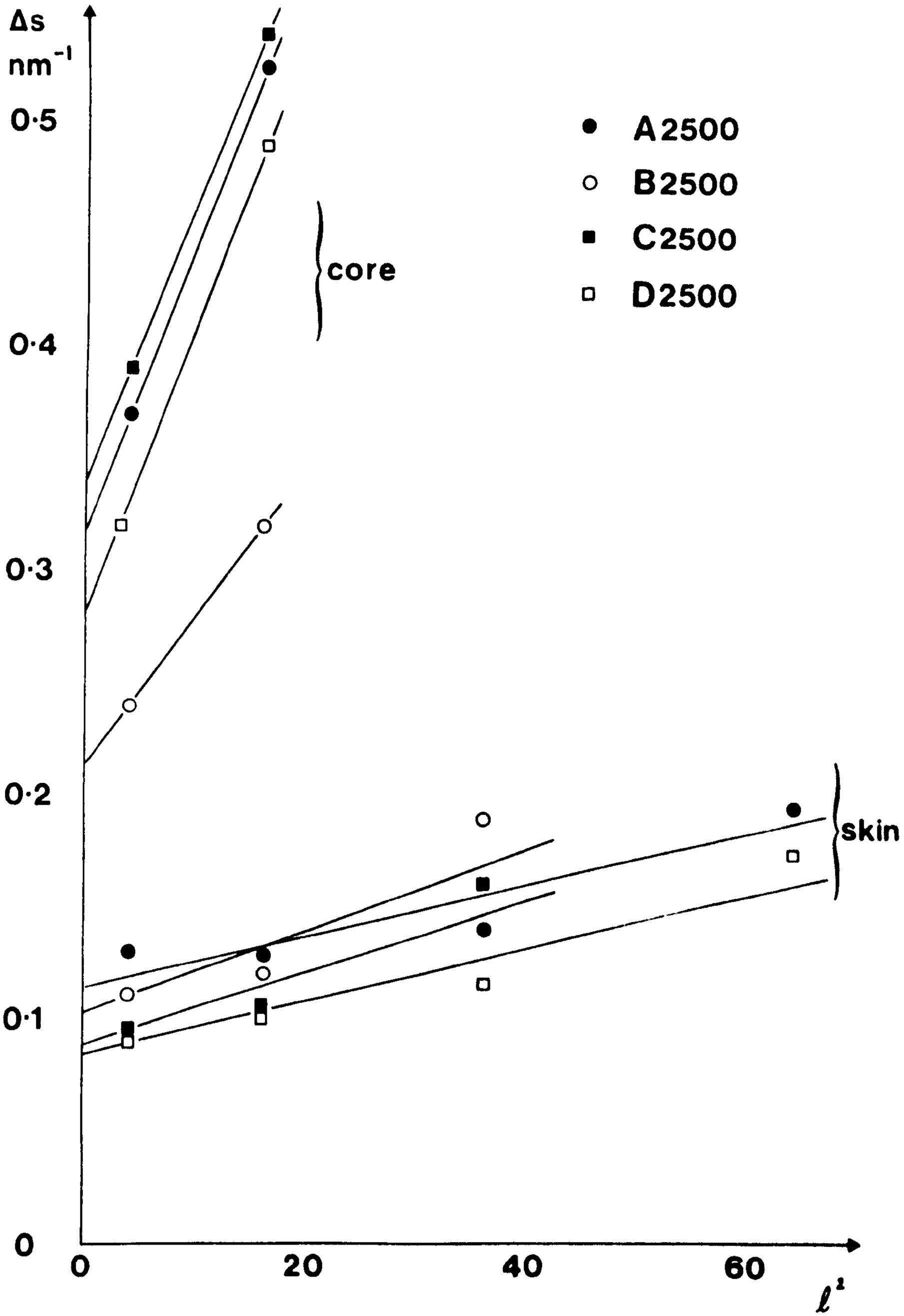

Fig. 28. The dependence of diffraction half-height width on ℓ^2 for skin and core regions of various specimens.

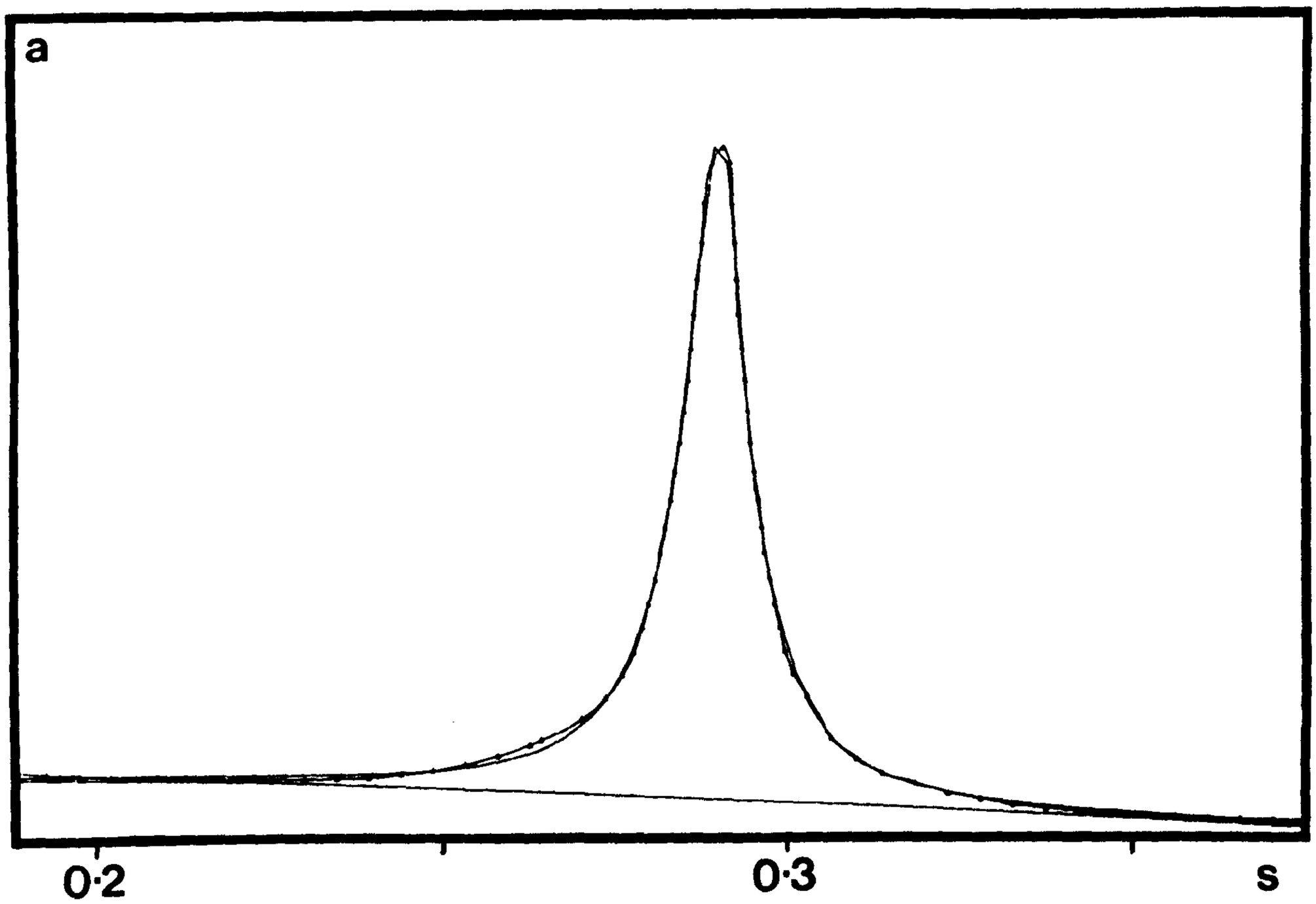

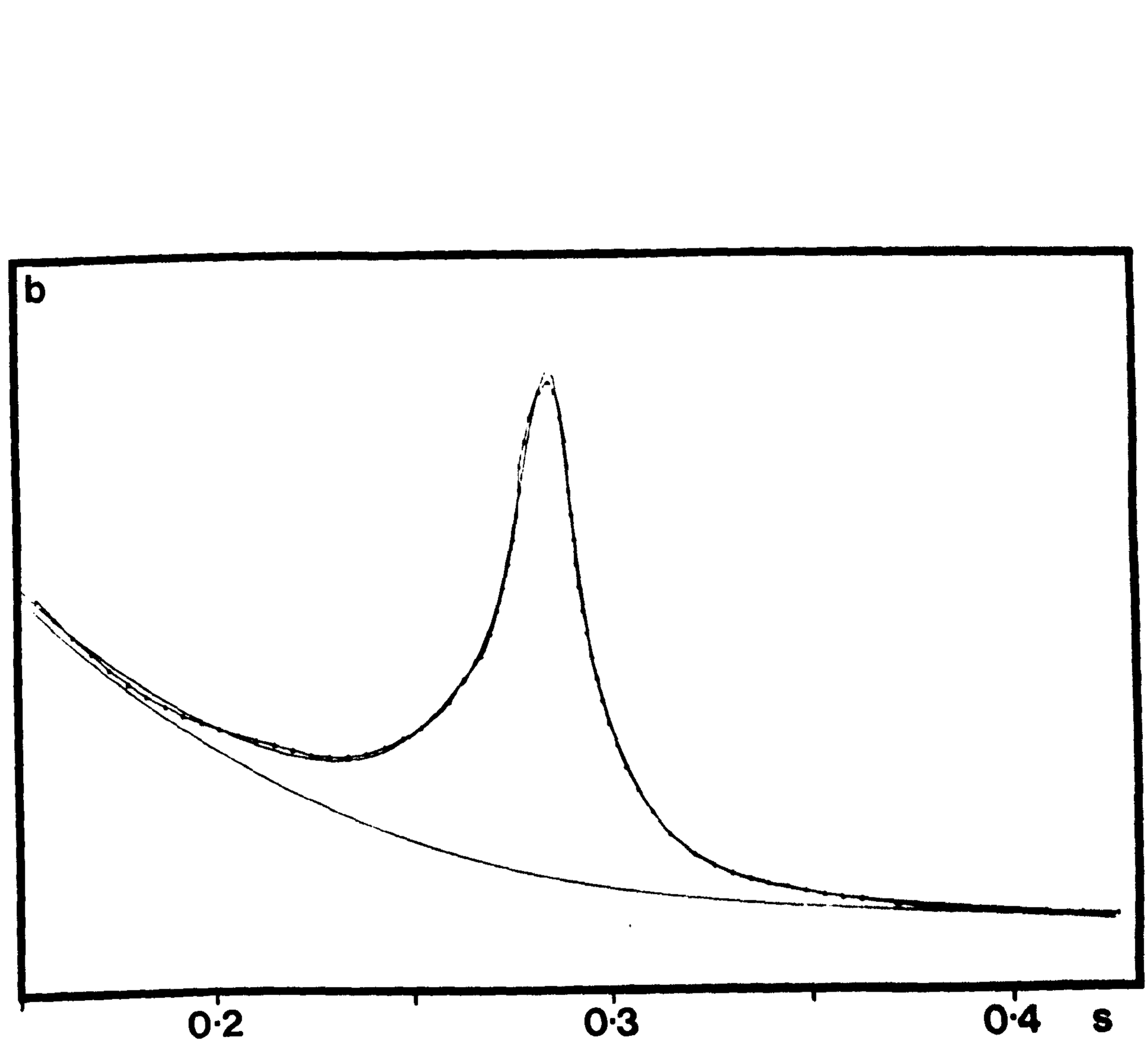

Fig. 29. Resolution of the (002) profile from (a) skin and (b) core of specimen B2500.

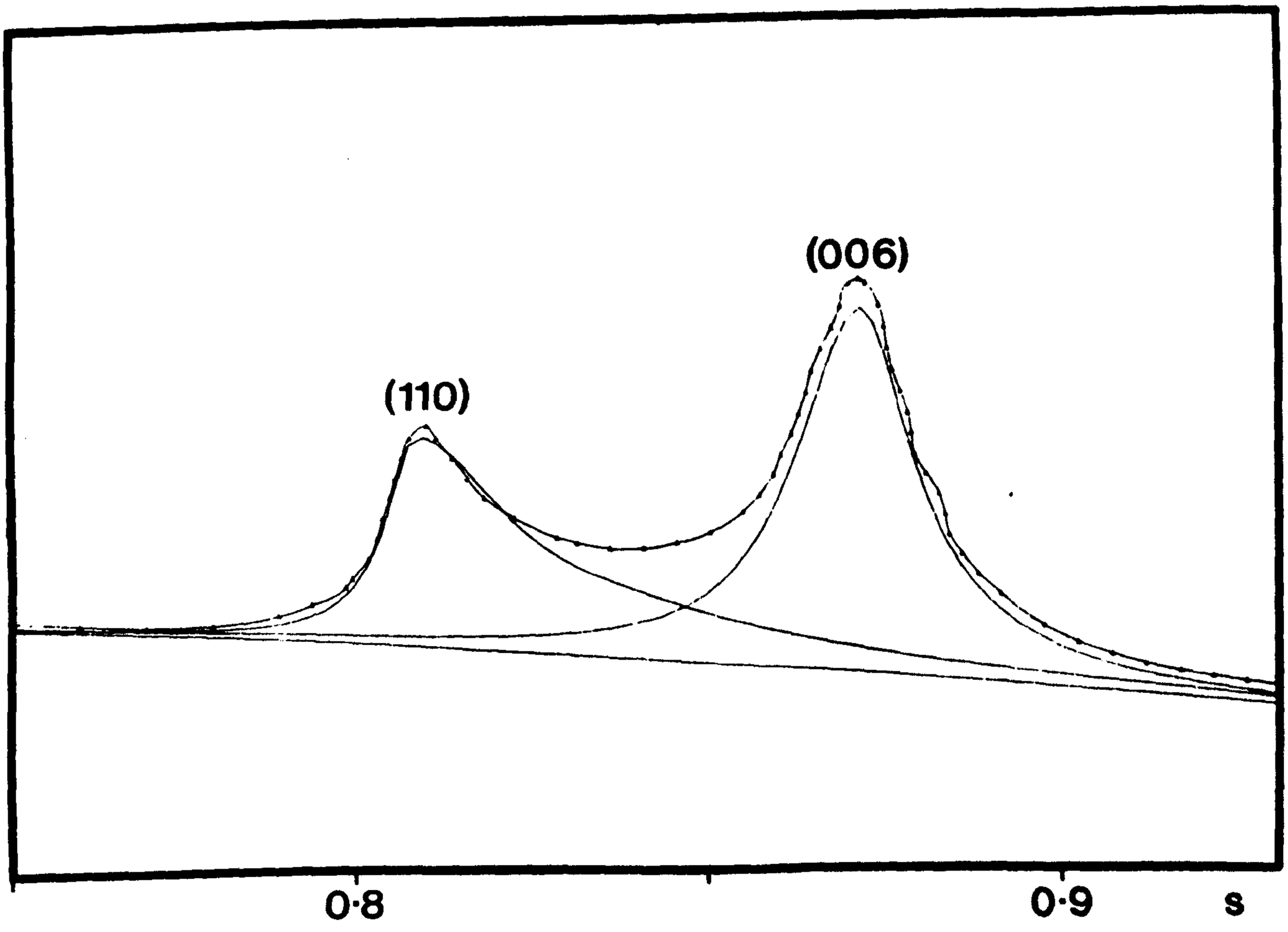

Fig. 30. Resolution of the overlapping asymmetric (110) and (006) profiles from the skin region of specimen B2500.

Table 2 Lattice Distortion (σ) and Mean Defect-free Distance (D_c) parameters

SPECIMEN	REGION IN SPECIMEN	σ (%)	D_c (nm)
A2500	Skin	0.54	8.9
	Core	1.66	3.0
B2500	Skin	0.66	9.8
	Core	1.21	4.5
C2500	Skin	0.62	11.4
	Core	1.63	2.8
D2500	Skin	0.52	11.8
	Core	1.73	3.5

Table 3 Mean Layer-plane Dimensions for Specimen B2500

REGION IN SPECIMEN	REFLECTION	SIZE PARAMETER (nm)
Skin	(100) Equatorial	$L_{a\perp} = 8.4$
Skin	(100) Meridional	$L_{a//} = 8.3$
Skin	(110) Meridional	$L_{a//} = 12.4$
Core	(100) Equatorial	$L_{a\perp} = 4.8$
Core	(100) Meridional	$L_{a//} = 7.7$
Core	(110) Meridional	$L_{a//} = 7.2$

A2500, B2500, C2500 and D2500. The values of D_c lie between about 9 nm and 12 nm for the skin, and 3 nm and 5 nm for the core, while σ is about 0.5 - 0.7% for the skin and in the range 1.2 - 1.7% for the core, irrespective of time of preoxidation.

Layer plane dimensions $L_{a//}$ (layer length) and $L_{a\perp}$ (layer width) shown in Table 3 were determined from the (hk0) reflections on the meridian and equator respectively. In the case of the (100) equatorial reflection K was taken as 1.84, for the (100) meridional reflection as 1, and for the (110) meridional reflection as 0.87 as described by Ruland and Tompa[120]. In the skin region the layer length was found to be 8.3 nm, while the depth was estimated at 8.4 nm. It is apparent from lattice-resolution images of carbon fibres that the layer planes are continuous in the direction of the fibre axis for many tens of nanometres, and as such it is important to stress that the value quoted for $L_{a//}$ is only a measure of the average length of straight sequences of layer planes. In the core it is noticeable that $L_{a//}$ has changed only slightly at 7.7 nm, while $L_{a\perp}$ has altered significantly to 4.8 nm. This indicates that the layer planes are not as wide in the core as they are in the skin, but that there is little difference in length.

Preferred orientation

The values of preferred orientation, Z, for skin and core regions in specimens A2500, B2500, C2500, and D2500 are shown in Table 4. As with stacking size and lattice distortion it is evident that time of preoxidation has no significant effect on orientation. The Z values for the skin are between 12^{o} and 16^{o}, while for the core the range is 20^{o} to 32^{o}. It is significant that the mean values of these orientations, 14^{o} for the skin and 24^{o} for the core are remarkably close to those observed by Johnson et al.[90] for T1 and T2 phases in high-modulus PAN-based fibres.

Table 4 Preferred Orientation Parameters

SPECIMEN	REGION IN SPECIMEN	Z^o
A2500	Skin	15
	Core	22
B2500	Skin	13
	Core	21
C2500	Skin	16
	Core	32
D2500	Skin	12
	Core	20

Table 5 Crystallite Size, Lattice Spacing and Orientation of Various Specimens

SPECIMEN	REGION IN SPECIMEN	L_c nm	c/2 nm	Z o
A1000	Skin	1.1	0.38	-
	Core	1.1	0.37	42
A1500	Skin	1.6	0.36	43
	Core	1.6	0.35	-
D1000	Skin	1.2	0.37	43
	Core	1.1	0.37	-
D1500	Skin	1.9	0.35	-
	Core	1.8	0.35	42
E1000	Skin	1.4	0.36	-
	Core	1.3	0.36	44
E1500	Skin	1.2	0.35	-
	Core	1.4	0.35	48
F1000	Skin	1.3	0.36	-
	Core	1.3	0.37	42
F1500	Skin	1.6	0.35	-
	Core	1.4	0.36	42

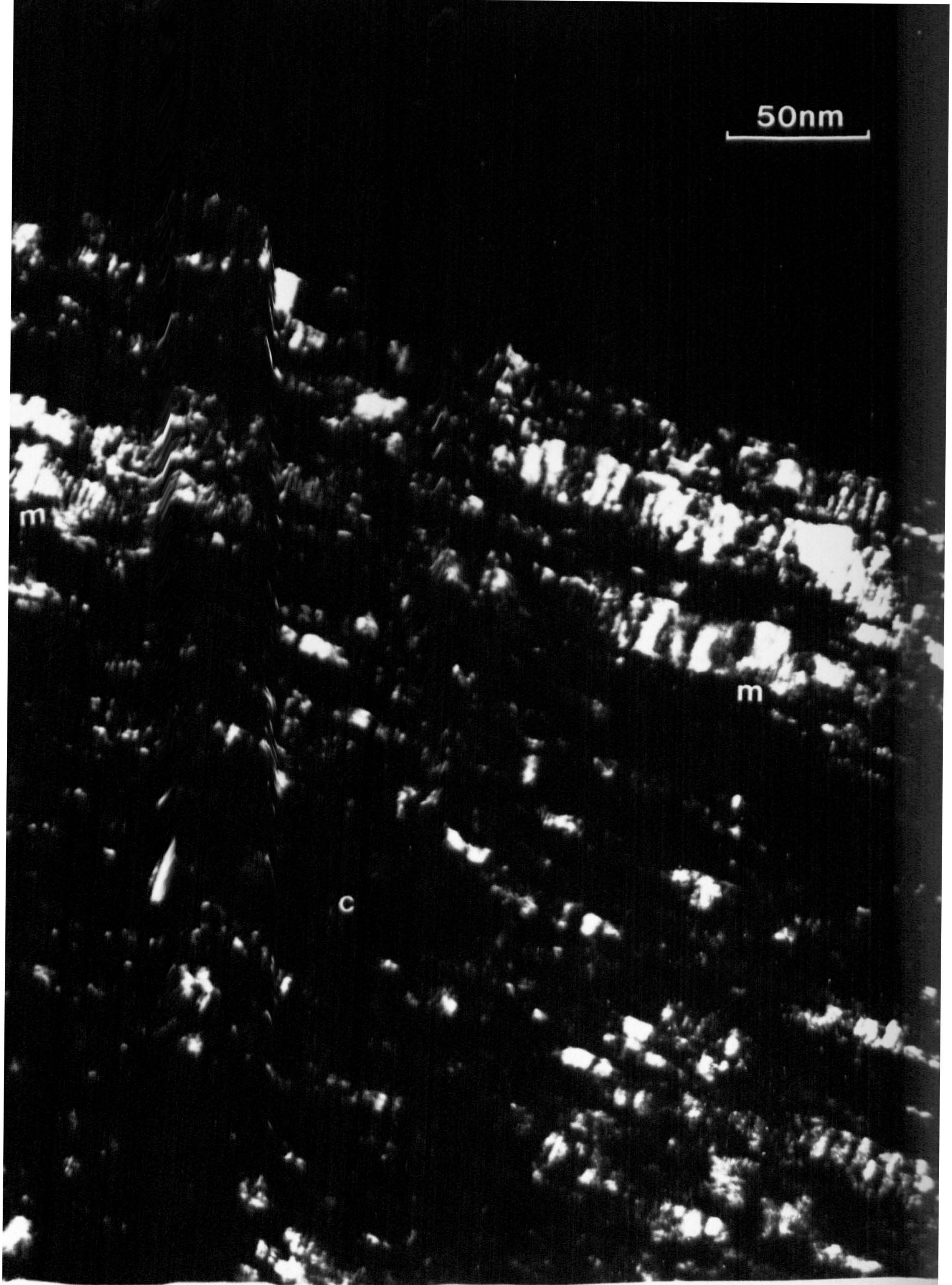

Plate XX. Intermediate-magnification (002) dark-field image of the skin structure of specimen J2500.

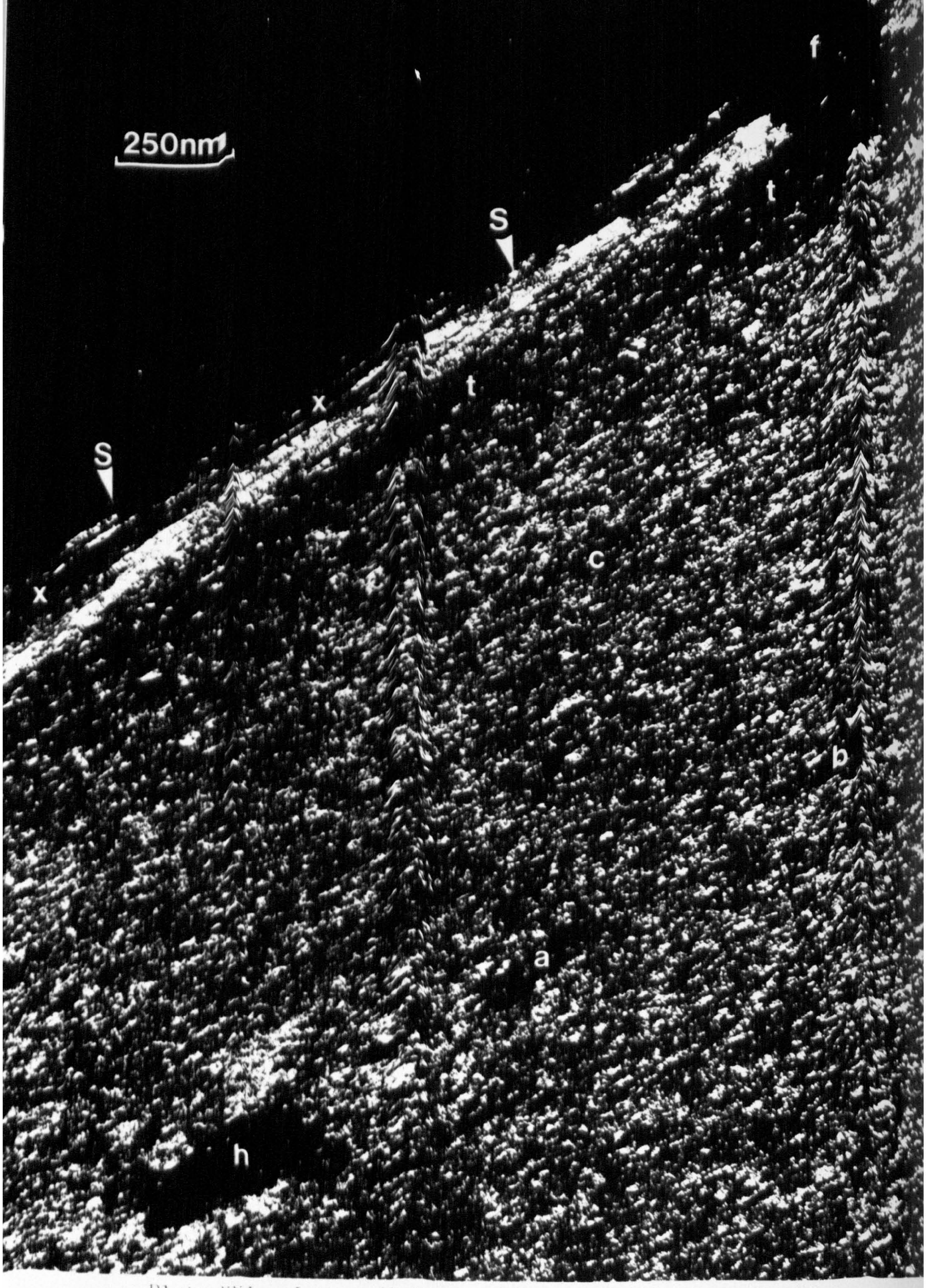

Plate XXI. Intermediate-magnification (002) dark-field image of the structure of specimen K2500, showing skin and core regions, surface flaws and internal voids.

B. The effect of different stabilization cycles

Watt and Johnson have found[17] that the chemical composition of the precursor acrylic is of fundamental importance in the formation of 'oxidation zones'. In an attempt to relate the presence or absence of these zones to the skin-core regions seen in high-modulus circular cross-section fibres ex-special Courtelle, specimens J2500 and K2500 were examined. The first of these had experienced a conventional stabilization cycle, while the latter had been vacuum-stabilized prior to oxidation and inert heat treatment. In both cases a skin structure identical to that observed earlier was identified. Again it was characterized by a wide range of crystallite sizes and mis-orientations, and, significantly, appeared to vary considerably in extent.

a. Skin-core structure

Plate XX shows the typical skin structure of specimen J2500 in the (002) dark-field mode. Extending to a maximum thickness of about 120 nm this region is characterized by both larger crystallite size, and higher preferred orientation than the core, c. Extensive regular Moiré-fringe patterns indicate crystallite overlapping at m.

Specimen K2500, which received a vacuum stabilization prior to oxidation, exhibits the same type of skin-core structure (Plate XXI) as specimen J2500, which was not vacuum-stabilized. In this case a skin of thickness about 150 nm has formed close to the surface, s. It is significant that the skin structure, again characterized by large crystallite size and high preferred orientation, neither extends fully to the edge, s, of the section (for example along x-x), nor homogeneously to the core, c (for example along t-t). This effect is similar to that reported for specimen F2500 (Plate V). It is evident, however, that formation of a skin-core macrostructure in fibres based on special

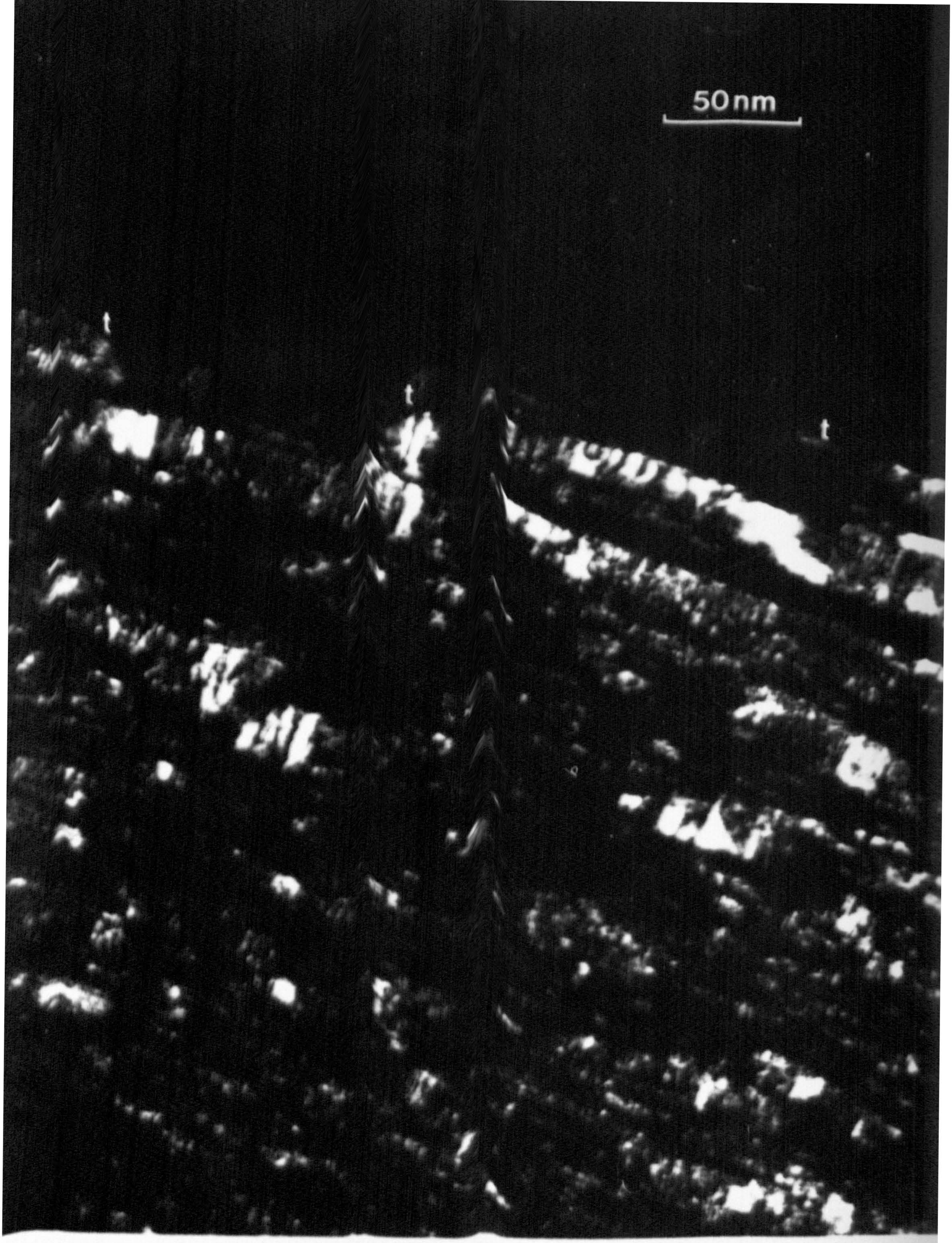

Plate XXII. Intermediate-magnification (002) dark-field image of the skin structure of specimen J2500, showing apparent surface steps.

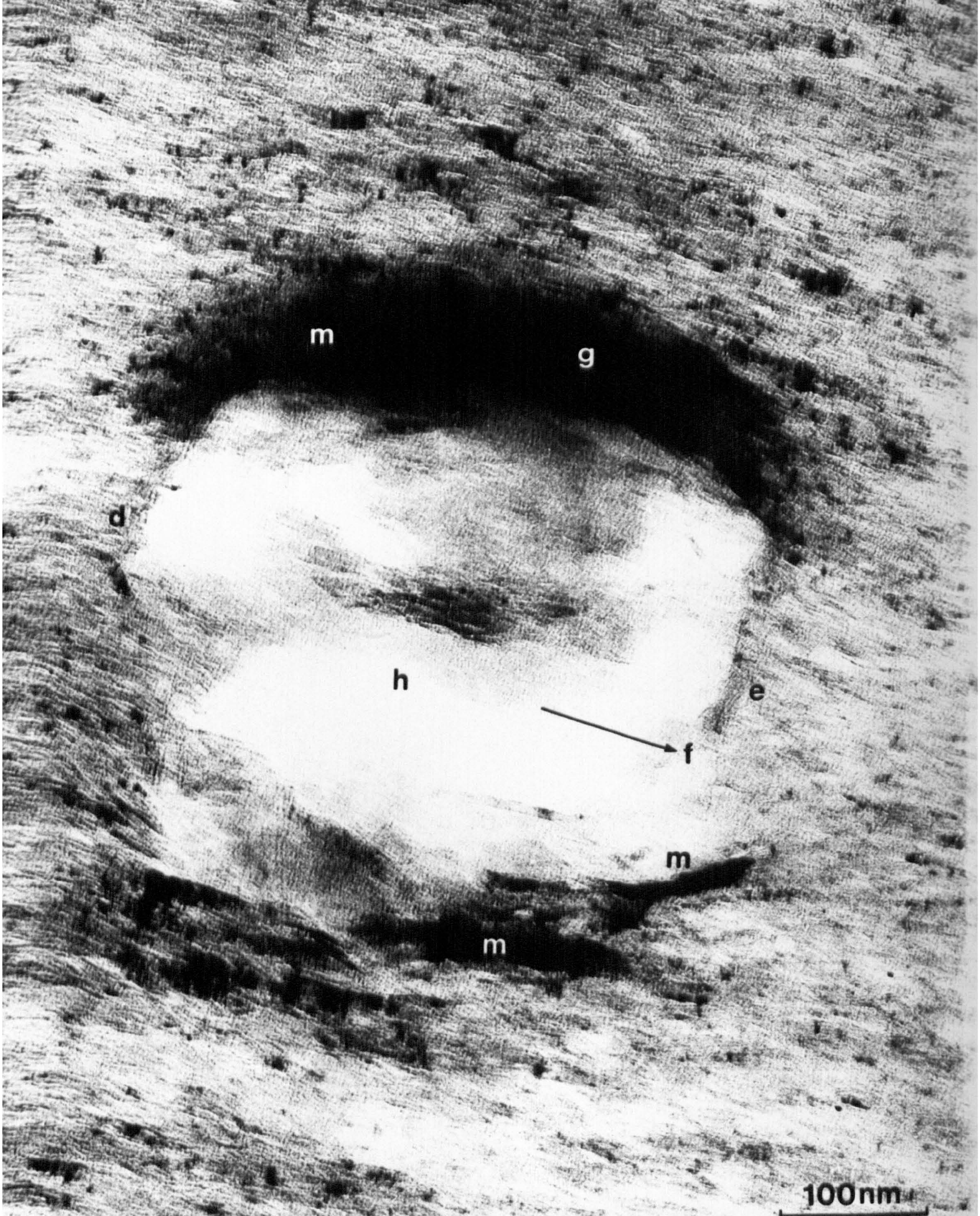

Plate XXIII. Intermediate-magnification bright-field image of an internal void in specimen J2500.

Plate XXIV. Intermediate-magnification (002) dark-field image of an internal void in specimen J2500.

Courtelle is not dependent on the stabilization cycle used.

b. Defect structure

Plate XXII shows an apparently stepped surface in specimen J2500, formed by the termination of surface crystallites of width 25 nm at t. In view of the strict orientation limitations imposed on dark-field images of this type this interpretation may be invalidated by the twisting of crystallites out of the Bragg diffraction condition.

Plate XXI exhibits some interesting flaws, for example, at f the skin structure is apparently discontinuous, and the area showing a low (002) diffracted intensity (referred to as t above) is considerably wider at 200 nm than elsewhere. In the core, c, of the fibre a large hole of width 150 nm and length 0.45 μm is shown at h, while subsidiary inclusions can be seen at a and b. These are in the same direction parallel to the fibre axis as h, and as such may have been produced during precursor drawing. In the case of the larger hole, catalytic graphitization has occurred parallel to the c-axes of the crystallites on either side of the flaw.

Similarly, an interesting internal flaw in specimen J2500 of width and length about 0.5 μm is depicted in Plate XXIII in bright-field ((000) only) mode, and in Plate XXIV in the (002) dark-field mode. The hole, h, can be seen to be bordered by highly-graphitized crystallites, g, of width up to about 100 nm. Crystallites, m, mis-oriented at large angles to the direction, f, of the fibre axis clearly evident in Plate XXIII are missing from Plate XXIV since they are diffracting outside the small objective aperture used. This demonstrates the orientation limitations of dark-field images when such a small aperture is used. It is noticeable that extensive catalytic graphiti-zation has not occurred in those areas, d and e, along the direction of the fibre axis; graphitization only proceeding normal to f, and thus

parallel to the c-axis of the crystallites as in Plate XXI.

c. Resumé

Carbon fibres made from circular cross-section special Courtelle, and heat-treated to 2500°C exhibit a skin-core structure, the dimensions of which are independent of time of preoxidation and type of stabilization cycle. The width of the skin, which has a mean stacking size of around 10 nm, and preferred orientation about 15°, is extremely variable up to a maximum of about 0.5 μm. The core structure, of mean stacking size about 4 nm and preferred orientation 25° is characterized by complex three-dimensional interlinking and interweaving, and forms more than 90% of the total volume of the fibre. Although possessing higher preferred orientation than the core, there is a higher chance of the skin containing a large crystallite mis-oriented from the fibre axis at an angle greater than the mean, and structural continuity between these and the core might be expected to lead ultimately to failure. There is no evidence to suggest that light and dark zones seen in polarized-light microscopy of cross sections of oxidized fibres are related to structural zones in fibres heat treated to 2500°C.

2.3.2 Fibres heat treated to 1000°C and 1500°C

In an effort to identify the origin of skin-core heterogeneity and surface flaws in carbon fibres made from special Courtelle and heat treated to 2500°C, specimens A1000, A1500, D1000, D1500, E1000, E1500, F1000 and F1500 were thin sectioned at RAE and examined in the electron microscope. Owing to the large amounts of specimen damage to these lower temperature fibres during sectioning, only those regions of the section which appeared undistorted were examined; intermediate-magnification bright and dark-field images, lattice-resolution images and electron-diffraction patterns being obtained from relevant areas.

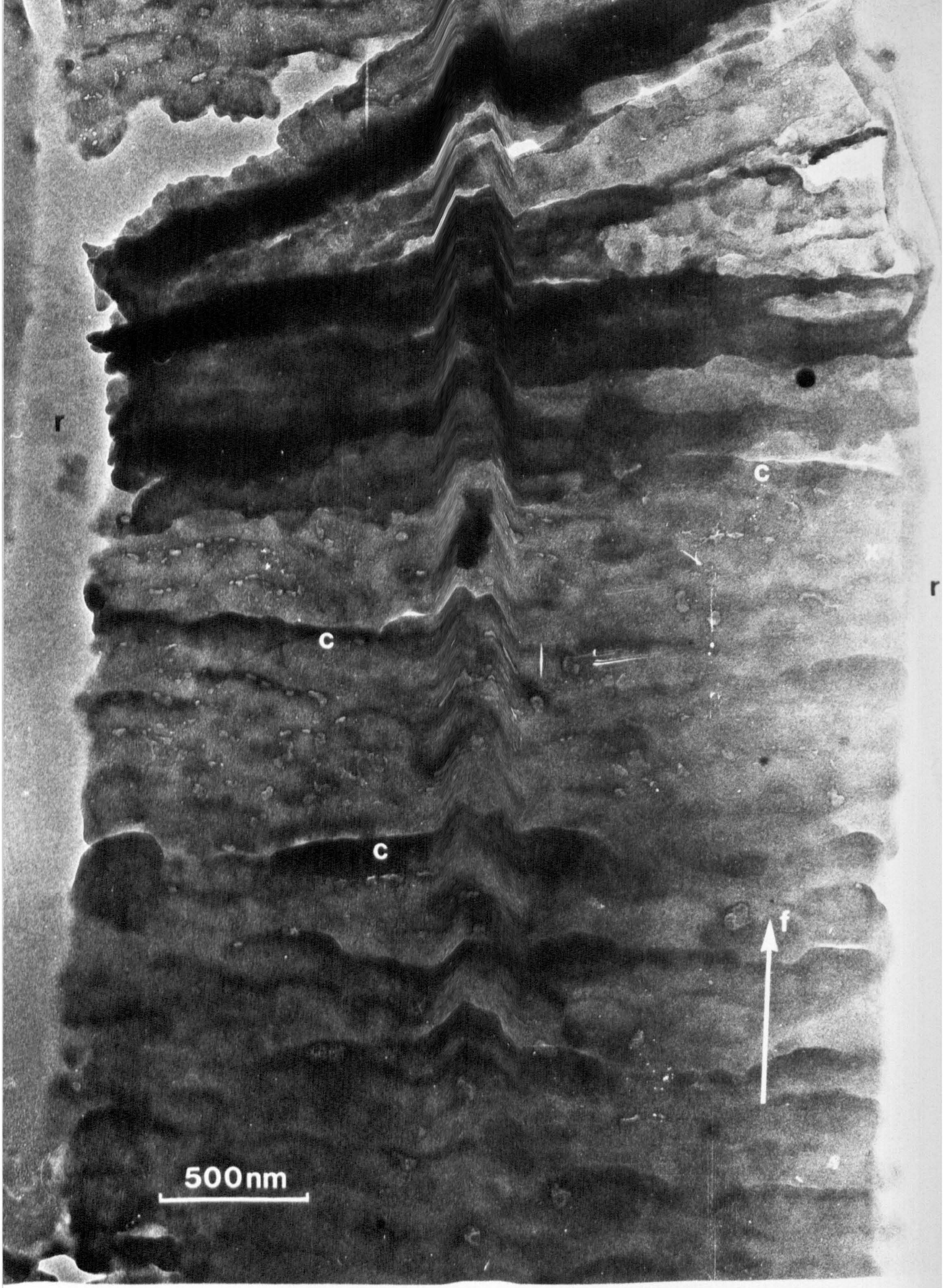

Plate XXV. Low-magnification bright-field image of a longitudinal section cut from specimen D1000.

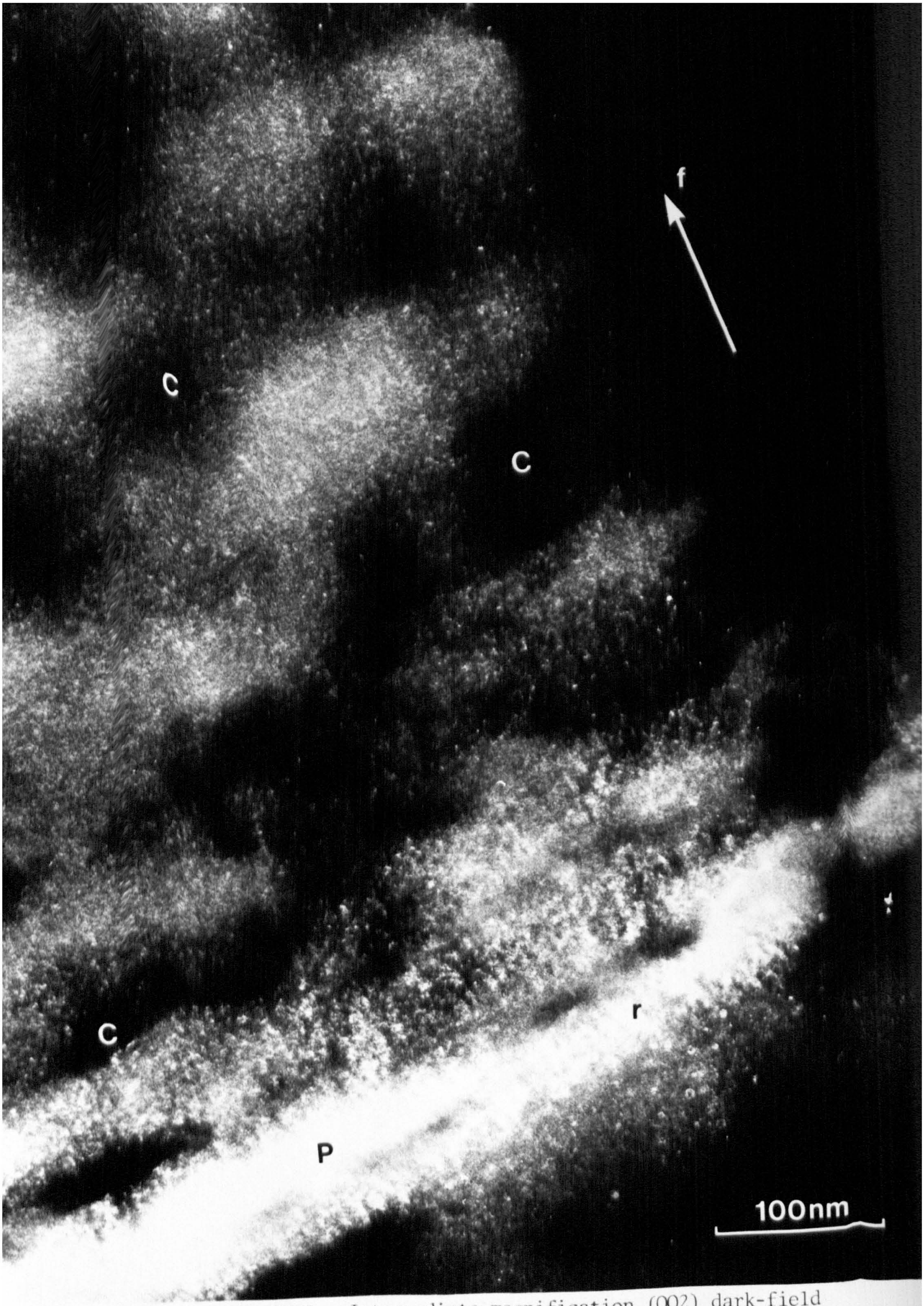

Plate XXVI. Intermediate-magnification (002) dark-field image of the longitudinal structure of specimen D1000.

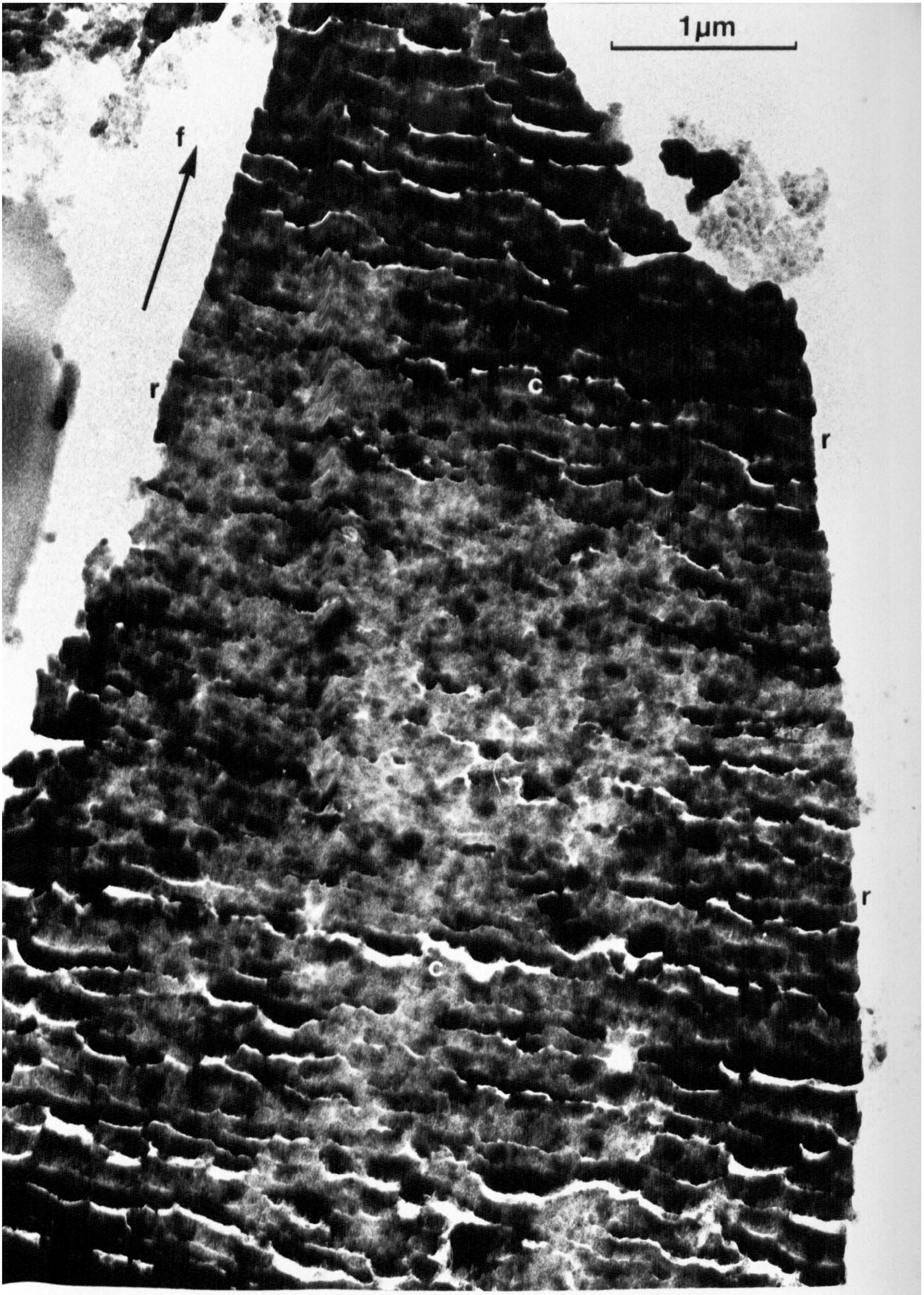

Plate XXVII. Low-magnification bright-field image of a longitudinal section cut from specimen E1000.

Values of L_c (from the (002) reflection only) and c/2 were obtained as described above, and the results are shown in Table 5.

It is evident from Table 5 that for fibres heat treated at $1000^{o}C$, L_c is of the order of 1.1 - 1.4 nm, and that there is no skin-core effect. Similarly, fibres heat treated at $1500^{o}C$ showed no evidence of structural heterogeneity, with stacking sizes of 1.2 - 1.9 nm being found for both skin and core zones. The c/2 parameter was found to decrease from a value in the range 0.36 - 0.38 nm at $1000^{o}C$ to about 0.35 - 0.36 nm at $1500^{o}C$. The Z values shown in Table 5 confirm that there is no diffraction evidence of gross heterogeneity in carbon fibres prepared at either $1000^{o}C$ or $1500^{o}C$, since they are in the range $42 - 48^{o}$ irrespective of selected area.

The quantitative electron-diffraction analysis is confirmed by subjective examination of appropriate bright and dark-field images. Plate XXV shows a thin section of specimen D1000 in the bright-field mode. The cracks, c, which run at 90^{o} to the direction, f, of the fibre axis are due to sectioning, which in this case was parallel to f. However, the resin embedding medium, r, can be seen present along the edges of the fibre, and this is indicative that some regions (such as at x) are not badly distorted, and these were used for electron-diffraction and high-resolution studies.

Plate XXVI shows, in the (002) dark-field mode, specimen D1000. This section is characterized by artefacts such as 'pile-up', p, and chatter marks, c, caused during sectioning, but it is apparent that there is no evidence of structural heterogeneity in terms of a sheath-core macrotexture. Regions where there is evidence of higher (002) diffracted intensity, for example at r, constitute a crumpled structure again caused by sectioning.

Plate XXVII shows a section cut from specimen E1000, which again shows not only the transverse cracks, c, typical of cutting along

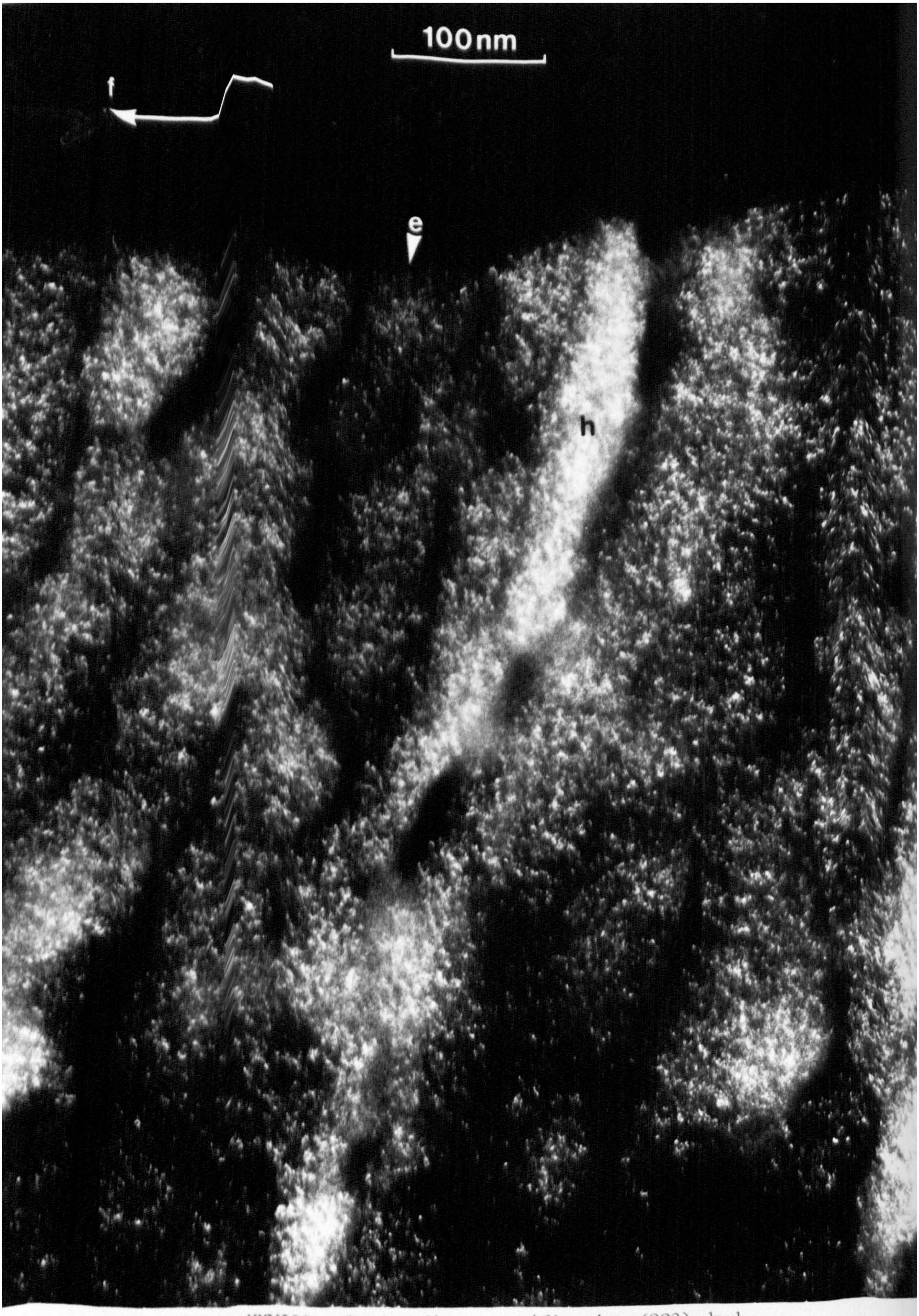

Plate XXVIII. Intermediate-magnification (002) dark-field image of the longitudinal structure of specimen E1000.

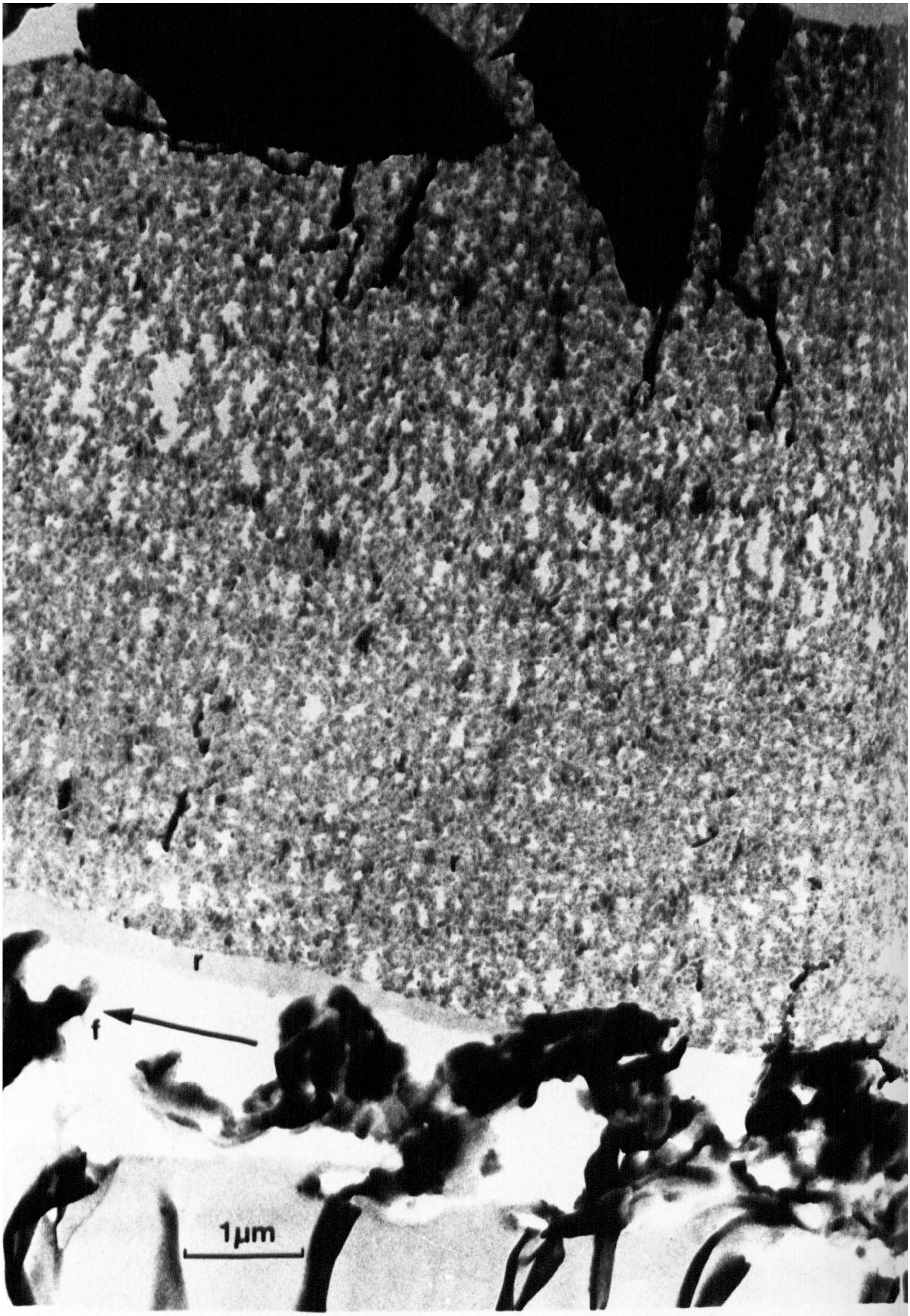

Plate XXIX. Low-magnification bright-field image of a longitudinal section cut from specimen E1500.

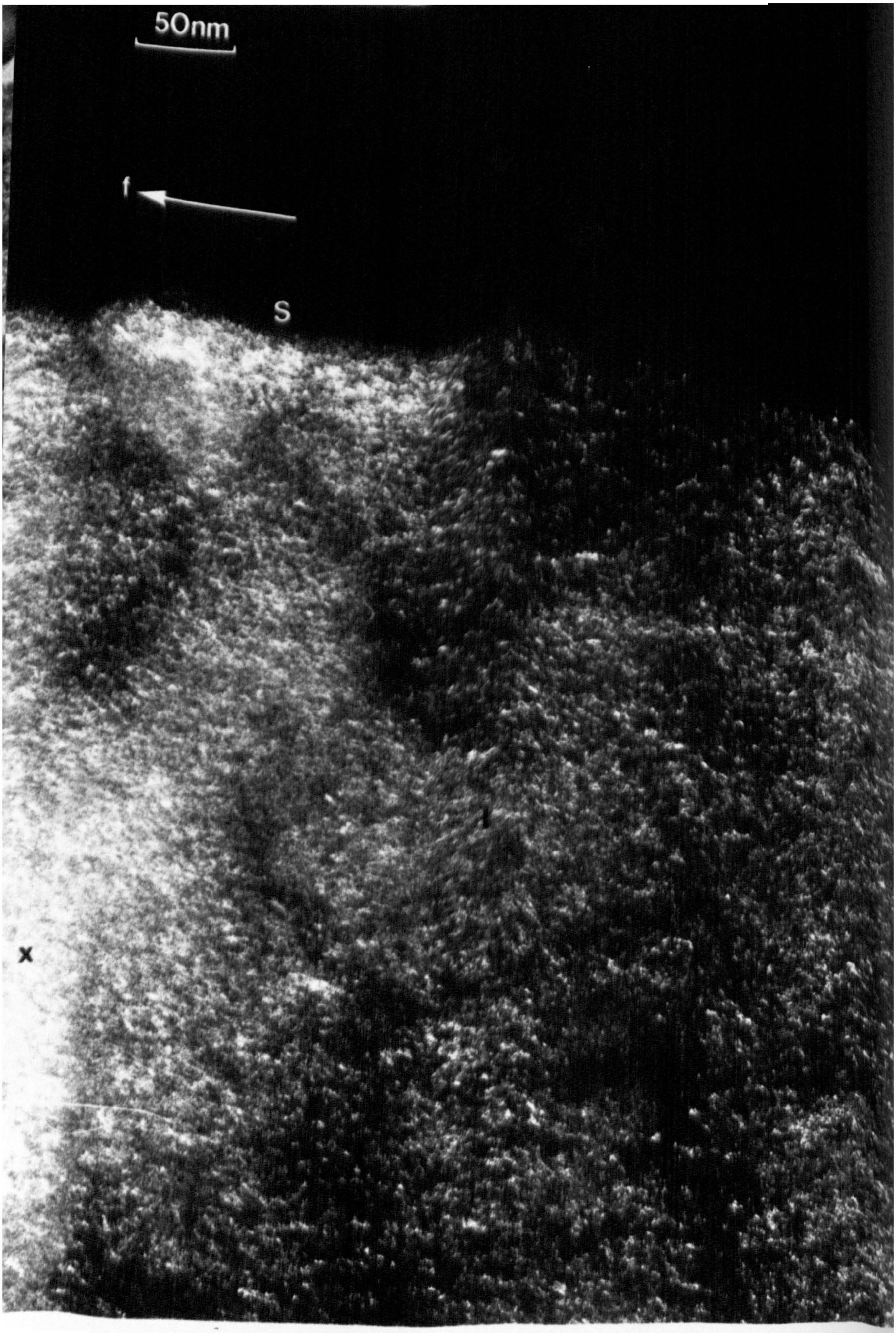

Plate XXX. Intermediate-magnification (002) dark-field image of the longitudinal structure of specimen D1500.

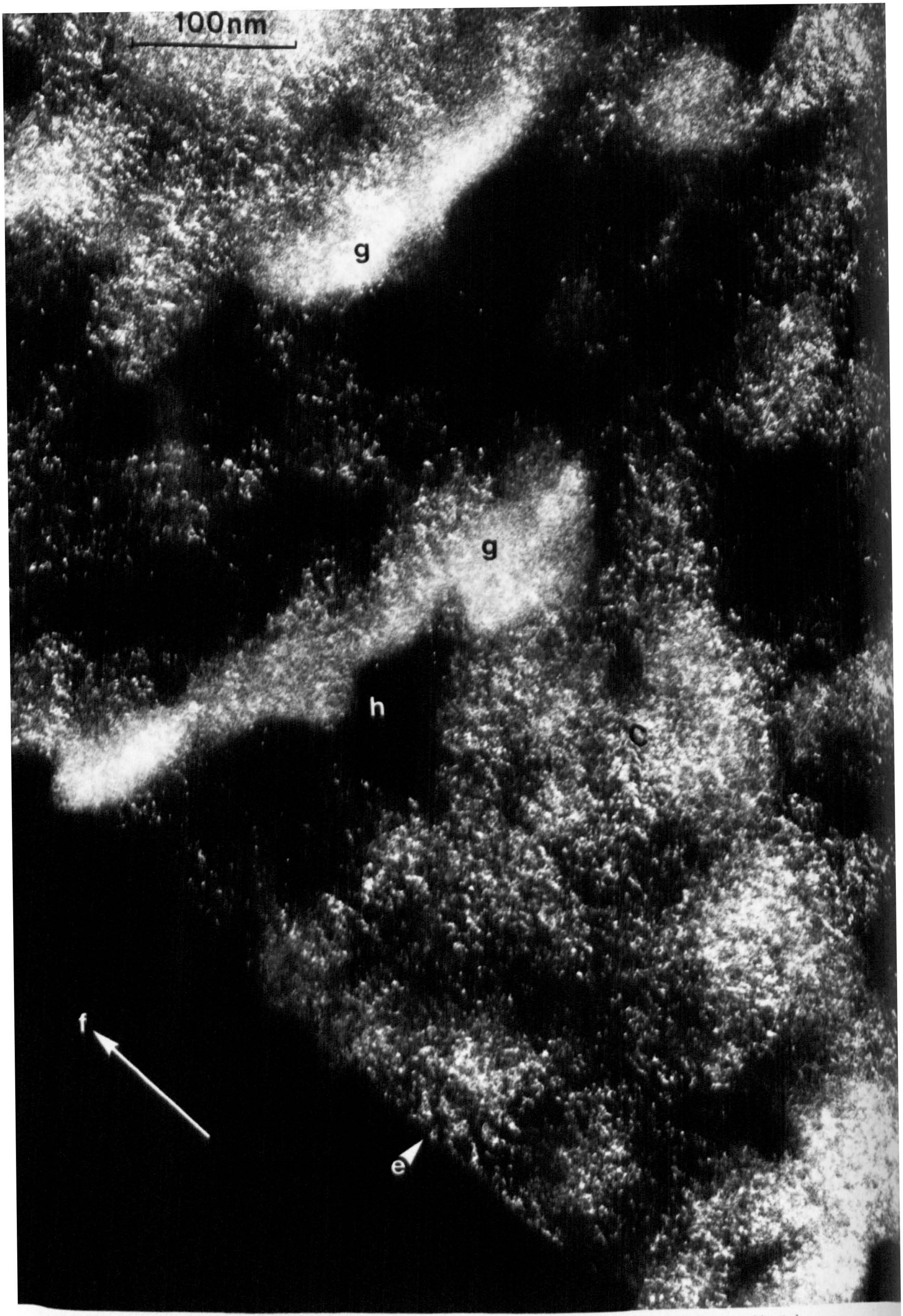

Plate XXXI. Intermediate-magnification (002) dark-field image of the longitudinal structure of specimen F1500.

the fibre axis direction, but also small, relatively undistorted areas, r, suited to high-resolution studies. In the (002) dark-field mode (Plate XXVIII) this specimen clearly shows no skin-core heterogeneity, the density and size of crystallites being remarkably uniform right up to the edge, e, of the section. Again, a higher density of (002) diffraction (for example at h) is indicative of a thicker region in the specimen caused by crumpling and pile-up. The direction, f, of the fibre axis is shown.

The superior sectioning properties of material heat treated at 1500°C is shown in Plate XXIX, which is a bright-field image of specimen E1500. The transverse cracks are less evident, and again, relatively undistorted regions, r, can be located for high-resolution and diffraction analysis.

After heat treatment at 1500°C the crystallites are slightly larger than at 1000°C, there being little change in preferred orientation (Table 5). Plate XXX shows the more discrete nature of these crystallites in specimen D1500. There is some evidence of a narrow skin of width 40 nm at s, which exhibits apparently larger crystallite size than the more typical structure at t. This effect may be a sectioning artefact since a similar structure at x apparently extends into the fibre normal to the direction, f, of the fibre axis.

A similar structure for specimen F1500 is depicted in Plate XXXI. The homogeneous core structure, c, extends fully to the edge, e, of the section, while holes, h, and other anomalous effects, g, are clearly related to sectioning artefacts.

At lattice resolution, there is some evidence for a slight increase in crystallite size and orientation at the very edge of the section. Although no clear-cut demarcation between skin and core can be seen it is clear from the high-resolution image of specimen F1500 in

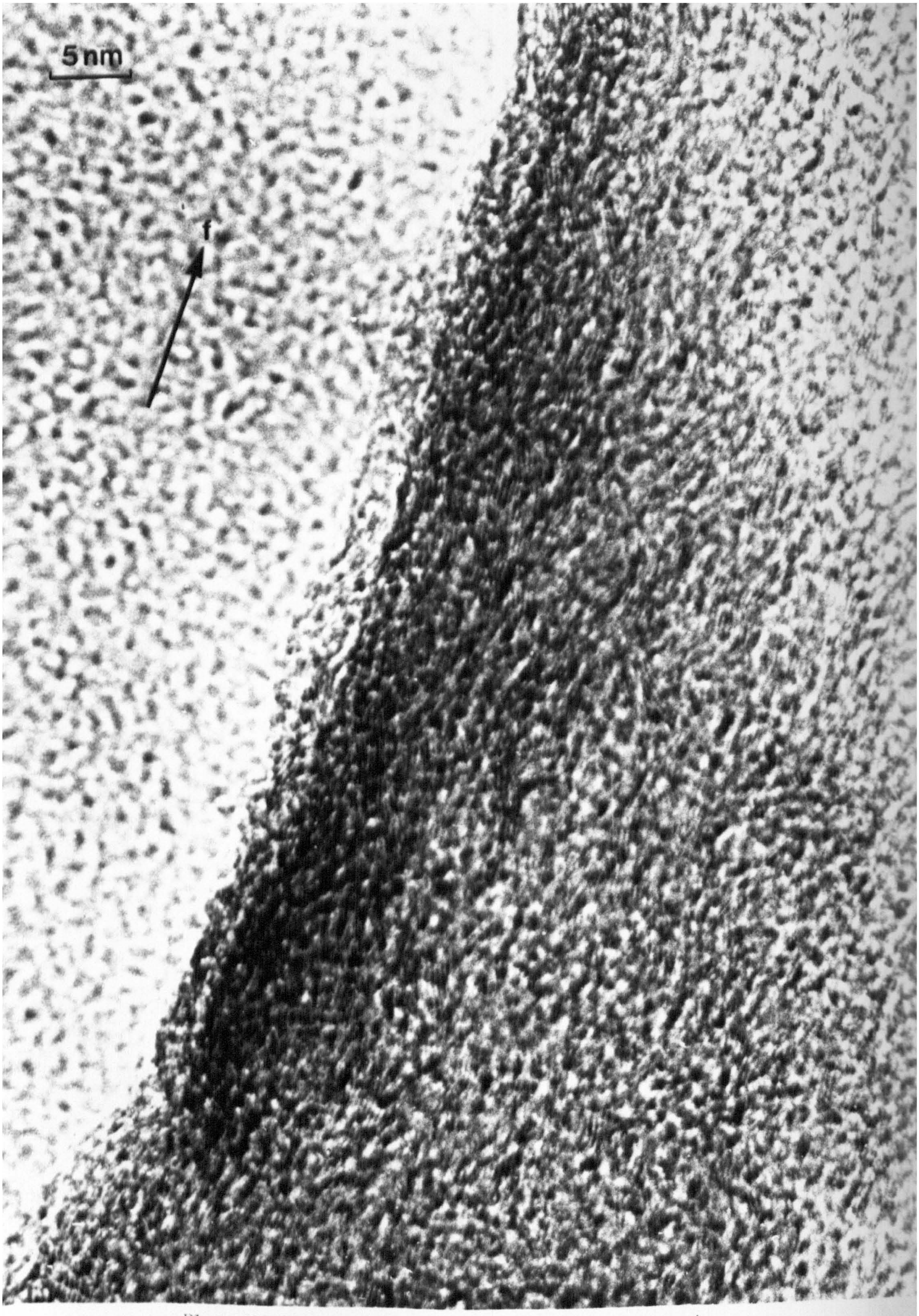

Plate XXXII. Lattice-resolution image of a region close to the surface of specimen F1500.

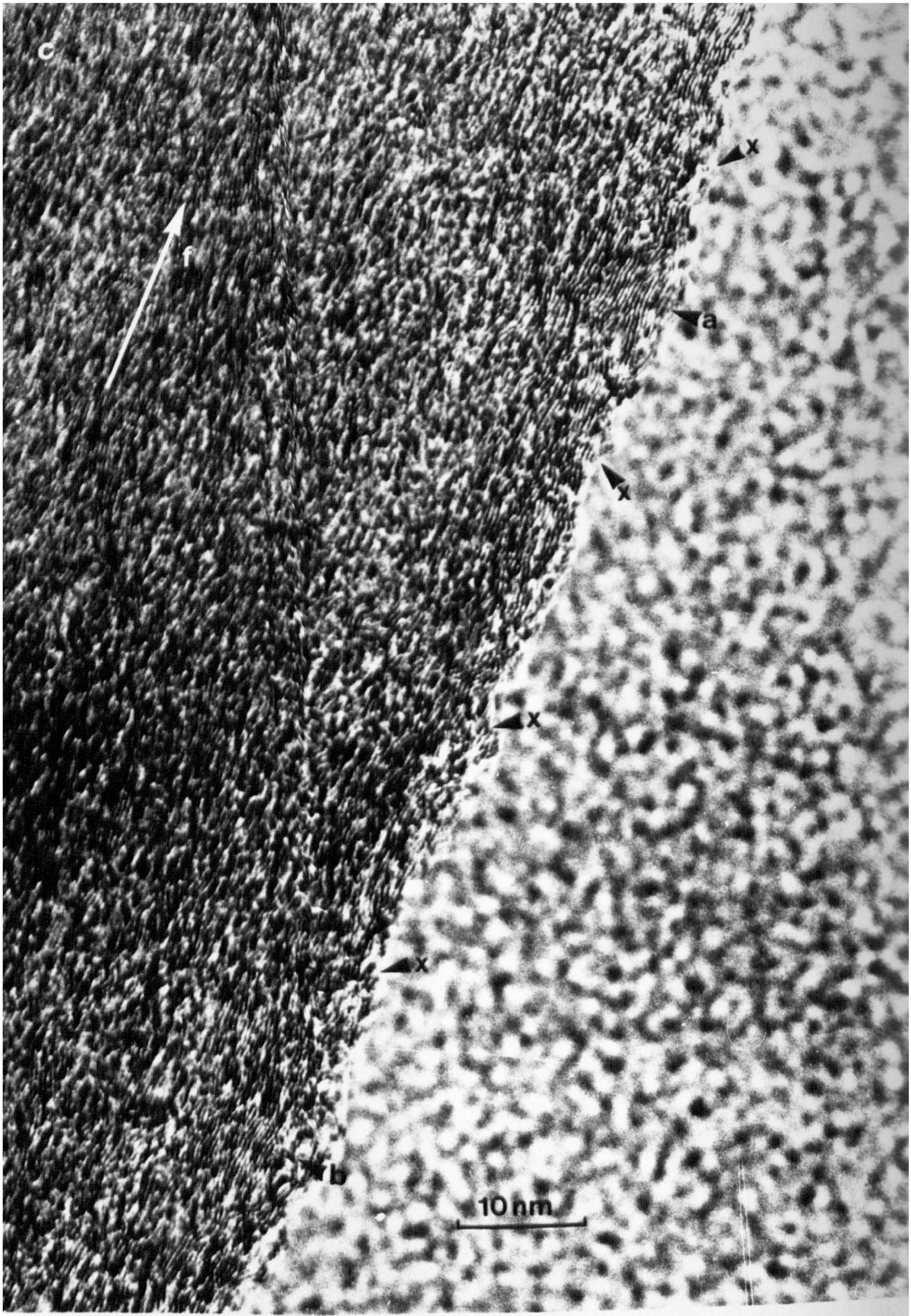

Plate XXXIII. Lattice-resolution image of a region close to the surface of specimen F1500.

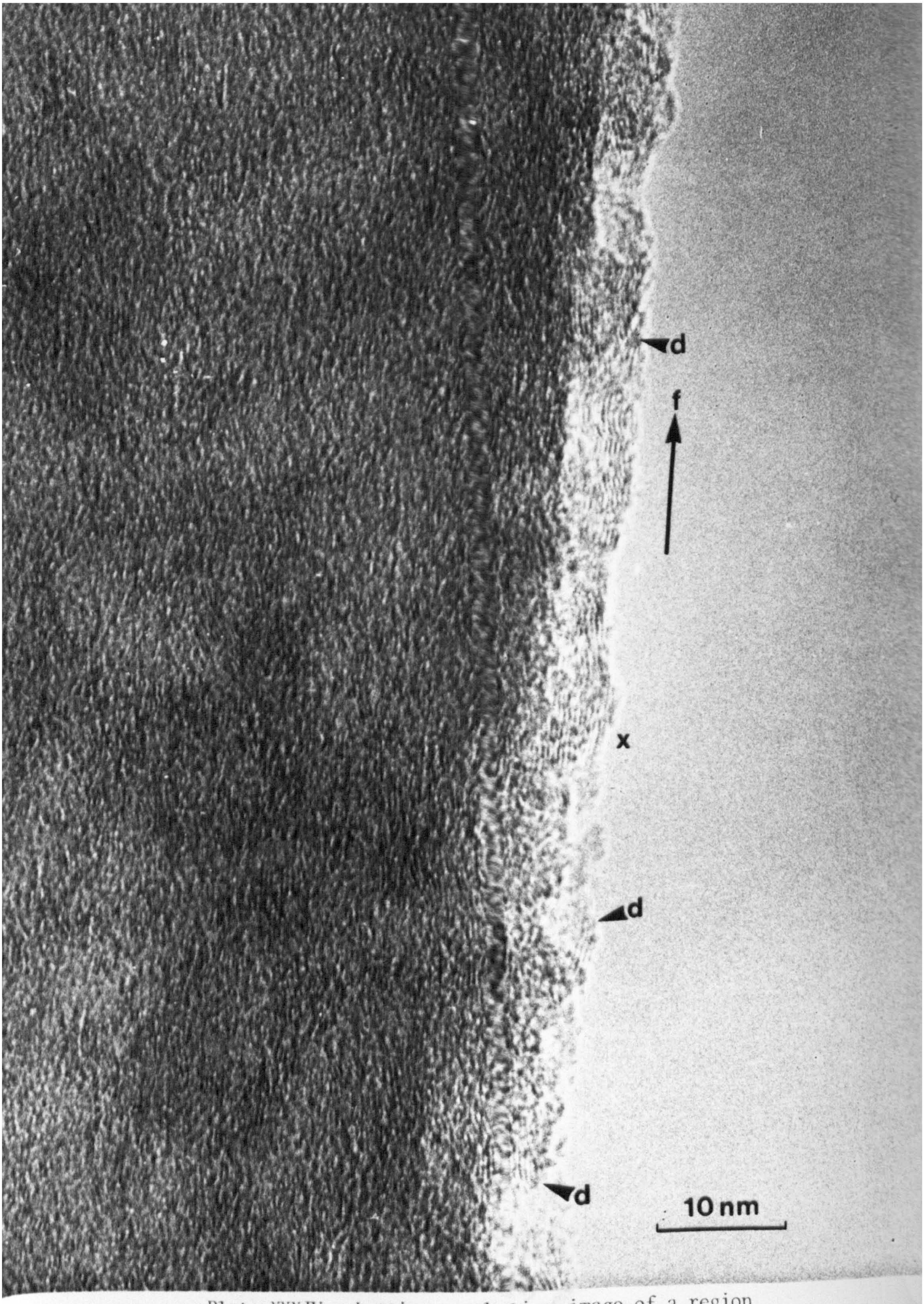

Plate XXXIV. Lattice-resolution image of a region close to the surface of specimen F1000.

Plate XXXII that the surface of the fibre constrains the crystallization of the turbostratic graphite lattice planes into a well-oriented, but extremely thin layer. In order to confirm this, longitudinal sections cut normal to the fibre axis were examined. In this case the leading edge is relatively distortion-free after cutting, and unambiguous conclusions may be drawn from relevant images. Plate XXXIII shows the edge of a section cut from specimen F1500, and it is clear that crystallite orientation and perfection is higher at the very edge than in the core, c. For example, at a and b there are crystallites of width 6 nm and 5 nm respectively, and the layer-plane length in the direction of the fibre axis is evidently much greater in this narrow skin region than in the core. Plate XXXIV is a similar image from specimen F1000, showing grouping of layer planes at the very edge of the fibre to form the start of surface crystallites, and at x a more crystalline area of width 6 nm extending into the section.

2.4 FIBRES HAVING A DOG-BONE CROSS SECTION

Recently Watt and Johnson have shown[17] that the different chemical composition of dog-bone cross-section fibres (i.e. Orlon and Dralon) compared with circular cross-section fibres (special Courtelle) is of importance in the formation of oxidation zones. In particular, conventionally-stabilized dog-bone shaped fibres were found to exhibit no oxidation zones, a skin of thickness greater than 1 μm only being formed after a vacuum stabilization prior to oxidation. In order to test whether or not these observed zones are related to the skin-core zones seen in all high-modulus carbon fibres ex-special Courtelle specimens G2500, H2500, L2500, M2500, N2500, and P2500 were thin sectioned and examined.

2.4.1 Macrostructure

Plate XXXV shows the longitudinal structure of specimen

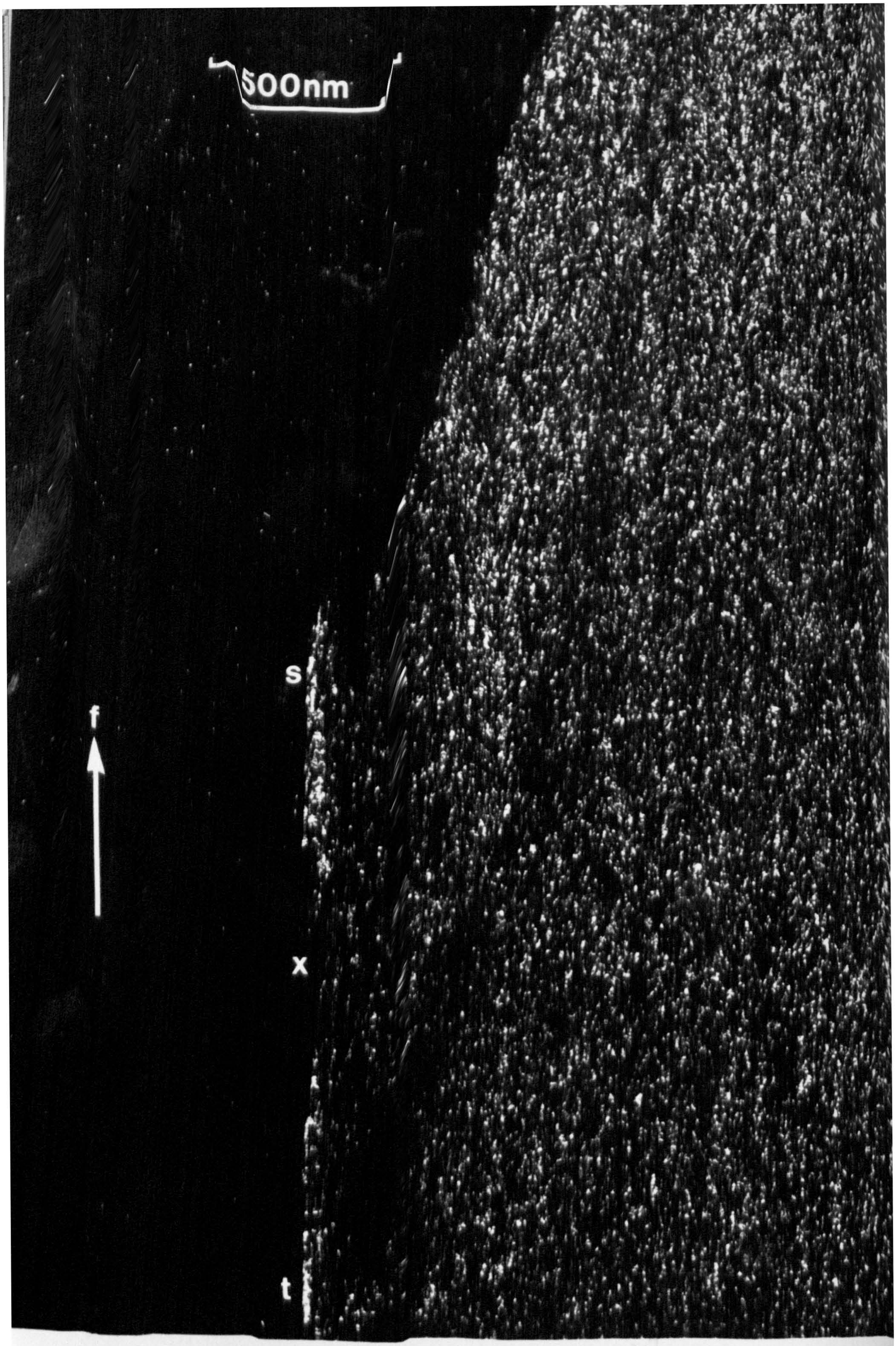

Plate XXXV. Intermediate-magnification (002) dark-field image of the longitudinal structure of specimen M2500.

Plate XXXVI. Intermediate-magnification (002) dark-field image of the skin structure of specimen L2500.

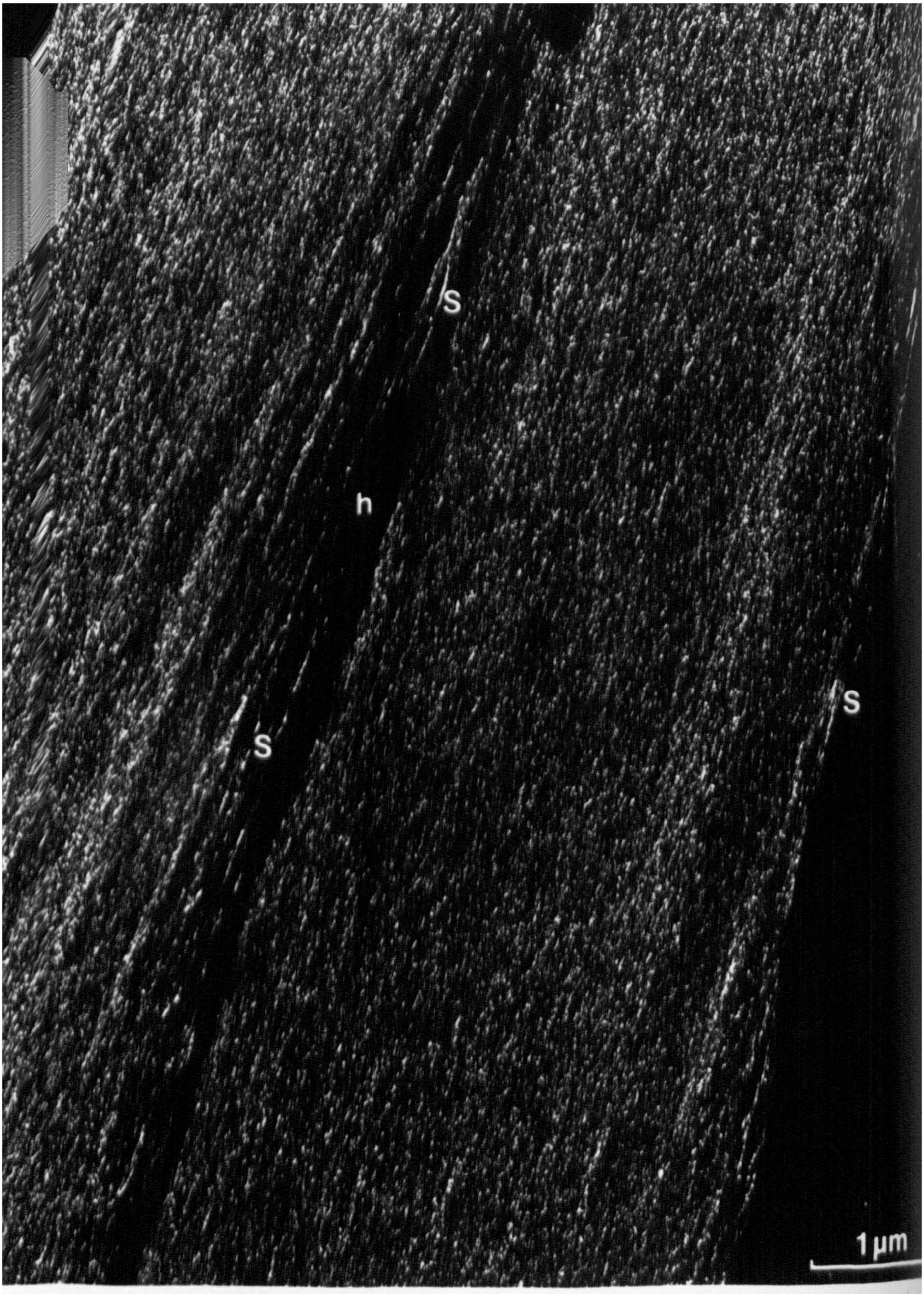

Plate XXXVII. Low-magnification (002) dark-field image of the longitudinal structure of specimen L2500.

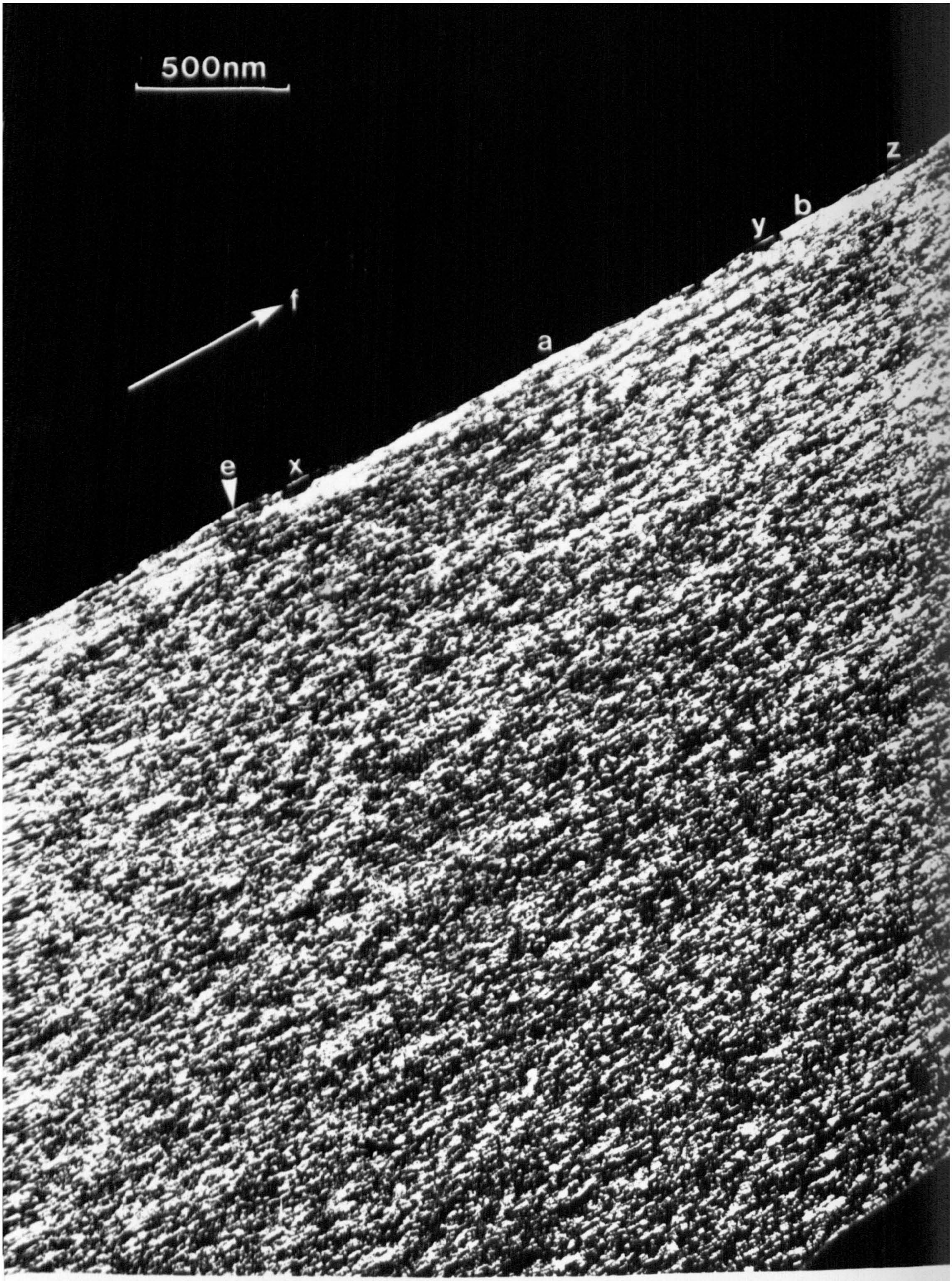

Plate XXXVIII. Low-magnification (002) dark-field image of the longitudinal structure of specimen L2500.

M2500 in the (002) dark-field mode. Evidently a skin of thickness about 75 nm has formed at s and t, though there is discontinuity, x, extending over about 0.5 μm between these two regions. The core structure is homogeneous with no evidence of the zones of different orientations predicted by polarized-light microscopy.

The specimens which do not exhibit oxidation zones, viz. L2500 and N2500, were similarly examined, and found to possess the characteristic skin-core structure. Plate XXXVI shows this typical structure in specimen L2500. The crystallite size and orientation is higher within a 60 nm region close to the edge, e, of the section, although there is some evidence, for example at x, y, and z of a larger than average crystallite size in the core. Extensive Moiré-fringe patterns are indicative of crystallite overlapping and interlinking, and the direction, f, of the fibre axis is shown.

Plate XXXVII, from the same specimen, L2500, apparently shows a hole, h, running down the centre of a 7 μm wide section. When the dog-bone cross section of Orlon is considered, however, it is evident that this image represents a cut through the two lobes as in Fig. 31. If this is the case, then skin structure should be apparent at the regions labelled x in Fig. 31. Examination of the relevant areas, s, in Plate XXXVII shows that this is in fact so. A core structure possessing no preferred c-axis orientation is assumed in Fig.31.

A skin-core structure indistinguishable from that of type I fibres ex-special Courtelle is shown in Plate XXXVIII for specimen L2500. A skin of high orientation and large crystallite size can be seen to extend over an area of maximum width 200 nm at the edge, e, of the section, while it is clear that the core structure is completely homogeneous. There is some evidence of crystallites twisting out of the diffraction condition at the very edge of the section at x, y, and z,

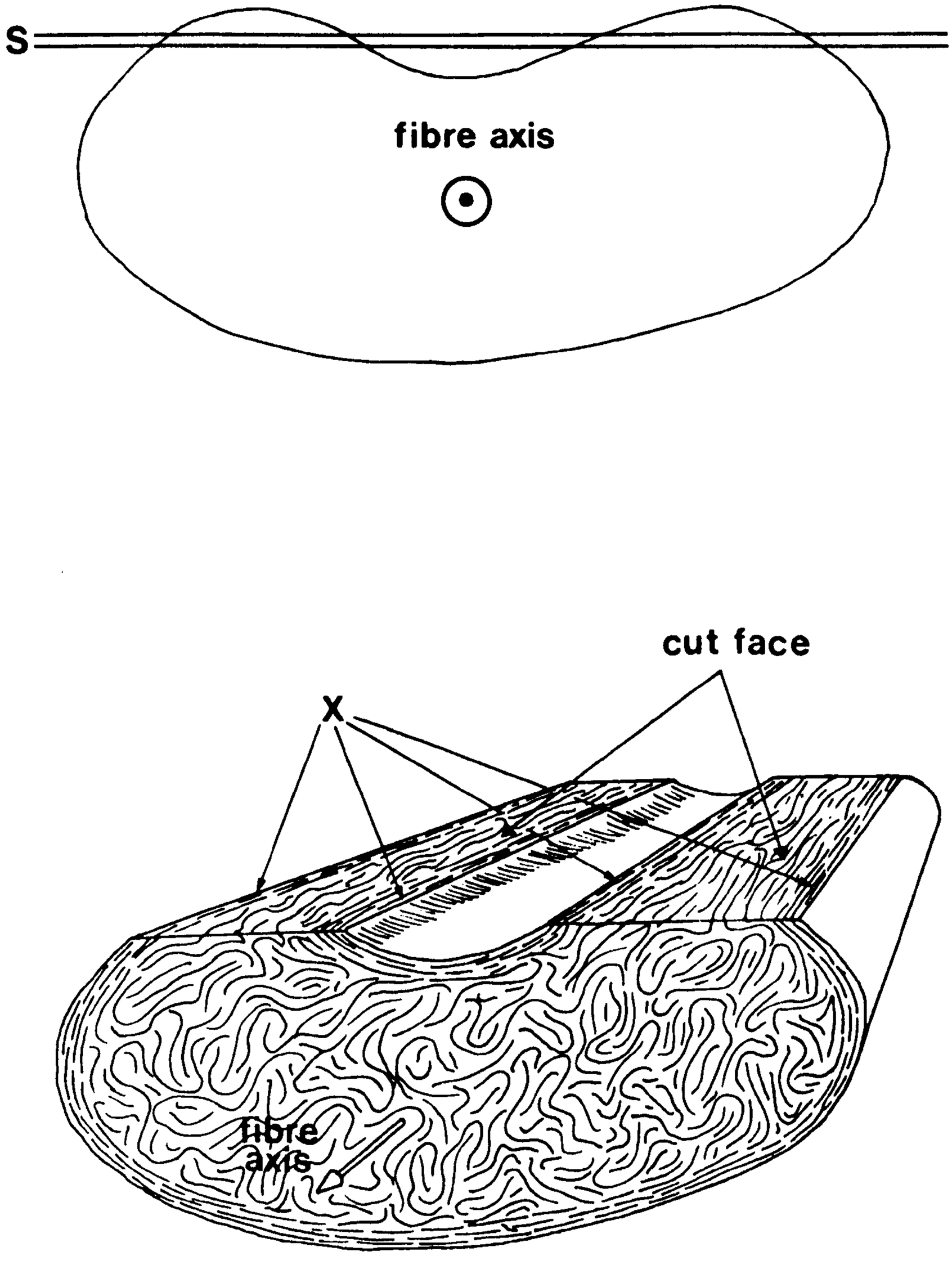

Fig. 31. Schematic representation of the cut face expected from a dog-bone cross section fibre.

Plate XXXIX. Intermediate-magnification (002) dark-field image of a highly-graphitized region close to the surface of specimen P2500.

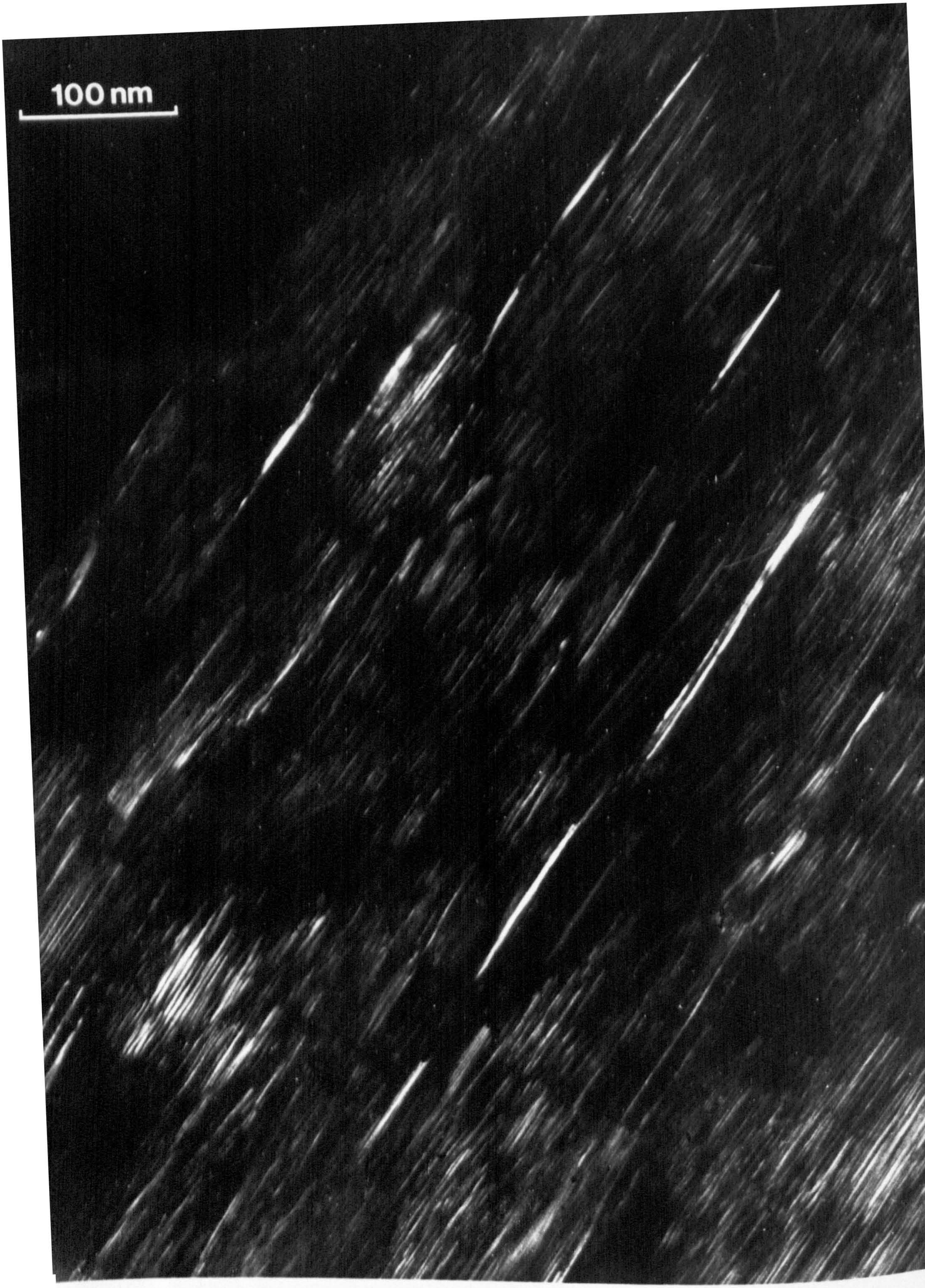

Plate XL. Intermediate-magnification (110) dark-field image of the region depicted in Plate XXXIX.

but in general, the large edge crystallites present a smooth, presumably basal plane fibre surface, for example at a and b.

2.4.2 Defect structure

A remarkable area of well-graphitized, but completely atypical, skin structure in specimen P2500 is depicted in Plate XXXIX. From the edge, S, of the section extending some 0.5 μm into the fibre is an area containing six highly-oriented crystallites which do not appear to interlink in the normal manner. Moiré patterns, M, however, indicate that there is extensive crystallite overlapping, and presumably interlinking through the voids, T, even though the crystallites must be either out of the diffraction condition, or diffracting outside the objective aperture. This is confirmed in Plate XL, the (110) meridional dark-field image of the same area, which shows an essentially continuous structure. This pair of images emphasizes the importance of understanding the orientation limitations imposed in the (002) dark-field mode of image formation.

2.4.3 Résumé

Although different stabilization cycles appear to produce dissimilar transverse structures as revealed by polarized-light microscopy, in dog-bone cross sectionally shaped fibres, there is no evidence that these zones are carried through to fibres prepared at heat-treatment temperatures of 2500°C. In particular those fibres which exhibited no oxidation zones after a conventional stabilization cycle were shown to possess a skin-core heterogeneity indistinguishable from that of circular cross section fibres and vacuum-stabilized dog-bone fibres heat treated to 2500°C.

CHAPTER 3

Surface and Transverse Structure.

3.1 SURFACE STRUCTURE

3.1.1 Introduction

Since carbon fibres are used as structural reinforcing agents in composite materials it is important to characterize the nature of the fibre surface in order to understand bonding of fibres with the resin matrix. The number of edge sites on the fibre surface, i.e. the number of terminating graphite sheets, is of importance, and this can only be assessed directly by using high-resolution electron microscopy, where images recorded under the appropriate conditions provide a faithful representation of the layer-plane structure at the fibre surface.

3.1.2 Fibres heat treated to 2500°C

An essentially continuous graphite-sheet surface structure has been predicted for PAN-based fibres by Raman spectroscopy[106], thus confirming the circumferential crystallite orientation in the outer layers of the fibre. SEM studies[89], however, have tended to suggest a fibrillar surface structure, these fibrils being arranged parallel to the fibre axis, while bright- and dark-field transmission images obtained from thin surface areas have been interpreted[53] in terms of a rippled-sheet structure. Evidently, considerable discrepancies exist between models derived from different techniques.

Using high-resolution phase-contrast electron microscopy Hugo et al.[76] have shown that the layer planes close to the surface of rayon-based fibres are highly oriented, and indeed do form the surface layer itself; however, thin regions in fluted fibres may not be representative of the surface structure in these specimens. It is evident, however, from the lattice-resolution images depicted in Plates IV, X, XV, XVI and XVII that certain areas of the surface of PAN-based type I material are perfectly basal plane in nature. However, other images tend to suggest that highly-graphitic crystallites do not

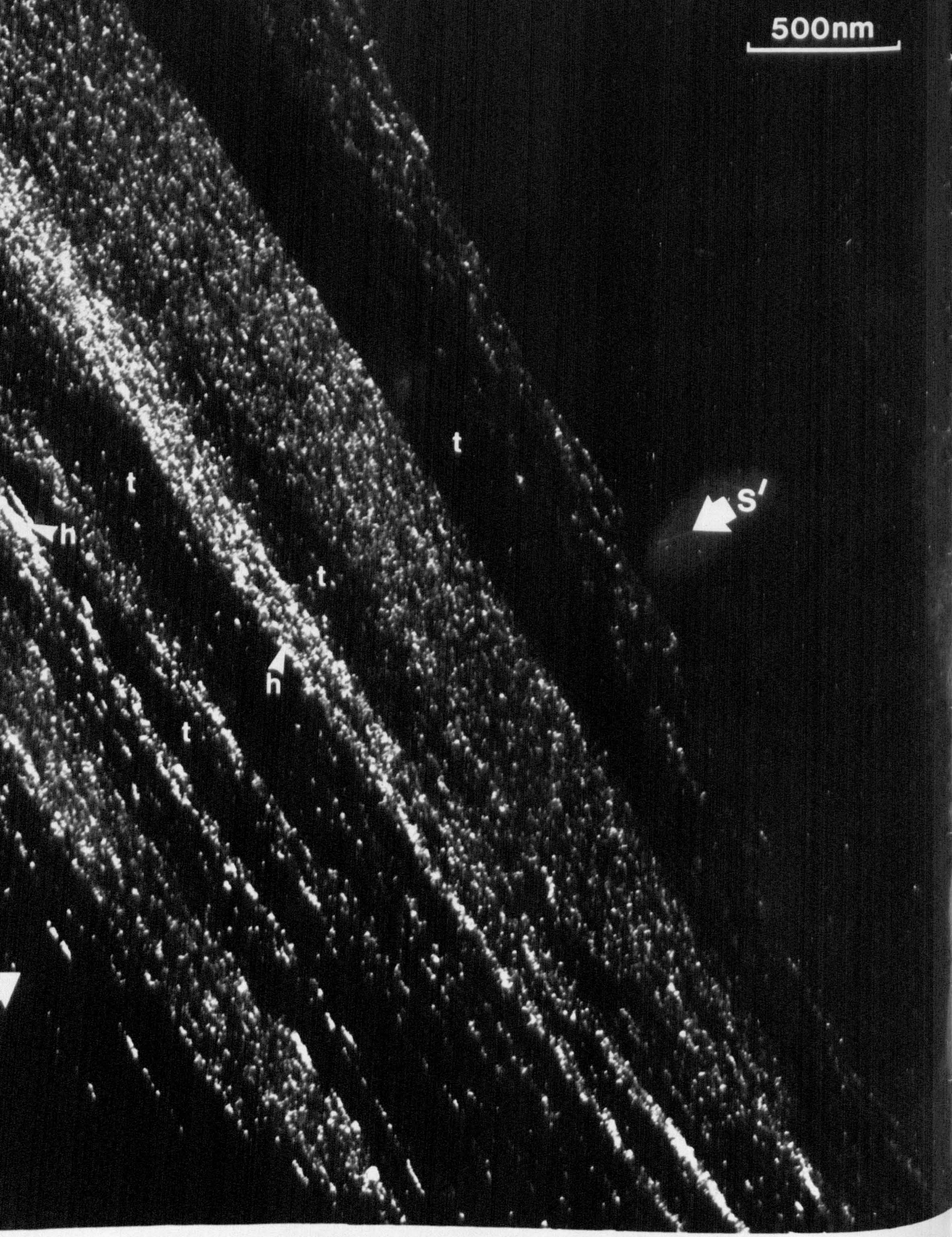

Plate XLI. Low-magnification (002) dark-field image of a 'first-cut' longitudinal section from specimen M2500.

extend fully to the edge of the section, for example, in Plate I there is a non-diffracting region of width 150 nm and in Plate V a similar region 50 nm - 80 nm wide.

Figures 26 and 27 show the anomalies of structure expected from examination of sections cut at varying depths into the fibre, and by taking this to an extreme one can envisage a first or last-cut section which will give information about the structure of the fibre surface. Plate XLI shows just such a section, cut from specimen M2500, in the (002) dark-field mode. Apparently, structural heterogeneity exists across the entire section, but bearing in mind that this is a first (or last) cut, the variations in (002) diffracted intensity are representative of the c-axis orientation of those crystallites at or close to the very surface of the fibre. The striations of high diffracted intensity, h, are those areas where the c-axes of the crystallites are perpendicular to the incident electron beam, while the intermediate regions of low or no diffraction, t, are characterized by an orientation of crystallites out of the diffraction condition. A microdensitometer scan along SS′ in Plate XLI gives the intensity trace of Fig. 32(a). There are regions, f, where the diffracted intensity is low, and here the graphite sheets must be normal to the electron beam. In other regions, g, the diffracted intensity is high, and the turbostratic crystallites must be oriented so that the layer planes are parallel to the incident beam. Using this simple interpretation, which implies that the (002) layer planes at the fibre surface follow the surface (i.e. the c-axis of a surface crystallite is always normal to the surface of the fibre) a schematic projection of the surface irregularity can be made (Fig. 32(b)). If such a simple model holds, the surface structure is characterized by rippling, the mean wavelength of a ripple being about 250 nm.

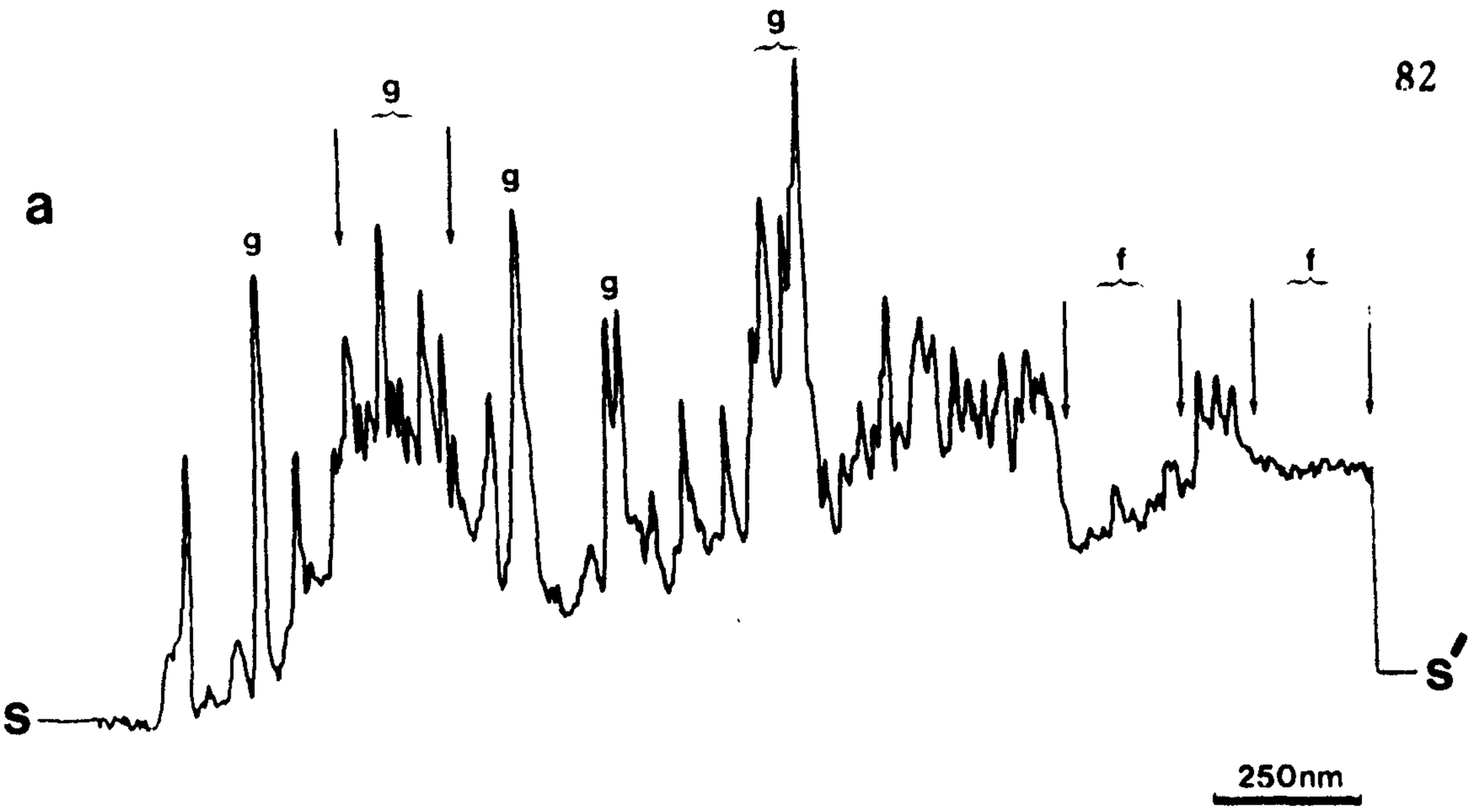

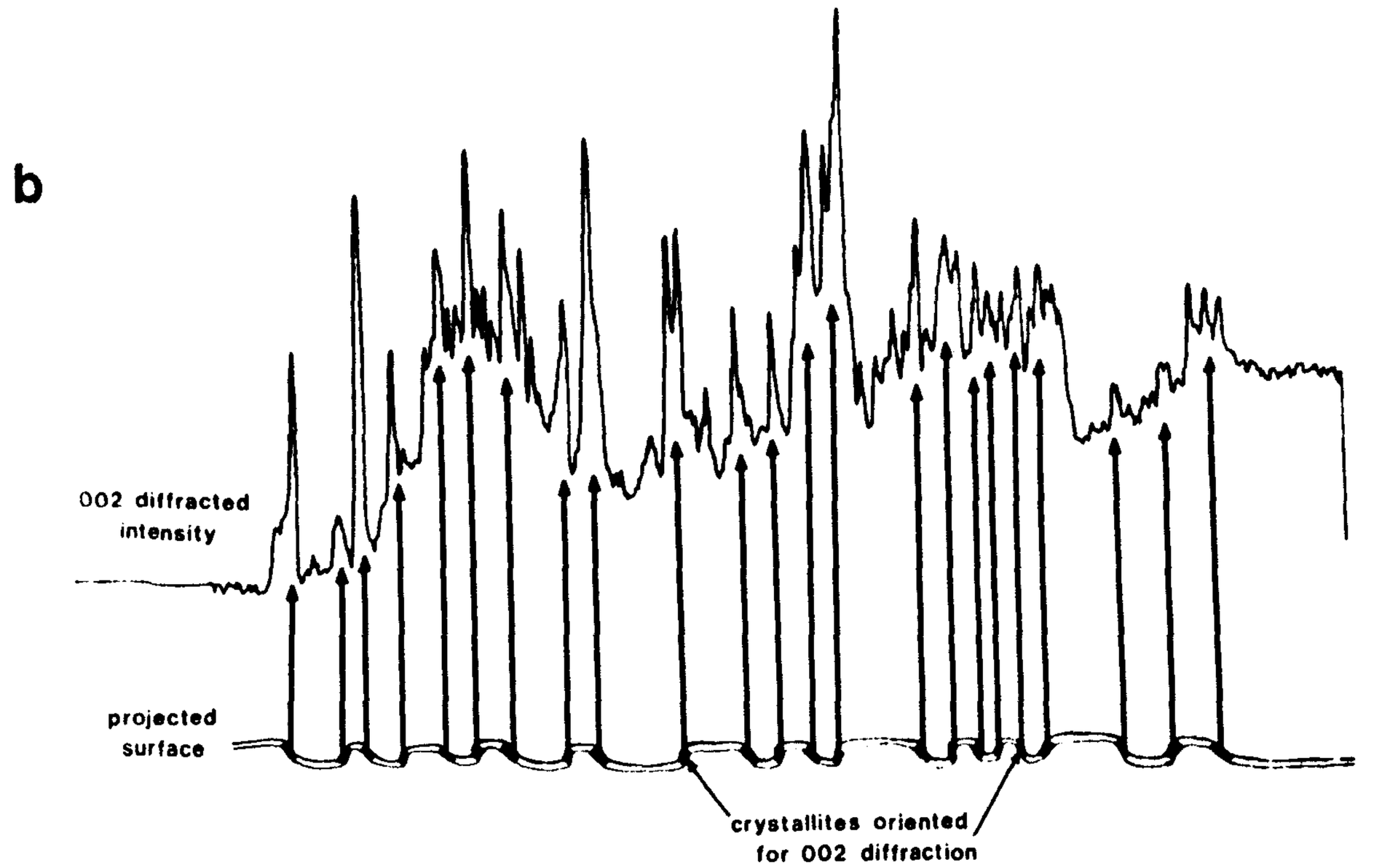

Fig. 32. Microdensitometer scan across a first-cut section showing (a) regions of high and low diffracted intensity, and (b) the projected fibre surface.

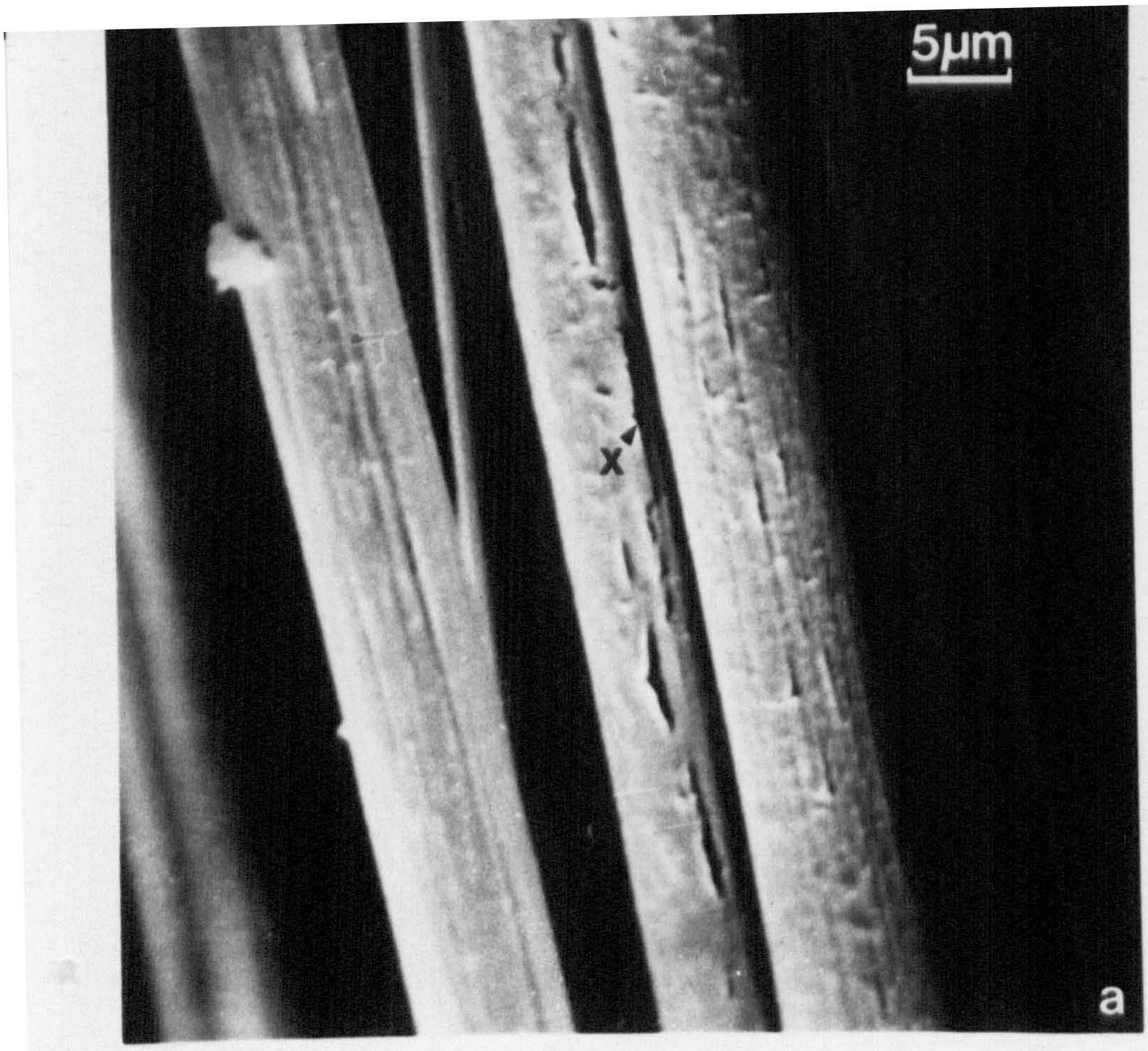

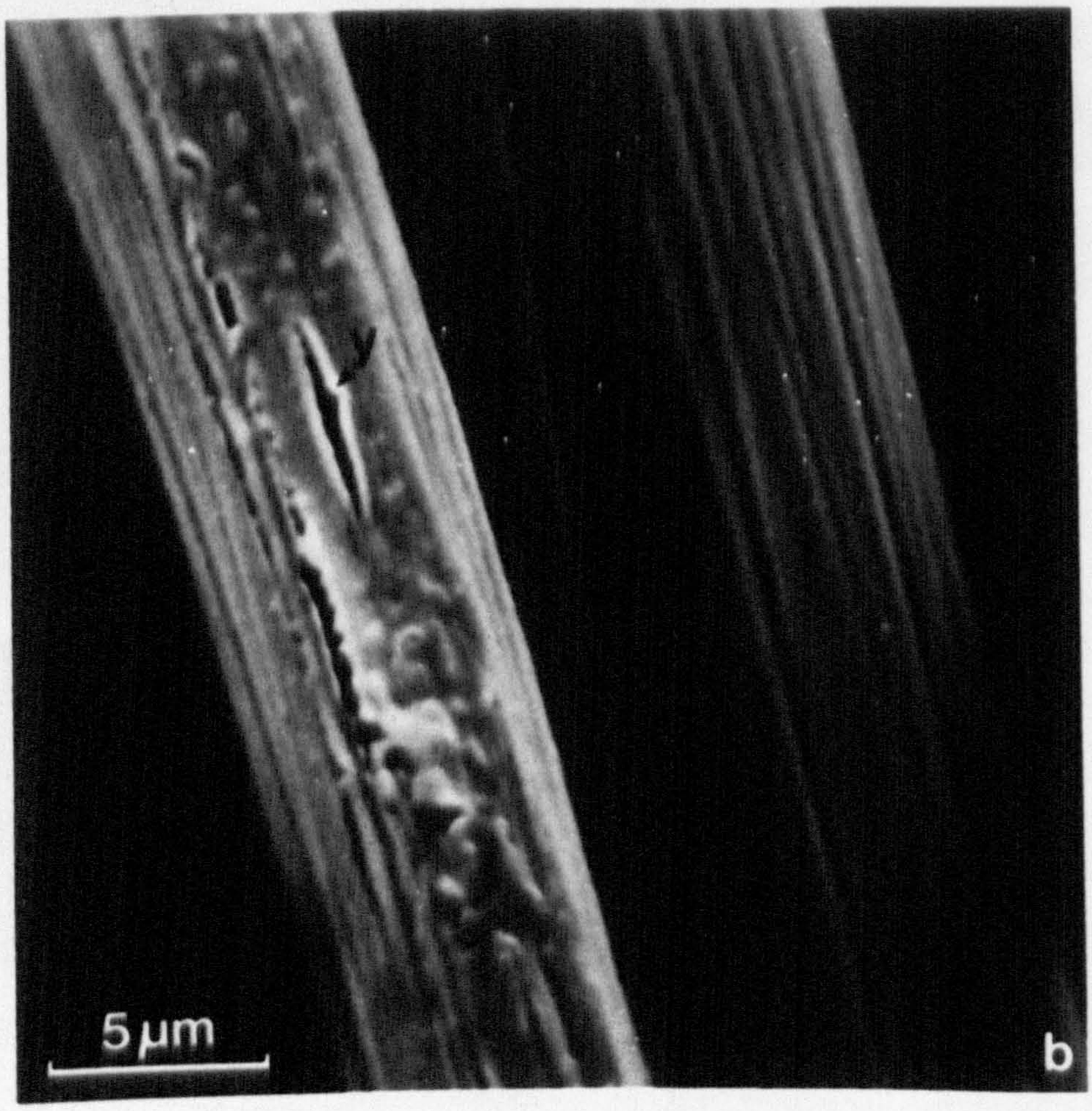

Plate XLIII. Scanning electron microscope images of gross surface flaws in specimen F2500.

This type of surface macrostructure is confirmed in the SEM micrographs depicted in Plate XLII, where striations of separation about 250 nm - 500 nm are arrowed. There is no evidence that heat treatment at different temperatures has any effect on this type of surface structure, as can be seen in Plate XLII(a), (b), and (c) which are images of specimens heat treated at 1000°C, 1500°C and 2500°C respectively. Some interesting surface flaws, typical of specimen F2500, are shown in Plate XLIII. At x a crack of length 15 μm and width 0.5 μm runs parallel to the surface striations, while at higher magnification a similar flaw of length 5 μm and width ranging between 100 nm and 500 nm can be seen at y. This type of surface flaw was not observed in specimens heat treated at 1000°C and 1500°C and is presumably a heat-treatment effect.

Using this new model of layer-plane stacking at the surface of type I fibres coupled with the calculated periodicity of the surface-ripple repeat it is possible to explain observed anomalous skin effects. It has been stressed that the skin seen in type I material varies considerably in thickness and longitudinal extent. Figure 33 shows the schematic (002) dark-field images, a, b, and c, expected from sections cut at different depths into a fibre of circular cross-section. A surface irregularity of wavelength about 250 nm and section thickness of 30 nm - 50 nm is assumed, and this means that there is always a high probability of edge crystallites being out of the diffraction condition. The dark-field pattern, a, of the first-cut section is shown to exhibit the striations typical of Plate XLI. Figure 34 is a microdensitometer scan across the dark-field image of a conventional longitudinal section of the type c in Fig. 33. It is clear that at one edge of the section there is a skin region, s, of high diffracted intensity about 200 nm wide, while at the other edge the surface crystallites are not oriented for diffraction, the

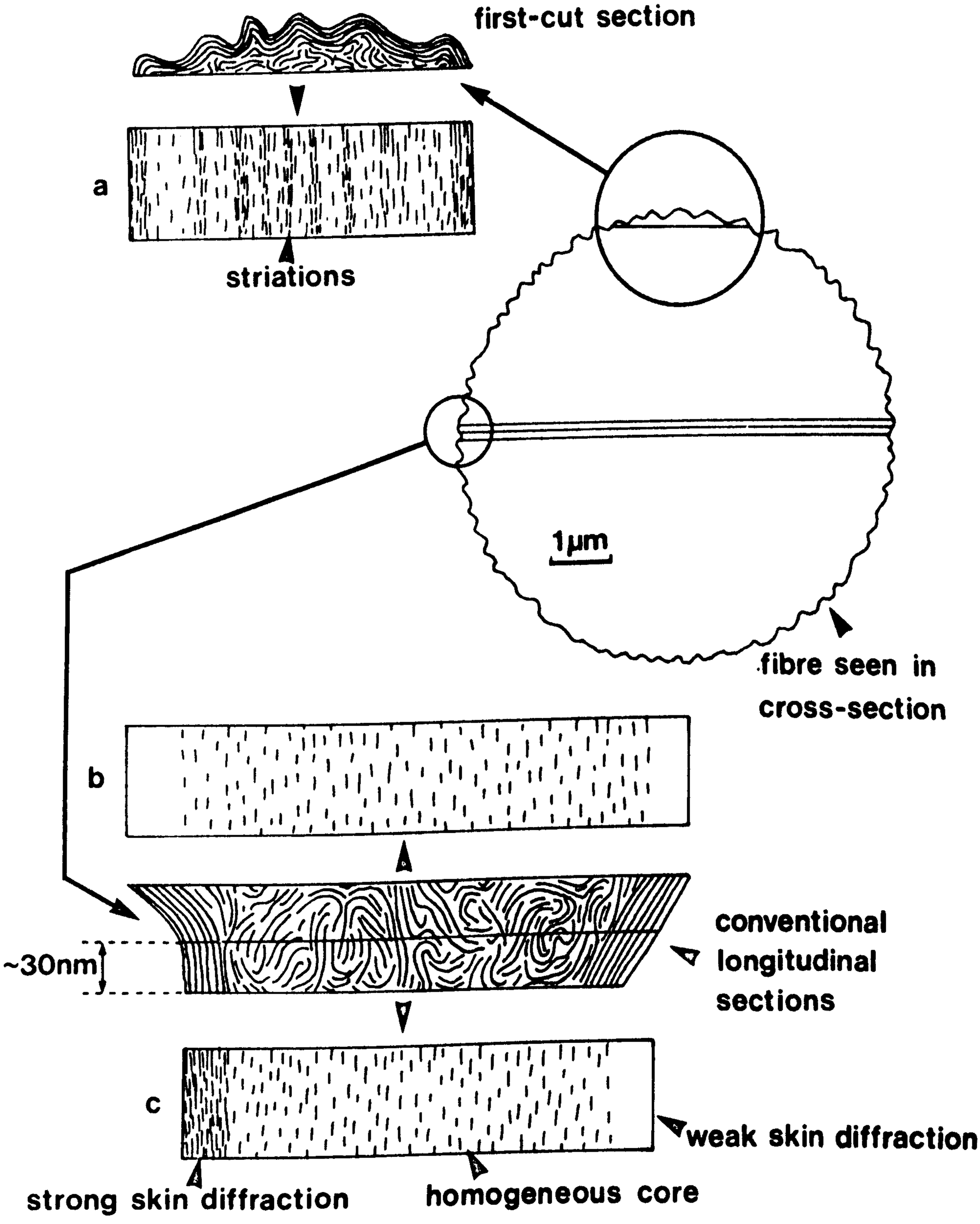

Fig. 33. The origin of anomalous dark-field images obtained from first-cut and conventional longitudinal sections.

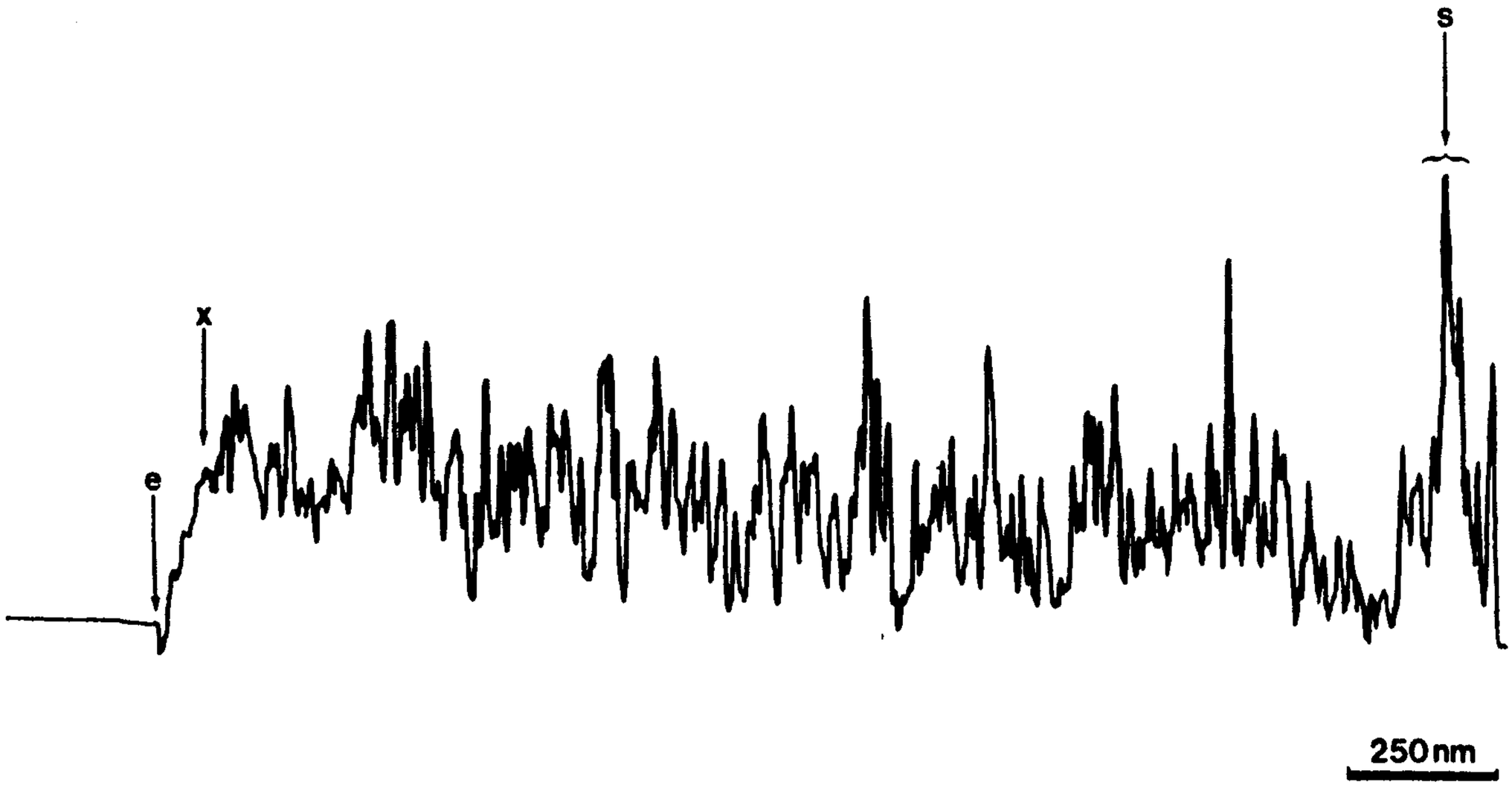

Fig. 34 Microdensitometer scan across a conventional longitudinal section.

intensity falling off from the general core level at x to the very edge of the section, e. Similarly, the anomalous structural band of low diffracted intensity occasionally observed between the skin and core regions (see, for example, region b in Plate V and t in Plate XXI) can be explained in terms of the structural model depicted in Fig. 35.

3.1.3 Fibres heat treated at 1000°C and 1500°C

Since the graphite layer planes formed at heat-treatment temperatures of 1000°C and 1500°C are both less continuous and less perfect than those formed at heat treatment at or above 2500°C the chance of finding an edge site in any given area must be higher in fibres prepared at the lower temperatures. Plate XXXIII shows the edge structure in a longitudinal section of specimen F1500, and at

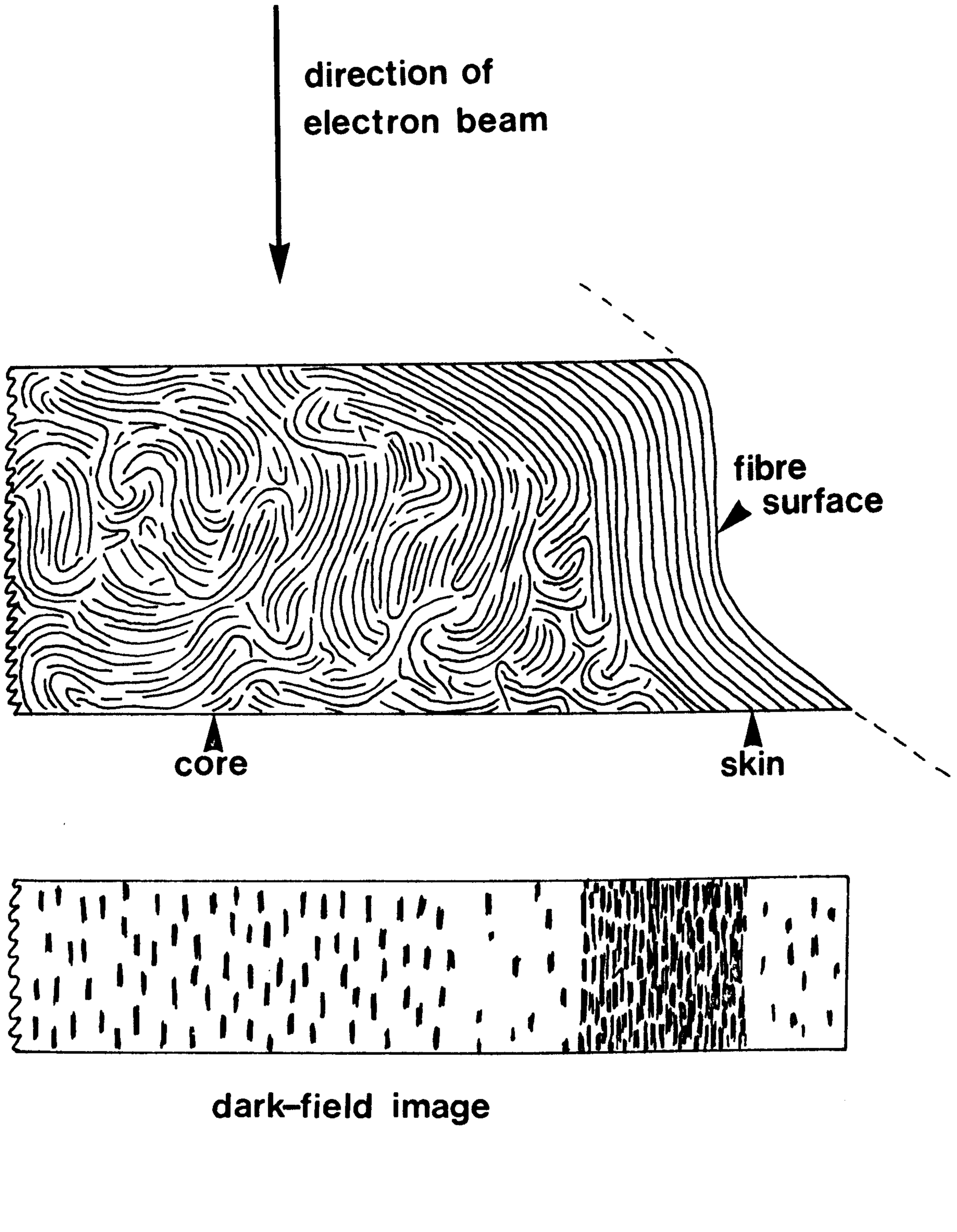

Fig. 35. The origin of anomalous diffraction effects in a dark-field image of a longitudinal section.

those regions labelled x layer-plane packets can be seen to terminate, forming edge sites suited to bonding with the resin matrix. Similarly, in specimen F1000 (Plate XXXIV) those regions labelled d will presumably form good bonding sites. It is evident from Plate XLII that the gross rippled surface structure of fibres heat treated to 2500°C is also present in fibres prepared at lower temperatures, but there is no evidence of the type of surface defect shown in Plate XLIII at either 1000°C or 1500°C.

3.1.4 Résumé

In type I fibres the skin layer contains large, highly-graphitic crystallites oriented with their c-axes predominantly normal to the fibre surface. In certain areas the actual fibre surface is purely basal plane in nature, but crystallite orientation effects preclude the possibility of following the surface layer at lattice resolution over long distances in the direction of the fibre axis. Examination of first-cut sections shows that the fibre surface is rippled, with a periodicity of about 250 nm, and this is confirmed by scanning electron microscopy. Gross surface flaws involving cracks and elongated cavities of considerable size are only seen in type I material, but the general striated surface structure is indistinguishable from that existing at lower heat-treatment temperatures. Type A and type II material contains regions at the fibre surface where layer-plane packets terminate to give edge sites for matrix bonding. A new structural model for type I fibres summarizing the essential macrostructural findings is depicted in Fig. 36. The fibre axis, f, is shown.

3.2. TRANSVERSE STRUCTURE

3.2.1. Introduction

Although certain conclusions and structural models may

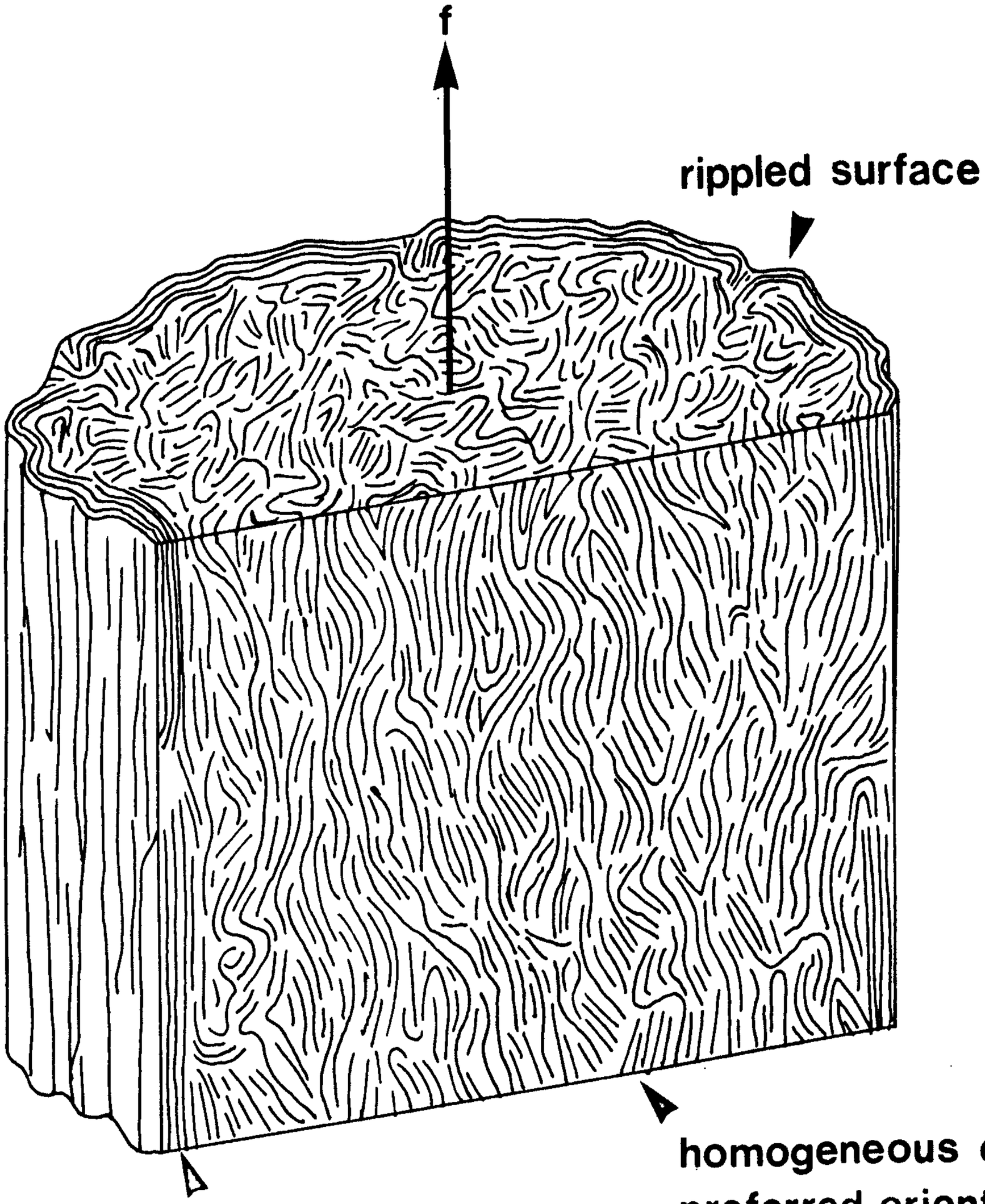

Fig. 36. Three-dimensional structural model of circular cross section type I fibres, summarizing electron-microscopical observations.

be drawn from the two-dimensional images obtained from longitudinal sections, in order to complete a comprehensive three-dimensional structural characterization it is necessary to examine thin transverse sections. This becomes essential since zones of different orientation seen in light-microscope images of thick cross sections, from fibres which have only been oxidized, have also been identified[89] in similar sections of fibres heat treated at 1000°C, 1500°C and 2500°C, but are not evident in thin longitudinal sections. Unfortunately, the oriented structure of carbon fibres makes the preparation of thin undistorted transverse sections almost impossible.

3.2.2 Cross sections

In an attempt to characterize the transverse structure of carbon fibres containing oxidation zones and heat treated to 2500°C, Johnson at RAE has obtained thin cross sections of suitably embedded fibres; these contain dissimilar zones of dimensions compatible with those observed in the light microscope. Plate XLIV shows the structure of a typical section. The direction of cutting, d, is shown, and the fibre axis is normal to the plane of the image. In spite of severe disruption during sectioning, as shown by the ellipticity of the section which should be circular with a diameter of 8 μm, it is apparent that a two-zone system exists, the core, c, having sectioned better than the outer sheath, s. Compression of the structure has resulted in thick areas, t, while pull-out of longitudinal structure has occurred to a limited extent at, for example, p. The leading edge, that is the edge sectioned first, contains areas, e, from which lattice-resolution images can be obtained, while the core and sheath also contain thin, undistorted areas suited to high-resolution microscopy at c and s respectively.

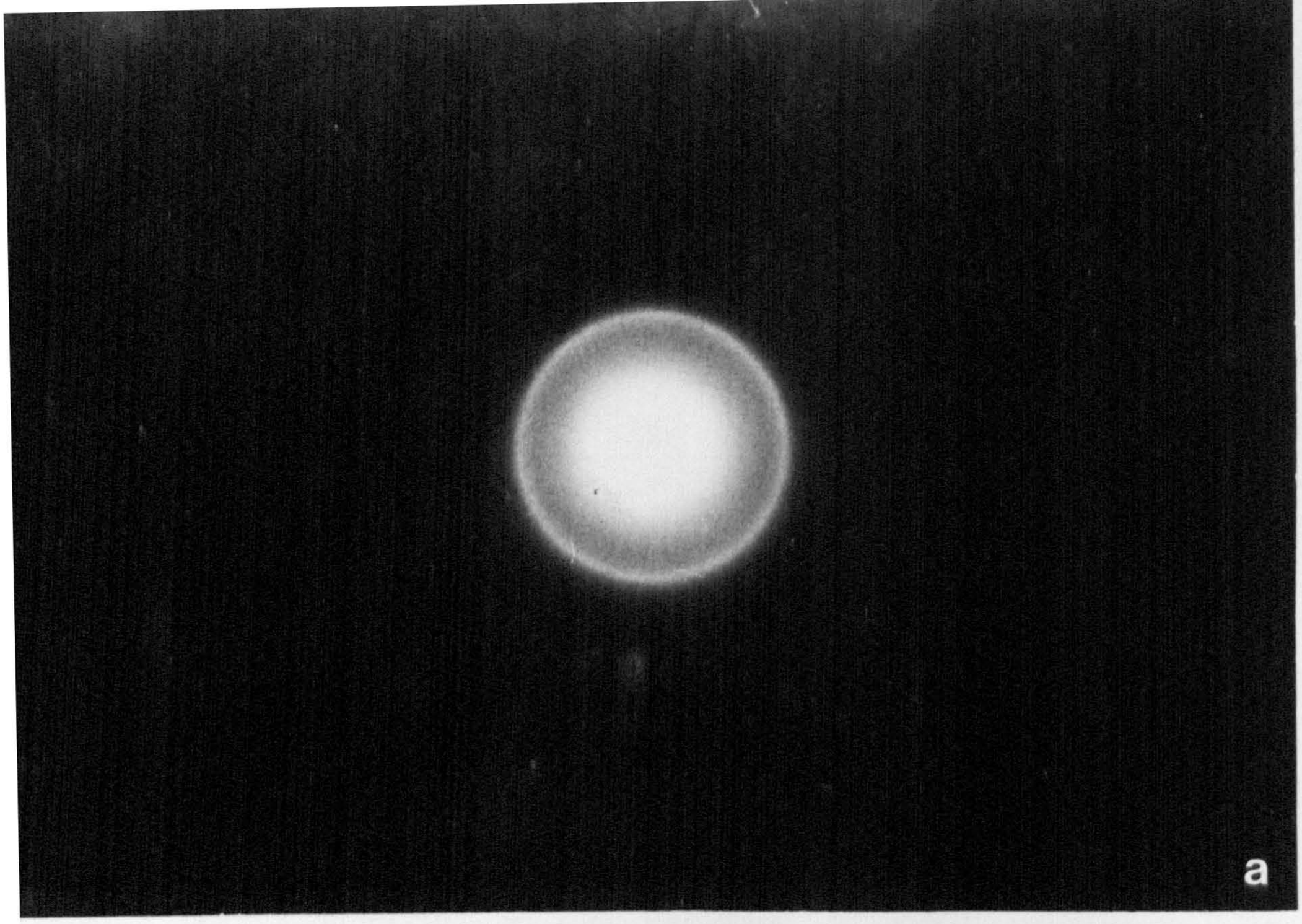

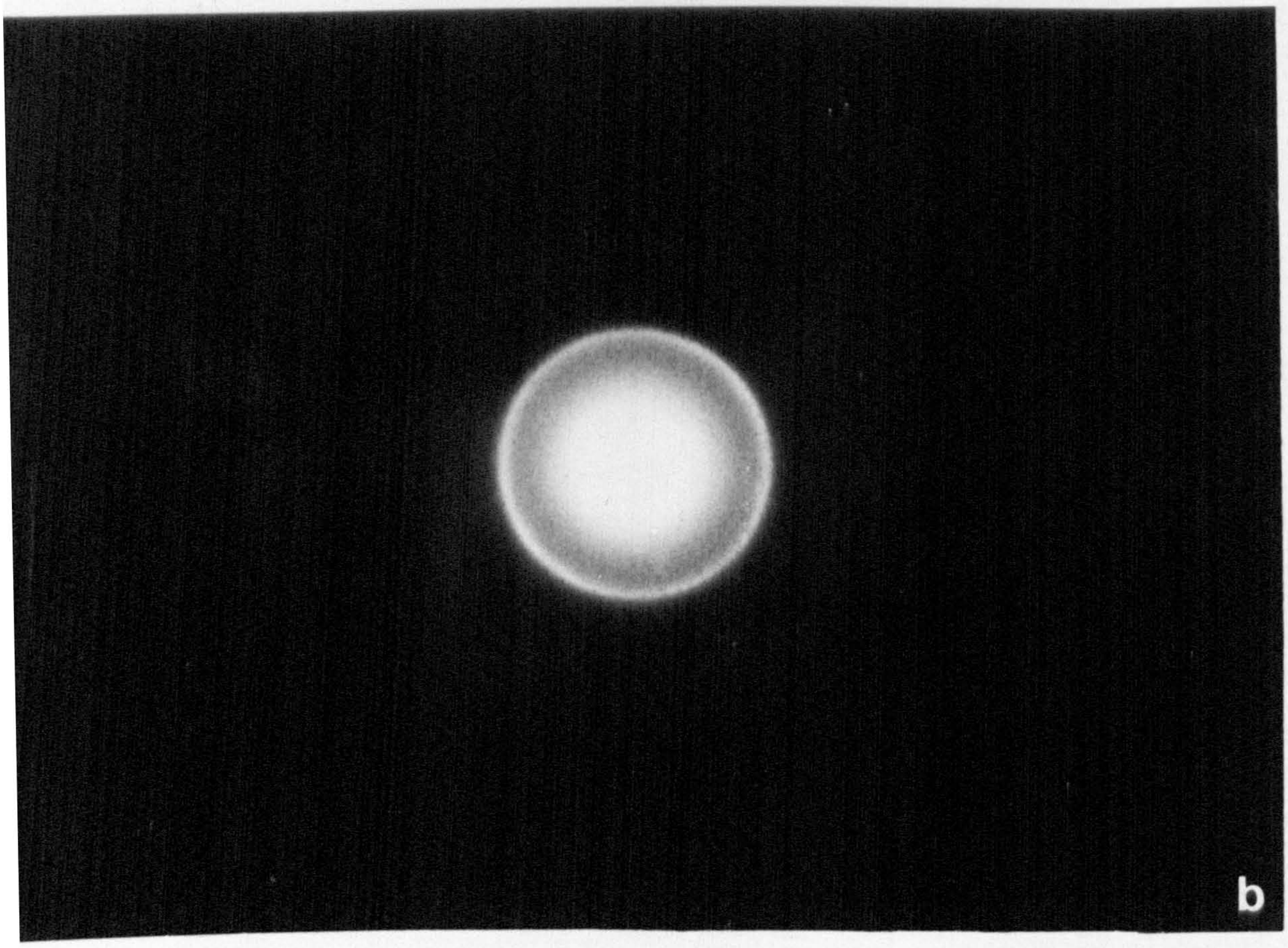

Plate XLV. Electron-diffraction patterns from (a) sheath and (b) core regions in a transverse section cut from specimen R2500.

Plate XLVI. Lattice-resolution image of the core structure in a transverse section of specimen R2500.

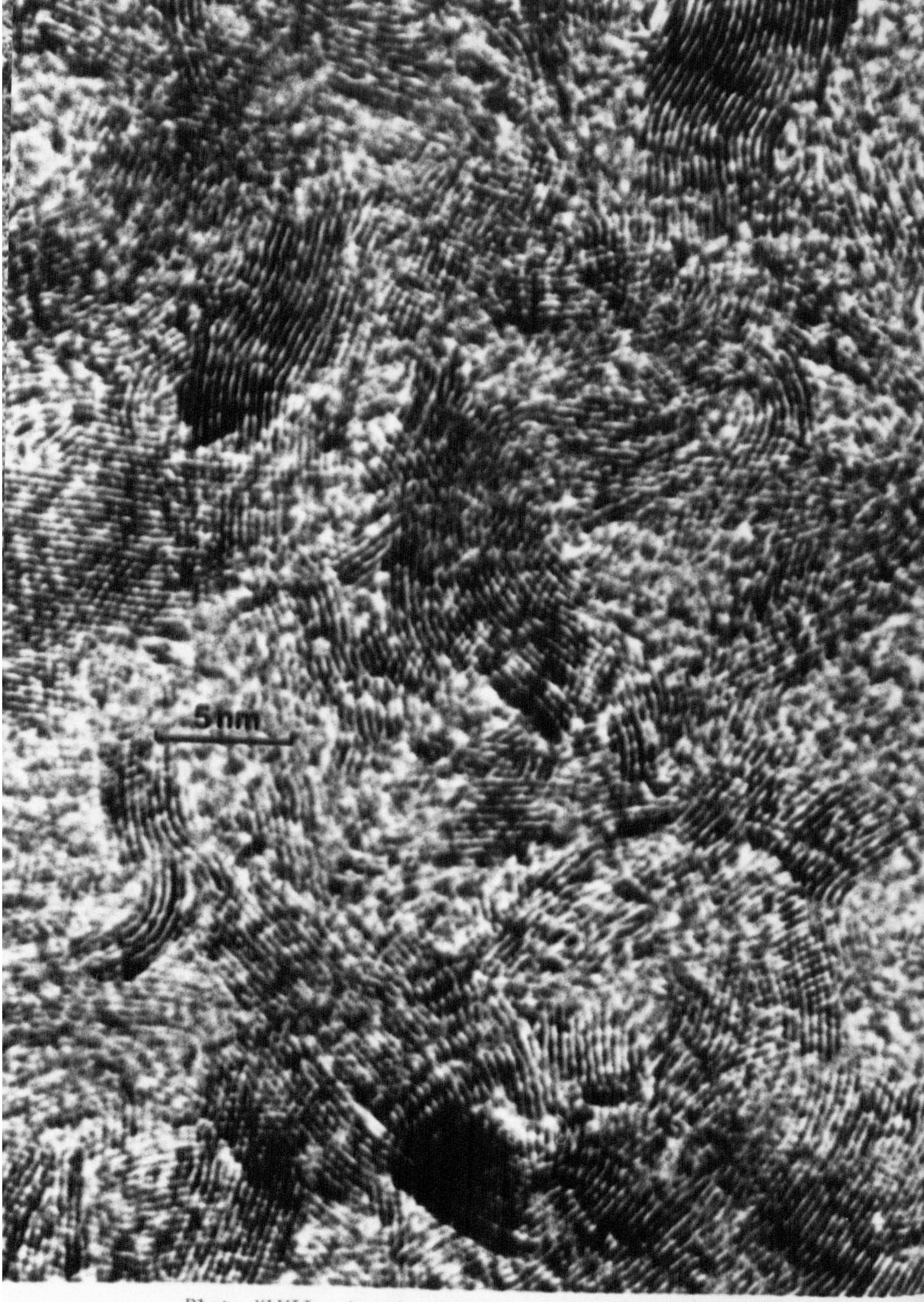

Plate XLVII. Lattice-resolution image of the core structure in a transverse section of specimen R2500.

3.2.3 Sheath-core structure

In order to assess the gross orientation effects in cross section, a selected-area electron-diffraction study was performed with a 30 μm diameter intermediate-lens aperture selecting an area of diameter 1.25 μm at the specimen. Although many different areas were selected, the (002) reflection was found to be a continuous ring in all cases (Plate XLV), indicating that there is no c-axis preferred orientation in either sheath or core. This was confirmed by a similar study using a 10 μm diameter selected-area aperture. Analysis of microdensitometer traces by the methods described earlier indicates that the mean stacking size in the core is 2.1 nm, while in the outer sheath it is 2.0 nm. These values, while significantly lower than those of about 3 - 4 nm typically found for core structure in conventional longitudinal sections, are not significantly different, clearly showing that there is no difference between sheath and core zones from a diffraction point of view.

To explain the anomalous sectioning behaviour, lattice-resolution images were obtained from thin, undistorted regions such as at c and s in Plate XLIV; the core structure of specimen R2500 being shown in Plate XLVI. It is apparent from this image that there is no preferred orientation, and that the crystallites interlink in an extremely complex manner to form a densely-packed structure. There is very little evidence of enclosed voids between crystallites, a continuous, compact, highly-interlinked structure being envisaged.

At higher magnification the essential conclusions regarding the core structure of specimen R2500 are confirmed in Plate XLVII. Rarely are the layer planes straight over lengths of more than 2 or 3 nm, and the high density of crystallite packing is achieved through a complex three-dimensional interlinking of layer planes.

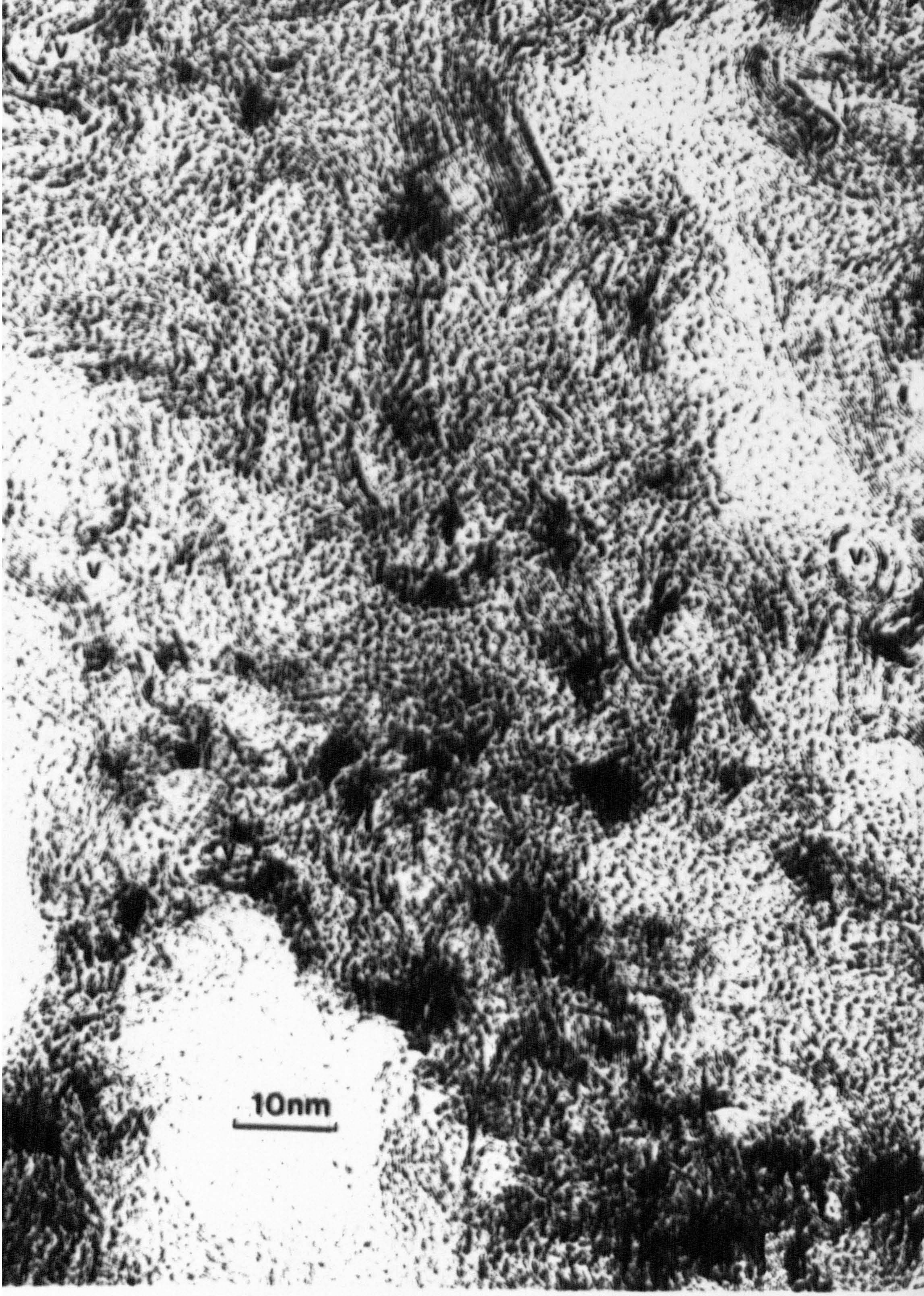

Plate XLVIII. Lattice-resolution image of the sheath structure in a transverse section of specimen R2500.

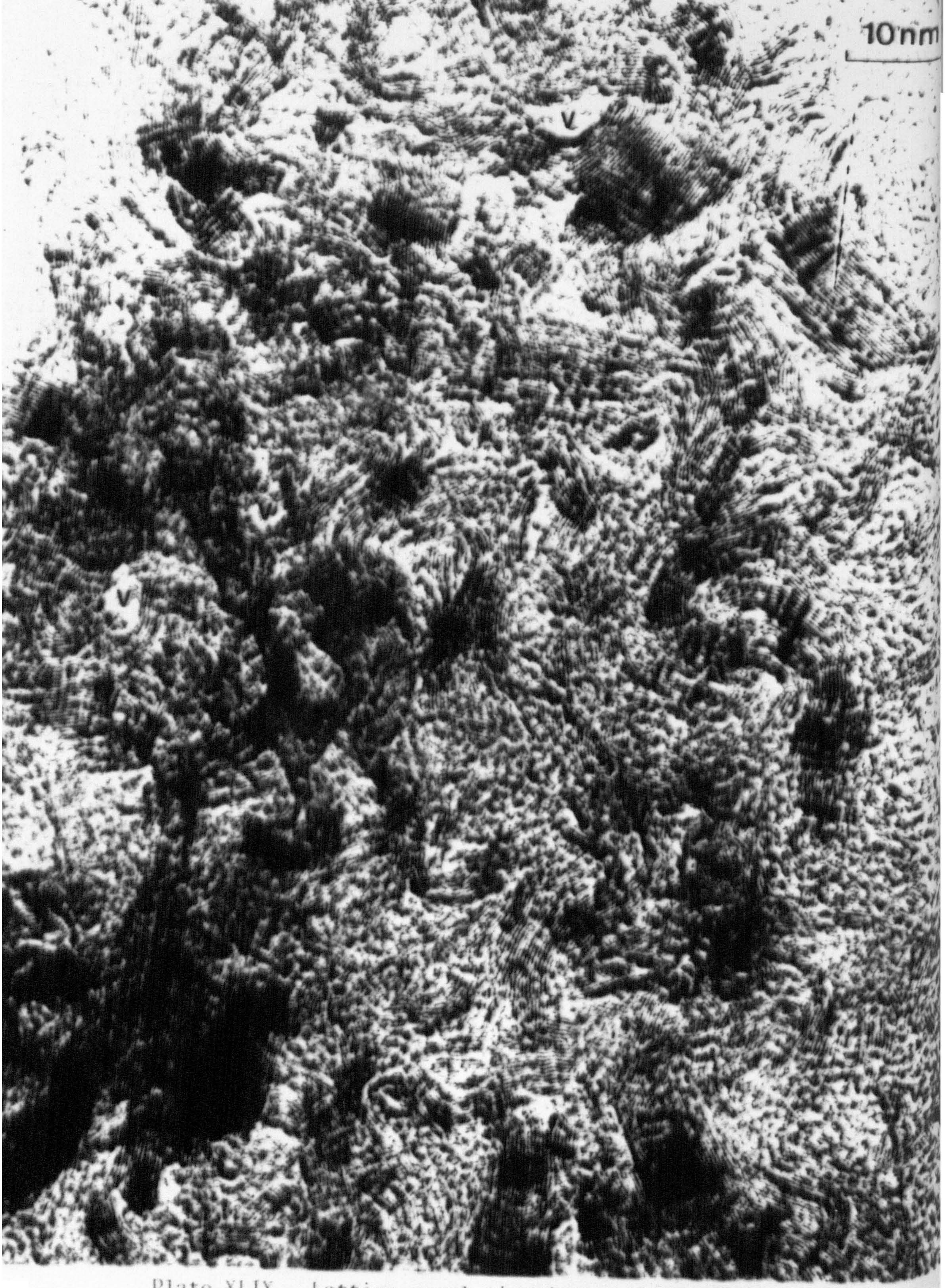

Plate XLIX. Lattice-resolution image of the sheath structure in a transverse section of specimen S2500.

There is no diffraction evidence of differences in preferred orientation and stacking size between sheath and core zones. With lattice resolution, however, it is clear that the sheath structure of specimen R2500 shown in Plate XLVIII contains enclosed voids, v, not apparent in the core. This leads to a less-dense, and less-compact structure. This essential difference is confirmed in Plate XLIX which shows the sheath structure of specimen S2500 at lattice resolution. Numerous small sharp-edged voids, v, can be seen enclosed by bent and folded crystallites. It is envisaged that the origin of these voids lies in the greater layer-plane width (layer-plane length as seen in transverse section) enabling the graphitization of crystallites in the fully-oxidized sheath in a folded form enclosing the small voids. In the under-stabilized core, where layer-plane width is smaller, crystallization into a dense, void-free, structure is assumed. If this mechanism is valid it seems probable that a more highly-crosslinked layer structure develops in the fully-oxidized sheath than in the under-stabilized core.

The reason that structural differences between sheath and core zones are not found by diffraction analysis of thin longitudinal sections is presumably due to the misleading nature of $L_{a//}$ and $L_{a\perp}$ measurements. Since these are only measurements of the *average straight* dimensions of layer-plane sequences they give no information regarding total layer-plane length or width. Additionally, the unambiguous interpretation of the appearance of voids in longitudinal sections is complicated by the orientation limitations discussed earlier. Schematic representations of the three-dimensional structures envisaged for the sheath and core are depicted in Fig. 37.

3.2.4 Skin structure

The structural model for the surface described above

a

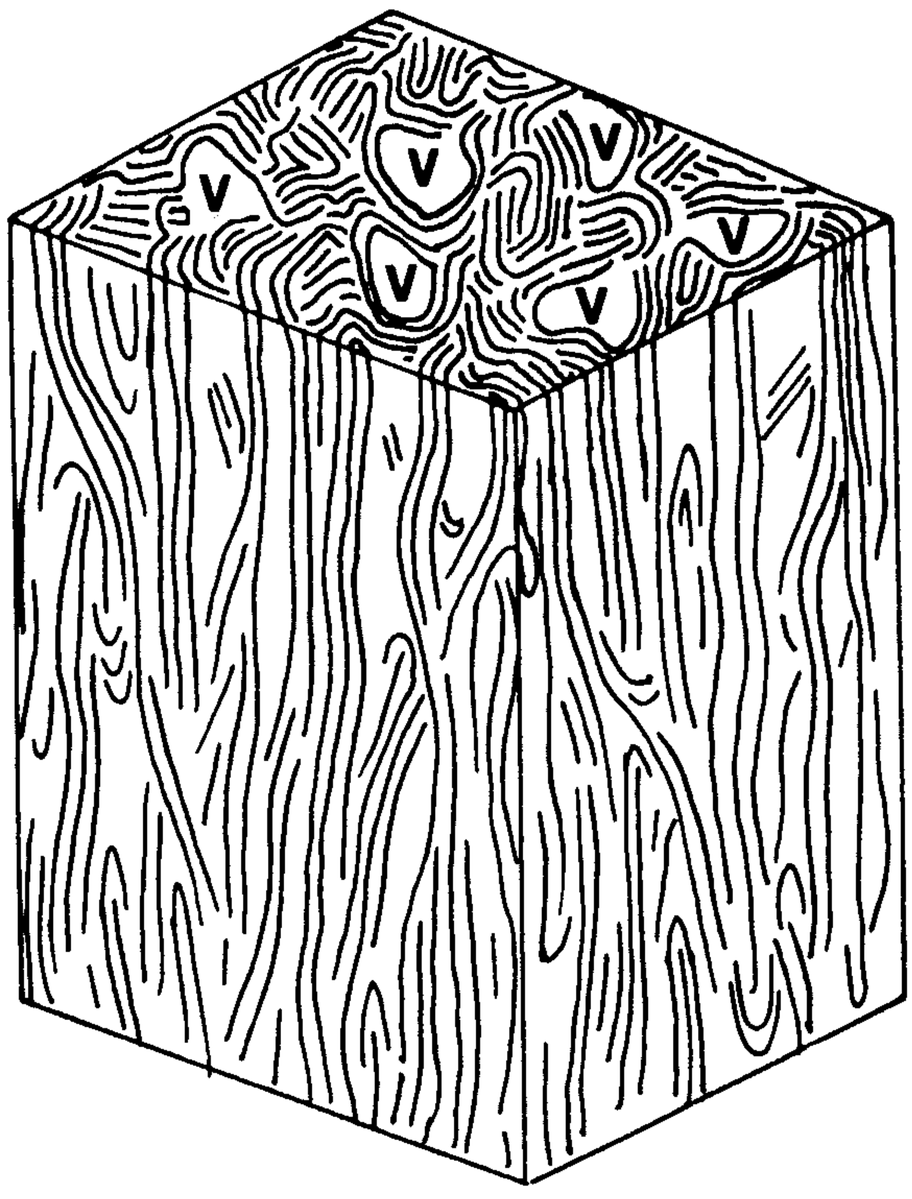

b

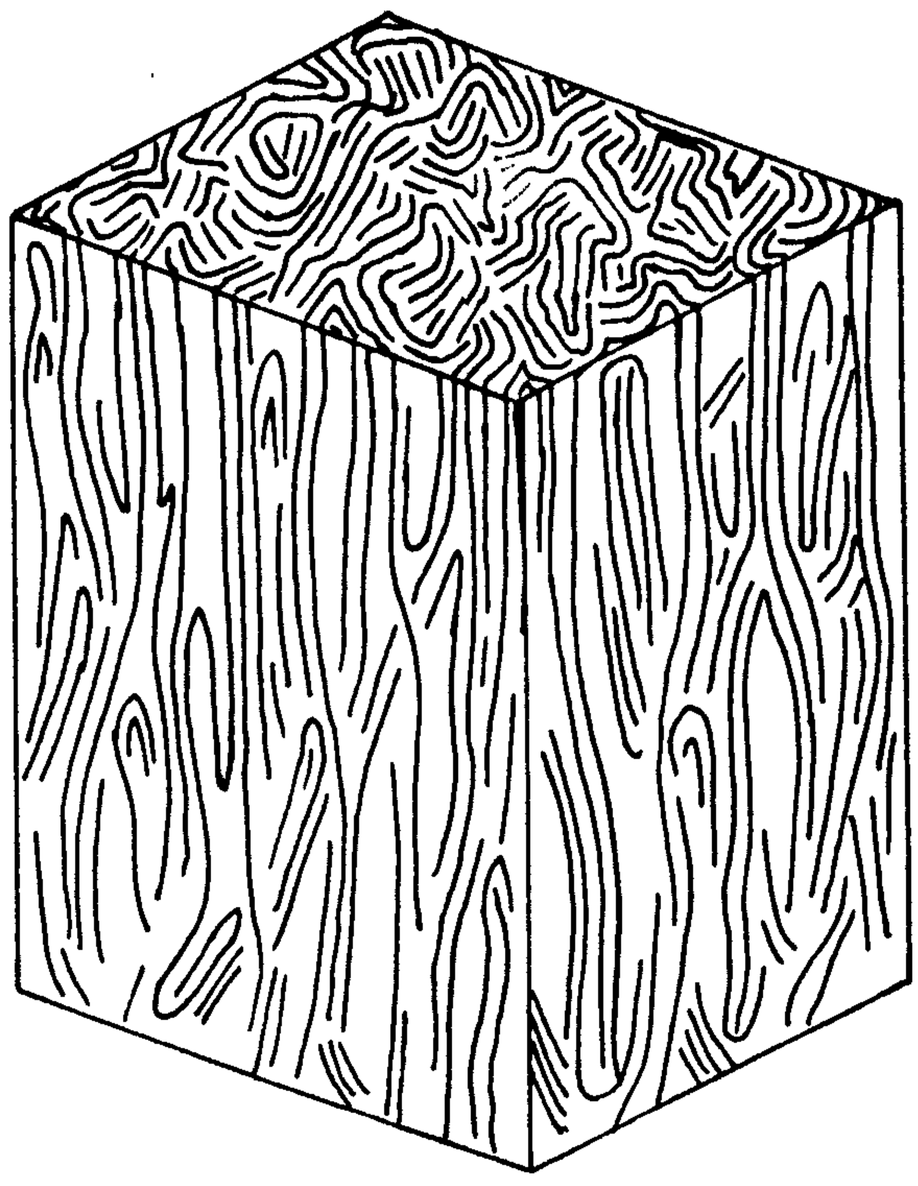

Fig. 37. Three-dimensional structural models for (a) sheath and (b) core of a partially-oxidized circular cross section type I fibre.

Plate L. Lattice-resolution image of the skin structure in a transverse section of specimen S2500.

Plate LI. Lattice-resolution image of the skin structure in a transverse section of specimen R2500.

assumes that the layer planes follow the fibre surface when close to it, and this is confirmed in Plate L, which shows the skin structure of specimen S2500 at lattice resolution. A large crystallite, e, of width 18 nm and bent along t-t forms the surface, s, of the fibre. The complex crystallite interlinking between skin and sheath structural zones is evident at several regions, x. The skin in this image has a maximum thickness of about 70 nm, and it is evident that there are extensive areas where the surface of the fibre is purely basal plane. The general rippling of the fibre surface is confirmed, and crystallite bending through angles up to 90^{o} means that a first-cut longitudinal section will exhibit striations of (002) diffracted intensity as predicted.

A similar complex interlinked, but less-graphitic, skin structure in specimen R2500 is shown at lattice resolution in Plate LI. Crystallites of widths ranging up to maximum of about 18 nm can be seen to be oriented with their c-axes normal to the fibre surface, s. Several Moiré patterns, m, are indicative of crystallite overlapping and interlinking, while irregularly-spaced dark extinction bands, b, mean that the crystal lattice is considerably distorted.

3.2.5 Résumé

With the exception of a thin outer layer which is circumferentially oriented, there is no preferred orientation of c-axes in transverse sections of type I fibres ex-special Courtelle. Although structurally different zones, undoubtedly related to the oxidation zones observed in optical microscopy, have been identified, there is no evidence to suggest that these are characterized by either different crystallite size or orientation. It is tentatively proposed that the origin of the difference lies in the increased layer-plane width through crosslinking during low-temperature stabilization, enclosed sharp-edged voids being formed during subsequent crystallization of the

folded and bent plane packets. In the core it is proposed that the smaller values of layer-plane width enable crystallization into a less-interlinked, but extremely dense structure.

CHAPTER 4

QUANTITATIVE ELECTRON MICROSCOPY.

4.1 INTRODUCTION

Subjective examination of images obtained from longitudinal and transverse sections indicates that the thin outer skin of type I material represents less than 10% of the total fibre volume. The *intrinsic* mechanical properties of these fibres must therefore be directly related to the structure of the core which comprises the bulk of the material. The modulus is a function of preferred crystallite orientation, as described initially by Ruland[57], and the ultimate tensile strength in the absence of internal and surface flaws of a gross nature, and the surface skin may be classified in these terms, is governed by the orientation, size and interlinking of the constituent crystallites. In order to perform a quantitative characterization of the core structure various direct and indirect methods of electron-microscopical and x-ray diffraction examination techniques were employed, and the relationships between these assessed.

4.2 EXPERIMENTAL

Longitudinal sections of specimen F2500 were examined in a Philips EM300 electron microscope fitted with a French 'PF' type pointed filament, used at low filament heating, a 0.3 mm gun bias cap, and condenser-lens apertures of C1 - 100 μm and C2 - 200 μm. Micrographs of the same area of the core of a thin section were recorded in the following modes at 100 kV utilizing a liquid nitrogen anticontamination trap:-

(i) Multibeam bright-field image at Gaussian focus (Plate LII).

(ii) Multibeam bright-field lattice-fringe image at that defocus position which gives maximum fringe contrast as determined empirically by Johnson and Crawford[121] (Plate LIII).

(iii) (000) - (002) two-beam symmetric bright-field lattice-fringe image at the optimum focal position, see Appendix 1, other beams eliminated with a 39 μm objective aperture (Plate LIV).

(iv) (002) - (004) two-beam symmetric dark-field lattice-fringe image

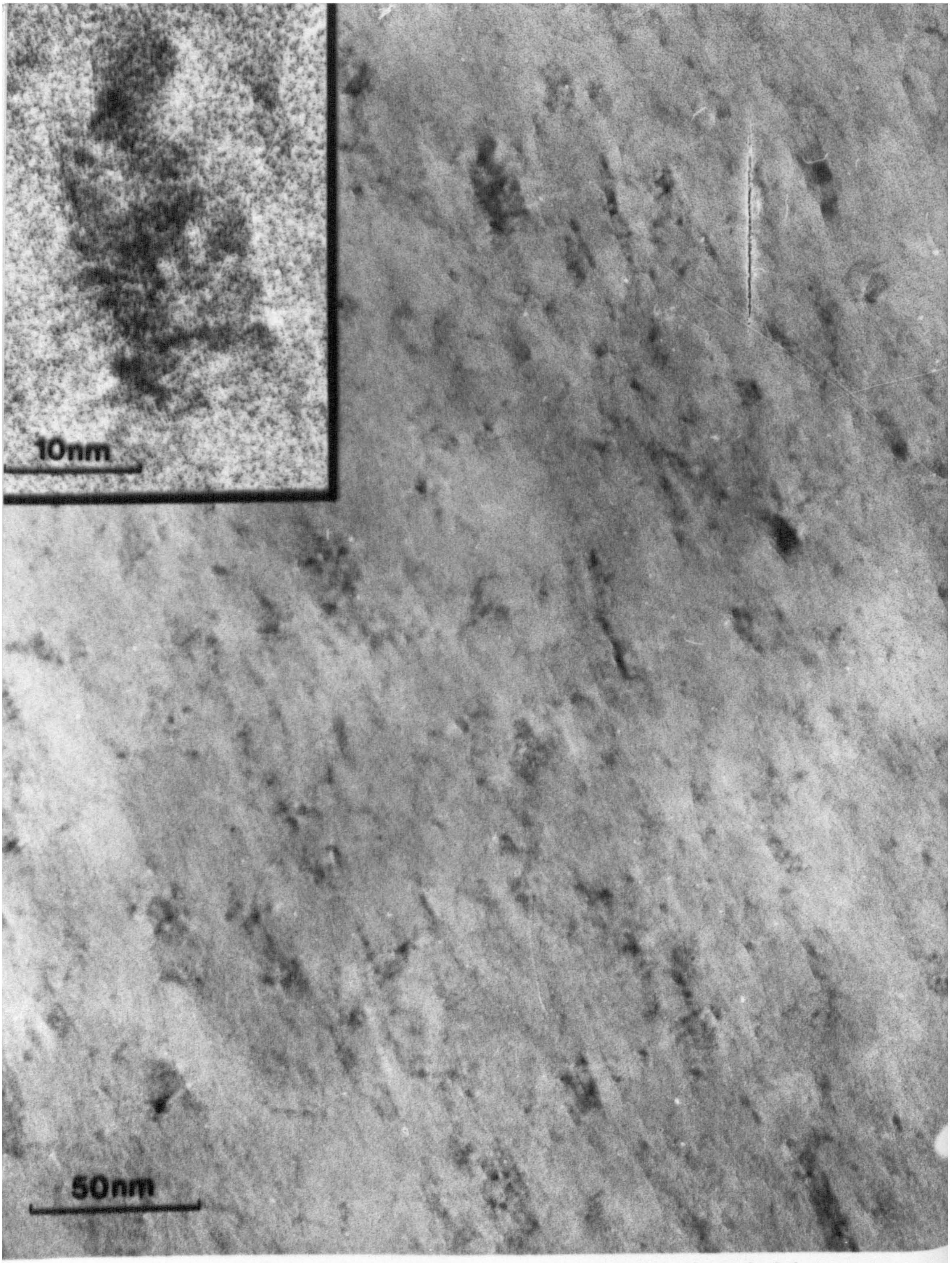

Plate LII. Intermediate-magnification multibeam bright-field image at Gaussian focus of the core structure of specimen F2500. Inset: crystallite from same image at magnification used for statistical analysis.

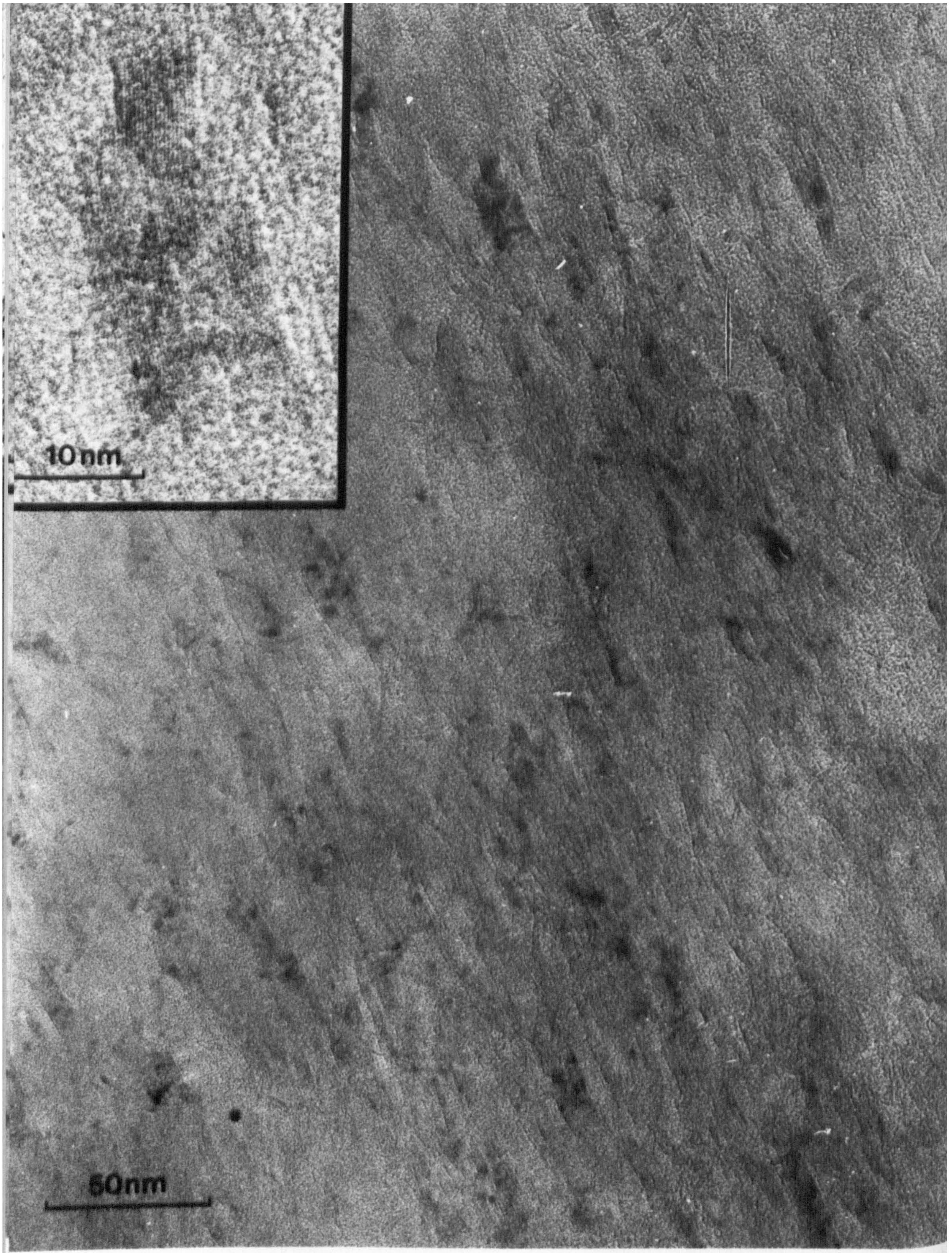

Plate LIII. As for Plate LII except imaging mode is multibeam bright-field at a defocus which gives enhancement of 0.34 nm.

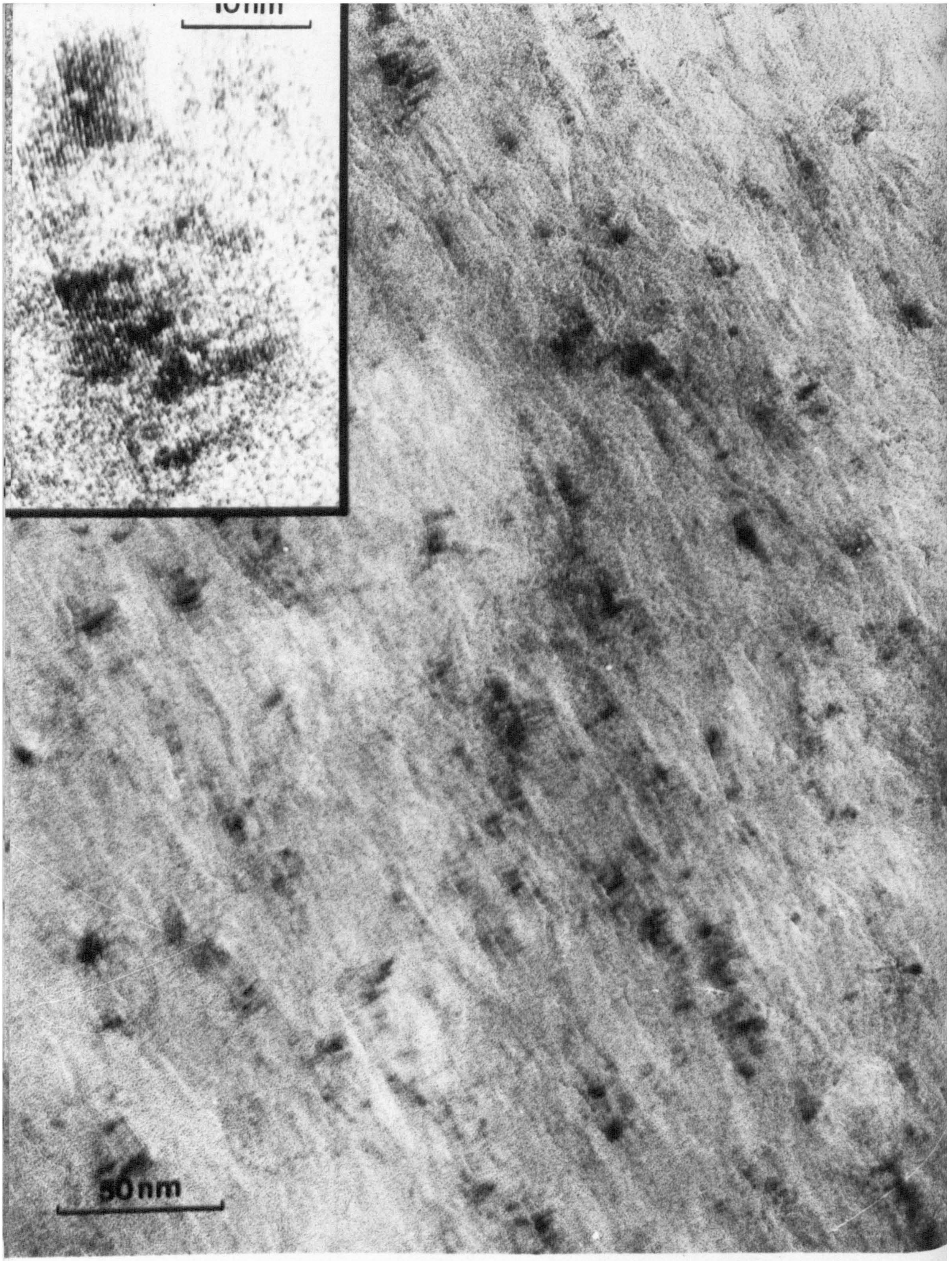

Plate LIV. As for Plate LII except imaging mode is (000) - (002) symmetric bright-field at optimum focus.

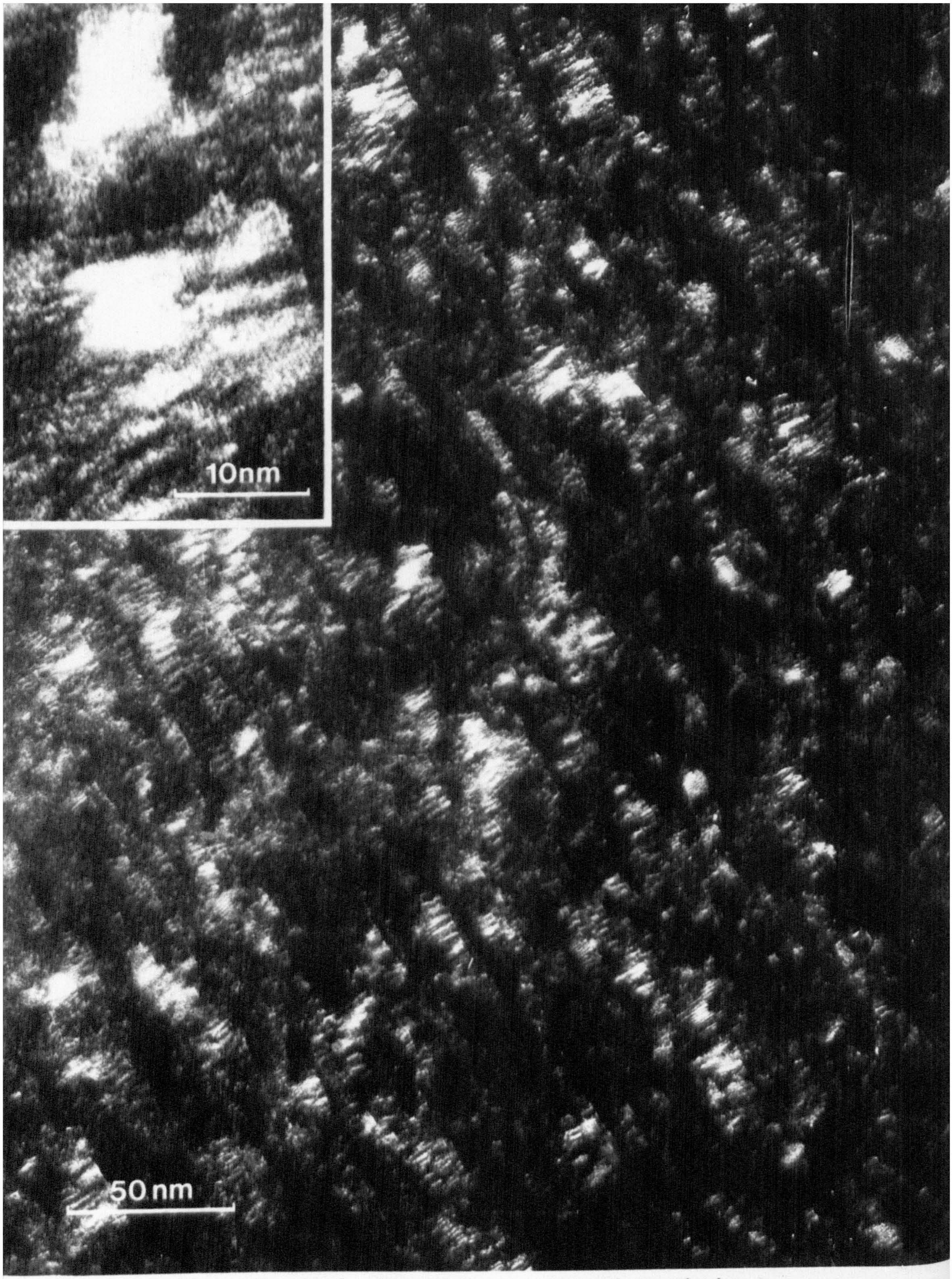

Plate LV. As for Plate LII except imaging mode is (002) - (004) symmetric dark-field.

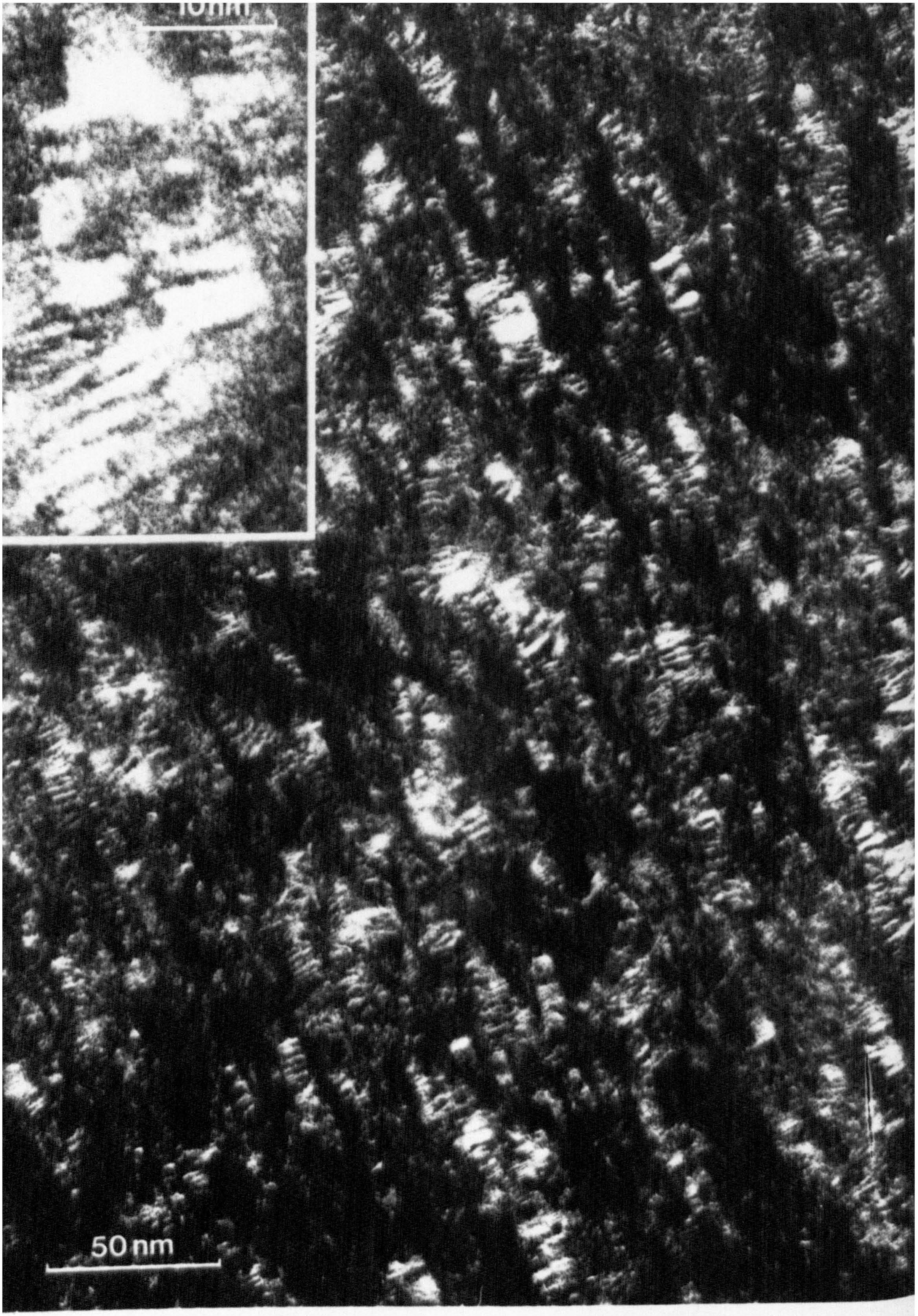

Plate LVI. As for Plate LII except imaging mode is (002) axial dark-field.

recorded at the same focal level as in (iii) above (Plate LV).

(v) (OO2) axial dark-field image using a 28 μm objective aperture. Astigmatism was corrected with an axial zero-order beam and the 28 μm objective aperture in place. The appropriate focal level was determined by obtaining the optimum (OO2) axial bright-field lattice-fringe image using the 39 μm objective aperture; the 28 μm aperture was then introduced in order to record the high-resolution dark-field image (Plate LVI).

A low electron-optical magnification compatible with resolution of 0.34 nm and precise judgement of focus was used in order to form an image of an area of 2×10^4 nm^2 considered to be representative of the core structure in this specimen. The electron-diffraction pattern of the same region was recorded using a 10 μm diameter intermediate-lens aperture which selects an area of 12.5×10^4 nm^2 at the specimen. Width measurement of single crystallites in each type of image was made over an area equivalent to 90 x 170 nm^2 at a step interval of 1.7 nm to give 300 - 500 values. The arithmetic mean, L_c, and standard deviation, s, were calculated from the frequency distributions of crystallite size for each high-resolution image (Fig. 38), and are given in Table 6. These values of L_c obtained by direct measurement are quoted to ± 0.2 nm at the 95% confidence level.

For an array of N lattice points separated by a constant spacing d, the diffracted intensity, I, is given by:-

$$I_\delta \alpha \frac{\sin^2(N\delta)}{\sin^2(\delta)}$$ where, using the usual notation,

$\delta = \frac{8d\pi\sin\theta}{\lambda}$. For i such arrays the total diffracted intensity is given by:-

$$I_\delta \alpha \sum_i \frac{\sin^2(N_i\delta)}{\sin^2(\delta)} \qquad \ldots\ldots\ldots\ldots\ldots (2)$$

In order to investigate the theoretical diffraction profile as obtained from Eqn.(2) the five separate distributions of Fig. 38 were aggregated

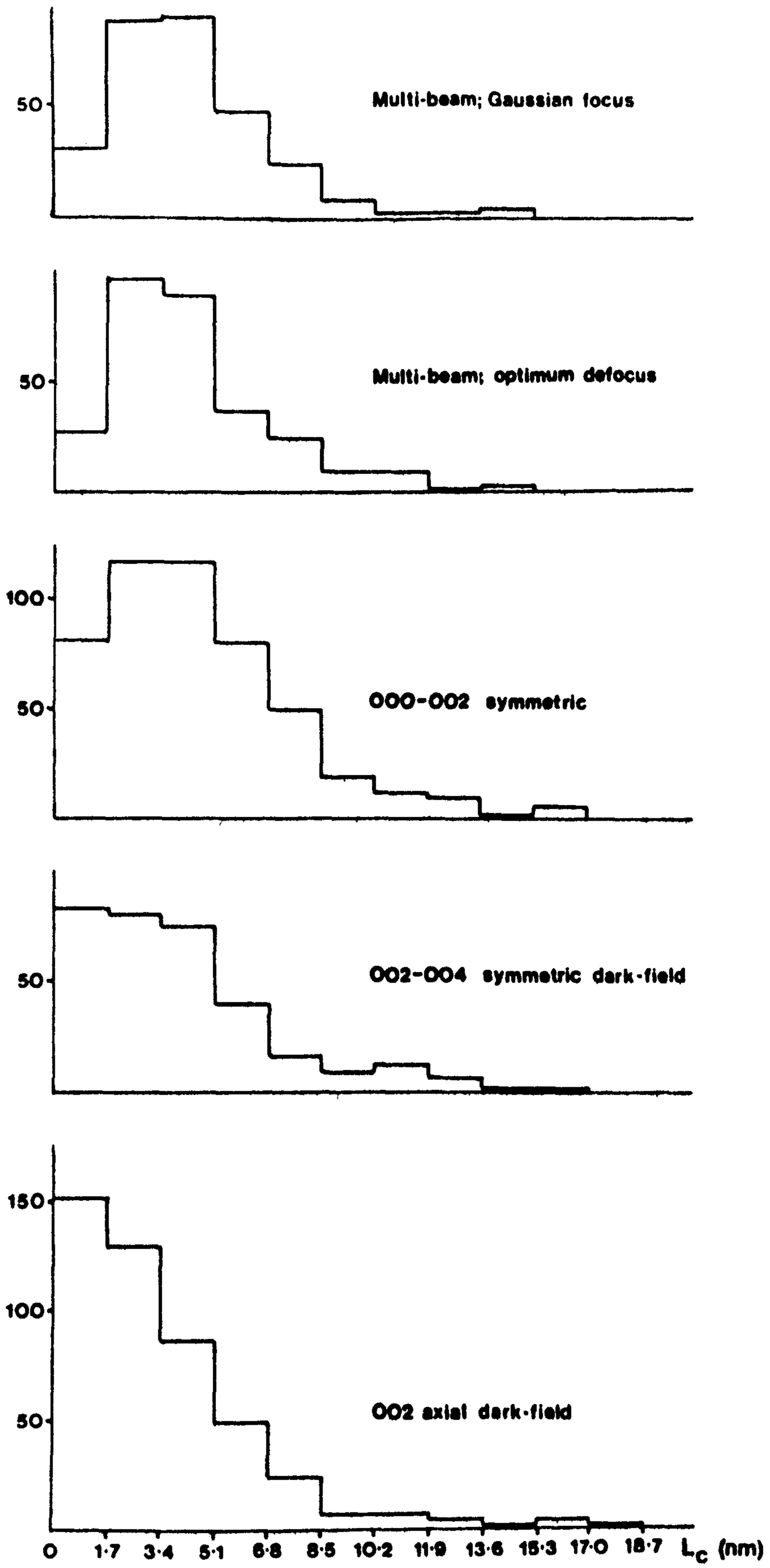

Fig. 38. Frequency distributions of crystallite size measured from images recorded using different instrumental conditions.

Table 6 Measurement of Crystallite Size, L_c, by different techniques

TECHNIQUE	L_c nm	s nm
Direct measurement on high-resolution images		
(i) Multibeam bright-field image at Gaussian focus	4.5	2.3
(ii) Multibeam bright-field image at maximum fringe-contrast focus	4.5	2.5
(iii) 000 - 002 symmetric bright-field image	4.7	3.0
(iv) 002 - 004 symmetric dark-field image	4.0	2.9
(v) 002 axial dark-field image	3.5	2.8
Electron Diffraction		
$(90 - \psi) = \pm 2^{o}$	5.2	
$(90 - \psi) = \pm 90^{o}$ (from Fig. 40c)	4.3	
Mean defect-free distance (D_c)	5.9	
X-ray Diffraction		
$(90 - \psi) = \pm 1^{o}$	5.1	
$(90 - \psi) = \pm 90^{o}$ (rotated specimen)	3.8	
Powder photograph	5.9	
Computation		
Distortion-free stacking size	8.3	

Table 7 The effect on direct measurements of crystallite size of discounting all crystallites of width 1.7 nm or less

TECHNIQUE	L_c nm
(i) Multibeam bright-field image at Gaussian focus	4.9
(ii) Multibeam bright-field image at maximum fringe-contrast focus,	4.8
(iii) 000 - 002 symmetric bright-field image	5.4
(iv) 002 - 004 symmetric dark-field image	5.1
(v) 002 axial dark-field image	4.7

and normalized to give one distribution. From the resolution analysis of the resultant peak, the half-height width was measured and the distortion-free stacking height derived from this is included in Table 6.

The electron-diffraction pattern was analyzed in the conventional manner by means of an equatorial scan with a Joyce-Loebl double-beam recording microdensitometer at a ratio-arm magnification of 50x. After logarithmic correction for saturation of the photographic emulsion[117], the width at half-height, Δ s, of each (00ℓ) reflection was measured, L_c calculated from the Scherrer equation applied to the (002) reflection, and the 'mean defect-free distance', D_c, obtained following the method of Thrower and Nagle[119].

The x-ray diffraction pattern of this specimen, which has a preferred orientation of 20^o, had been analyzed in this laboratory in another context[122]. To eliminate the orientation effect in the present study, x-ray photographs of both powdered and rotated specimens were recorded and analyzed. All x-ray diffraction results are included in Table 6.

The widths at half-height, Δ s, of the (002) and (00$\bar{2}$) reflections were measured at angles of azimuthal orientation (90 - ψ), Fig. 39, between $\pm\ 1^o$ and $\pm\ 45^o$, with the results shown in Fig. 40(a), where L_c' is the calculated stacking size at any angle of azimuthal orientation, ψ. Additionally, the area, A, under the (002) and (00$\bar{2}$) profiles was measured as a function of ψ, Fig. 40(b).

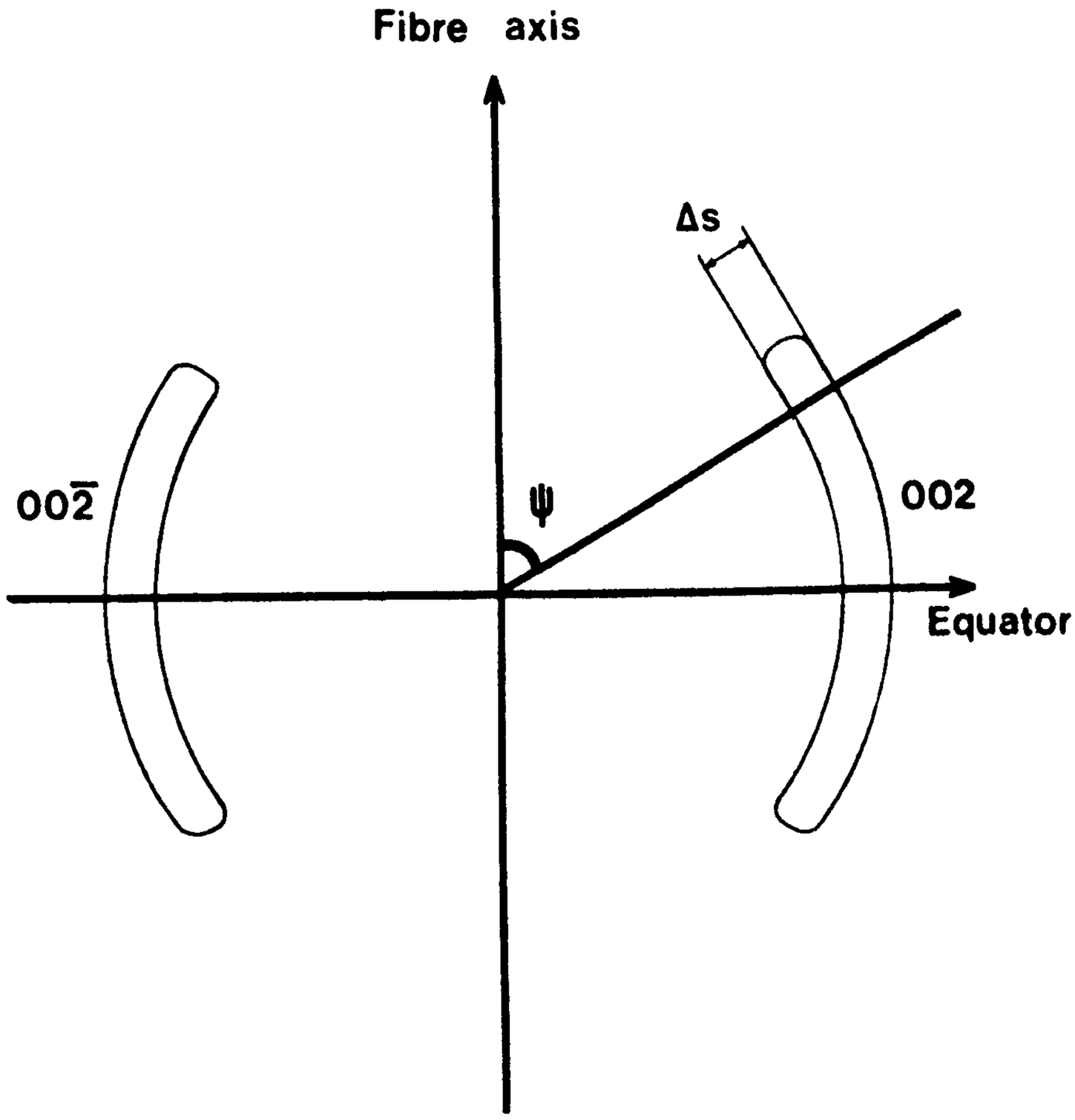

Fig. 39. Schematic representation of the width (Δ s) of the (002) reflection at an angle of misorientation, ψ.

4.3 RESULTS FOR SPECIMEN F2500

From Table 6 it is evident that the stacking size values, L_c, obtained from high-resolution images recorded under precise control of instrumental conditions are significantly lower than those values obtained from conventional diffraction methods, which in turn are lower than the value computed from the normalized aggregated stacking-height distribution based on all images. The arithmetic mean of this distribution is 4.2 nm, approximately half the computed stacking size. It might be expected that the computed value of L_c would approximate more closely to the diffraction values than the electron-microscope values, since the former will be increased by the enhanced contribution of larger crystallites to the diffracted intensity. However, it is

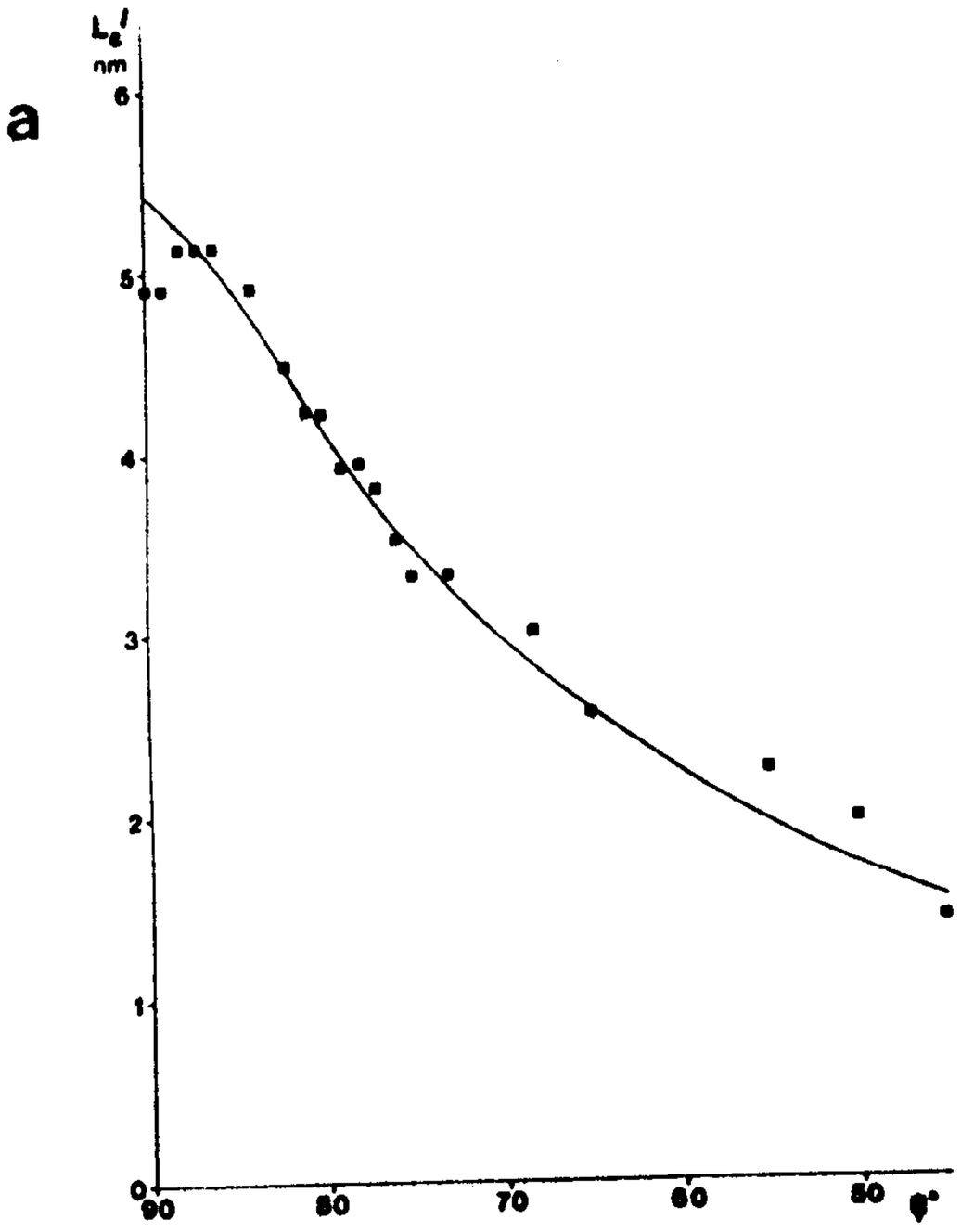

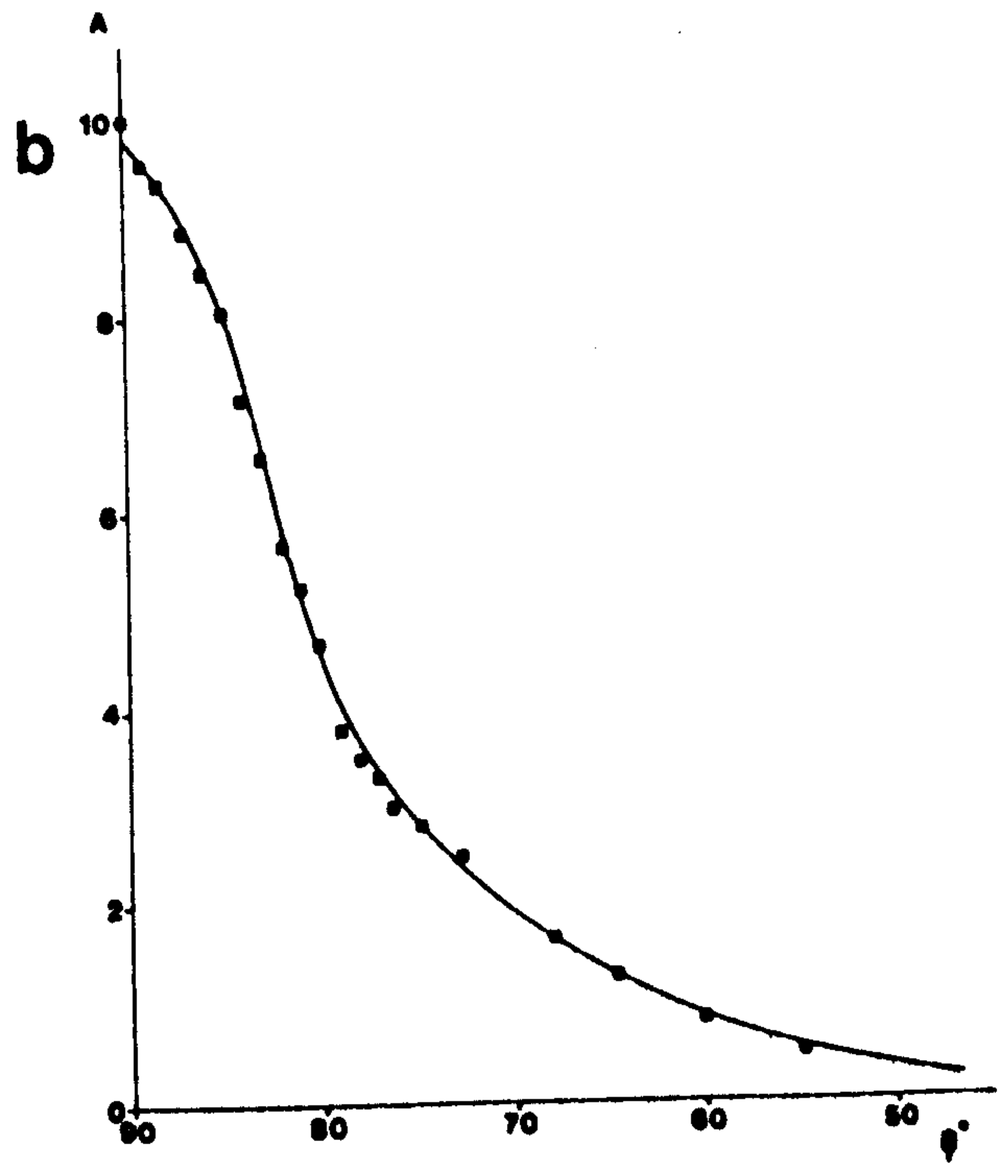

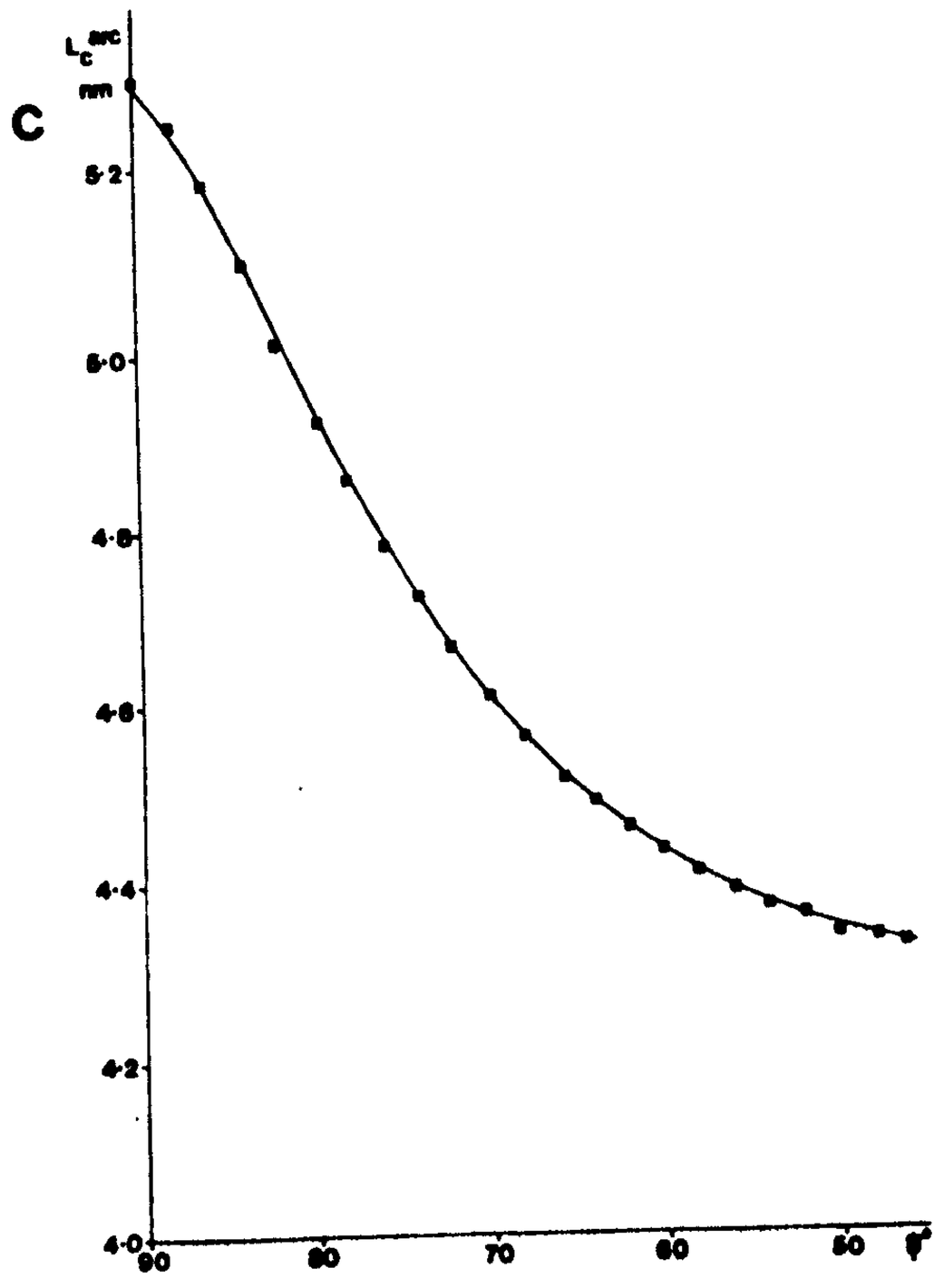

Fig. 40. The dependence of (a) L_c', (b) A, and (c) L_c^{arc} on ψ.

important to note that the computed value represents the diffraction from an idealized system with no defects.

The more detailed analysis of the diffraction profiles confirms the observation[63] that the width at half-height of the (002) reflection is a function of the misorientation from the fibre axis. Indeed, in a bright-field lattice-fringe image, a high proportion of small crystallites, (see, for example, at x in Plate V), can be seen to be misoriented by large angles. These crystallites will be excluded from results obtained from conventional diffraction techniques which only sample the (002) profile within a finite off-equatorial angle of about $\pm 2^{o}$ for electron diffraction, and about $\pm 1^{o}$ for x-ray diffraction. In an attempt to obtain an electron-diffraction measurement more representative of the true microstructure of the specimen, the effect on apparent crystallite size, defined here as L_c^{arc}, of including an increasing proportion of the arc associated with the (002) and $(00\bar{2})$ reflections has been calculated. If the mean crystallite size at any angle $(90 - \psi)$ is defined as L_c', and the normalized area under the (002) and $(00\bar{2})$ profiles at that angle is A, then L_c^{arc} is given by:-

$$L_c^{arc} = \frac{\sum_{\psi=90}^{\psi} L_c' \cdot A}{\sum_{\psi=90}^{\psi} A}$$

Hence when $\psi = 0^{o}$, L_c^{arc} gives the most representative measure of stacking size. The effect of including an increasing proportion of the arc, as shown in Fig. 40(c), is to significantly reduce the apparent mean crystallite size from 5.2 nm at $\psi = 90^{o}$ to approximately an asymptotic value of 4.3 nm at $\psi = 0^{o}$. This value is in much closer agreement with the stacking size of 3.8 nm evaluated from the pattern of the rotated specimen in x-ray diffraction, where orientation effects

were eliminated in a different manner. Powdering techniques when applied to these specimens tend to give granular (002) reflections, presumably because the fibre fragments are still large in comparison with the crystallite size. Consequently, a limited scan across such a pattern may involve, for example, an oriented fragment of skin material unrepresentative of the intrinsic structure. A representative size value will only be obtained in x-ray diffraction when there is a random dispersion of *individual* crystallites, and this is best achieved through specimen rotation.

Results of this thorough diffraction analysis can now be compared with values of mean stacking size obtained from direct measurement of high-resolution images. There is no significant difference between the results for L_c obtained from the three different bright-field modes (4.5 - 4.7 nm), and since the number of fringes in the (000) - (002) symmetric bright-field lattice-fringe image is relatively insensitive to defocus (see Appendix 1), the appropriate focal levels for this type of measurement have presumably been chosen in recording the multibeam images. There will be no contribution to the image in the tilted modes from crystallites oriented at angles of ψ less than 40^{o} since the diffracted waves from the (002) planes will then lie outside the objective aperture (Fig. 41). In the ideal case a continuous change of imaging conditions might be expected for crystallites not aligned along the fibre axis. In practice, all crystallites appear to be imaged with similar lattice-fringe contrast, and it is thought that this may well be a result of finite beam divergence.

The value for L_c determined from each bright-field image is higher than those predicted from either thorough electron-diffraction analysis (4.3 nm) or the x-ray diffraction analysis (3.8 nm). Whilst the trend of a reduction in crystallite size with increasing angle of

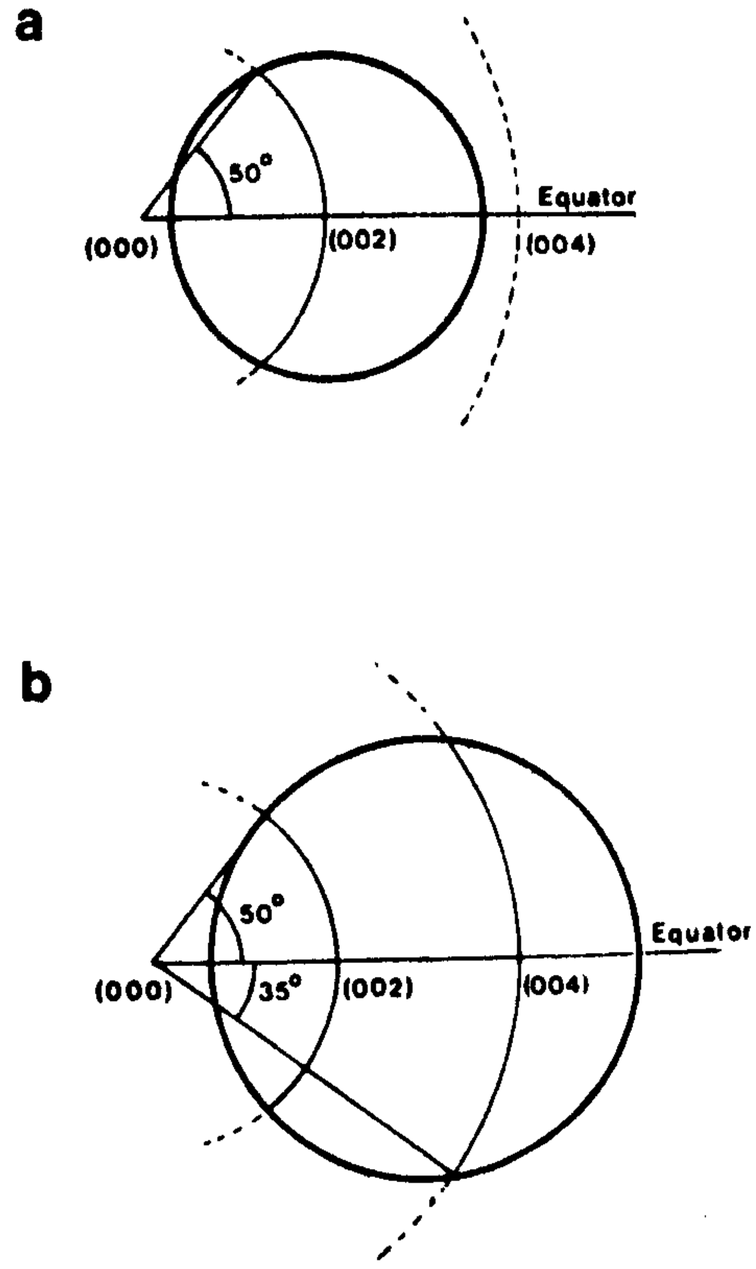

Fig. 41. Dark-field conditions for (a) (002) axial with 28 μm objective aperture, and (b) (002) - (004) symmetric with 39 μm objective aperture.

misorientation can be unequivocally established from these images, it is clear from the histograms that fewer small crystallites (1 - 5 layer planes) are counted in bright-field compared with dark-field conditions. Indeed, the image in bright-field is typically of much lower contrast than in dark-field, with the consequence that small crystallites cannot always be detected. It is interesting to note the effect of ignoring the small crystallites measured in each image on the values obtained for L_c. Table 7 shows that L_c determined by each method now corresponds much better with the value from conventional x-ray and electron-diffraction analysis.

In dark-field conditions, image contrast is so great that nearly all crystallites can be readily detected and measured. The appearance of crystallites in a high-resolution image is a function of that segment of arc of the diffracted beam or beams permitted to pass through the objective aperture. In the present case both the (002) - (004) symmetric, and the (002) axial, dark-field images are formed from $\pm 50^{o}$ of the (002) arc (Fig.41).

However, the lower value for L_c, and the higher contrast obtained from the (002) axial image, are clearly due to differences in image formation; the symmetric image is the result of interference between the (002) and (004) beams, while the axial image contains information from the (002) beam only. Additionally, spherical aberration will have minimal effect in the (002) axial case.

4.4 ELECTRON-DIFFRACTION ANALYSIS OF SPECIMENS HEAT TREATED AT 1000°C AND 1500°C

The success of the detailed analysis of the electron-diffraction patterns from the 2500°C material prompted a similar investigation of other specimens heat treated at 1000°C and 1500°C. The results of conventional orientation and size measurements in various regions of specimens A1000, A1500, D1000, D1500, E1000, E1500, F1000 and F1500 are shown in Table 2 (Chapter 2). It is evident that there are no significant differences between the sets of samples heat treated at 1000°C and 1500°C, nor are there any differences between skin and core regions in the longitudinal sections. The dependence of stacking size on azimuthal orientation in these specimens was analyzed by the methods described above, the values being averaged for the two sets of specimens at 1000°C and 1500°C. Coupled with the analysis of the core structure of specimen F2500 described in section 4.3 above, a graph of the percentage change (ΔL_c^{ψ}) in L_c at any angle ψ from the equatorial value of L_c was plotted against heat-treatment temperature at 5° intervals of ψ from 85° to 55°, Fig. 42. For example, for the 2500°C specimen L_c has fallen by 10% at $\psi = 85°$ in comparison with its value at $\psi = 90°$ (on the equator), while for the 1500°C specimens the relative change is 5%, and for the 1000°C specimens only 3%. It is evident that for each value of ψ the ΔL_c^{ψ} values lie on a straight line. Extrapolation of this set of lines suggests that they have a common origin, where $\Delta L_c^{\psi} = 0\%$, in the 400°C to 600°C temperature range. *If this*

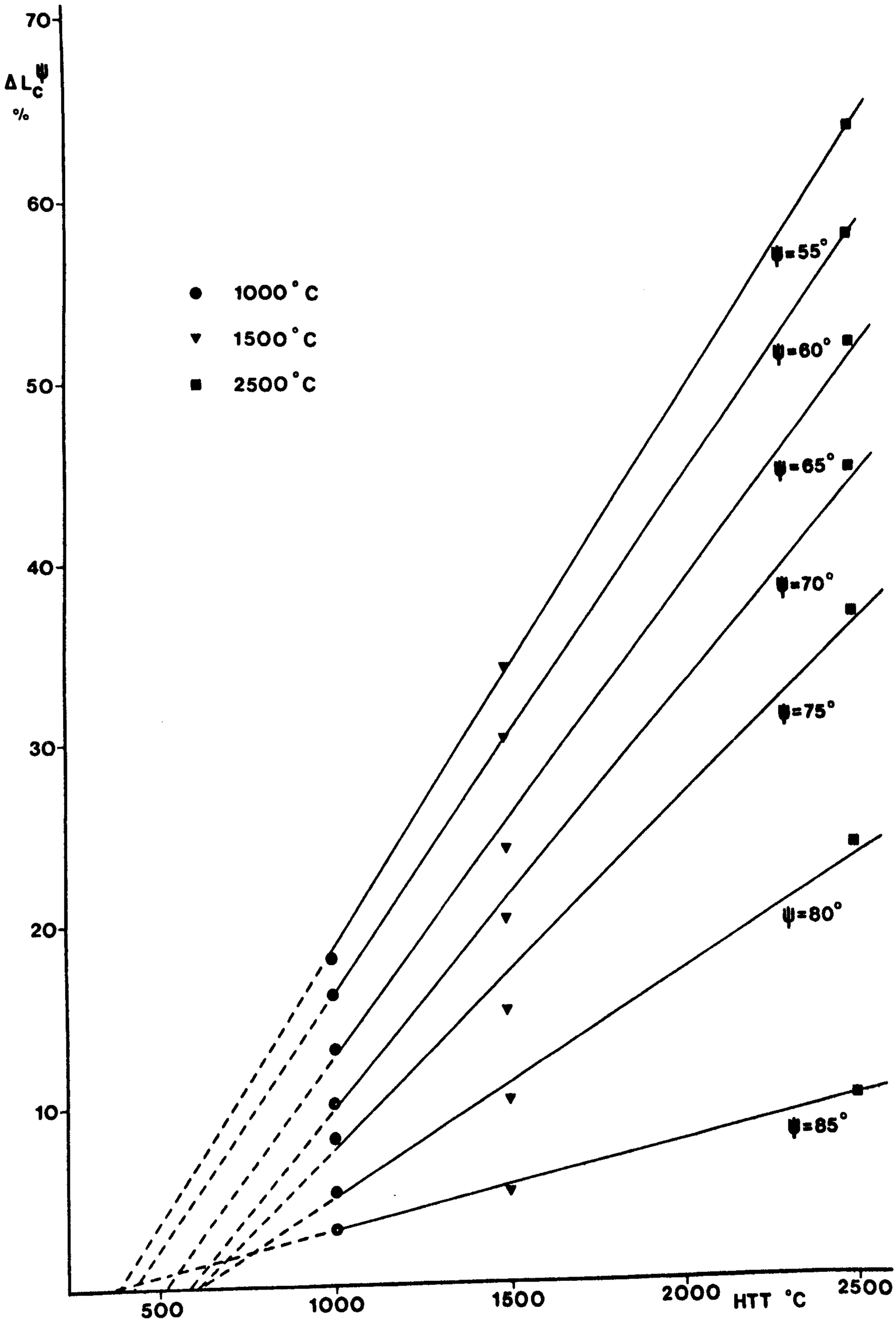

Fig. 42. The dependence of relative change in crystallite size with misorientation on heat-treatment temperature.

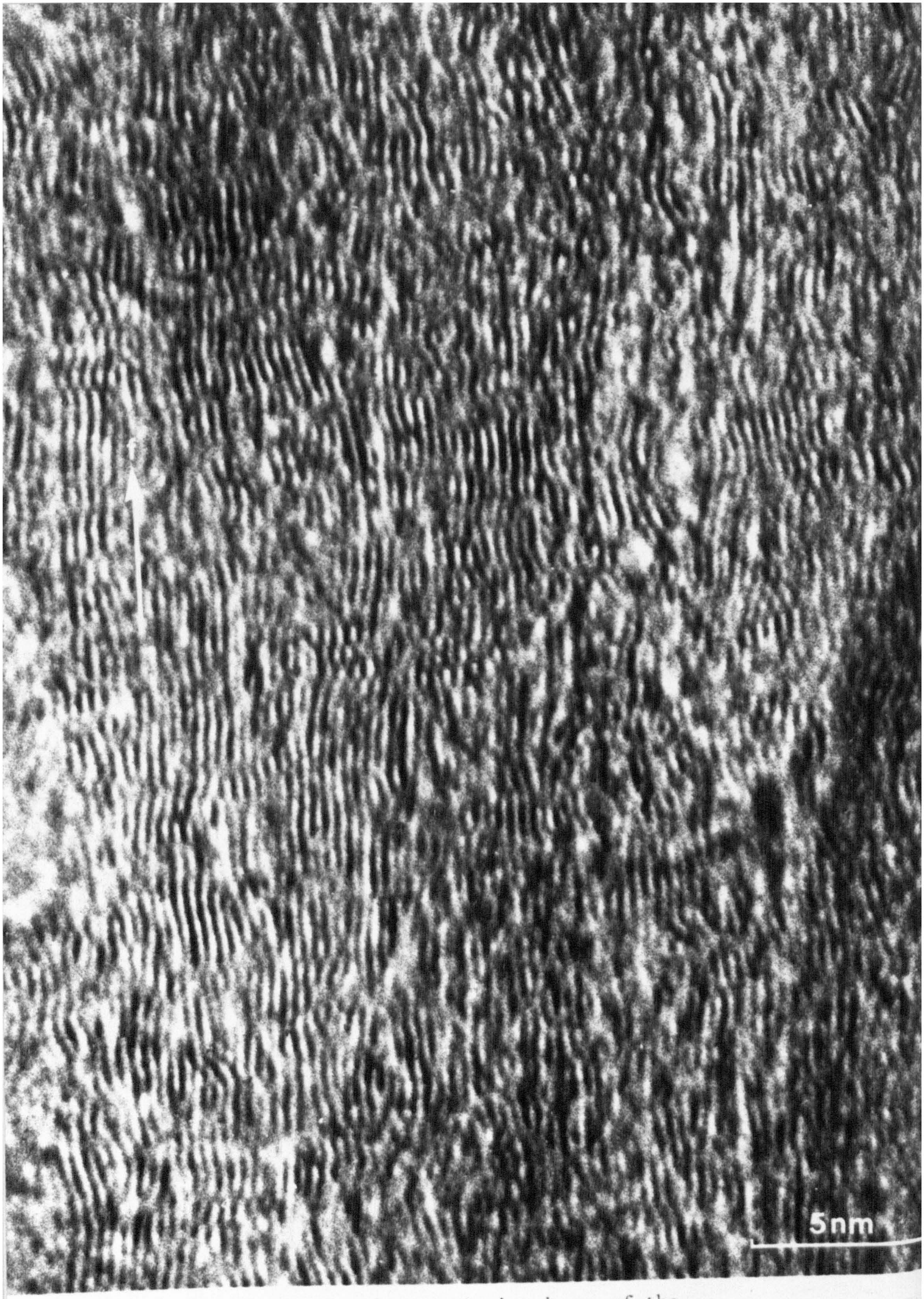

Plate LVII. Lattice-resolution image of the longitudinal structure of specimen K1500.

extrapolation is valid, then it can be assumed that heat treatment at this temperature results in a structure containing a uniform angular distribution of stacking size.

Fortunately, reference can be made to earlier work in this laboratory and at RAE of a rigorous study of the pyrolysis process[70, 79,123]. Crystallites with a mean stacking size of around 1.7 nm were measured in lattice-fringe images of a 600°C specimen, as compared to an L_c value of 1.3 nm from x-ray diffraction, although it is certain that the latter value is low due to the lack of a correction for distortion-broadening effects. No significant increase in L_c over the range 300°C to 800°C was detected by direct measurement, but there was an increase in $L_{a//}$ together with an increased intensity in the (100) meridional scatter. Taken in conjunction with chemical analysis of the pyrolysis products, the results indicate an interlinking of the ladder polymer sequences along the direction of the vestigial crystallites from the preoxidized PAN. Obviously, the distribution of vestigial crystallites is normal about the fibre axis, and the length-wise interlinking of units will proceed most favourably for those crystallites aligned close to the fibre axis. Thus a skeletal structure is formed. At 1000°C, this brings about the angular distribution noted in Fig. 42, although the L_c value (1.7 nm from direct measurement) is hardly altered. Plate LVII shows the structure of specimen K1500 at lattice resolution, discontinuous layer planes being aligned predominantly parallel to the direction, f, of the fibre axis, with little evidence of severe misorientation. At higher temperatures, particularly 2500°C, crystallization processes favour those crystallites aligned closest to the fibre axis, which are enlarged by accretion of those layer planes in favourable configurations.

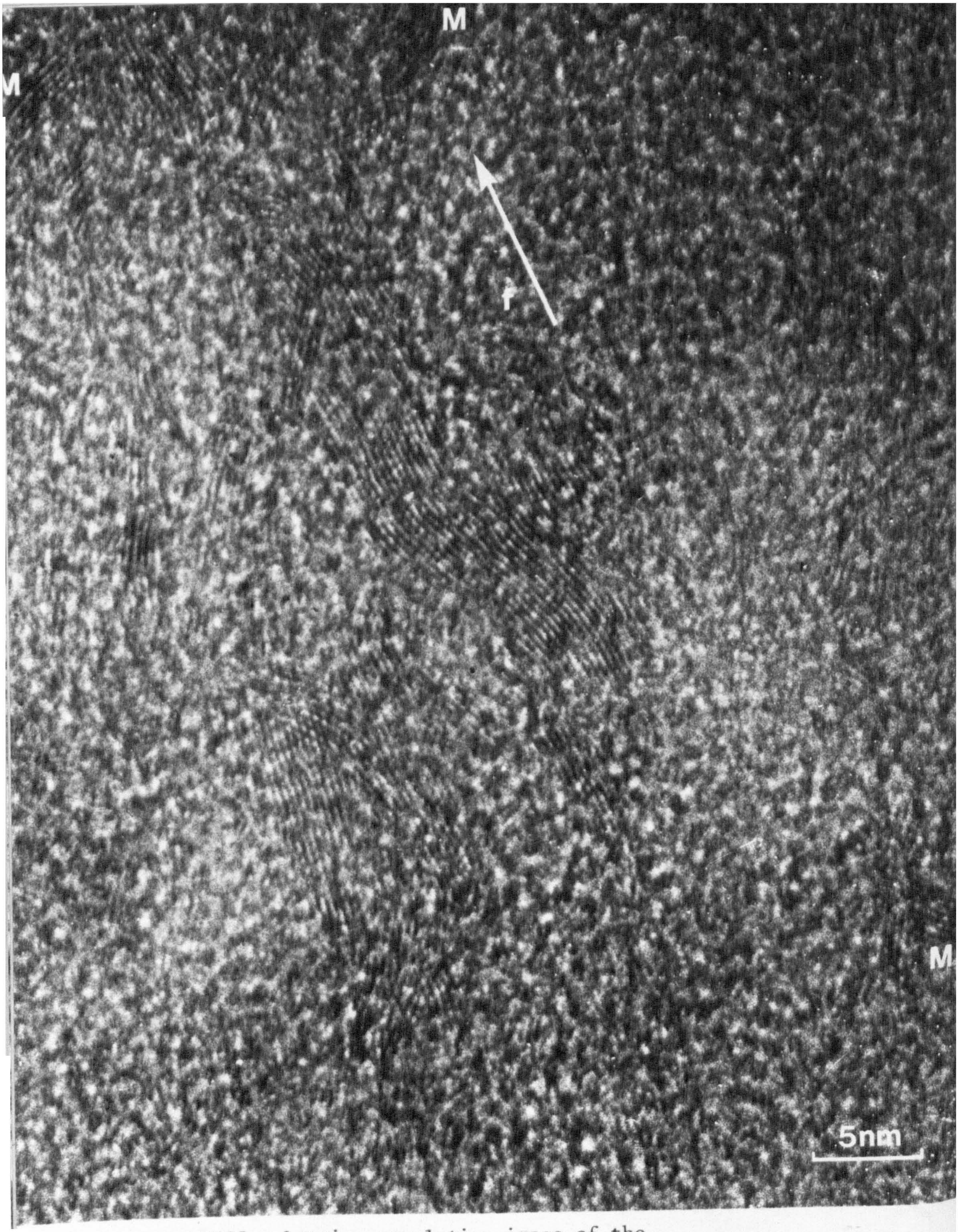

Plate LVIII. Lattice-resolution image of the longitudinal structure of specimen Q2500.

4.5 STRUCTURAL ANALYSIS OF SPECIMEN Q2500

The longitudinal structure of specimen Q2500, which did not receive an oxidative stabilization, but was heat treated to 2500°C, was analyzed using the methods described above. As can be seen from Fig. 43 the dependence of L_c' on ψ is much less marked in this fibre than in the conventionally-stabilized specimen (Fig. 40(a)). Figure 43 also indicates that the preferred orientation of this specimen (i.e. that orientation at which the area under the (002) reflection had fallen to 50% of its value on the equator) is 36° as compared with 18° for specimen F2500 (Fig. 40(b)). Similarly, the relative change in L_c^{arc} over the range from $\psi = 90^o$ to $\psi = 60^o$ is much smaller than that obtained from previous analysis (Fig. 40(c)). Although the mean axial crystallite size in a conventionally-treated fibre is as high as 5.2 nm, when the dependence of L_c' on ψ is quantitatively assessed the value of L_c^{arc} (for all misorientations from $\psi = 90^o$ to $\psi = 0^o$) is only 4.3 nm. Similar analysis of the unoxidized fibre shows that the comparative values are 2.9 nm and 2.7 nm respectively. So although the mean crystallite size in a fibre which has not been oxidatively stabilized is smaller than that normally found in conventional fibres, the dependence of stacking size on misorientation is small relative to that usually observed.

The poor preferred orientation present in specimen Q2500 is confirmed at lattice resolution in Plate LVIII, which shows crystallites, M, misoriented at large angles to the fibre axis direction, f. The lower value of mean stacking size is also evident from this image when compared with, for example, Plates VII and VIII. From a macrostructural viewpoint, it is significant that no skin-core heterogeneity was observed in these unoxidized specimens.

4.6 RÉSUMÉ

Conventional diffraction analysis, for example, of an equatorial

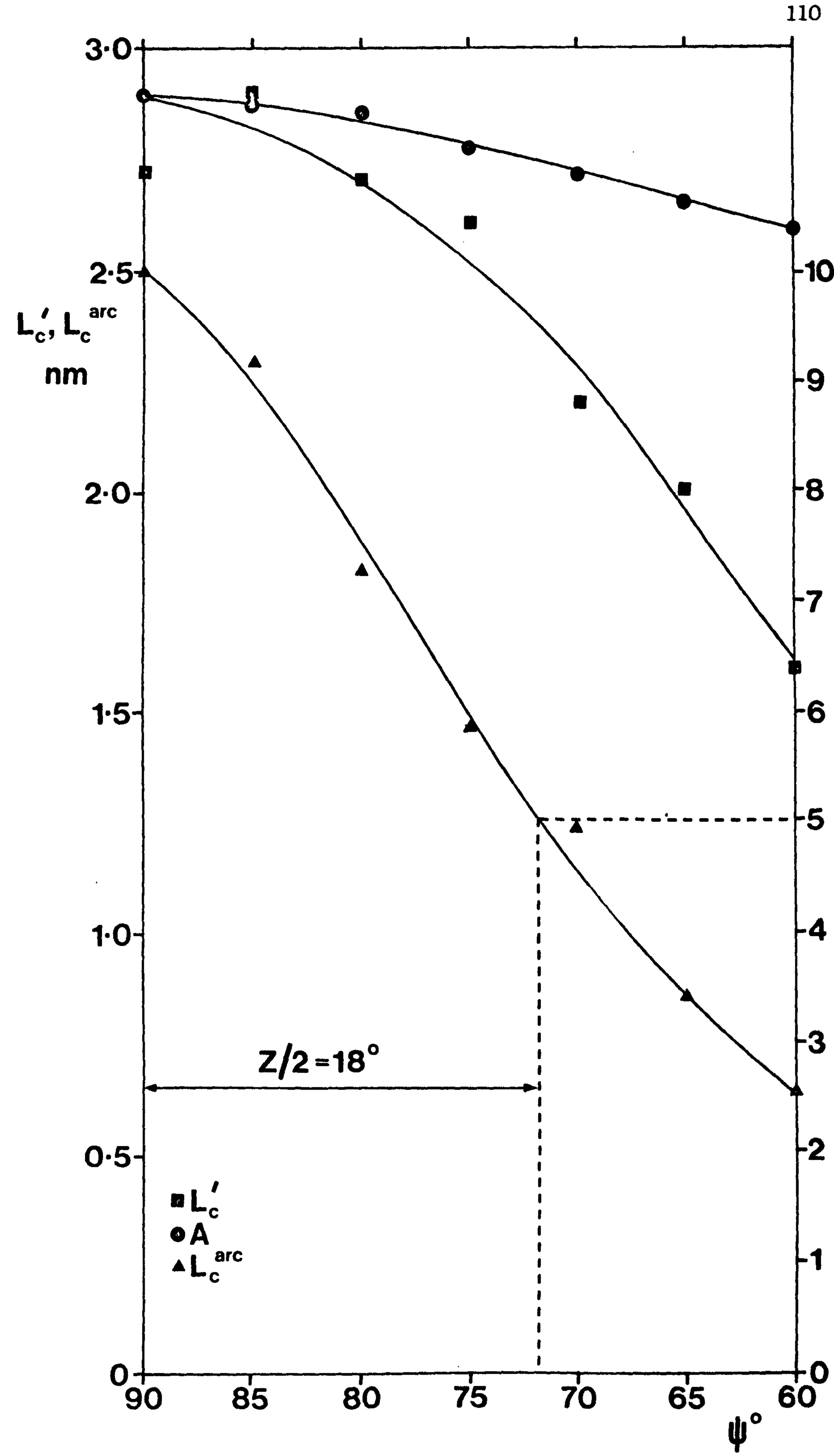

Fig. 43. The dependence of L_c', A, and L_c^{arc} on ψ for specimen Q2500.

section of an oriented fibre pattern, gives misleading measurement of crystallite stacking size, appropriate size evaluation only being obtained when the full range of crystallites, oriented at all angles to the fibre axis, is included. High-resolution electron images, particularly those of the dark-field type, afford not only a direct measurement of the true mean size, but also a unique characterization of the full range of size present (Fig. 38). The dependence of stacking size on misorientation is found to be most marked in fibres heat treated at 2500^{o}C, decreasing linearly at lower heat-treatment temperatures until in the range 400 - 600^{o}C there is a uniform angular distribution of size. Fibres which have not been oxidatively stabilized, but have been heat-treated to 2500^{o}C exhibit a very poor preferred crystallite orientation (36^{o}) in comparison with conventionally-treated fibres (18^{o}), and the dependence of stacking size on ψ was found to be considerably less significant than usually observed at this HTT.

CHAPTER 5

DISCUSSION

5.1 MACROSTRUCTURE

5.1.1 Introduction

The images obtained from polarized-light microscopy have suggested that transverse c-axis orientation in carbon fibres is directly related to both type and time of preoxidation cycle, and chemical composition of the fibres concerned. 'Oxidation zones' observed in light-microscope images of 1 μm thick transverse sections of oxidized-only fibres are carried through subsequent inert heat treatment to 1000, 1500 and 2500°C. The fully-stabilized sheath zone supposedly exhibits circumferential crystallite orientation, while the under-oxidized core is thought to be radially oriented.

5.1.2 Fibres heat treated to 2500°C

The preferred radial and circumferential crystallite orientations in core and sheath zones, predicted from polarized-light microscopy, should be seen in thin longitudinal sections, according to Figs.26 and 27; these are not observed in practice. Careful examination of transverse sections, however, has indicated that structurally-different zones, compatible with the oxidation zones observed in polarized-light microscopy, do exist in under-stabilized fibres, but selected-area electron-diffraction analysis indicates that they possess no preferred transverse c-axis orientation. The different sectioning properties of the dissimilar sheath and core zones, and also the reason for the appearance of such zones in optical microscopy, is presumably related to crystallite packing density and perfection as discussed in 5.2 below. Examination of relevant longitudinal sections from dog-bone cross-section fibres confirms the light-microscope observation that there is no preferred c-axis orientation in cross section, with the exception of a thin outer skin which is circumferentially oriented. In view of these anomalies the use of polarized-light microscopy where specimen shape may be important

(for example, with circular cross-section fibres) could be misleading.

The findings of Butler and Diefendorf[83] regarding larger crystallite size and higher preferred axial orientation close to the fibre surface in comparison with the material which forms the core of the fibre have been confirmed in this study. PAN-based type I fibres, irrespective of origin and stabilization cycle (with the exception of one fibre which was inert, non-oxidatively stabilized) have been found to possess a thin skin of *maximum* thickness 0.5 μm, exhibiting a large crystallite size and higher preferred crystallite orientation in comparison with the core component, which forms the bulk (> 90%) of the fibre. The skin zone, which is variable in both longitudinal extent and width, is characterized by a mean axial crystallite stacking size of about 10 nm and preferred orientation about 15^{o}, while the core, which is much more homogeneous, has a mean axial stacking size of about 4 nm and a preferred orientation of about 25^{o}. The most significant macrostructural conclusion from this study concerns the thickness of this skin zone. Polarized-light microscopy and plasma-etching techniques (see Chapter 1) suggest that a circumferential crystallite orientation exists in an outer sheath of at least 1 μm thickness compatible with the 'oxidation zone' observed by Watt and Johnson[84]. The direct transmission electron-microscope techniques used in the present study have indicated, however, that the skin zone is very thin in comparison with fibre diameter, being typically 50 - 150 nm in thickness.

The interpretation of surface features as revealed by scanning-electron microscopy in terms of macrofibrils carried through pyrolysis and heat treatment from the precursor PAN must now be considered erroneous. Examination of thin longitudinal and transverse sections, and 'first-cut' sections has shown unequivocally that the

c-axes of the more highly graphitized skin crystallites are oriented predominantly normal to the fibre surface. Rippling of the fibre surface, with an average periodicity of about 250 nm is proposed, and this is sufficient to explain striations of (002) diffracted intensity in dark-field images of first-cut sections, and anomalous skin effects in conventional longitudinal sections. Since scanning-electron microscopy reveals no structural differences (with the exception of crystallization flaws in type I fibres) between the surfaces of fibres heat treated at 1000, 1500 or 2500°C, it is proposed that the origin of the surface rippling lies in precursor spinning. The high orientation and crystallization, coupled with the preferred c-axis orientation of skin crystallites at the very surface of type I material means that these fibres possess large surface areas of entirely basal-plane nature. This is obviously undesirable in terms of matrix bonding in a composite structure, which is presumably through edge sites.

A dense core structure, essentially homogeneous at a macro-level, is proposed, the model comprising crystalline webs enclosing random pockets of less-crystalline material[99,100] not being supported by the present study.

High-voltage electron microscopy[49,95] has shown that large crystallite misorientations occur in the vicinity of internal voids in type I fibres, and this has been confirmed. Volatilization of impurity particles, presumably originating in the precursor PAN, at high heat-treatment temperatures causes catalytic graphitization parallel to the c-axes of the turbostratically-stacked crystallites bordering the void. This crystallization process does not appear to proceed parallel to the fibre axis (normal to the c-axis), and thus the formation of spherical voids is precluded, diconical shapes being prevalent.

5.1.3 Fibres heat treated to 1000°C and 1500°C

In type I fibres, heat treated to 2500°C, a thin skin incompatible with the oxidation zones observed in transverse sections has been characterized in terms of relatively large crystallite size and high axial preferred orientation. Such a skin region is not observed in fibres heat treated at 1000°C or 1500°C. At low magnification it is clear that a homogeneous core structure extends fully to the edge of longitudinal sections, and it is only at lattice resolution that a *very* thin skin region exhibiting *slightly* larger crystallite size and better orientation becomes apparent. This region actually forms the fibre surface. It is proposed that the surface of the fibre, being a discontinuity of structure, forms a restraint on the possible orientations taken up by those crystallites within one crystallite width of it. At 1000°C, crystallites at the fibre surface of width up to about 5 nm showing high axial orientation, yet relatively unconnected lengthwise, are proposed. At 1500°C such crystallites have started to link and interconnect lengthwise and grow in width, whilst maintaining orientation, so that the basic skin structure is established. Subsequent heat treatment at 2500°C or above is thought to cause the growth inwards of this skin structure; highly-graphitic, yet misoriented crystallites being formed in the skin structure from regions of surface variability of relatively minor importance at lower heat-treatment temperatures. A schematic representation of the origin and growth of the skin structure throughout the temperature range 1000 - 2500°C is shown in Fig. 44. Since the formation of such a skin structure is purely a heat-treatment artefact, unconnected with type of stabilization cycle, the interlaminar shear strength of composite structures fabricated from unmodified fibres (i.e. not surface treated) should be a unique function of final heat-treatment temperature, the relationship being inverse.

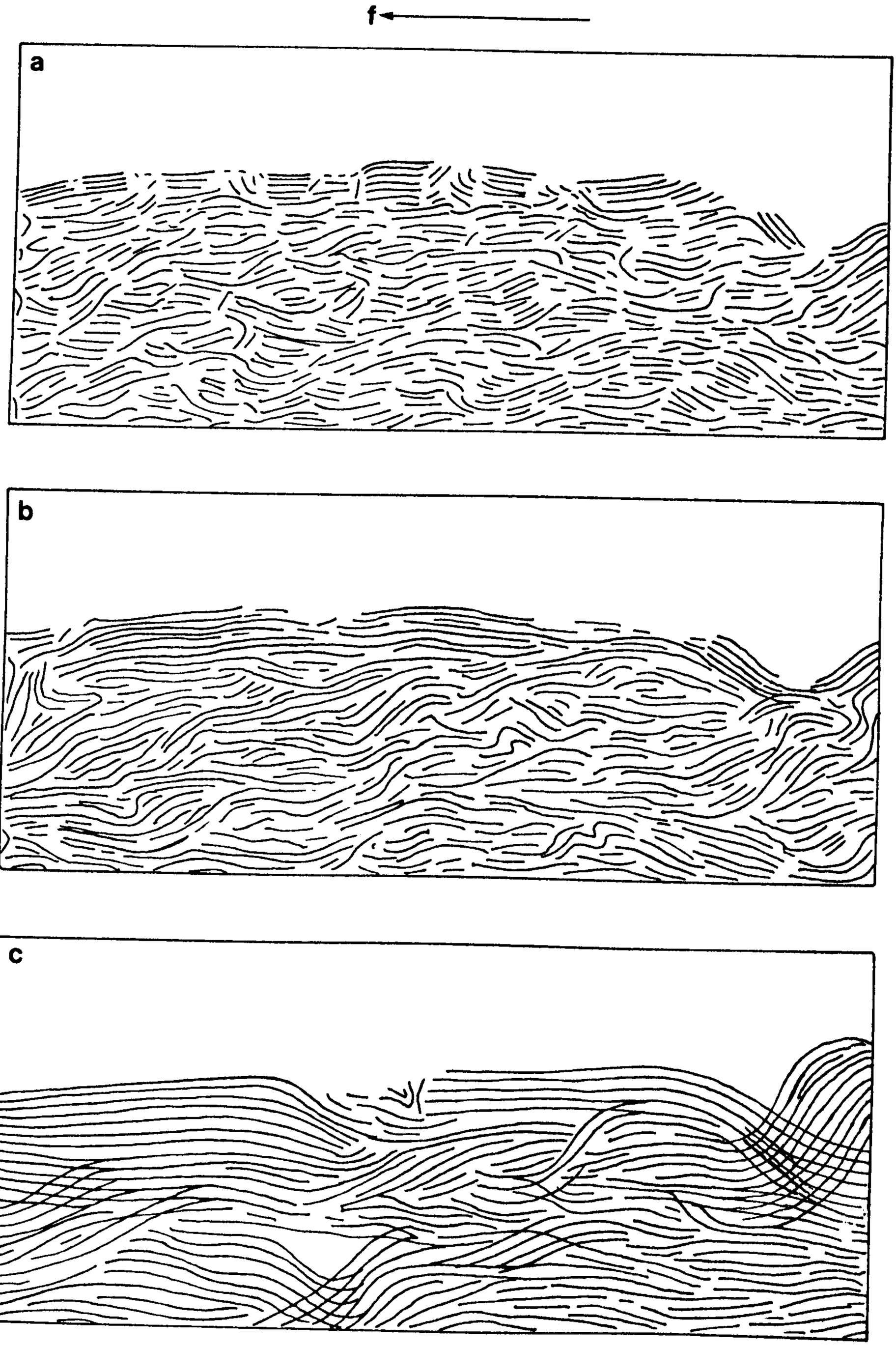

Fig. 44. Schematic representation of the development of skin structure from (a) 1000°C, to (b) 1500°C and (c) 2500°C. (**f** denotes direction of fibre axis).

Sections obtained from early attempts to section low-temperature fibres[72] predicting the presence of 80 - 100 nm fibrils in 1000°C material, thought to originate in the precursor, have now been shown to be misleading, since the orientation of such 'fibrils' can be changed by altering the direction of cutting. For example, axially-aligned structures can be formed by cutting longitudinal sections normal to the direction of the fibre axis, while cutting along the axis produces macrostructures oriented normal to the fibre axis. These findings have recently been independently confirmed[124].

5.2 MICROSTRUCTURE

5.2.1 Introduction

The direct observation of representative lattice-fringe images of the turbostratically-stacked layer planes is necessary in order to obtain a meaningful characterization of the intrinsic micro-structure. However, images of this type are essentially a two-dimensional representation of a complex three-dimensional object, and to overcome this problem examination of both longitudinal and transverse sections is essential. The traditional microstructural models (see Chapter 1) are based on images obtained from either sections or fragments exhibiting longitudinal structure only, and in the light of the present study, the acceptance of such models must be critically questioned when they are used for the calculation of mechanical properties.

5.2.2 Fibres heat treated to 2500°C

The complex interlinking of layer planes and crystallites in transverse sections of type I fibres indicates that the widely-accepted 'wrinkled-ribbon' structural model[63] (Fig. 15) is grossly simplistic. However, the conclusions regarding the rôle of small crystallites misoriented off the fibre axis as interlinking agents between the larger axially-aligned crystallites[63] (Fig. 16) can be accepted, since a

continuous change in mean apparent stacking size with orientation was found for a typical core structure.

The three-dimensional structural model developed by Crawford and Johnson (Fig. 17) showing a complex three-dimensional structure characterized by bending and twisting of layer-plane packets is thought to more closely resemble the actual structure. The limitation of this model, however, is that the crystallites in cross section bend too sharply, a smoothly-curved 'thumb-print' type structure as proposed initially by Phillips et al.[78], and later adapted by Wicks[98] (Fig. 19) being more realistic.

The basket-weave model (Fig. 18) of Diefendorf and Tokarsky[53] is a typical product of an over-simplified approach to structural analysis from inappropriate low-resolution images, while the rippled-sheet model for fibre surfaces is explained by orientation effects of skin crystallites.

Stewart and Feughelman[82] have suggested that regular Moiré patterns are due to crystallite overlapping, while irregular dark extinction bands arise from interference effects where basal planes cross over within *a single* crystallite. In the present study, such bands are often observed in large skin crystallites, and these are clearly attributable to lattice-distortion effects, while core crystallites, as seen in transverse section, evidently turn and fold on themselves within a length (5 nm) considerably less than the thickness of a typical thin longitudinal section (30 nm). In this case dark bands might be expected. The fundamental difference between skin crystallites, which often extend fully through the section, and core crystallites which rarely do, is reflected in the very different values obtained from $L_{a\perp}$, while $L_{a//}$ is basically the same for both structures (see 2.3.1.*A.d*).

Structurally-different sheath and core zones of dimensions

compatible with the oxidation zones observed in optical microscopy are only observed in transverse sections. This indicates that the origin of the structural difference does not lie in an orientation effect, and this is confirmed by the continuous ring nature of the (002) reflection of both zones in transverse section. Additionally, computation of the apparent stacking size for each zone shows no difference, and it is only at lattice resolution that the differences are discernible. In the core the crystallite packing density is greater than in the sheath since the layer-plane width (length as seen in transverse section) is not as great. In the sheath zone the layer planes are wider, with the result that they are able to fold back on themselves enclosing micro-voids. These differences are not observed in longitudinal sections since the unambiguous interpretation of regions showing no (002) interference fringes in terms of voids is not possible due to layer-plane orientations, which may be out of the diffraction condition. Undoubtedly the origin of the difference lies in preoxidation; it would appear that during this critical stage,the sheath, which is 'fully'-oxidized, contains ladder polymer which is more heavily crosslinked than the 'under'-oxidized core, and consequently layer plane width on crystallization is greater in the former case than in the latter. As such the rôle of oxidation in stabilization would seem to be one of crosslinking. A schematic representation of the structure of PAN-based type I carbon fibres is depicted in Fig. 45. Note that the longitudinal structure of both sheath and core zones is identical. This is due to the void-like appearance of crystallites out of the diffraction condition, which are indistinguishable from true enclosed voids.

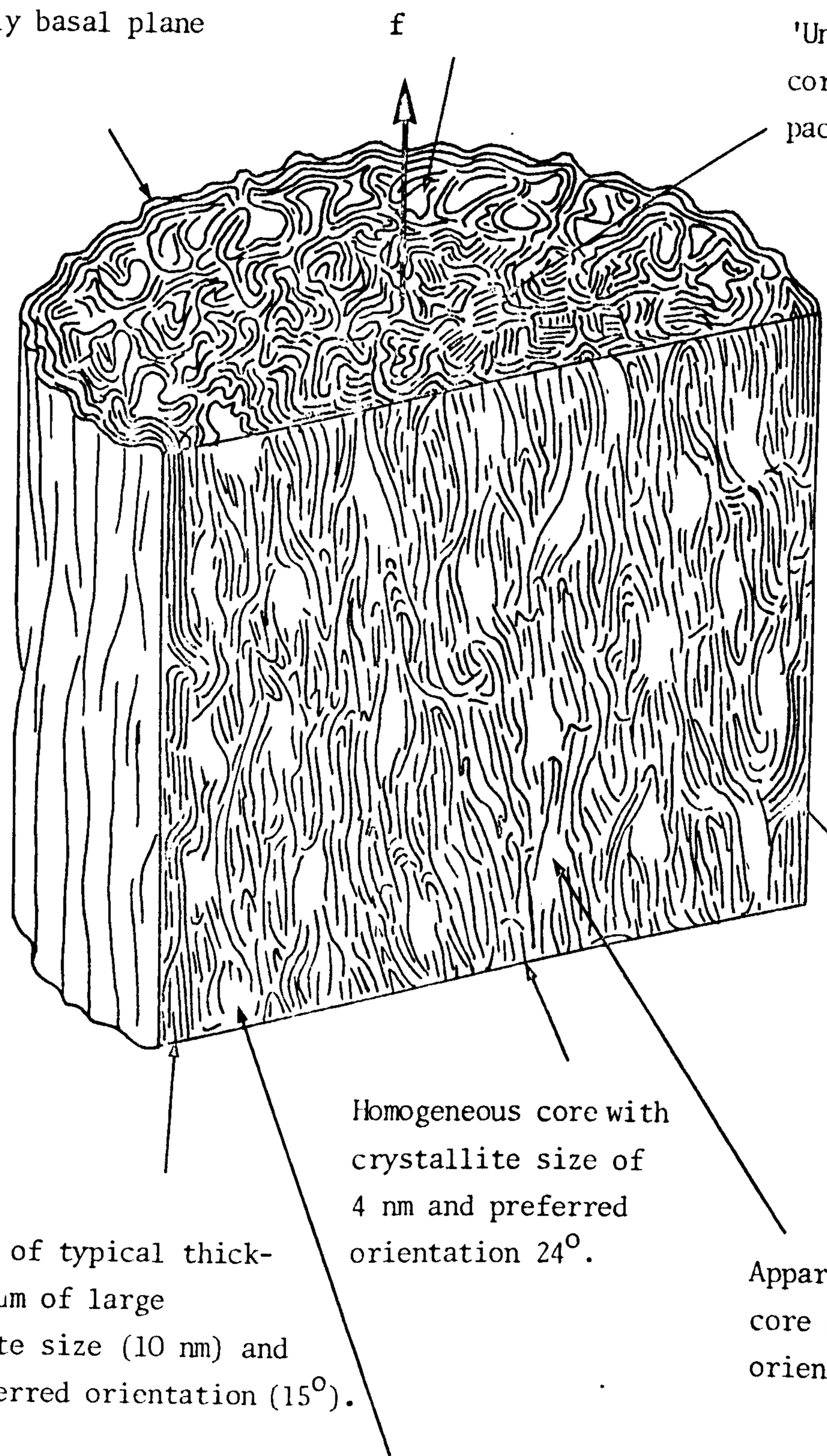

Fig. 45. Schematic representation of the three-dimensional structure of PAN-based type I carbon fibre; **f** denotes fibre axis (N.B. voids are not to scale)

5.2.3 Fibres heat treated at 1000°C, 1500°C and 2500°C - the true origin of structure in PAN-based carbon fibres

The longitudinal structure of type I carbon fibres is characterized by relatively large crystallites oriented preferentially along the fibre axis, interlinked by smaller crystallites misoriented by angles up to 90° with respect to the axis. From Fig. 46, which shows the dependence of A on ψ for various carbon fibres, it can be calculated that about 60% of the crystallites are oriented within 10° of the fibre axis, and these have a *mean* stacking size between 4.2 nm and 5.3 nm (Fig. 47, the dependence of L_c' on ψ). The remaining 40% of crystallites, oriented at angles greater than 10° to the fibre axis have *mean* sizes between 4.3 nm and 1.5 nm (Fig. 47). At lower heat-treatment temperatures the relative mean size of those crystallites misoriented at large angles with respect to those oriented axially changes significantly. For example, at 1500°C, the mean size of the 60% of crystallites which are oriented within about 15° of the fibre axis is between 1.3 and 1.5 nm, while the total range of mean size is only 1.2 - 1.5 nm. Similarly, at 1000°C, a narrow mean stacking size range between 0.8 and 1.0 nm exists. Figure 42 shows the development of the dependence of crystallite stacking size on orientation with increasing heat-treatment temperature, and it is evident that at 500 ± 100°C the structure consists of crystallites having a uniform mean size oriented at all angles within the azimuthal spread of the (002) reflection. In the early stages of pyrolysis, it seems that extensive fragmentation occurs, with only two or three graphite-like layers stacking together on average. Heat treatment to 1000°C then produces a relatively insignificant change in L_c, but a lengthwise interlinking of layer planes, added stability being gained by cross-linking with the evolution of HCN and N_2. Once the small highly-distorted crystallites are linked together along the direction of the

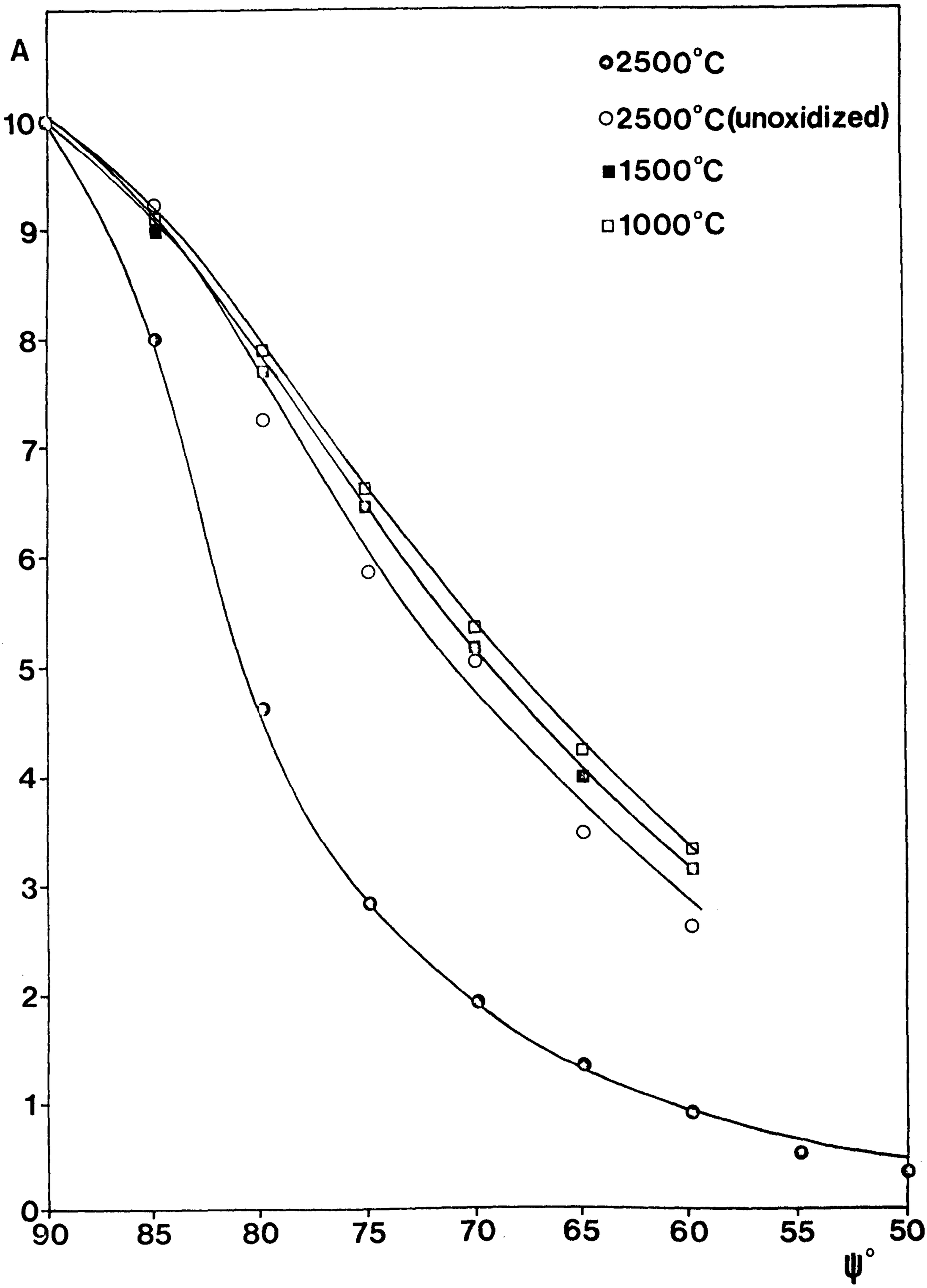

Fig. 46. The dependence of A on ψ for various PAN-based carbon fibres.

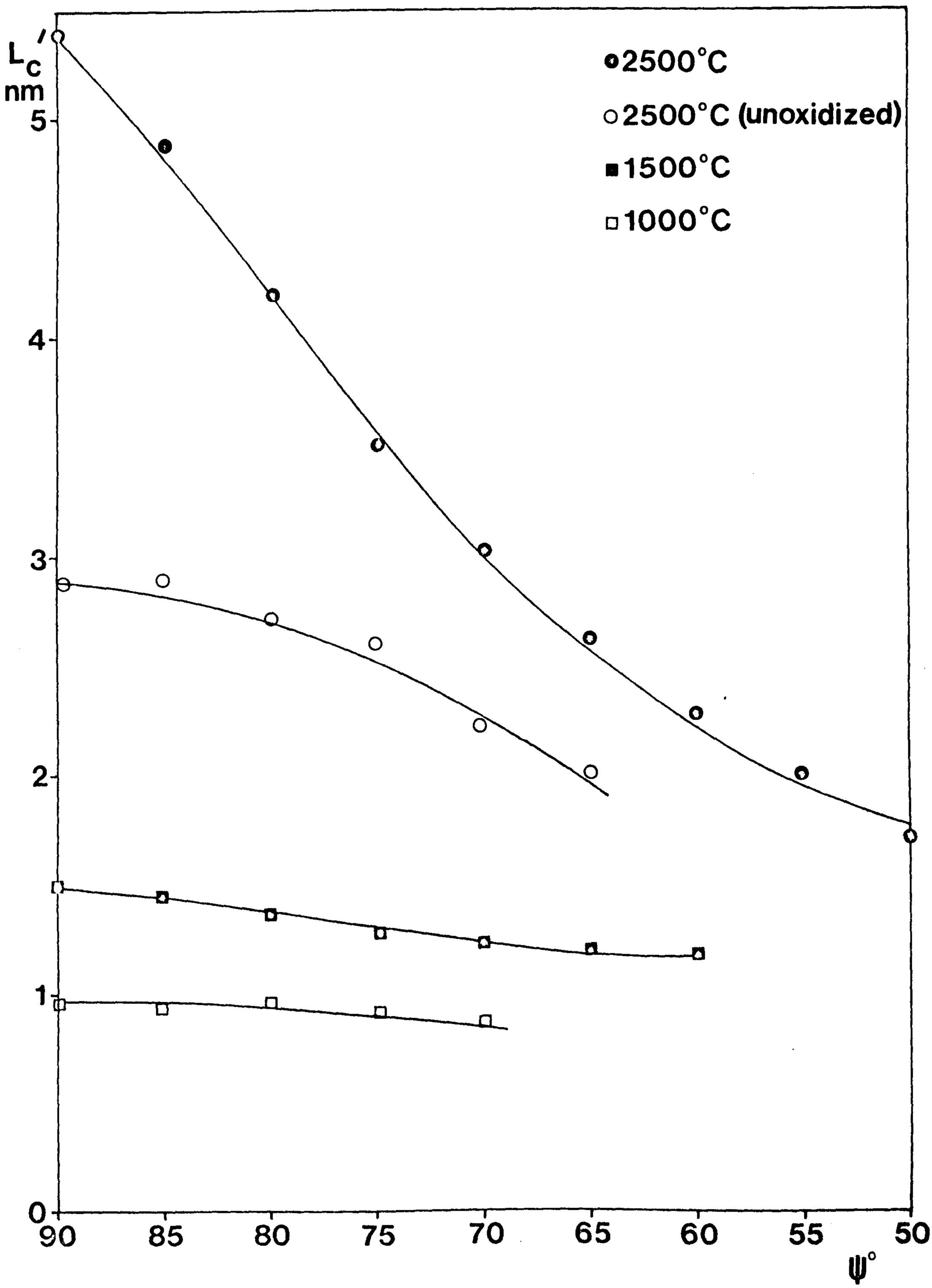

Fig. 47. The dependence of L_c' on ψ for various PAN-based carbon fibres.

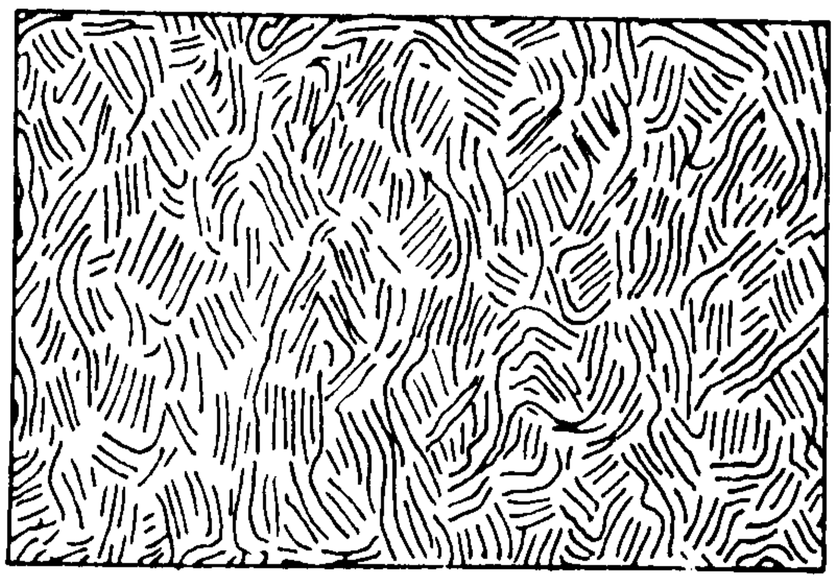

HTT 500°C, $L_c^{eq} = L_c^{arc} < 1{\cdot}0$ nm, $Z = 55°$.

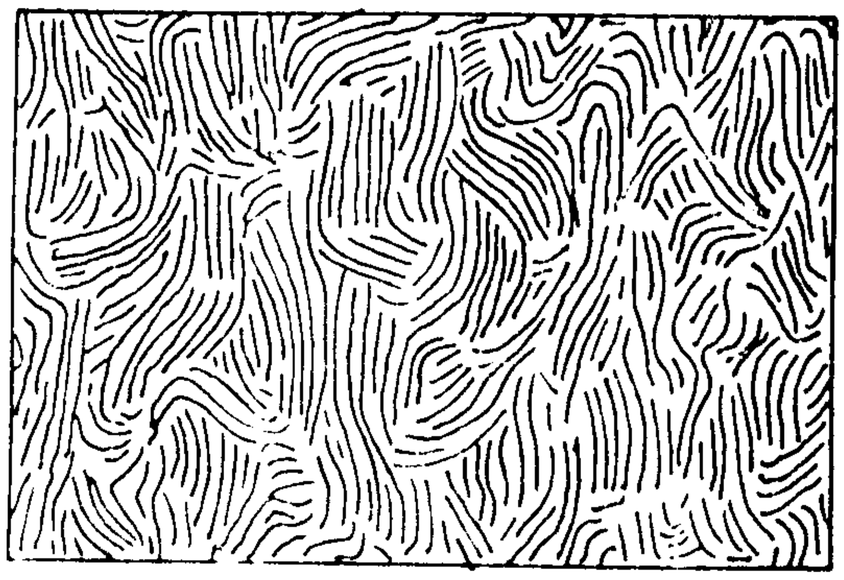

HTT 1000°C, $Z = 45°$, $L_c^{eq} = 1{\cdot}0$nm, $L_c^{arc} = 0{\cdot}9$nm.

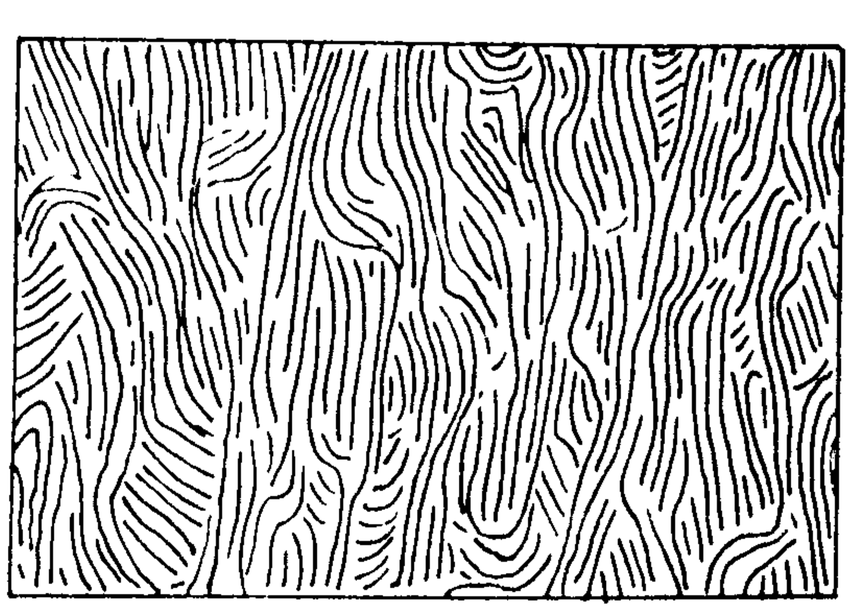

HTT 1500°C, $Z = 40°$, $L_c^{eq} = 1{\cdot}5$nm, $L_c^{arc} = 1{\cdot}3$nm.

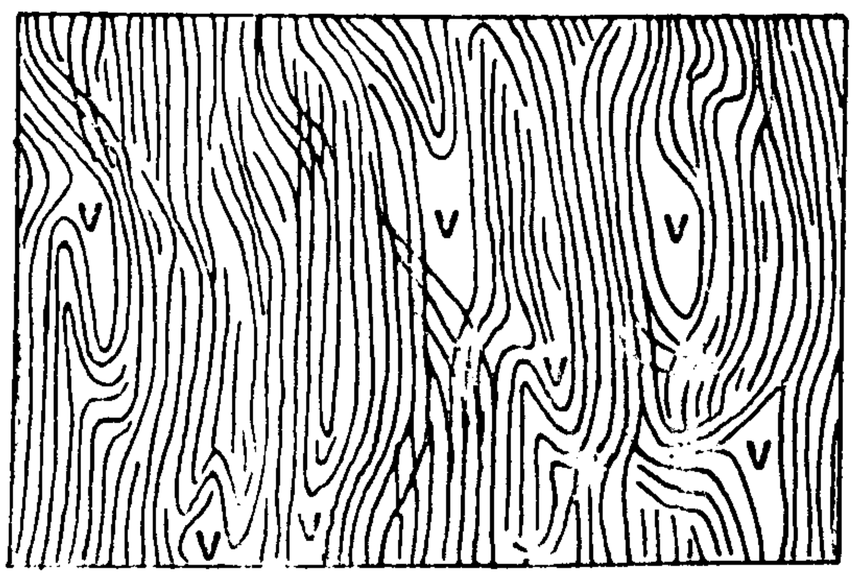

HTT 2500°C, $Z = 20°$, $L_c^{eq} = 5{\cdot}3$ nm, $L_c^{arc} = 4{\cdot}3$nm.

Fig. 48. The origin and development of structure with heat-treatment temperature of PAN-based carbon fibres.

fibre axis a skeletal structure is formed, and it is on this that subsequent heat-treatment crystallization occurs. By 2500°C, axially-aligned crystallites have grown in width to a mean size of more than 5 nm, while those crystallites oriented at 40° to the fibre axis have a mean size of only 1.5 nm. Evidently the rôle of these smaller crystallites is one of interlinking. A schematic representation of the origin and growth of structure in PAN-based carbon fibres is depicted in Fig. 48, enclosed voids, v, being shown for the 2500°C specimen. The formation of these is through lengthwise and widthwise growth of layer planes, and crystallization processes. The values given for L_c^{eq} are the mean stacking sizes at $\psi = 90^o$.

In view of the very disordered structure present during the early stages of pyrolysis, chemical formulae proposed for long sequences of oxidized and/or inert-stabilized PAN[22] would appear to be too idealized. A scheme which involves fragmentation, where the rôle of oxygen is as an interlinking agent is favoured by the present study. Since the changes in microstructure between sheath and core zones in 'under'-oxidized fibres would appear to be too insignificant to affect the mechanical properties of carbon fibres, the need to completely stabilize the precursor seems to have been overemphasized in the past. In view of these anomalies, a more critical analysis of the mechanism and effect of oxidation on crystallite orientation and microstructure is now needed.

5.2.4 Unoxidized fibres heat treated to 2500°C

It is evident from lattice-resolution images and diffraction analysis of non-oxidized fibres heat treated to 2500°C that the skeletal structure developed during pyrolysis is not formed to the same extent during inert stabilization. A cyclized condensed naphthyridine ring structure for vacuum-stabilized PAN (Fig. 6) is clearly not as thermally stable as the oxidized ladder polymer formed during the conventional

process. Reference to Fig. 46 shows that the preferred orientation of unoxidized fibres heat treated to 2500°C is close to that found in conventionally-produced fibres heat treated to only 1000°C and 1500°C, while from Fig. 47 the differences in stacking size can be directly assessed. At $\psi = 90^{o}$ (on the fibre axis) the mean crystallite stacking size for unoxidized fibres heat treated to 2500°C is 2.9 nm, while it is 5.4 nm for conventional type I fibres. Yet at $\psi = 65^{o}$ (corresponding to a misorientation of 25^{o}) the corresponding values are 2.6 nm and 2.0 nm. Evidently, since a well-developed axially-aligned skeletal structure is not formed during inert stabilization and pyrolysis the preferential growth in width of axial crystallites is not substantial in comparison with misoriented crystallites. Additionally, the non-appearance of the skin structure characteristic of type I fibres in unoxidized fibres heat treated to 2500°C must be related to this relatively non-selective crystallization process. If this is the case, the formation of an oxidatively-stabilized skeletal structure, although unrelated to the oxidation zones observed in polarized-light microscopy, is a prerequisite to the crystallization of a skin structure at high heat-treatment temperatures.

5.3 THE TENSILE STRENGTH OF PAN-BASED CARBON FIBRES

5.3.1 Intrinsic strength

A. Introduction

Reynolds and Sharp[113] have shown that failure of single graphitic crystallites might be expected when they experience a strain of greater than 20%. In order for such strains to be realized in fibres which typically fail at 1 - 2% the crystallites must be misoriented from the fibre axis by an angle ϕ such that:-

$$\varepsilon_s = \frac{\varepsilon E}{c_{44}} \sin\phi \cos\phi \qquad \ldots\ldots\ldots\ldots\ldots\ldots (3)$$

where ε_s is the crystallite shear strain-to-failure, ε is the fibre strain-to-failure, E is the Young's modulus of the fibre, and c_{44} is the crystallite shear modulus (4.0 GNm^{-2} in the absence of basal dislocations). Taking ε_s as 20%, a plot of ε against ϕ for type I (E=350 GNm^{-2}), type II (E=250 GNm^{-2}), and type A fibres (E=200 GNm^{-2}) can be made, and is shown in Fig. 49.

B. Fibres heat treated to 2500°C

a. Conventional type I fibres

Since it has been shown that the larger crystallites present in the core structure are aligned preferentially along the fibre axis, while smaller interlinking crystallites are misoriented at large angles with respect to the fibre axis, failure of a single crystallite in the latter category, which is the most likely occurrence, would not be expected to lead to intrinsic failure of the fibre. Figure 38 indicates that a range of crystallite size up to a maximum of about 18 nm exists in the core structure of type I carbon fibres, while qualitative examination of lattice-fringe images suggests that these large crystallites are oriented within about 5° of the fibre axis. From Fig. 49 it can be shown that if fibre failure is only initiated by failure of one or more of these crystallites, then fibre strains-to-failure of 2 - 3% and strengths of 7 - 10 GNm^{-2} might be expected. Using the Griffith relationship:-

$$c = \frac{\alpha . 2E}{\pi \sigma^2}$$

with $\alpha = 4.2\ Jm^{-2}$ a critical flaw size, c, of 9 - 19 nm can be calculated for such fibres. From high-resolution dark-field images (Fig. 38) it is estimated that about 7% of the crystallites present have stacking sizes in this range. Misorientation of such crystallites by 5° would thus theoretically lead to fibre failure without needing the condition

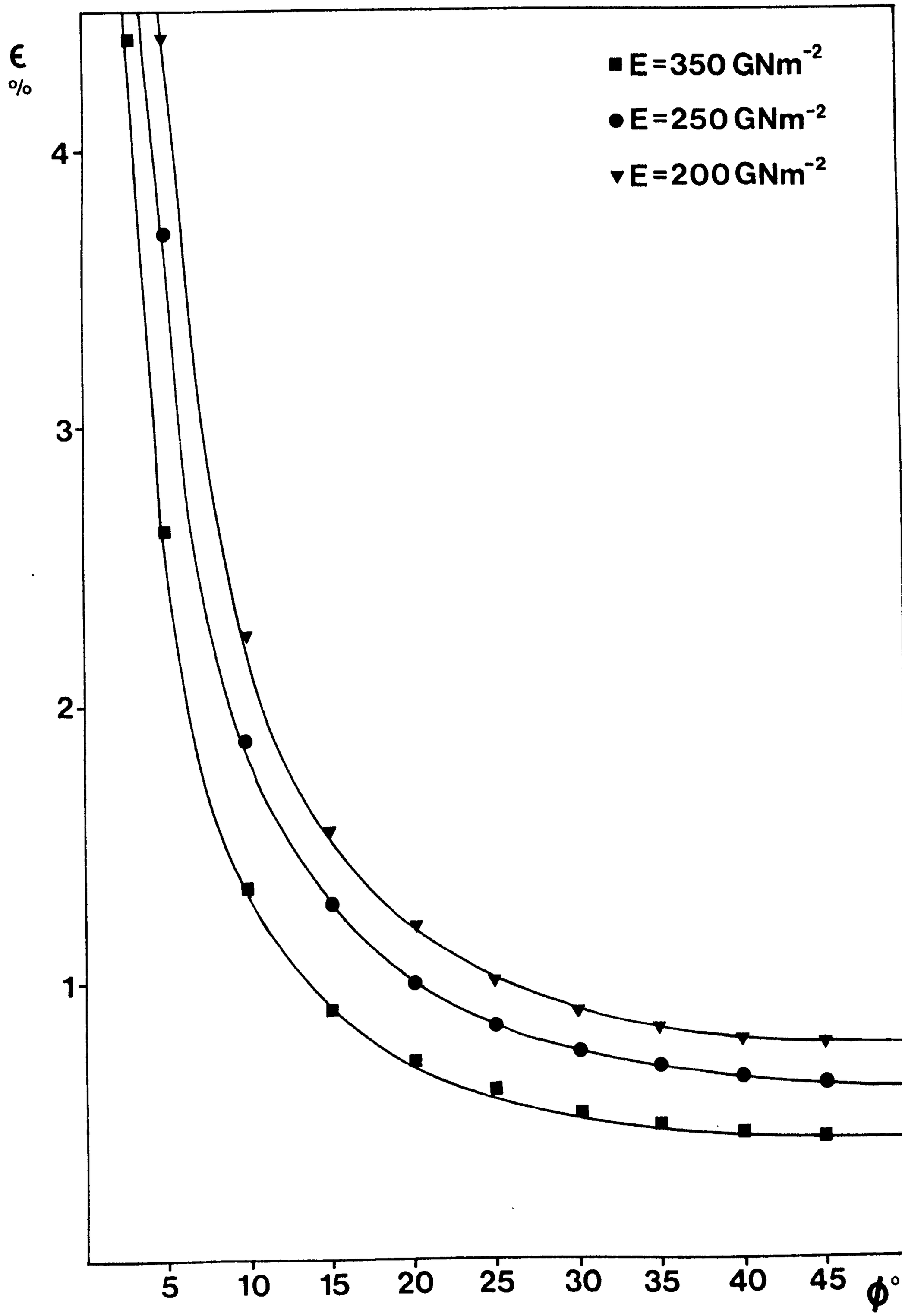

Fig. 49. Fibre strain-to-failure (ϵ) as a function of crystallite misorientation (ϕ) for various fibres.

of structural continuity. Since the core structure of these fibres does not contain crystallites larger than about 18 nm in width this may be taken as the maximum possible critical flaw size for fibre failure initiated from the failure of a single crystallite, and it can be shown that a fibre strength of about 7 GNm^{-2} would be expected.

Where failure involves crack propagation through a structural continuity, however, lower intrinsic strengths would be exhibited by the fibres. For example, if a crystallite misoriented at $\geq 10^{o}$ to the fibre axis fails, then a fibre strain-to-failure of $\leq 1.3\%$ would be expected. This means an ultimate tensile strength of $\leq 4.5\ GNm^{-2}$, and a critical flaw size of ≥ 46 nm, the latter value being considerably greater than the maximum observed crystallite size in the core. The average size of crystallites oriented at angles greater than 10^{o} to the fibre axis ranges from 4.2 nm to 1.5 nm, and fibre failure will only occur if, once formed, a crack will propagate either through these small misoriented crystallites, or through the larger more axially-aligned crystallites.

To summarize, it would seem that if failure of a single crystallite, of size greater than the critical flaw size as calculated from the Griffith equation, only leads to fibre failure, then ultimate tensile strengths of greater than 7 GNm^{-2} and strains-to-failure of at least 2% could be realized. If, however, fibre failure involves the propagation of a crack, initiated in a small relatively highly-misoriented crystallite, through a structural continuity, then strengths around 5 GNm^{-2} and strains-to-failure of about 1.3% would be expected. These values are lower than those predicted by Diefendorf and Tokarsky[53] (see 1.3.1.*C*).

b. Non-oxidatively-stabilized fibres heat treated to 2500°C

Figure 46 shows that the preferred orientation for PAN fibres stabilized in nitrogen and heat treated to 2500°C (specimen

Q2500) is about 36^{o}, as compared with 18^{o} for a typical core structure from type I material conventionally processed. Since the modulus is about 200 GNm^{-2} (Table 8) a crystallite misoriented by 20^{o} could be expected to cause fibre failure at a strain of 1.2%, yet from Table 8 it can be seen that the observed strain-to-failure of 0.35% is significantly less than this value. Indeed, from Fig. 49 it is evident that the theoretical minimum strain-to-failure of a fibre of modulus 200 GNm^{-2} is about 0.7%. Clearly, it is possible that the structure of conventionally-stabilized carbon fibres heat treated to $2500^{o}C$ is such that the relief of shear stress in misoriented crystallites is, as suggested by Reynolds and Sharp[113], through basal-plane rupture, rather than shear failure between basal planes, while in these special non-oxidatively-stabilized type I fibres a different fracture mechanism is occurring. This could be due to the significant proportion of graphitic crystallites misoriented at large angles to the fibre axis, which are still of a mean size only slightly less than the axially-aligned crystallites. An additional possibility is that Equation (3) does not hold in this special case. A value of c_{44} of 4.0 GNm^{-2} (the dislocation-free value) has been used in the calculation of the theoretical ε vs. ϕ curves of Fig. 49, yet it is certain that the basal planes in specimen Q2500 are far from perfect, and, coupled with the turbostratic nature of layer-plane stacking, much lower values of c_{44} might be expected. Seldin and Nezbeda[125], for example, have measured the shear modulus, c_{44}, for compression-annealed pyrolytic graphite (CAPG) and single-crystal graphite (SCG) both before and after neutron irradiation. They found values in the ranges 0.18 - 0.35 GNm^{-2} for unirradiated CAPG, and 0.4 - 1.7 GNm^{-2} for unirradiated SCG. After neutron irradiation at $50^{o}C$, however, the ranges were found to increase to 2.2 - 4.0 GNm^{-2}, and 1.6 - 3.9 GNm^{-2} respectively. It is therefore reasonable to suggest that the

Table 8 Properties of Carbon Fibres made from Special Courtelle

CARBON FIBRES FROM 3 DENIER COURTELLE					
HEAT-TREATMENT TEMPERATURE °C	OXIDATION TIME (h) / PROPERTY	5	10	20	40
1000	Diameter (μm)	11.5	10.8	10.4	9.8
	UTS (GNm^{-2})	1.30	2.08	2.38	2.42
	E (GNm^{-2})	179	202	216	254
	ε (%)	0.73 (A1000)	1.03	1.10	0.95 (D1000)
1500	Diameter (μm)	10.6	10.8	9.9	9.6
	UTS (GNm^{-2})	1.36	1.62	1.76	1.60
	E (GNm^{-2})	232	240	279	267
	ε (%)	0.59 (A1500)	0.67	0.63	0.60 (D1500)
2500	Diameter (μm)	9.7	10.1	9.4	8.9
	UTS (GNm^{-2})	1.70	1.83	1.89	1.62
	E (GNm^{-2})	344	388	398	352
	ε (%)	0.49 (A2500)	0.47 (B2500)	0.47 (C2500)	0.46 (D2500)
2500	UTS (GNm^{-2})	0.73)			
	E (GNm^{-2})	210) unoxidized-stabilized for 16h in N_2			
	ε (%)	0.35) (Q2500)			

Note: UTS = Ultimate Tensile Strength
E = Young's Modulus
ε = Fibre strain-to-failure

Identification numbers for specimens examined in the electron microscope are shown in brackets.

Table 8 (continued) Properties of Carbon Fibres made from Special Courtelle

CARBON FIBRES FROM 1½ DENIER SPECIAL COURTELLE				
HEAT-TREATMENT TEMPERATURE °C	OXIDATION TIME (h) / PROPERTY	1	3	9
1000	Diameter (μm)	9.2	8.5	7.9
	UTS (GNm^{-2})	2.33	2.63	2.76
	E (GNm^{-2})	187	212	232
	ε (%)	1.25 (E1000)	1.24	1.19 (F1000)
1500	Diameter (μm)	8.0	8.7	8.2
	UTS (GNm^{-2})	3.15	2.79	1.97
	E (GNm^{-2})	248	252	268
	ε (%)	1.27 (E1500)	1.11	0.74 (F1500)
2500	Diameter (μm)	8.2	8.3	7.9
	UTS (GNm^{-2})	2.25	2.09	2.35
	E (GNm^{-2})	345	391	386
	ε (%)	0.65 (E2500)	0.53	0.61 (F2500)

Note: UTS = Ultimate Tensile Strength
E = Young's Modulus
ε = Fibre strain-to-failure

Identification numbers for specimens examined in the electron microscope are shown in brackets.

theoretical curves predicted in Fig. 49 may not hold for highly-imperfect specimens.

C. Fibres heat treated to 1000°C and 1500°C

The direct electron-microscopical techniques used in this study have indicated that, with the exception of a very thin outer skin of insignificant proportions at a macroscopic level, the structure of type A and type II fibres is homogeneous. It is evident that a significant proportion of relatively large crystallites are oriented at large angles to the axis of these fibres (see Figs. 46 and 47), and this means that intrinsic initiation of cracks might be expected in crystallites misoriented by angles of, say, 10^{o}. If the crack propagates through the structure and failure occurs, ultimate tensile strengths of about 4 - 5 GNm^{-2} would be expected. Thorne[54], however, using loop-testing techniques has reported a much higher intrinsic strain-to-failure of 5%, and an ultimate tensile strength in excess of 10 GNm^{-2}, so it would appear that crack propagation at lower strains does not occur in fibres having no gross flaws. Consequently, the most likely reason for failure at low strains (less than 2%) is the presence of surface irregularities and flaws. Although enhanced crystallization around these regions certainly will not have occurred at low heat-treatment temperatures, flaw sizes in the range 100 - 200 nm would be expected to lead to fibre failure at, according to the Griffith equation, only 0.8 - 1.0%, in fibres heat treated in the range 1000 - 1500°C.

Recently Johnson at RAE[126] has carbon coated type A and type II fibres from a hydrocarbon gas, and predicted intrinsic strains-to-failure of more than 2%. A commercially-available type A fibre, which had received no surface treatment had a mean strain-to-failure of 1.42% (maximum 1.67%), yet showed an increase to 1.70% (maximum

2.03%) after carbon coating. Since such coating techniques have no effect on crystallite orientation, such an improvement is presumably obtained through simple healing of surface flaws, and it is possible that the Reynolds-Sharp theory breaks down for these lower-temperature, highly-disordered fibres.

5.3.2 Observed fibre strengths

A. Fibres heat treated to 2500°C

From Table 8 it is apparent that conventionally-produced type I fibres containing internal defects have mean strains-to-failure in the range 0.46 - 0.65%. Reference to Fig. 49 indicates that failures at such strains are initiated by failure of crystallites misoriented at angles of greater than 20° to the fibre axis. Using the Griffith failure criterion, a critical flaw size in the range 0.15 - 0.35 μm would be expected for such fibres.

a. Surface flaws

Plate XI shows a large surface flaw in specimen B2500, where at s a skin crystallite of width 60 nm is oriented at 45° to the fibre axis. Athough the break at x is almost certainly due to the disruptive effect of sectioning, it is likely that in its undisturbed state such a crystallite may have been oriented at $\phi = 20°$, resulting in a theoretical fibre strain-to-failure of about 0.7%. For fibre failure to occur, a critical flaw size of 150 nm would be needed, and although the observed crystallite size is less than this, once initiated a crack would be expected to propagate through the adjacent core structure.

The surface flaw depicted at lattice resolution in Plate XII and at lower magnification in Plate XIII is represented by a 40 nm step on the fibre surface comprising crystallites misoriented at 45° to the fibre axis. Such crystallite misorientation would be expected

to lead to fibre failure at a strain of less than 0.5%, and although the 'inverted hairpin' flaw is smaller than the critical flaw size of 350 nm structural continuity is maintained through x and y (Plate XII), while the misoriented region extends to a depth of 25 nm into the section at z (Plate XIII).

Plates XIV and XV show a bulge in the skin structure of specimen D2500, resulting in a surface crystallite of width 17 nm being oriented at $\phi = 15^{o}$. A theoretical strain-to-failure for this system of about 0.9% can be predicted from Fig. 49, with a corresponding critical flaw size of 95 nm. If structural continuity, not evident from the image obtained from this particular section is maintained at a different point in the fibre skin-core interface, a crack initiated in such a crystallite could be expected to propagate through smaller, equally-misoriented adjacent core crystallites.

A type of bulging skin structure, comprising a knee-shaped crystallite, is depicted at lattice resolution in Plate XVI. Twisting through an angle of 40^{o} along a-a, this region can be thought of as two crystallites each misoriented at 20^{o} to the fibre axis. In this case a theoretical strain-to-failure of 0.7% and critical flaw size of about 150 nm would be expected.

A similar knee-shaped crystallite is shown in Plate XVII, where misorientation of a crystallite of width 17 nm at $\phi = 20^{o}$ is evident. Again the calculated fibre strain-to-failure of about 0.7% is slightly higher than typically observed in these specimens (Table 8), while a critical flaw size of 150 nm would mean that structural continuity between skin and core is necessary in order for fibre failure to occur.

b. Internal flaws

A striking internal flaw in specimen J2500 is shown in Plates XXIII and XXIV. A hole, h, is bordered by large, highly-

graphitic crystallites misoriented by angles up to at least 40^{o}. Failure of such crystallites would theoretically occur at a fibre strain of less than 0.5%, with a corresponding critical flaw size of more than 300 nm. This latter figure is less than the size of the void (0.5 μm x 0.5 μm), so fibre failure would be expected from this flaw alone, without need for the usually necessary conditions of structural continuity.

Similar internal voids can be seen at a, b, and h in Plate XXI. Since this is a (002) dark-field image, recorded using a small objective aperture, crystallites misoriented at $\phi \gtrsim 20^{o}$ will be absent from the image since they are diffracting outside the aperture. It is clear that the hole h is bordered by crystallites which are larger than normally found in the core, and it is reasonable to assume that some of them are highly misoriented. The size of the hole, which has a length of 0.45 μm, would be expected, from the Griffith failure criterion, to initiate failure at a fibre strain of 0.41%. Similarly, holes a and b, being smaller, would be expected to lead to fibre failure in the strain range 0.55 - 0.62%.

c. Résumé

In type I fibres the observed ultimate tensile strengths and strains-to-failure can be explained in terms of the presence of internal voids. Severe misorientation of catalytically-graphitized crystallites bordering such holes are predicted to lead to fibre failure at strains of 0.5 - 0.6%, remarkably close to the observed values (0.46 - 0.65%). In many cases structural continuity with the surrounding core material in order for fibre failure to occur is unnecessary, since the critical flaw size, as calculated from the Griffith equation, is less than the size of the void.

In the absence of internal voids of such a gross type, failure

is initiated at surface flaws, and strains-to-failure in the range 0.5 - 1.0% are predicted. Invariably the crystallite which fails initially is smaller than the critical flaw size, and for fibre failure to occur, propagation of a crack through adjacent skin or core material would be necessary. The predictions of critical flaw size for such failure are in the range 80 - 300 nm, remarkably similar to the typical dimensions of the skin region. In this case, since there is a finite probability of finding a large misoriented crystallite in the skin structure of fibres heat treated to 2500^{o}C, this region must be considered as a flaw.

Moreton and Watt[50,51,52] have shown that internal voids, and the more gross surface flaws can be removed by dope filtration and clean room spinning. This produces a concomitant increase in strength and thus strain-to-failure in comparison with conventionally-produced fibres. The present study supports this view, since fibre failure at internal voids is proposed in the range 0.5 - 0.6%, while at surface flaws between 0.5 and 1.0%. These values are significantly lower than the predicted intrinsic strain-to-failure of 2.0% (see 5.3.1.*B.a*) which will only be realized in the absence of both internal voids, and the characteristic skin structure of type I fibres.

B. Fibres heat treated to 1000^{o} and 1500^{o}C

Table 8 shows that the observed mechanical properties of type A and type II fibres are disappointingly low in comparison with the estimates of intrinsic strength made by Johnson[126] and Thorne[54]. Since these fibres have been shown to be macrostructurally homogeneous in the present study, these differences must lie in the presence of internal voids and surface irregularities, not associated with enhanced crystallization effects. Using the Griffith relationship, typical observed strains-to-failure in type A and type II fibres

will be obtained if the critical flaw size is in the range 100 - 150 nm. This is of the order of the width of surface irregularities observed in SEM pictures of whole fibres, and it is proposed that these may initiate failure. Where gross surface and internal flaws can be removed, however, failure of single crystallites, and subsequent crack propagation through the continuous, but highly-disordered structure of these materials, may form the fracture mechanism at strains of greater than 2%.

5.4 FUTURE WORK

Since the use of carbon fibres is entirely in composite structures it is important to successfully understand the nature of fibre-resin bonding. In order to perform such a characterization direct observation of the fibre surface at layer-plane level is necessary, and this can only be achieved through high-resolution electron microscopy.

It is known that commercial surface treatments are capable of significantly increasing the interlaminar shear strength (ILSS) of a composite fabricated using type I fibres, while for fibres heat treated at a lower temperature (1000 - 1500^{o}C) the improvement is much less substantial. This effect can be adequately explained by reference to the observations made in this thesis. The surface of type I fibres is of a mainly basal-plane nature, with few edge sites, while type A and type II fibres surfaces are characterized by the presence of a considerable number of terminating graphite sheets, and hence many carbon atoms having an unsatisfied valence suited to matrix bonding. A useful extension of this work would involve the examination of surface-treated type I fibres, in order to explain the increases in ILSS.

Similarly, carbon coating of type A fibres has recently been shown to produce a 20% increase in fibre strength, and this

remains unexplained in terms of a model which uses failure of misoriented crystallites as a fracture-initiation mechanism. Although not necessarily associated with large crystallite misorientations, the gross surface flaws present in these low-temperature fibres, which apparently initiate fibre failure, are 'healed' by carbon coating. It would be very interesting to examine the microstructure of such a carbon coat, and the nature of its bonding to the fibre surface.

The presence of internal and surface flaws, theoretically leading to failure of type I fibres at strains close to those observed practically, has been verified in the present study. Practical assessment of the nature of such flaws would now seem to be possible. If a fracture-causing flaw in a type I fibre of known mechanical properties can be located, and serial thin sections obtained from it, a three-dimensional characterization of crystallite size and orientation in the vicinity of the flaw can be made. In this case, the applicability of theoretical fibre-failure models to a real system can be directly assessed.

APPENDICES

A1. ELECTRON MICROSCOPY

A1.1 Introduction

Since Heidenreich et al.[75] published the first phase-contrast lattice-fringe images of graphitized carbons in 1968, high-resolution transmission electron microscopy has found increasing use in the analysis of the microcrystalline structure of carbons. However, accurate and meaningful interpretation of the recorded two-dimensional image, which contains no phase information, in terms of a three-dimensional structural model is only possible if the fundamental information-transfer processes of the microscope are understood.

A plane wave of electrons incident on a specimen is modulated such that it can be regarded as split into real and imaginary parts which can be treated separately. For a *perfect lens system*, free of aberrations, the real part of the modulation due to a weak object is transferred into the image intensity, whereas the imaginary part is cancelled by the conjugate complex terms which appear. For weak objects the real part of the object modulation is identical to the amplitude component of the object, while the imaginary part is identical to the phase component; the two components being transferred independently. If, however, lens aberrations are present simultaneous transfer of both components occurs. Individual micrographs become ambiguous since there is no means of deciding which part of the image intensity is related to the amplitude compoment, and which part to the phase component of the object.

For example, in an idealized situation, a phase shift of $\pi/2$ due to aberration removes the amplitude component of the object from the image, while the phase part is transferred with maximum contrast. Since the wave aberration is, however, a function of spatial frequency it is impossible to obtain maximum phase *or* amplitude contrast

simultaneously for *all* frequencies. Typically, only a small band of the spatial frequency spectrum is recorded with positive contrast in the electron micrograph, other parts having either negative or no contrast. In order to successfully interpret images it is important to understand the dependence of contrast on spatial frequency, lens aberrations, and defocus phase-shifts.

A1.2 Theoretical background - the weak-phase approximation

If the three-dimensional potential field in an object is given by:

$$\phi'(x,y,z)$$

then an incident coherent plane wave of unit amplitude, when passing through this field, is modified by a transmission function of the type:

$$\exp\ [i\ \sigma\ \phi\ (x,y)]$$

where $\phi\ (x,y) = \int_{-\infty}^{\infty} \phi'\ (x,y,z)\, dz$ is the projection in the beam direction of the three-dimensional potential distribution in the object, and $\sigma = \pi / \lambda E$, E being the accelerating potential and λ the electron wavelength.

The wave function immediately behing the object is therefore:

$$\psi\ (x_o,y_o) = 1.\ \exp\ [i\ \sigma\ \phi\ (x_o,y_o)] \quad \ldots\ldots\ldots\ldots\ldots(4)$$

Using the weak phase approximation, that the effect of the potential field in the object on the incident electron beam is small, then (4) can be rewritten:

$$\psi\ (x_o,y_o) = 1 + i\ \sigma\ \phi\ (x_o,y_o)$$

The wave function at the diffraction plane [$\Psi\ (h,k)$] is the Fourier transform of $\psi\ (x_o,y_o)$ multiplied by a phase factor, P, given by:

$$P = \exp\ [i\ \chi(\beta)]$$

where β is the diffraction angle, hence:

$$\Psi\ (h,k) = F\ [\psi\ (x_o,y_o)]\ \ .P \quad \ldots\ldots\ldots\ldots\ldots(5)$$

Again, using the weak phase approximation (5) can be rewritten:

$$\Psi\ (h,k) = \delta\ (0,0) - \sigma\ \Phi\ (h,k).\sin\chi + i\,\sigma\,\Phi(h,k).\cos\chi \quad \ldots(6)$$

where $\delta\ (0,0)$ is a delta function representing the unscattered electron beam at the origin and

$$\Phi\ (h,k) = F\ [\phi\ (x_o,y_o)].$$

At the image plane the Fourier transform of $\Psi\ (h,k)$ gives the wave function $\psi\ (x_i,y_i)$. The intensity $\left|\psi(x_i,y_i)\right|^2$ is recorded in the electron microscope, and since

$$\sigma\ \Phi\ (h,k) \ll \delta\ (0,0)$$

it is clear that the imaginary part of (6) contributes to the image squared terms in very small quantities. Thus the Fourier transform of the intensity distribution in the image is proportional to:

$$\delta\ (0,0) - 2\ \sigma\ \Phi\ (h,k).\sin\chi\ .$$

$-2.\sin\chi$ is known as the phase-contrast transfer function (CTF), and it is a term which modulates the amplitudes of $\Phi\ (h,k)$ and the sign of its phases.

A1.3 Wave aberration due to defocus and spherical oberration

Scherzer[127] has shown that for image points near the optical axis:

$$\chi\ (\beta) = \frac{-2\,\pi}{\lambda}\left[\frac{C_s\,\beta^4}{4} - \frac{\Delta f\,\beta^2}{2}\right] \quad \ldots\ldots\ldots\ldots\ldots(7)$$

while Heidenreich[128] has derived an alternative form of this equation given a spherical aberration term four times larger.

The wave aberration, χ, describes the phase shift of the diffracted rays caused by the non-spherical wave surface. Figure 50 shows the real and imaginary parts of P calculated for the Gaussian image plane ($\Delta f = 0$) for the EM300 electron microscope ($C_s = 1.6$ mm). For an ideal lens ($C_s = 0$) it would follow that $P = 1$ in the Gaussian image plane, meaning that the real part of this function

would be characterized by a straight line parallel to the β axis in Fig. 50, while the imaginary part would be zero for all scattering angles in the Gaussian plane. By using such a lens, correct imaging would be possible for amplitude objects. Zernike[129] has shown that an ideal lens for phase objects corresponds to $P = \pm i$ for all $\beta \neq 0$ (i.e. real part is zero, and imaginary part is ± 1). From Fig. 50 it is clear that for a small range of β, P corresponds quite well to an ideal lens for amplitude objects.

If a small defocussing term (Δf>0) is included in (7) the β ranges of the same sign can be enlarged and shifted. Figure 51 shows the real and imaginary parts of the function P for an objective lens with a coefficient of spherical aberration 1.6 mm, at a defocus of Δf = +75.0 nm.

Using (7) it is evident that the CTF for a weak phase object is given by:

$$\text{CTF} = -2.\sin \chi$$

$$= -2.\sin\left[\frac{-2\pi}{\lambda}\left\{\frac{C_s \beta^4}{4} - \frac{\Delta f \beta^2}{2}\right\}\right] \quad \ldots\ldots\ldots\ldots\ldots\ldots(8)$$

Since it is thought[130] that during an elastic collision there is an additional phase shift of $\pi/2$ between scattered and unscattered waves, then aberration phase shifts of $n\pi - \pi/2$ will lead to maxima in (8).

Hence maximum phase contrast will be observed when:

$$n\pi - \frac{\pi}{2} = (2n-1)\frac{\pi}{2} = \frac{-2\pi}{\lambda}\left[\frac{C_s \beta^4}{4} - \frac{\Delta f \beta^2}{2}\right] \quad \ldots\ldots\ldots\ldots(9)$$

since $\beta = \lambda/r$, then

$$(2n-1)\frac{\lambda}{2} = -\frac{C_s}{2}\left(\frac{\lambda}{r}\right)^4 + \Delta f\left(\frac{\lambda}{r}\right)^2$$

which is a quadratic equation in $(\lambda/r)^2$ with solutions

$$\left(\frac{\lambda}{r}\right)^2 = \frac{\Delta f}{C_s} \pm \left[\frac{\Delta f}{C_s}^2 - \frac{(2n-1)\lambda}{C_s}\right]^{\frac{1}{2}}$$

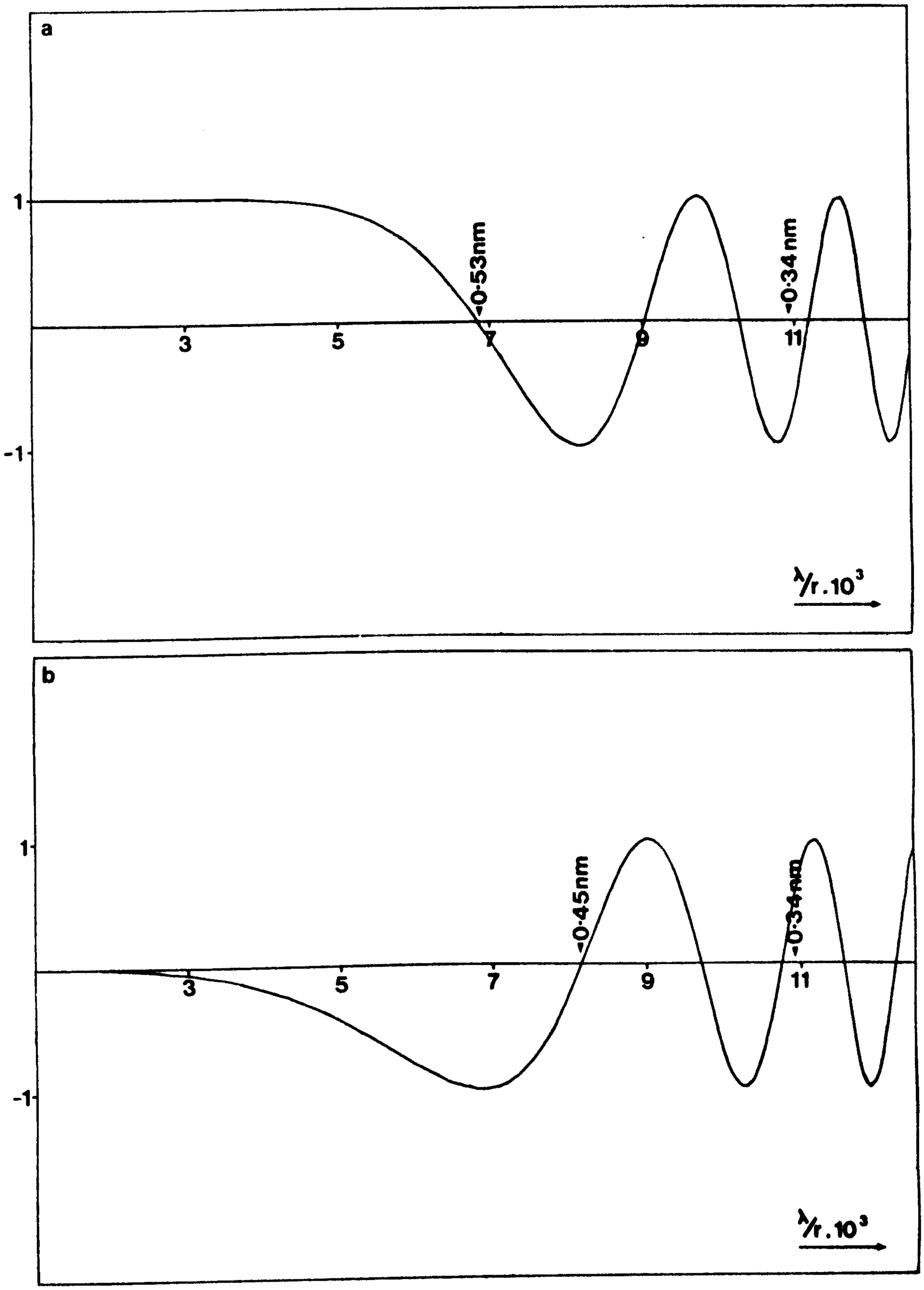

Fig. 50. Real part (a) and imaginary part (b) of P at $\Delta f = 0$, as a function of λ/r.

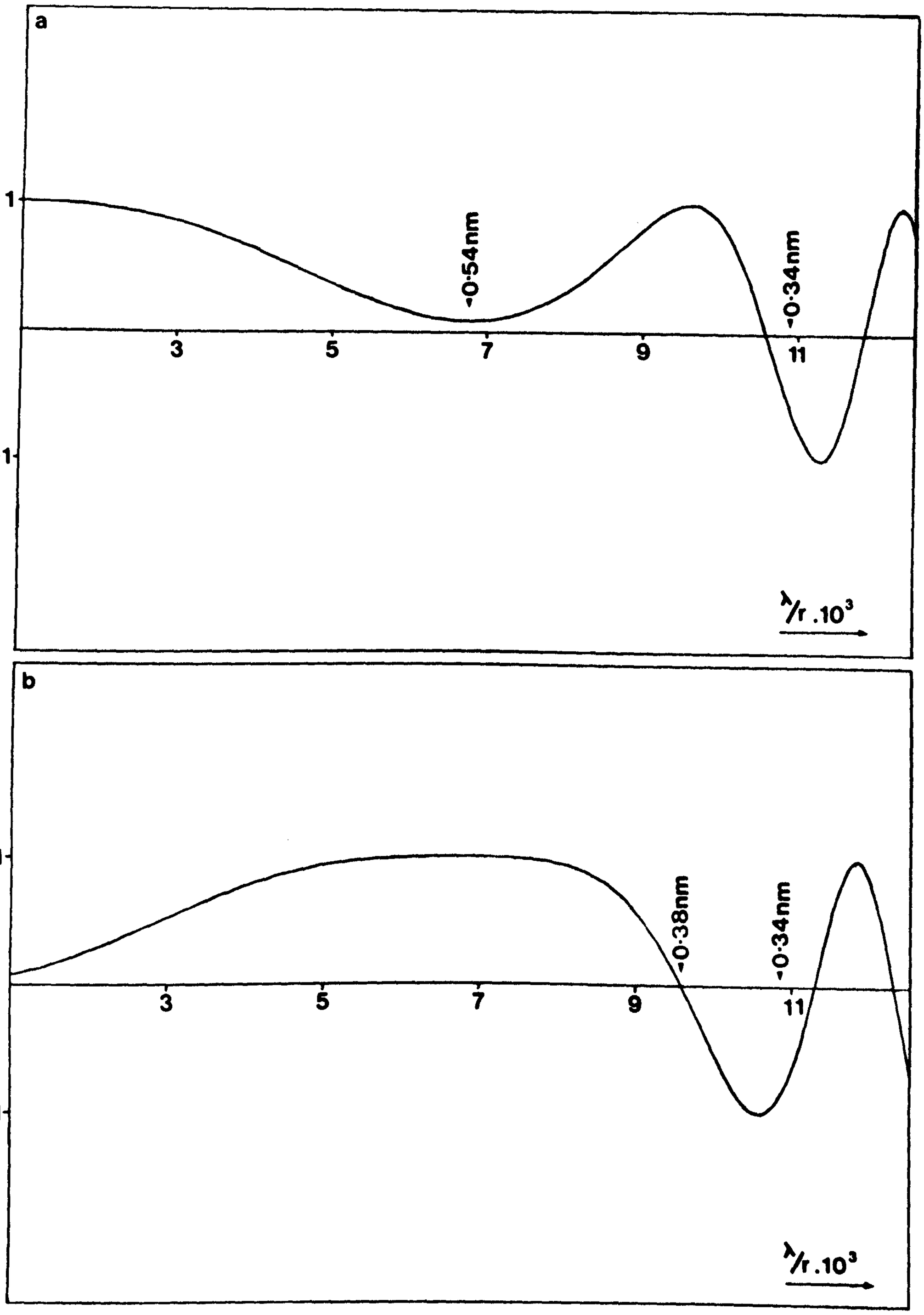

Fig. 51. Real part (a) and imaginary part (b) of P at $\Delta f = +75.0$ nm, as a function of λ/r.

and hence

$$r = \lambda \left[\frac{\Delta f}{C_s} \pm \left\{ \frac{\Delta f^2}{C_s^2} - \frac{(2n-1)\lambda}{C_s} \right\}^{\frac{1}{2}} \right]^{-\frac{1}{2}} \quad \ldots\ldots\ldots\ldots\ldots\ldots (10)$$

Equation (10) describes the dependence of phase contrast on spherical aberration (C_s) and defocussing (Δf), and a graph accoring to this equation is called a phase-contrast transfer characteristic. From such a graph one can read which reciprocal spatial frequencies $\wedge_i$ are transferred with maximum phase contrast at any given defocus Δf.

A1.4 Experimental evidence

A1.4.1 'Amorphous carbon films'

Thon[131] has shown experimentally that, for an objective lens with C_s = 4.0 mm, there is good agreement between the transfer intervals ($|CTF| < 0.6$) in the optical transforms of high-resolution images of thin 'amorphous' carbon films, recorded at various defocii, when compared with the theoretical predictions embodied in (10). Recently, however, attempts to repeat these experiments in a Philips EM300, with a coefficient of spherical aberration of 1.6 mm, have proved unsuccessful[132].

A1.4.2 Lattice-fringe images

From (9) it follows that:

$$\Delta f = \frac{(2n-1)\lambda}{2\beta^2} + C_s \frac{\beta^2}{2}$$

and hence $\Delta f_{n+1} - \Delta f_n = \frac{r^2}{\lambda}$

so a reversal of contrast for a 0.34 nm spacing at 100 kV (λ = 0.0037 nm) would be expected after a defocus of 31.0 nm.

Johnson and Crawford[121], however, have shown experimentally that the contrast reversals observed in lattice-fringe images of carbon fibres occur ever 50 ± 10 nm, and therefore do not fit the Scherzer 'integrated-ray' aberration term.

Crawford and Marsh[133] have confirmed the anomalous contrast reversal defocus period of 50 - 60 nm, while showing that the number of fringes observed in small crystallites is also a function of defocus. For their microscope (C_s = 1.4 mm) an optimum defocus (Δf_c) of about 80 nm gave images with the smallest apparent crystallite size, while micrographs recorded at:

$$+ \Delta f_c + n.\Delta f_r \text{ nm}, \qquad \ldots\ldots\ldots\ldots\ldots (11)$$

where n = ±1, +2, and +3, and Δf_r is the observed periodicity of contrast reversal, showed an increasing number of fringes. It was proposed that this value of Δf_c corresponds closely to that described by Höppe[134] at which the real part of the complex image amplitude derived from the scattering by a single sheet of carbon atoms has a point extension (Fig. 51(b)). As contrast is conventional at this defocus a high charge would be represented by a high density in the *printed* micrograph. The optimum defocus was shown to give an accurate mapping of object charge density in the recorded image, whereas another defocus position giving good contrast (n = +1 in (11)) was believed to show the graphite sheets in averaged conditions, and reversed contrast.

Recently, Crawford and Marsh[135] have confirmed that a faithful image of a disordered molecular structure, obeying the weak-phase approximation, can only be obtained at one level of underfocus - that corresponding to the Scherzer plateau[127]. At this underfocus position all detail within a wide, low spatial frequency interval is transferred without contrast bias or frequency gaps. Choice of an underfocus which gives a 'clean' image favouring the 0.34 - 0.36 nm spacing was found to give micrographs containing a frequency gap at about 0.6 nm. A system-induced improvement of order produced by such information filtering was shown to lead to erroneous measurement of crystallite size (both length and width) in comparison with the 'valid'

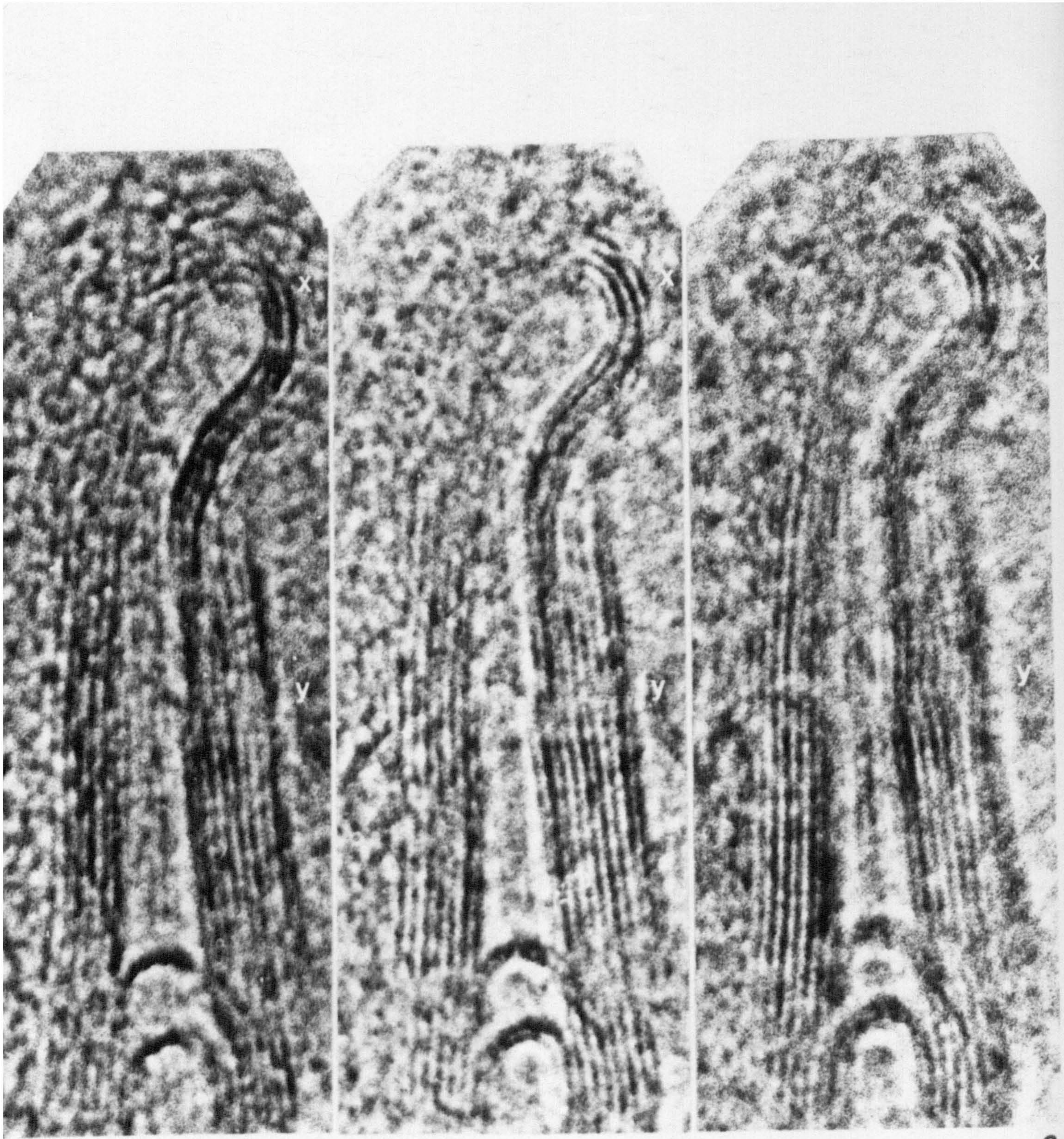

Plate LIX. The effect of objective-lens defocus on multibeam lattice-fringe images. (a) +162.5 nm, (b) +212.5 nm, and (c) +262.5 nm.

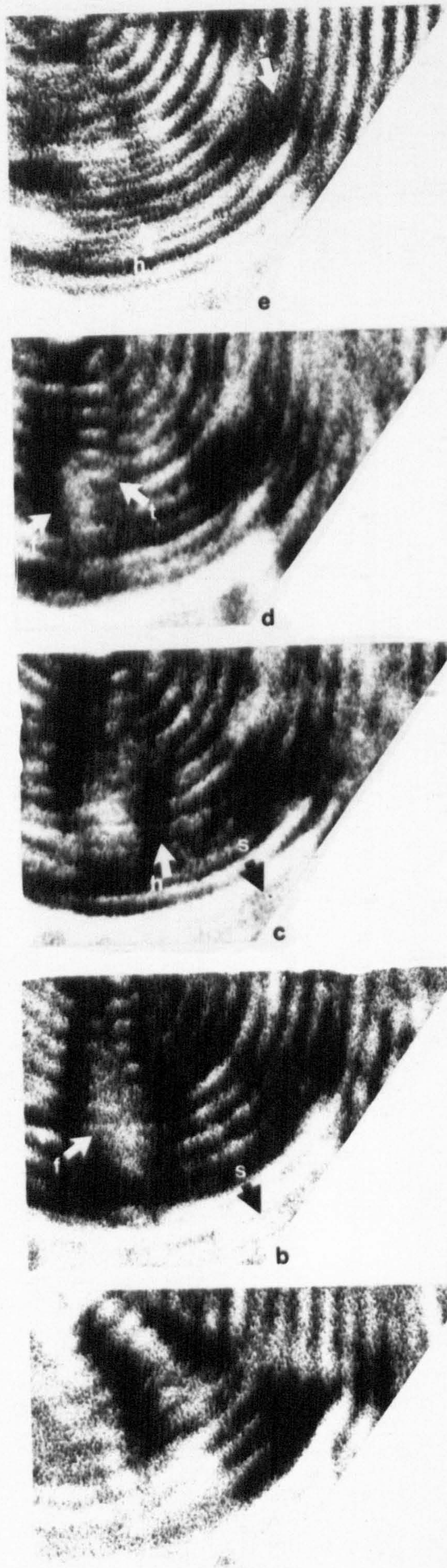

Plate LX. The effect of objective-lens defocus on three-beam ($00\bar{2}$-000-$00\bar{2}$) lattice-fringe images. (a) Gaussian focus, (b) +162.5 nm, (c) +212.5 nm, (d) +262.5 nm, (e) +350.0 nm.

image recorded at Δf_c.

In the Philips EM300 Electron microscope used in the present study, a spherical aberration coefficient of 1.6 mm means that the Scherzer plateau, observed at an objective lens defocus of + 75.0 nm, cuts off at a value corresponding to a spatial frequency r = 0.38 nm, Fig. 51(b). Lattices of spacing less than 0.38 nm are then imaged with much lower, and reversed contrast at this defocus. To overcome this problem the objective lens of the microscope was weakened to a value corresponding to either +162.5 ± 12.5 nm or +212.5 ± 12.5 nm, where high contrast for the graphite spacing is obtained. Although introducing frequency gaps at higher r values, it was considered that such action was justified since the highly-crystalline structure of fibres heat treated to 2500^{o}C contains mainly spacings in the range 0.3354 - 0.344 nm. In the case of fibres heat treated at lower temperatures, every effort was made to ensure that a transfer interval as wide as possible was utilized.

The present study has confirmed that the periodicity of contrast reversal for the 0.34 nm graphite lattice is 50 ± 10 nm. Plate LIX shows a defocus series recorded under multibeam conditions, with the (000) reflection axial. At +162.5 nm three fringes are observed at x, at +212.5 nm four fringes, and at +262.5 nm six fringes. The area y which at +162.5 nm shows considerable distortion and apparent layer-plane discontinuity, has, at +262.5 nm, been averaged, so that the lattice fringes, although bent, are continuous.

Plate LX shows a focal series recorded under three-beam conditions (002 - 000 - 00$\bar{2}$), with the (000) axial. At +162.5 nm an increase in contrast, together with the appearance of satellite fringes, s, in comparison with the Gaussian image is noticeable. At +212.5 nm, half-spacings, h, arising from the modulation of the 0.34 nm

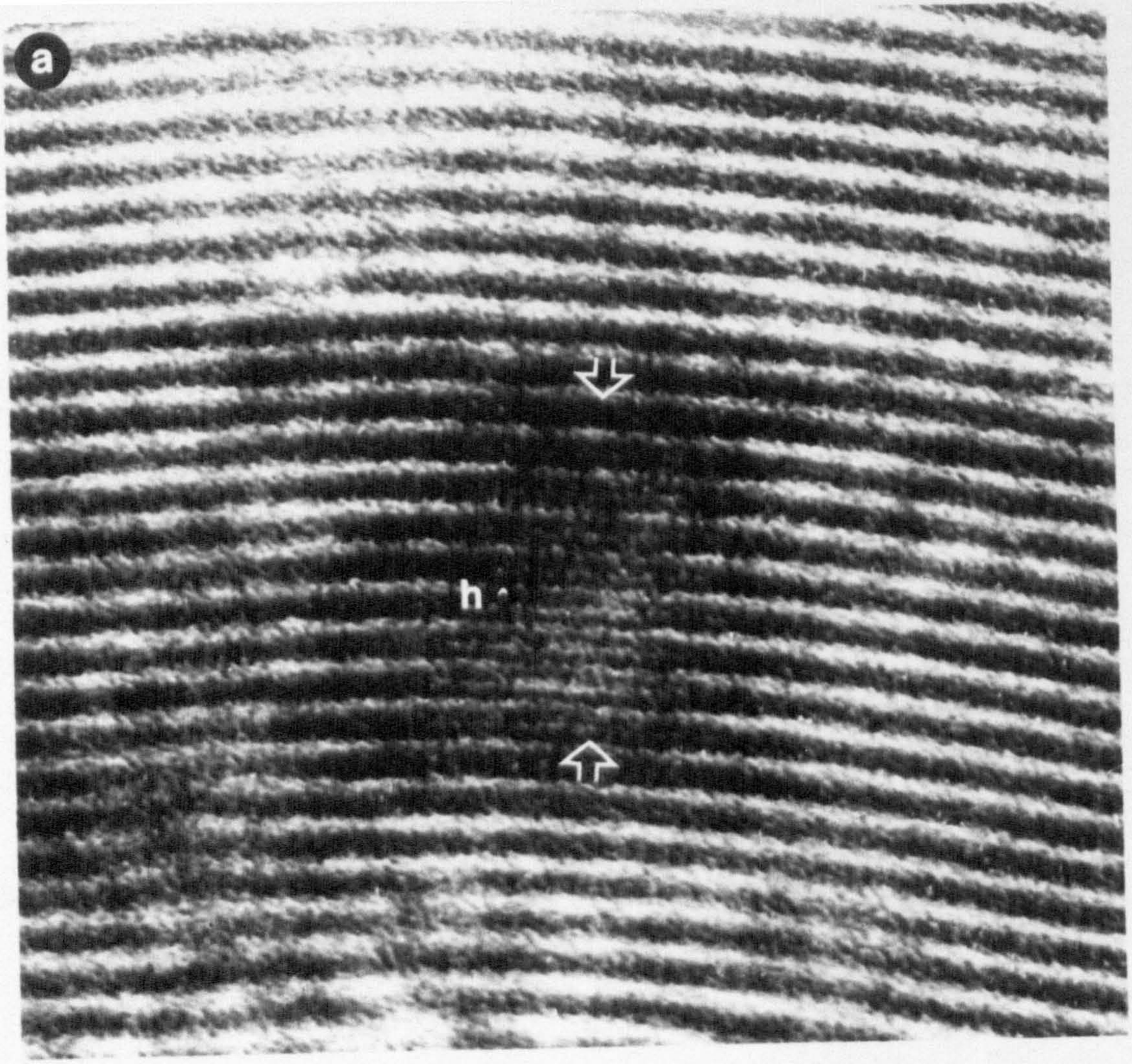

Plate LXI. The effect of mode of image formation on 0.34 nm lattice-fringe images. (a) Multibeam, (000) axial, (b) two-beam, (000)-(002) symmetric.

spacing, are evident, and these become increasingly resolved at +350 nm. Note also that the positions of the terminating fringes, t, and heavily-faulted regions, f, are a function of defocus. Jefferson et al.[136] have recently shown theoretically that the appearance of 0.17 nm fringes can arise from dynamical scattering effects, while in the present study these are usually observed in regions where the layer planes are smoothly curved. Explanations for the appearance of these lattice-fringe modulations still remain unsatisfactory, particularly in terms of the weak-phase approximation.

Cockayne et al.[137] have shown both experimentally and theoretically that there is not a one-to-one correlation between a two-beam lattice-fringe image and the lattice planes in the object. In experiments on crystallized germanium the number and positions of terminating fringes observed in high-resolution images were found to change with diffraction geometry, the algebraic total of 'edge dislocations', however, always remaining the same. In the present study the effect of type of imaging mode on the crystallite size distribution has been critically examined (Chap. 4). It was found that similar results were obtained from all bright-field images irrespective of defocus (within a certain range), and diffraction geometry. However, when lattice-fringe images from individual crystallites were examined closely, remarkable differences were observed between the two-beam (002 - 000) symmetric and multibeam images. Plate LXI shows such images from a highly-crystalline region. In the multibeam image, recorded at an objective-lens defocus of +212.5 nm, a large area of 0.17 nm 'half-fringes' can be seen at h, while in the two-beam symmetric lattice-fringe image of exactly the same area, recorded at an objective-lens defocus giving no edge fringes, several terminating fringes, t, can be clearly seen. Obviously, the unambiguous interpretation of these in terms of edge dislocations is

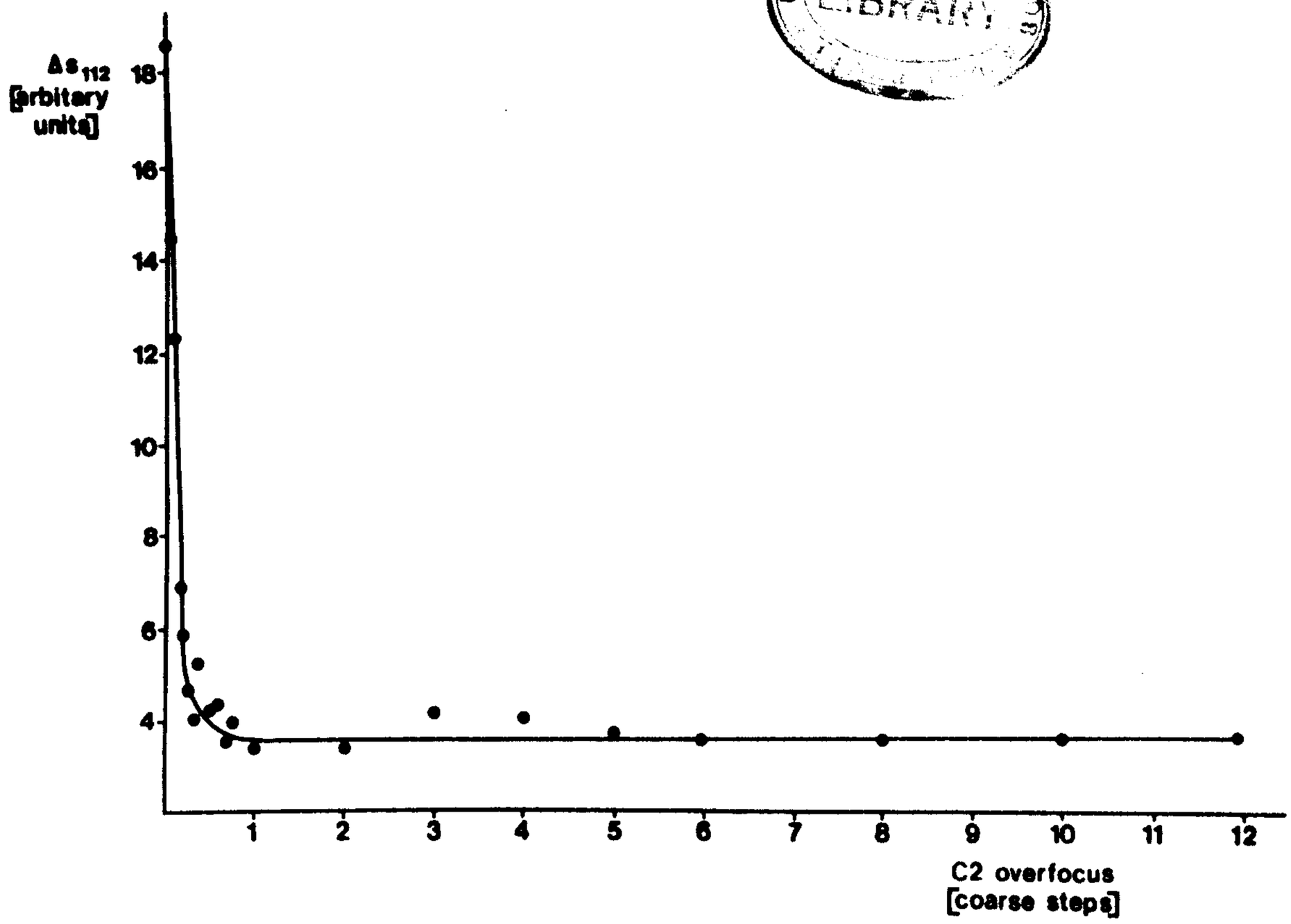

Fig. 52. Half-height width of (112) reflection (arbitraryunits) as a function of condenser two setting.

not possible. Similarly, in the two-beam image there are areas, such as at x, from which lattice fringes are absent. This is either a slightly-distorted area, seen in 'averaged' conditions in the multi-beam image, or, more likely, such effects are due to orientation out of the diffraction condition due to beam tilting.

A1.5 Electron microscope settings for electron diffraction

If representative quantitative data is to be obtained from electron-diffraction patterns the effects of instrumental broadening should be minimized. In the electron microscope this is facilitated by overfoc using the condenser two lens (C2). In order to assess the amount of overfocus required to minimize any broadening effects, electron-diffraction patterns of a longitudinal carbon-fibre section were recorded at various C2 settings, and the width at half height of the

(112) reflection measured in each case. Figure 52 shows a graph of half-height width of the (112) reflection (arbitrary units) as a function of C2 setting. It is clear that at a C2 setting of only one coarse step over-focus, instrumental broadening has been minimized. To allow for a certain margin of error the electron-diffraction patterns analyzed in the present study were all recorded at a C2 setting two coarse steps over-focus.

A2. CALIBRATION OF PHOTOGRAPHIC EMULSIONS

In order to derive quantitative measurements of half-height width and integral breath from electron-diffraction patterns it is necessary to understand the response of the photographic emulsion used, to the intensity and exposure time of the electron beam. Ilford EM4 and Special Lantern Contrasty (SLC) plates and SP332 cut film were exposed to different beam intensities, developed, fixed and washed, and the optical densities measured using a Joyce-Leobl double-beam recording microdensitometer fitted with a 3D wedge. Figure 53 shows the dependence of optical density, measured as mm of throw on the 3D wedge, on beam intensity (percentage full-scale deflection on the exposure meter of the microscope) for the three different recording mediums. It is evident that SP332 film is remarkably uniform in response, yet much slower than either EM4 or SLC plates, which, however, exhibit saturation at about 260 mm and 225 mm respectively. The response of all three emulsions up to one quarter of the saturation density (D_{sat}) is linear, and a correction for densities, D', above $0.25D_{sat}$ can be made logarithmically using Eqn. 12 as described by Valentine[117].

$$D \propto \ell n \left[\frac{D_{sat}}{D_{sat} - D'} \right] \qquad \ldots\ldots\ldots\ldots\ldots\ldots (12)$$

D

mm of throw on 3D wedge

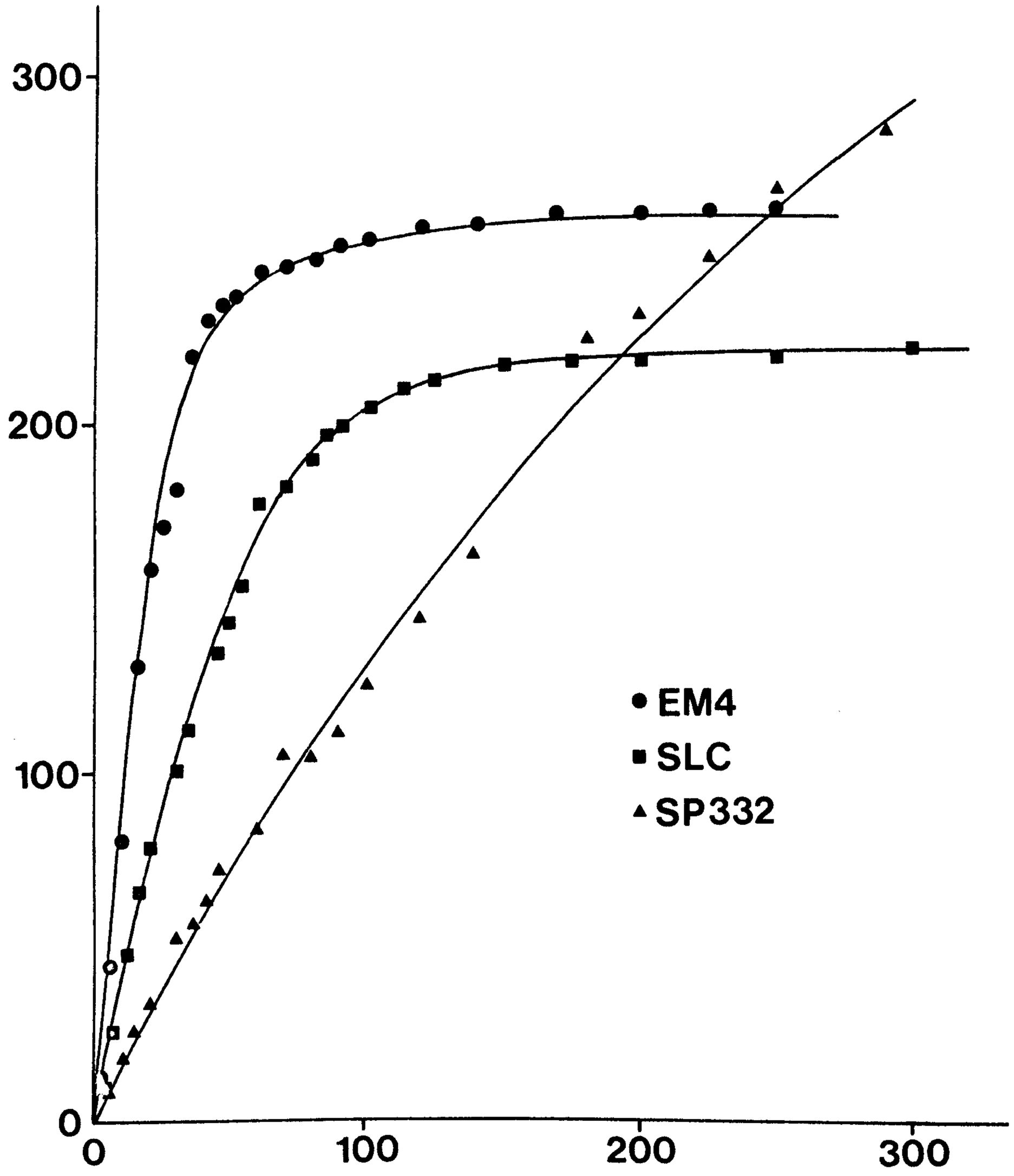

Fig. 53. The dependence of optical density (D), on beam intensity (B) for various recording mediums.

Since the response of the emulsion is linear up to a value of $0.25D_{sat}$ a considerable effort was made to ensure that electron-diffraction patterns were recorded in this range, thus obviating the need for the logarithmic correction. However, this was not practicable in certain cases, where, for example, several orders of the (OOℓ) reflections were of interest, and at such times a correction was applied. Since, in an example of this type, a considerable range of densities exists on a single plate, the whole range of wedges (0.25D - 3D) was used, and the saturation densities, D_{sat}, pertaining to SLC plates for each wedge are shown in Table 9.

Table 9

WEDGE	3D	2.5D	1.75D	1.5D	0.5D	0.25D
D_{sat}	225	265	310	587	627	1138

A3. COMPUTER PROGRAMS

A3.1 Iterative procedure for resolution of overlapping asymmetric electron-diffraction peaks, with graphical facilities

```
'LIBRARY' (ED,SUBGROUPLDSA)
'BEGIN' 'COMMENT' RESOLUTION OF OVERLAPPING ELECTRON-DIFFRACTION PEAKS.
      ASYMETRIC ELECTRON DIFFRACTION PEAKS IN CAT = 1
    WITH THE 000 TREATED AS THE FIRST PEAK.  DATA
    READ IN AS 3 PARAMETERS FOR FIRST PEAK, THEN  F,AMP,WIDTH,WIDTH,F
    FOR SUCCESSIVE PEAKS, THEN POSITIONS THEN BASELINE.
    CAT = 2 FOR SYMMETRIC E.D. PEAKS READ IN AS  3*PEAKS+BASELINE+
      POSITIONS. ASYMETRIC ELECTRON DIFFRACTION PEAKS IN
      CAT=4,  BUT NO 000. PARAMETERS ARE READ IN AS: F,A,W,W,F,
       FOR SUCCESSIVE PEAKS,THEN POSITIONS THEN BASELINE.
        Z VALUES ARE READ IN AS MM., AND THEN CHANGED TO S
      BY DIVISION BY THE FACTOR: CAMERA LENGTH IN CMS.(L)*
      DENSITOMETER MAGNIFICATION(DENSMAG)*
      WAVELENGTH OF ELECTRONS USED IN ANGSTROM UNITS(LAMBDA).
     "EMULSION BROADENING" IS LOGARITHMICALLY CORRECTED, DSAT
      BEING READ IN.
      THE ABILITY TO PLOT YOBS,BASELINE,AND YCALC
      WITHOUT ANY ITERATION IS INCLUDED IN REQUESTS 7,8,9;
'PROCEDURE' AP(NP,N,B,BL,REQUEST,CAT);
'VALUE' NP, B, BL, REQUEST;
'INTEGER' NP, B, BL, REQUEST, CAT, N;
'BEGIN'
      'IF' REQUEST=1 'THEN' N:=5*B-2;
      'IF' REQUEST=2 'THEN' N:=6*B-2;
      'IF' REQUEST=3 'THEN' N:=NP;
      'IF' REQUEST=4 'THEN' N:=3*B;
      'IF' REQUEST=5 'THEN' N:=3*B+BL;
      'IF' REQUEST=6 'THEN' N:=NP;
      'IF' REQUEST=7 'OR' REQUEST=8 'OR' REQUEST=9 'THEN' N:=0;
      'IF' REQUEST=10 'THEN' N:=5*B;
      'IF' REQUEST=11 'THEN' N:=6*B;
      'IF' REQUEST=12 'THEN' N:=NP;
      'IF' REQUEST<4 'OR' REQUEST=7 'THEN' CAT:=1;
      'IF' REQUEST=4 'OR' REQUEST=5 'OR' REQUEST=6
      'OR' REQUEST=8 'THEN' CAT:=2;
      'IF' REQUEST>8 'THEN' CAT:=4;
'END' OF AP;
'PROCEDURE' ACC(NP,B,BL,CAT,X,E);
'VALUE' NP,B,BL,CAT;
'INTEGER' NP,B,BL,CAT;
'ARRAY' X, E;
'BEGIN' 'INTEGER' I;
'FOR' I:=1 'STEP' 1 'UNTIL' NP 'DO'
'IF' X[I]'GE'1 'THEN' E[I]:=0.01 'ELSE' E[I]:=0.001;
'END' OF ACC;
'PROCEDURE' FUNCT(B,NP,M,CAT,BL,X,Z,YOBS,Q,
      SUMQ,BASE,YCALC,F,DV,ST);
'VALUE' B,NP,M,CAT,BL,DV,ST;
'REAL'    F;
'INTEGER' B,NP,M,CAT,BL,DV,ST;
'ARRAY' X,Z,YOBS,Q,SUMQ,BASE,YCALC;
'BEGIN' 'INTEGER' KK, T, I;
      F:=0;
AHIC:       'FOR' KK:=1 'STEP' 1 'UNTIL' M 'DO'
      'BEGIN'
            SUMQ[KK]:=0;
            'FOR' T:=1 'STEP' 1 'UNTIL' B 'DO'
            'BEGIN'
            'IF' CAT=1 'THEN'
            'BEGIN' 'IF' T=1 'THEN'
            Q[T]:=(X[1]*(X[2]*EXP(-LN(2)*((2*(Z[KK]-X[5*B-1])/X[3]
```

```
        )↑2)))) + ((1-X[1])*(X[2]/(1+((2*(Z[KK]-X[5*B-1
        ])/X[3])↑2))))
      'ELSE'  'IF' Z[KK] 'LE' X[5*B+T-2] 'THEN'
      Q[T]:=(X[5*T-6]*(X[5*T-5]* EXP(-LN(2) *
                  ((2*(Z[KK]-X[5*B+T-2])/X[5*T-4])↑2))))+
                  ((1-X[5*T-6])*(X[5*T-5]/(1+
                  ((2*(Z[KK]-X[5*B+T-2])/X[5*T-4])↑2))))
'ELSE' Q[T]:=(X[5*T-2]*(X[5*T-5]*EXP(-LN(2)*((2*(Z[KK]-
              X[5*B+T-2])/X[
      5*T-3])↑2))))+((1-X[5*T-2])*(X[5*T-5]
                  /(1+((2*(Z[KK]-X[5*B+T-2])/X[5*T-3])↑2))));
            SUMQ[KK]:=SUMQ[KK]+Q[T];
        'END';
        'IF' CAT=2 'THEN'
        'BEGIN' Q[T]:=(X[3*T-2]*(X[3*T-1]* EXP(-LN(2) *
                  ((2*(Z[KK]-X[3*B+BL+T])/X[3*T])↑2))))+
                  ((1-X[3*T-2])*(X[3*T-1]/(1+
                  ((2*(Z[KK]-X[3*B+BL+T])/X[3*T])↑2))));
            SUMQ[KK]:=SUMQ[KK]+Q[T];
        'END';
'IF' CAT=4 'THEN'
'BEGIN' 'IF' Z[KK] 'LE' X[5*B+T] 'THEN'
Q[T]:=(X[5*T-4]*(X[5*T-3]*EXP(-LN(2)*
((2*(Z[KK]-X[5*B+T])/X[5*T-2])↑2))))+
((1-X[5*T-4])*(X[5*T-3]/(1+
((2*(Z[KK]-X[5*B+T])/X[5*T-2])↑2))))
'ELSE'  Q[T]:=(X[5*T]*(X[5*T-3]*EXP(-LN(2)*((2*(Z[KK]-
X[5*B+T])/X[5*T-1])↑2))))+((1-X[5*T])*(X[5*T-3]
/(1+((2*(Z[KK]-X[5*B+T])/X[5*T-1])↑2))));
SUMQ[KK]:=SUMQ[KK]+Q[T];
'END';
      'END';
'IF' CAT=1 'THEN'
'BEGIN'
      'IF' BL=2 'THEN'
BASE[KK]:=X[NP-1] + ((Z[KK]-Z[1]) *
          (X[NP]-X[NP-1])/(Z[M]-Z[1]));
      'IF' BL=4 'THEN'
BASE[KK]:=          X[NP-3] + (X[NP-2] * Z[KK]) + (X[NP-1]
          * Z[KK]↑2) + (X[NP] * Z[KK]↑3);
'END';
'IF' CAT=2 'THEN'
'BEGIN'
      'IF' BL=2 'THEN'
 BASE[KK]:=X[3*B+1] + ((Z[KK]-Z[1]) * (X[3*B+2]
             -X[3*B+1])/(Z[M]-Z[1]));
      'IF' BL=4 'THEN'
 BASE[KK]:= X[3*B+1] + (X[3*B+2] * Z[KK]) +
             (X[3*B+3]* Z[KK]↑2) + (X[3*B+4]
            * Z[KK]↑3);
 'END';
 'IF' CAT=4 'THEN'
 'BEGIN'
 'IF' BL=2 'THEN'
 BASE[KK]:=X[NP-1]+((Z[KK]-Z[1])*
 (X[NP]-X[NP-1])/(Z[M]-Z[1]));
 'IF' BL=4 'THEN'
 BASE[KK]:=X[NP-3]+(X[NP-2]*Z[KK])+(X[NP-1]
 *Z[KK]↑2)+(X[NP]*Z[KK]↑3);
 'END';
```

```
      YCALC[KK]:= SUMQ[KK] + BASE[KK];
      F:=F + ((YCALC[KK] - YOBS[KK])↑2);
            'END';
AH1D:       'END' OF FUNCT;
'PROCEDURE' POWELL 64 (FUNCT, X,E,N,F,ESCALE,IPRINT,ICON,MAXIT, DV,
      B,NP,M,CAT,BL,Z,YOBS,Q,SUMQ,BASE,YCALC,SD,LIMIT,ST);
      'REAL' ESCALE, F,  SD, LIMIT;
      'INTEGER' B,NP,N,IPRINT,ICON,MAXIT,DV,M,CAT,BL,ST;
      'ARRAY' X,E,Z,YOBS,Q,SUMQ,BASE,YCALC;
      'PROCEDURE' FUNCT;
            'BEGIN' 'ARRAY' W[1:N*(N+3)];
            'REAL' DDMAG,FKEEP,SCER,SUM,FP,DMAX,DACC,DDMAX,
                  D,DL,FPREV,FA,DA,DD,FB,DB,FHOLD,DMAG,
                  FC,DC,A,BB,DI,FI,AAA;
            'INTEGER' JJ,JJJ,K,NFCC,IND,INN,I,J,ITERC,ISGRAD,
                  ITONE,IXP,IDIRN,ILINE,IS,JIL;
            'SWITCH' SW1:=L10,L11,L12,L13,L14,L96;
DDMAG:=0.1*ESCALE;
SCER:=0.05/ESCALE;
JJ:=N*N+N;
JJJ:=JJ+N;
K:=N+1;
NFCC:=IND:=INN:=ITERC:=1;
'FOR' I:=1 'STEP' 1 'UNTIL' N 'DO'
'BEGIN' 'FOR' J:=1 'STEP' 1 'UNTIL' N 'DO'
      'BEGIN' 'IF' I=J 'THEN'
            'BEGIN' W[K]:=ABS(E[I]);
                  W[I]:=ESCALE
            'END' 'ELSE'
            W[K]:=0;
            K:=K+1
      'END';
'END';
ISGRAD:=2;
FUNCT(B,NP,M,CAT,BL,X,Z,YOBS,Q,SUMQ,
BASE,YCALC,F,DV,ST);
AH8:      'IF' LIMIT>F 'THEN' 'GOTO' AH12;
FKEEP:=2*ABS(F);
L5:ITONE:=1;
FP:=F;
      SUM:=0;
IXP:=JJ;
'FOR' I:=1 'STEP' 1 'UNTIL' N 'DO'
'BEGIN' IXP:=IXP+1;
      W[IXP]:=X[I]
'END';
IDIRN:=N+1;
ILINE:=1;
L7:DMAX:=W[ILINE];
DACC:=DMAX * SCER;
DMAG:='IF' DDMAG<0.1*DMAX 'THEN' DDMAG 'ELSE' 0.1*DMAX;
DMAG:='IF' DMAG>20*DACC 'THEN' DMAG 'ELSE' 20*DACC;
DDMAX:=10*DMAG;
'IF' ITONE=3 'THEN' 'GOTO' L71;
DL:=0;
D:=DMAG;
FPREV:=F;
IS:=5;
FA:=F;
DA:=DL;
```

```
      L8:DD:=D-DL;
      DL:=D;
      L58:K:=IDIRN;
      'FOR' I:= 1 'STEP' 1 'UNTIL' N 'DO'
      'BEGIN' X[I]:=X[I]+DD*W[K];
            K:=K+1
      'END';
      FUNCT(B,NP,M,CAT,BL,X,Z,YOBS,Q,SUMQ,
      BASE,YCALC,F,DV,ST);
AH9:        'IF' LIMIT>F 'THEN' 'GOTO' AH12;
      NFCC:=NFCC+1;
      'GOTO' SW1[IS];
      L14:'IF' F<FA 'THEN' 'GOTO' L15;
      'IF' F>FA 'THEN' 'GOTO' L24;
      'IF' ABS(D)>DMAX 'THEN' 'GOTO' L18;
      D:=2*D;
      'GOTO' L8;
      L18 :WRITE TEXT('('''('CC')'MAXIMUM%CHANGE%DOES%NOT
                  %ALTER%FUNCTION '('CC')''')');
AH10:       ST:=1;
             'GOTO' L50;
      L15:FB:=F;
      DB:=D;
      'GOTO' L21;
      L24:FB:=FA;
      DB:=DA;
      FA:=F;
      DA:=D;
      L21:'IF' ISGRAD=1 'THEN' 'GOTO' L83;
      L23:D:=2*DB-DA;
      IS:=1;
      'GOTO' L8;
      L83:D:=0.5*(DA+DB-(FA-FB)/(DA-DB));
      IS:=4;
      'IF' (DA-D)*(D-DB)'GE'0'THEN' 'GOTO' L8;
      L25:IS:=1;
      'IF' ABS(D-DB)'LE'DDMAX 'THEN' 'GOTO' L8;
      L26:
D:=DB+('IF' DB'GE'DA 'THEN' ABS(DDMAX) 'ELSE' (-ABS(DDMAX)));
      IS:=1;
      DDMAX:=2*DDMAX;
AH11:       'IF' DDMAG>2&+76 'THEN'
      'BEGIN'
            ST:=2;
       'GOTO' L50;
      'END';
      DDMAG:=2*DDMAG;
      'IF' DDMAX'LE'DMAX 'THEN' 'GOTO' L8;
      DDMAX:=DMAX;
      'GOTO' L8;
      L13:'IF' F'GE'FA 'THEN' 'GOTO' L23;
      L28:FC:=FB;
      DC:=DB;
      L29:FB:=F;
      DB:=D;
      'GOTO' L30;
      L12:'IF' F'LE'FB 'THEN' 'GOTO' L28;
      FA:=F;
      DA:=D;
      'GOTO'L30;
```

```
L11:'IF' F'GE'FB 'THEN' 'GOTO' L10;
FA:=FB;
DA:=DB;
'GOTO'L29;
L71:DL:=D:=1;
DDMAX:=5;
FA:=FP;
DA:=-1;
FB:=FHOLD;
DB:=0;
L10:FC:=F;
DC:=D;
L30:A:=(DB-DC)*(FA-FC);
BB:=(DC-DA)*(FB-FC);
'IF' (A+BB)*(DA-DC)>0'THEN' 'GOTO' L34;
FA:=FB;
DA:=DB;
FB:=FC;
DB:=DC;
'GOTO' L26;
L34:D:=0.5*(A*(DB+DC)+BB*(DA+DC))/(A+BB);
DI:=DB;
FI:=FB;
'IF' FB'LE' FC 'THEN' 'GOTO' L44;
DI:=DC;
FI:=FC;
L44:'IF' ITONE#3'THEN' 'GOTO' L86;
ITONE:=2;
'GOTO' L45;
L86:'IF' ABS(D-DI)'LE'DACC 'THEN' 'GOTO' L41;
'IF' ABS(D-DI)'LE' 0.03*ABS(D)'THEN' 'GOTO'L41;
L45:'IF'(DA-DC)*(DC-D)<0'THEN' 'GOTO' L47;
FA:=FB;
DA:=DB;
FB:=FC;
DB:=DC;
'GOTO'L25;
L47:IS:=2;
'IF'(DB-D)*(D-DC)'GE'0'THEN' 'GOTO' L8;
IS:=3;
'GOTO' L8;
L41:F:=FI;
D:=DI-DL;
DD:=SQRT((DC-DB)*(DC-DA)*(DA-DB)/(A+BB));
    'FOR' I:=1'STEP' 1 'UNTIL' N 'DO'
    'BEGIN' X[I]:=X[I]+D*W[IDIRN];
            W[IDIRN]:=DD*W[IDIRN];
            IDIRN:=IDIRN+1
    'END';
    W[ILINE]:=W[ILINE]/DD;
    ILINE:=ILINE+1;
    'IF' IPRINT#1'THEN' 'GOTO' L51;
    L50:WRITE TEXT ('('('CC')'ITERATION')');
    WRITE(DV,FORMAT('('-NDDD')'),ITERC);
    WRITE(DV,FORMAT('('SSS-NDDD')'),NFCC);
    WRITE(DV,FORMAT('('SS-NDDDDD.DDDDDD')'), F);
AH13:       SD:=SQRT(F/M);
    WRITE(DV,FORMAT('('SSS-NDD.DDDDDDC')'),SD);
    'FOR' I:=1 'STEP' 1 'UNTIL' N 'DO'
    WRITE(DV, FORMAT('('SS-NDDD.DDDDDDD')'), X[I]);
```

```
AH14:       'IF' ST=1 'OR' ST=2 'OR' ST=3 'THEN' 'GOTO' L20;
      'IF' IPRINT=2'THEN' 'GOTO' L53;
      L51:'IF' ITONE=2'THEN' 'GOTO' L38;
      'IF' FPREV <F+SUM 'THEN' 'GOTO' L94;
      SUM:=FPREV-F;
      JIL:=ILINE;
      L94:'IF' IDIRN'LE'JJ'THEN' 'GOTO' L7;
      'IF' IND =2'THEN' 'GOTO' L72;
      L92:FHOLD:=F;
      IS:=6;
      IXP:=JJ;
      'FOR' I:=1'STEP' 1 'UNTIL' N 'DO'
      'BEGIN' IXP:=IXP+1;
            W[IXP]:=X[I]-W[IXP]
      'END';
      DD:=1;
      'GOTO' L58;
      L96:'IF' IND =2'THEN' 'GOTO' L87;
      'IF' FP<F'THEN' 'GOTO' L37;
      'IF' FP-F=0 'THEN' 'GOTO' L20 'ELSE' D:=2*(FP+F-2*FHOLD)/(FP-F)↑2;
      'IF' D*(FP-FHOLD -SUM)↑2'GE'SUM 'THEN' 'GOTO' L37;
      L87:J:=JIL*N+1;
      'IF' J>JJ'THEN' 'GOTO' L61;
      'FOR' I:=J'STEP' 1 'UNTIL' JJ 'DO'
      'BEGIN' K:=I-N;W[K]:=W[I]
      'END';
      'FOR' I:=JIL 'STEP' 1 'UNTIL' N 'DO' W[I-1]:=W[I];
      L61:IDIRN:=K:=IDIRN-N;
      ITONE:=3;
      IXP:=JJ;
      AAA:=0;
      'FOR' I:=1 'STEP' 1 'UNTIL' N 'DO'
      'BEGIN' IXP:=IXP+1;
            W[K]:=W[IXP];
            'IF' AAA <ABS(W[K]/E[I])'THEN' AAA :=ABS(W[K]/E[I]);
            K:=K+1
      'END';
      DDMAG:=1;
      W[N]:=ESCALE/AAA;
      ILINE:=N;
      'GOTO'L7;
      L37:IXP:=JJ;
      AAA:=0;
      F:=FHOLD;
      'FOR' I:=1'STEP' 1 'UNTIL' N 'DO'
       'BEGIN' IXP:=IXP+1;
            X[I]:=X[I]-W[IXP];
            'IF' AAA *ABS(E[I])<ABS(W[IXP])
            'THEN' AAA :=ABS(W[IXP]/E[I])
      'END';
      'GOTO' L72;
      L38: AAA:=AAA*(1+DI);
      'IF' IND=2 'THEN' 'GOTO' L106;
      L72:'IF' IPRINT'GE'2'THEN' 'GOTO' L50;
      L53:'IF' IND=2'THEN' 'GOTO' L88;
      'IF' AAA>0.1 'THEN' 'GOTO' L76;
      'IF' ICON=1'THEN'  'GOTO' L20;
      IND:=2;
      'IF' INN=2 'THEN' 'GOTO' L101;
      INN:=2;
```

```
K:=JJJ;
'FOR' I:=1 'STEP' 1 'UNTIL' N 'DO'
'BEGIN' K:=K+1;
        W[K]:=X[I];
        X[I]:=X[I]+10*E[I]
'END';
WRITE TEXT('('''('P')'%%FURTHER%CHANGE%OF%
        PARAMETERS%%FOR%%ICON2'('C')'')');
FKEEP:=F;
        FUNCT(B,NP,M,CAT,BL,X,Z,YOBS,Q,SUMQ,
        BASE,YCALC,F,DV,ST);
AH12:       'IF' LIMIT>F 'THEN'
        'BEGIN'         ST:=3;
                'GOTO' L50;
        'END';
        NFCC:=NFCC+1;
        DDMAG:=0;
        'GOTO' L108;
        L76:'IF' F<FP 'THEN' 'GOTO' L35;
        L78:WRITE TEXT('('''('CC')'ACCURACY%
                LIMITED%BY%ERRORS%IN%F'('CC')''
)');
        'GOTO' L20;
        L88:IND:=1;
        L35:DDMAG:=0.4*SQRT(FP-F);
        ISGRAD:=1;
        L108:ITERC:=ITERC+1;
        'IF' ITERC'LE'MAXIT 'THEN' 'GOTO' L5;
        WRITE (DV,FORMAT('('-NDDDD')'),MAXIT);
        WRITE TEXT('('ITERATIONS%COMPLETED'('CC')'')');
        'IF' F'LE'FKEEP 'THEN' 'GOTO' L20;
        F:=FKEEP;
        'FOR' I:=1'STEP' 1 'UNTIL' N 'DO'
        'BEGIN' JJJ:=JJJ+1;
                X[I]:=W[JJJ]
        'END';
        'GOTO' L20;
        L101:JIL:=1;
        FP:=FKEEP;
        'IF' F<FKEEP 'THEN' 'GOTO' L105
        'ELSE' 'IF' F=FKEEP 'THEN' 'GOTO'
L78;
        JIL:=2;
        FP:=F;
        F:=FKEEP;
        L105:IXP:=JJ;
        'FOR' I:=1'STEP' 1 'UNTIL' N 'DO'
        'BEGIN' IXP:=IXP+1;
                K:=IXP+N;
                'IF' JIL=2'THEN' 'GOTO' L115;
                W[IXP]:=W[K];
                'GOTO' L113;
                L115:W[IXP]:=X[I];
                X[I]:=W[K];
        L113:'END';
        JIL:=2;
        'GOTO'L92;
        L107:INN:=1;
        'GOTO'L35;
        L106:'IF' AAA>0.1 'THEN' 'GOTO' L107;
```

```
      L20:
'END' POWELL 64;
'PROCEDURE' RESULTS(NP,N,M,REQUEST,OP,X,Z,YOBS,SUMQ,
      BASE,YCALC,F,SD,DV);
'VALUE' NP,N,M,REQUEST,OP,DV;
'REAL' F,SD;
'INTEGER' NP,N,M,REQUEST,OP,DV;
'ARRAY' X,Z,YOBS,SUMQ,BASE,YCALC;
'BEGIN' 'INTEGER' I,KK, FORM1, FORM2, FORM3, FORM4, FORM5;
FORM1:=FORMAT('('SS-NDDSSSS')');
FORM2:=FORMAT('('S-NDDD.DDDDDDDDC')');
FORM3:=FORMAT('('S-NDDD.DDD')');
FORM4:=FORMAT('('S-NDDD.DDDC')');
FORM5:=FORMAT('('S-NDDDDD.DDDDDDC')');
'IF' OP=1 'THEN' 'GOTO' AH;
      WRITETEXT('('''('CCC')'%%ADJUSTED%PARAMETERS'('C')'')');
      'FOR' I:=1 'STEP' 1 'UNTIL' N 'DO'
      'BEGIN'  WRITE(DV, FORM1, I);
            WRITE(DV, FORM2, X[I]);
      'END';
      'IF' REQUEST=3 'OR' REQUEST=6 'THEN' 'GOTO' AH;
      WRITE TEXT('('''('C')'%%FIXED%%PARAMETERS'('C')'')');
      'FOR' I:=(N+1) 'STEP' 1 'UNTIL' NP 'DO'
      'BEGIN'      WRITE(DV, FORM1, I);
            WRITE(DV, FORM2, X[I]);
      'END';
AH:      WRITETEXT('('''('C')'%'('6S')'Z'('7S')'Y%OBS'('5S')'SUMQ
      '('6S')'BASE'('6S')'YCALC'('4S')'YCALC-YOBS'('C')'')');
      'FOR' KK:=1 'STEP' 1 'UNTIL' M 'DO'
      'BEGIN'      WRITE(DV, FORM3, Z[KK]);
            'IF' REQUEST=7 'THEN'
            'BEGIN'      WRITETEXT('('%'('11S')'%')');
                  'GOTO' H1;
            'END';
            WRITE(DV, FORM3, YOBS[KK]);
H1:         WRITE(DV, FORM3, SUMQ[KK]);
            WRITE(DV, FORM3, BASE[KK]);
            'IF' REQUEST=7 'THEN'
            'BEGIN'      WRITE(DV, FORM4, YCALC[KK]);
                  'GOTO' H2;
            'END';
            WRITE(DV, FORM3, YCALC[KK]);
            WRITE(DV, FORM4, (YCALC[KK]-YOBS[KK]));
H2:      'END';
      'IF' REQUEST=7 'THEN' 'GOTO' H3;
      SD:=SQRT(F/M);
      WRITETEXT('('''('C')'%%F'('8S')'%=%')');
      WRITE(DV, FORM5, F);
      WRITETEXT('('%%SD'('8S')'=%%%')');
      WRITE(DV, FORM2, SD);
H3:      'END' OF RESULTS;
'BEGIN' 'COMMENT' DATA INPUT;
'INTEGER' B,NP,N,M,F1,F2,F3,F4,F5,F6,F7,CYCLES,REQUEST,CAT,
            I,KK,VV,T,IPRINT,ICON,MAXIT,DV,BL,MM,OP,ST,SYMB;
      'REAL' ESCALE,PC,STEP,L,DENSMAG,LAMBDA,XFACTOR,DSAT,
          ZA,ZB,AA,BBB,CC,DD,EE,FF;
DV:=0;
WRITETEXT('('''('CC')'%%HINDELEH%%11%(
        RESOLUTION%OF%OVERLAPPING%PEAKS)
      '('CC')'%%SAMPLE%%%%%:%')');
```

```
COPYTEXT('('';')');
B:=READ;
BL:=READ;
NP:=READ;
M:=READ;
CYCLES:=READ;
F1:=FORMAT('('SSS-NDDDC')');
F2:=FORMAT('('SSS-NDDD.DDDDDDDC')');
F3:=FORMAT('('SSS-NDDD.DDDC')');
F4:=FORMAT('('SSS-NDDSS')');
F5:=FORMAT('('SSS-NDDD.DDD')');
F6:=FORMAT('('SDDC')');
F7:=FORMAT('('SSS-NDDD.DC')');
      'BEGIN' 'REAL' 'ARRAY' PARAMETER[1:NP], X[1:NP], E[1:NP],
            Q[1:NP], REQ[1:CYCLES], MAX[1:CYCLES];
            'REAL' LIMIT, F, SD, TOA, TPA, TBA,PCE;
            LIMIT:=F:=TOA:=TPA:=TBA:=PCE:=0;
      'FOR' VV:=1 'STEP' 1 'UNTIL' CYCLES 'DO'
      REQ[VV]:=READ;
      'FOR' VV:=1 'STEP' 1 'UNTIL' CYCLES 'DO'
      MAX[VV]:=READ;
      IPRINT:=READ;
      PC:=READ;
      L:=READ;
      DENSMAG:=READ;
      LAMBDA:=READ;
      XFACTOR:=READ;
      DSAT:=READ;
      STEP:=READ;
      ICON:=2;
      ESCALE:=100;
      WRITETEXT('('''('CC')'%%B'('10S')'=%')');
      WRITE(DV, F1, B);
      WRITETEXT('('%%BL'('9S')'=%')');
      WRITE(DV, F1, BL);
      WRITETEXT('('%%NP'('9S')'=%')');
      WRITE(DV, F1, NP);
      WRITETEXT('('%%M'('10S')'=%')');
      WRITE(DV, F1, M);
      WRITETEXT('('''('CC')'%%CYCLES%%%%=%')');
      WRITE(DV, F1, CYCLES);
      WRITETEXT( '('%%REQUEST%%%=%')');
      'FOR' VV:=1 'STEP' 1 'UNTIL' CYCLES 'DO'
      WRITE(DV, F4, REQ[VV]);
      WRITETEXT('('''('C')'%%MAXIT%%%%%=%')');
      'FOR' VV:=1 'STEP' 1 'UNTIL' CYCLES 'DO'
      WRITE(DV, F4, MAX[VV]);
      WRITETEXT('('''('C')'%%IPRINT'('5S')'=%')');
      WRITE(DV,F3, IPRINT);
      WRITETEXT('('%%PC'('9S')'=%')');
      WRITE(DV, F3, PC);
      WRITETEXT('('%%L'('10S')'=%')');
      WRITE(DV, F3, L);
      WRITETEXT('('%%DENSMAG'('4S')'=%')');
      WRITE(DV, F3, DENSMAG);
      WRITETEXT('('%%LAMBDA'('5S')'=%')');
      WRITE(DV, F3, LAMBDA);
      WRITETEXT('('%%XFACTOR'('4S')'=%')');
      WRITE(DV, F3, XFACTOR);
      WRITETEXT('('%%DSAT'('7S')'=%')');
```

```
        REQUEST:=REQ[VV];
        MAXIT   :=MAX[VV];
        AP(NP,N,B,BL,REQUEST,CAT);
        ACC(NP,B,BL,CAT,X,E);
        POWELL 64(FUNCT,X,E,N,F,ESCALE,IPRINT,ICON,MAXIT,
              DV,B,NP,M,CAT,BL,Z,YOBS,Q,SUMQ,
              BASE,YCALC,SD,LIMIT,ST);
AH18:       'IF' ST=1 'THEN'
        'BEGIN'
        AH19:       ESCALE:=2*ESCALE;
        AH19A:      'FOR' I:=1 'STEP' 1 'UNTIL' N 'DO'
              X[I]:=PARAMETER[I];
              WRITETEXT('('''('C')'%%CYCLE')');
              WRITE(DV, F4, VV);
              WRITETEXT('('%%WILL%BE%REPEATED'('C')'')');
              'GOTO' AH17;
        'END';
        'IF' ST=4 'THEN' 'GOTO' AH17A;
AH20:       'IF' ST=2 'THEN'
        'BEGIN'       WRITETEXT('('''('CC')'%%
          INTEGER%OVERFLOW%AT%AH11')');
              'GOTO' AH19;
        'END';
AH21:       'IF' ST=3 'THEN' WRITETEXT('('''('CC')'%%LIMIT%OF%F%HAS%
              BEEN%REACHED'('CC')'')');
        FUNCT(B,NP,M,CAT,BL,X,Z,YOBS,Q,SUMQ,BASE,YCALC,F,DV,ST);
        RESULTS(NP,N,M,REQUEST,OP,X,Z,YOBS,SUMQ,BASE,
              YCALC,F,SD,DV);
        ST:=0;
AH22:       'IF' LIMIT>F 'THEN' 'GOTO' AH24;
AH23:       'FOR' I:=1 'STEP' 1 'UNTIL' NP 'DO'
        PARAMETER[I]:=X[I];
AH23A:      'END';
AH24:      WRITETEXT('('''('CCC')'%%CALCULATION%OF%COORDINATES%AND%
              AREAS%OF%THE%PEAKS%AND%BACKGROUND'('CC')'')');
              AA:=READ;  AA:=AA/2.54;
              BBB:=READ;  BBB:=BBB/2.54;
              CC:=READ;  DD:=READ;  EE:=READ;  FF:=READ;
              LIMITS(0,AA,1,BBB);
              REGION(Z[1],Z[M]+0.005,CC,DD);
              CRSET(4);  CRSIZE(0.01*DD);
        MM:=(((Z[M]-Z[1])/STEP)+1);
        'BEGIN' 'REAL' 'ARRAY' XX[1:MM], BA[1:MM], AR[1:B];
              'FOR' KK:=1 'STEP' 1 'UNTIL' MM 'DO'
              XX[KK]:=(Z[1]+(STEP*(KK-1)));
'COMMENT' CALCULATION OF THE COORDINATES OF THE BACKGROUND;
AH25: 'FOR' KK:=1 'STEP' 1 'UNTIL' MM 'DO'
        'BEGIN'
        'IF' CAT=1 'THEN'
        'BEGIN'       'IF' BL=2 'THEN'
        BA[KK]:=X[NP-1] + ((XX[KK]-Z[1]) * (X[NP]-X[NP-1])/
                (Z[M]-Z[1]));
              'IF' BL=4 'THEN'
        BA[KK]:=       X[NP-3] + (X[NP-2] * XX[KK]) + (X[NP-1] *
              XX[KK]↑2) + (X[NP] * XX[KK]↑3);
        'END';
        'IF' CAT=2 'THEN'
        'BEGIN'       'IF' BL=2 'THEN'
        BA[KK]:=X[3*B+1]+ ((XX[KK] - Z[1]) * (X[3*B+2]
              -X[3*B+1])/(Z[M]-Z[1]));
```

```
        'IF' BL=4 'THEN'
BA[KK]:= X[3*B+1] + (X[3*B+2] * XX[KK])  + (X[3*B+3]
            * XX[KK]↑2) + (X[3*B+4]* XX[KK]↑3);
'END';
  'IF' CAT=4 'THEN'
  'BEGIN'
  'IF' BL=2 'THEN'
  BA[KK]:=X[NP-1]+((XX[KK]-Z[1])*
  (X[NP]-X[NP-1])/(Z[M]-Z[1]));
  'IF' BL=4 'THEN'
        BA[KK]:=X[NP-3]+(X[NP-2]*XX[KK])+(X[NP-1]
        *XX[KK]↑2)+(X[NP]*XX[KK]↑3);
        'END';
        'END';
SYMB:=50;
CURPTO(Z,YOBS,1,M,50);
CURPTO(XX,BA,1,MM,10);
'COMMENT' CALCULATION OF THE AREA UNDER THE BACKGROUND;
AH26: 'FOR' KK:=1 'STEP' 2 'UNTIL' (MM-2) 'DO'
      TBA:=TBA + (((BA[KK]+(4*BA[KK+1])+BA[KK+2])/6)*
            (XX[KK+2]-XX[KK])*1);
'COMMENT' CALCULATION OF THE COORDINATES OF EACH PEAK;
AH27:       WRITETEXT('('('('CC')'%'('7S')'XX'('11S')'
        Q'('9S')'BASE'('5S')
'
                Y%CALC=Q+BASE'('C')'')');
      'FOR' T:=1 'STEP' 1 'UNTIL' B 'DO'
'BEGIN'       'REAL' 'ARRAY' Q,BOTH[1:MM];
      'REAL' AREA;
      AREA:=0;
WRITETEXT('('('('CCC')'%%PEAK%%NO.')');
WRITE(DV, F6, T);
'FOR' KK:=1 'STEP' 1 'UNTIL' MM 'DO'
'BEGIN'
      'IF' CAT=1 'THEN'
      'BEGIN' 'IF' T=1 'THEN'
      Q[KK]:=(X[1]*(X[2]*EXP(-LN(2)*((2*(XX[KK]-X[5*B-1])/
          X[3])↑2)))) + ((1-X[1])*(X[2]/(1+((2*(XX[KK]
          -X[5*B-1])/X[3])↑2))))
      'ELSE' 'IF' XX[KK] 'LE' X[5*B+T-2] 'THEN'
          Q[KK]:=(X[5*T-6]*(X[5*T-5]* EXP(-LN(2) *
           ((2*(XX[KK]-X[5*B+T-2])/X[5*T-4])↑2))))+
           ((1-X[5*T-6])*(X[5*T-5]/(1+
           ((2*(XX[KK]-X[5*B+T-2])/X[5*T-4])↑2))))
      'ELSE' Q[KK]:=(X[5*T-2]*(X[5*T-5]*EXP(-LN(2)*((2*
                    (XX[KK]-X[5*B+T-2])/X[5*T-3])↑2))))+
                    ((1-X[5*T-2])*(X[5*T-5]/(1+((2*(XX[KK]-
                    X[5*B+T-2])/X[5*T-3])↑2))));
        'END';
    'IF' CAT=2 'THEN'
'BEGIN'
    Q[KK]:=(X[3*T-2]*(X[3*T-1]* EXP(-LN(2) *
          ((2*(XX[KK]-X[3*B+BL+T])/X[3*T])↑2))))+
          ((1-X[3*T-2])*(X[3*T-1]/(1+
          ((2*(XX[KK]-X[3*B+BL+T])/X[3*T])↑2))));
'END';
'IF' CAT=4 'THEN'
'BEGIN' 'IF' XX[KK] 'LE' X[5*B+T] 'THEN'
Q[KK]:=(X[5*T-4]*(X[5*T-3]*EXP(-LN(2)*
((2*(XX[KK]-X[5*B+T])/X[5*T-2])↑2))))+
```

```
   ((1-X[5*T-4])*(X[5*T-3]/(1+
   ((2*(XX[KK]-X[5*B+T])/X[5*T-2])↑2))))
   'ELSE' Q[KK]:=(X[5*T]*(X[5*T-3]*EXP(-LN(2)*((2*(XX[KK]-
   X[5*B+T])/X[5*T-1])↑2))))+((1-X[5*T])*(X[5*T-3]
   /(1+((2*(XX[KK]-X[5*B+T])/X[5*T-1])↑2))));
   'END';
        'IF' Q[KK]'GE'0.001 'THEN'
'BEGIN'       WRITE(DV, F5, XX[KK]);
      WRITE(DV,F5, Q[KK]);
      WRITE(DV, F5, BA[KK]);
            WRITE(DV, F3, (Q[KK]+BA[KK]));
            'END';
      'END';
'FOR' KK:=1 'STEP' 1 'UNTIL' MM 'DO' BOTH[KK]:=Q[KK]+BA[KK];
CURPTO(XX,BOTH,1,MM,-10);
'COMMENT' CALCULATION OF THE AREA UNDER EACH PEAK;
AH28: 'FOR' KK:=1 'STEP' 2 'UNTIL' (MM-2) 'DO'
      AREA:=AREA+(((Q[KK]+(4*Q[KK+1])+Q[KK+2])/6) *
            (XX[KK+2]-XX[KK])*1);
      AR[T]:=AREA;
'COMMENT' TOTAL AREA UNDER THE PEAKS;
AH29:       TPA:=TPA+AREA;
      'END';
AXESSI(EE,FF);  CRSET(0);  CRSIZE(0.02*DD);
LIMITS(0,AA,0,BBB);
REGION(Z[1],Z[M],CC-2,DD);
      WRITETEXT('('''('CC')'%%PEAK%NO.'('24S')'
        SQ%CM'('6S')'PER%CENT'('C'
)''')');
      'FOR' T:=1 'STEP' 1 'UNTIL' B 'DO'
      'BEGIN'
            WRITE(DV, F4 , T);
            WRITETEXT('('%'('17S')'%')');
            WRITE(DV, F5, AR[T]);
            WRITE(DV, F3, (AR[T]*100/(TPA+TBA)));
      'END';
AH30:       WRITETEXT('('%%TOTAL%AREA%UNDER%THE%PEAKS')');
      WRITE(DV, F5, TPA);
      WRITE(DV, F7, (TPA*100/(TPA+TBA)));
      WRITETEXT('('%%TOTAL%%BACKGROUND%%AREA%%%')');
      WRITE(DV, F5, TBA);
      WRITE(DV, F7, (TBA*100/(TPA+TBA)));
      WRITETEXT('('%%TOTAL%%CALCULATED%%AREA%%%')');
      WRITE(DV, F3, (TPA+TBA));
BORDER;
GREND;
      'END';
      'IF' REQUEST=7 'OR' REQUEST=9 'THEN' 'GOTO' AH32;
'COMMENT' CALCULATION OF THE INTEGRATED AREA
            UNDER THE ORIGINAL CURVE;
AH31:       'FOR' KK:=1 'STEP' 2 'UNTIL' (M-2) 'DO'
      TOA:=TOA+(((YOBS[KK]+(4*YOBS[KK+1])+YOBS[KK+2])/6)
            *(Z[KK+2]-Z[KK])*1);
      WRITETEXT('('%%TOTAL%%OBSERVED%%AREA%%%%%')');
      WRITE(DV, F3, TOA);
      'COMMENT' CALCULATION OF THE SQUARE PERCENTAGE ERROR;
      'FOR' KK:=1 'STEP' 1 'UNTIL'M 'DO'
      PCE:=PCE+(((YOBS[KK]-YCALC[KK])/YOBS[KK])↑2);
      PCE:=SQRT(PCE/M);
      PCE:=100*PCE;
```

```
        WRITETEXT('('%%PERCENTAGE%ERROR%%%%%=%%%%%')');
        PRINT(PCE,4,3);
        'END';
AH32:       'END';

        'END';
'END'
<EBTAH9110SPU>
****
```

A3.2 Procedure for calculation of contrast-transfer function, with graphical facilities

```
'LIBRARY'(ED,SUBGROUPLDSA)
'BEGIN'
'REAL' CS,DELTAF,CHI,X,A,B;
'INTEGER'M,K;
CS:=READ;
DELTAF:=READ;
A:=READ;
B:=READ;
M:=200;
'BEGIN'
'ARRAY'D,C,ALPHA[1:M];
X:=0.001;
'FOR'K:=1'STEP'1'UNTIL'M'DO'
'BEGIN'
X:=X+0.0001;
ALPHA[K]:=X;
D[K]:=0.0037/ALPHA[K];
CHI:=-3.1416*(A*(CS/2)*ALPHA[K]↑4-B*DELTAF*ALPHA[K]↑2)/0.0037;
C[K]:=-2*SIN(CHI);
PRINT(D[K],2,2);
SPACE(5);
PRINT(C[K],2,3);
SPACE(5);
PRINT(ALPHA[K],2,4);
NEWLINE(1);
'END';
LIMITS(0,15,2,8);
REGION(ALPHA[1],ALPHA[M],-2.5,2.5);
CURPTO(ALPHA,C,1,M,-10);
AXESSI(0.002,0.25);
BORDER;
GREND;
'END';
'END'
```

A4 Electron-microscope plate and film reference numbers

Plate Number	Reference Number	Plate Number	Reference Number
I	11088	XXXII	11920
II	11078	XXXIII	13405
III	11320	XXXIV	13410
IV	11288	XXXV	14213
V	12165	XXXVI	14077
VI	12166	XXXVII	14081
VII	11310	XXXVIII	14199
VIII	11310	XXXIX	14102
IX	11079	XL	14104
X	09851	XLI	14212
XI	11099	XLII	EU18, EU20 & EU25
XII	11323	XLIII	EU27 & EU30
XIII	11319 - 11325	XLIV	14615
XIV	11282	XLV	14617 & 14618
XV	11281	XLVI	14638
XVI	11303	XLVII	14634
XVII	12163	XLVIII	14656
XVIII	12159	XLIX	14686
XIX	11364 & 11376	L	14684
XX	14038	LI	14629
XXI	14064	LII	13356
XXII	14040	LIII	13358
XXIII	14198	LIV	13359
XXIV	14197	LV	13360
XXV	12073	LVI	13362
XXVI	12130	LVII	14231
XXVII	12104	LVIII	14362
XXVIII	12099	LIX	12627, 12631 & 12636
XXIX	12120	LX	13570 - 13574
XXX	12076	LXI	13348 & 13352
XXXI	12154		

Table 1 Specimen Identification

PRECURSOR	VACUUM HEAT TREATMENT PRIOR TO OXIDATION	OXIDATION	HEAT-TREATMENT TEMPERATURE		
			1000°C	1500°C	2500°C
3 denier special Courtelle*	None	5h at 220°C	A1000	A1500	A2500
	None	10h at 220°C	-	-	B2500
	None	20h at 220°C	-	-	C2500
	None	40h at 220°C	D1000	D1500	D2500
1.5 denier special Courtelle*	None	1h at 220°C	E1000	E1500	E2500
	None	9h at 220°C	F1000	F1500	F2500
2 denier Dralon+	None	5h	G1000	G1500	G2500
	None	10h	H1000	H1500	H2500
1.5 denier special Courtelle*	None	2h at 230°C	J1000	J1500	J2500
	6h at 230°C	2h at 230°C	K1000	K1500	K2500
1.8 denier Orlon+	None	4h at 230°C	L1000	L1500	L2500
	6h at 230°C	1h at 230°C	M1000	M1500	M2500
Dralon+	None	3¼h at 230°C	N1000	N1500	N2500
	6h at 230°C	½h at 230°C	P1000	P1500	P2500
1.5 denier special Courtelle*	Nominal	None	-	-	Q2500
3 denier special Courtelle*	None	2h at 220°C	-	-	R2500
	None	6h at 220°C	-	-	S2500

* - circular cross section, + dog-bone cross section

Table 2 Lattice Distortion (σ) and Mean Defect-free Distance (D_c) parameters

SPECIMEN	REGION IN SPECIMEN	σ (%)	D_c (nm)
A2500	Skin	0.54	8.9
	Core	1.66	3.0
B2500	Skin	0.66	9.8
	Core	1.21	4.5
C2500	Skin	0.62	11.4
	Core	1.63	2.8
D2500	Skin	0.52	11.8
	Core	1.73	3.5

Table 3 Mean Layer-plane Dimensions for Specimen B2500

REGION IN SPECIMEN	REFLECTION	SIZE PARAMETER (nm)
Skin	(100) Equatorial	$L_{a\perp} = 8.4$
Skin	(100) Meridional	$L_{a//} = 8.3$
Skin	(110) Meridional	$L_{a//} = 12.4$
Core	(100) Equatorial	$L_{a\perp} = 4.8$
Core	(100) Meridional	$L_{a//} = 7.7$
Core	(110) Meridional	$L_{a//} = 7.2$

Table 4 Preferred Orientation Parameters

SPECIMEN	REGION IN SPECIMEN	Z^o
A2500	Skin	15
	Core	22
B2500	Skin	13
	Core	21
C2500	Skin	16
	Core	32
D2500	Skin	12
	Core	20

Table 5 Crystallite Size, Lattice Spacing and Orientation of Various Specimens

SPECIMEN	REGION IN SPECIMEN	L_c nm	c/2 nm	Z o
A1000	Skin	1.1	0.38	-
	Core	1.1	0.37	42
A1500	Skin	1.6	0.36	43
	Core	1.6	0.35	-
D1000	Skin	1.2	0.37	43
	Core	1.1	0.37	-
D1500	Skin	1.9	0.35	-
	Core	1.8	0.35	42
E1000	Skin	1.4	0.36	-
	Core	1.3	0.36	44
E1500	Skin	1.2	0.35	-
	Core	1.4	0.35	48
F1000	Skin	1.3	0.36	-
	Core	1.3	0.37	42
F1500	Skin	1.6	0.35	-
	Core	1.4	0.36	42

Table 6 Measurement of Crystallite Size, L_c, by different techniques

TECHNIQUE	L_c nm	s nm
Direct measurement on high-resolution images		
(i) Multibeam bright-field image at Gaussian focus	4.5	2.3
(ii) Multibeam bright-field image at maximum fringe-contrast focus	4.5	2.5
(iii) 000 - 002 symmetric bright-field image	4.7	3.0
(iv) 002 - 004 symmetric dark-field image	4.0	2.9
(v) 002 axial dark-field image	3.5	2.8
Electron Diffraction		
$(90 - \psi) = \pm 2^{o}$	5.2	
$(90 - \psi) = \pm 90^{o}$ (from Fig. 40c)	4.3	
Mean defect-free distance (D_c)	5.9	
X-ray Diffraction		
$(90 - \psi) = \pm 1^{o}$	5.1	
$(90 - \psi) = \pm 90^{o}$ (rotated specimen)	3.8	
Powder photograph	5.9	
Computation		
Distortion-free stacking size	8.3	

Table 7 The effect on direct measurements of crystallite size of discounting all crystallites of width 1.7 nm or less

TECHNIQUE	L_c nm
(i) Multibeam bright-field image at Gaussian focus	4.9
(ii) Multibeam bright-field image at maximum fringe-contrast focus	4.8
(iii) 000 - 002 symmetric bright-field image	5.4
(iv) 002 - 004 symmetric dark-field image	5.1
(v) 002 axial dark-field image	4.7

Table 8 Properties of Carbon Fibres made from Special Courtelle

CARBON FIBRES FROM 3 DENIER COURTELLE					
HEAT-TREATMENT TEMPERATURE °C	OXIDATION TIME (h) / PROPERTY	5	10	20	40
1000	Diameter (μm)	11.5	10.8	10.4	9.8
	UTS (GNm^{-2})	1.30	2.08	2.38	2.42
	E (GNm^{-2})	179	202	216	254
	ε(%)	0.73 (A1000)	1.03	1.10	0.95 (D1000)
1500	Diameter (μm)	10.6	10.8	9.9	9.6
	UTS (GNm^{-2})	1.36	1.62	1.76	1.60
	E (GNm^{-2})	232	240	279	267
	ε (%)	0.59 (A1500)	0.67	0.63	0.60 (D1500)
2500	Diameter (μm)	9.7	10.1	9.4	8.9
	UTS (GNm^{-2})	1.70	1.83	1.89	1.62
	E (GNm^{-2})	344	388	398	352
	ε (%)	0.49 (A2500)	0.47 (B2500)	0.47 (C2500)	0.46 (D2500)
2500	UTS (GNm^{-2})	0.73)			
	E (GNm^{-2})	210) unoxidized-stabilized for 16h in N_2			
	ε (%)	0.35) (Q2500)			

Note: UTS = Ultimate Tensile Strength
E = Young's Modulus
ε = Fibre strain-to-failure

Identification numbers for specimens examined in the electron microscope are shown in brackets.

Table 8 (continued) Properties of Carbon Fibres made from Special Courtelle

CARBON FIBRES FROM 1½ DENIER SPECIAL COURTELLE				
HEAT-TREATMENT TEMPERATURE °C	OXIDATION TIME (h) / PROPERTY	1	3	9
1000	Diameter (μm)	9.2	8.5	7.9
	UTS (GNm^{-2})	2.33	2.63	2.76
	E (GNm^{-2})	187	212	232
	ε (%)	1.25 (E1000)	1.24	1.19 (F1000)
1500	Diameter (μm)	8.0	8.7	8.2
	UTS (GNm^{-2})	3.15	2.79	1.97
	E (GNm^{-2})	248	252	268
	ε (%)	1.27 (E1500)	1.11	0.74 (F1500)
2500	Diameter (μm)	8.2	8.3	7.9
	UTS (GNm^{-2})	2.25	2.09	2.35
	E (GNm^{-2})	345	391	386
	ε (%)	0.65 (E2500)	0.53	0.61 (F2500)

Note: UTS = Ultimate Tensile Strength
E = Young's Modulus
ε = Fibre strain-to-failure

Identification numbers for specimens examined in the electron microscope are shown in brackets.

Table 9

WEDGE	3D	2.5D	1.75D	1.5D	0.5D	0.25D
D_{sat}	225	265	310	587	627	1138

REFERENCES

1. Debye P. and Scherrer P., Physik Z., 18, 291, 1917.
2. Hull, A.W., Phys. Rev., 20, 113, 1922.
3. Bernal J.D., Proc. Roy. Soc. (Lond.), A100, 749, 1924.
4. Lipson H. and Stokes A.R., Nature, 149, 328, 1942.
5. Idem., Proc. Roy. Soc. (Lond.), A181, 101, 1942.
6. Kochanovska A., Czech. J. Phys., 3, 193, 1953.
7. Bacon R., J. Appl. Phys., 31, 283, 1960.
8. Bacon R., Pallozzi A.A. and Slosarik S.E., 21st Techn. and Man. Conf., Section 8e, Soc. Plast. Ind., 1966.
9. Shindo A., Osaka Kogyo Gijitsu Skikuko Kiko, 12, 110, 1961.
10. Idem., Rept. Govt. Ind. Res. Inst., Osaka, No. 317, 1961.
11. Idem., Carbon, 1, 391, 1964.
12. Watt W., Phillips L.N. and Johnson W., Engineer, 221, 815, 1966.
13. Moreton R., Watt W. and Johnson W., Nature, 213, 690, 1967.
14. BP 1 168 619, 1969.
15. Standage A.E. and Prescott R., Nature, 211, 169, 1966.
16. Grassie N. and Hay J., J. Polym. Sci., 56, 189, 1962.
17. Watt W. and Johnson W., Nature, 257, 210, 1975.
18. Potter W.D. and Scott G., ibid., 236, 30, 1972.
19. Watt W., Proc. 3rd. Conf. Ind. Carbon Graphite, Soc. Chem. Ind., 1970.
20. Standage E. and Matkowsky R., Nature, 224, 688, 1969.
21. Clarke A. and Bailey J., ibid., 234, 529, 1971.
22. Goodhew P., Clarke A. and Bailey J., Mat. Sci. Eng., 17, 3, 1975.
23. Kennedy J.P. and Fontana C.M., J. Polym. Sci., 39, 501, 1959.
24. Miyamichi K. et al., J. Soc. Fibre Sci. Tech. Jap., 22, 538, 1966.
25. Hay J.N., J. Polym. Sci., A-1, 6, 2127, 1968.
26. Watt W., Nature, 236, 10, 1972.
27. Clarke A. and Bailey J., ibid., 243, 146, 1973.

28. Watt W., RAE Tech. Rpt. 69145, 1969.

29. Watt W. and Green J., Proc. 1st. Int. Carbon Fibre Conf., Plast. Inst., London, 1971.

30. Gaulin C.A. and McDonald W.R., SAMSO, Tech. Rpt. No. TR-72-304, 1972.

31. Kriegbaum W.R. and Tokita No., J. Polym. Sci., 43, 467, 1960.

32. Blakslee O.L., Proctor D.G., Seldin E.J., Spence G.B. and Weng, T., J. Appl. Phys., 41, 3373, 1970.

33. Williams W.S., Steffens D. and Bacon R., ibid., 4893.

34. Soule D.E. and Nezbeda C.W., ibid., 39, 5122, 1968.

35. Watt W. and Johnson W., RAE Tech. Rpt. 68288, 1968.

36. Curtis G.J., Milne J.M. and Reynolds W.N., Nature, 220, 1024, 1968.

37. Allen S., Cooper G.A. and Mayer R.M., ibid., 224, 684, 1969.

38. Bacon R. and Schalamon W.A., Proc. 8th. Carbon Conf., Buffalo, USA, 1967.

39. Johnson W., Proc. 3rd. Conf. Ind. Carbon Graphite, Soc. Chem. Ind., 1970.

40. Moreton R., ibid.

41. Idem., J. Fibre Sci. Tech., 1, 273, 1969.

42. Johnson J.W., Appl. Polym. Symp., 9, 1969.

43. Thorne D.J., Proc. 3rd. Conf. Ind. Carbon Graphite, Soc. Chem. Ind., 1970.

44. Moreton, R., Proc. 1st. Int. Carbon Fibre Conf., Plast. Inst., London, 1971.

45. USP 3 917 776, 1975.

46. LeMaistre C.W., Ph.D. Thesis, Rensselaer Poly. Inst., Troy, N.Y., 1971.

47. LeMaistre C.W. and Diefendorf R.J., Proc. 10th. Carbon Conf., Bethlehem, USA, 1971.

48. Jones B.F. and Duncan R.G., J. Mat. Sci., 9, 162, 1974.

49. Sharp J.V. and Burnay S.G., Proc. 1st. Int. Carbon Fibre Conf., Plast. Inst., London, 1971.

50. Moreton R., Driffil S. and Watt W., RAE Tech. Rpt. 73048, 1973.

51. Moreton R. and Watt W., Nature, 247, 360, 1974.

52. Idem., Carbon, 12, 543, 1974.

53. Diefendorf R.J. and Tokarsky E.W., Polym. Eng. Sci., 15, 150, 1975.

54. Thorne D.J., Nature, 248, 754, 1974.

55. Badami D.V., Joiner J.C. and Jones G.A., ibid., 215, 387, 1967.

56. Johnson J.W., Marjoram J.R. and Rose P.G., ibid., 221, 357, 1969.

57. Ruland W., Polym. Preprints, 9, 1368, 1968.

58. Perret R. and Ruland W., Proc. 9th. Carbon Conf., Boston, USA, 1969.

59. Johnson D.J. and Tyson C.N., J. Phys. D.: Appl. Phys., 2, 787, 1969.

60. Idem., ibid., 3, 526, 1970.

61. Johnson D.J., Crawford D. and Oates C., Proc. 10th Carbon Conf., Bethlehem, USA, 1971.

62. Ergun S., Proc. 9th. Carbon Conf., Boston, USA, 1969.

63. Fourdeux A., Perret R. and Ruland W., Proc. 1st. Int. Carbon Fibre Conf., Plast. Inst., London, 1971.

64. Diefendorf R.J. and Tokarsky E.W., AFML Rpt. No. TR-72-133, Part II, 1973.

65. Ergun S., Nature, 238, 137, 1972.

66. Stewart M., Zubzanda O. and Feughelman M., ibid., 242, 43, 1973.

67. Rose P.G., Proc. 4th. Conf. Ind. Carbon Graphite, Soc. Chem. Ind., 1974.

68. Takahashi H., Kuroda H. and Akamatu H., Carbon, 2, 432, 1965.

69. Oates C., Ph.D. Thesis, Univ. Leeds, 1974.

70. Watt W., Johnson D.J. and Parker E., Proc. 2nd. Int. Carbon Fibre Conf., Plast. Inst., London, 1974.

71. Tyson C.N., J. Phys. D.: Appl. Phys., 8, 749, 1975.

72. Johnson W. and Watt W., Nature, 215, 384, 1967.

73. Fourdeux A., Perret R. and Ruland W., J. Appl. Cryst., 1, 252, 1968.

74. Idem., Proc. 9th. Carbon Conf., Boston, USA, 1969.

75. Heidenreich R.D., Hess W.M. and Ban L.L., J. Appl. Cryst., 1, 1, 1968.

76. Hugo J.A., Phillips V.A. and Roberts B.W., Nature, 226, 144, 1970.

77. Johnson D.J., ibid., 750, 1970.

78. Phillips V.A., Hugo J.A. and Roberts B.W., Proc. 29th. Ann. EMSA Meeting, 1971.

79. Crawford D., Ph.D. Thesis, Univ. Leeds, 1972.

80. Johnson D.J., Proc. 1st. Int. Carbon Fibre Conf., Plast. Inst., London, 1971.

81. Crawford D. and Johnson D.J., J. Microsc., 94, 51, 1971.

82. Stewart M. and Feughelman M., Nature, 241, 67, 1973.

83. Butler B.L. and Diefendorf R.J., Proc. 9th. Carbon Conf., Boston, USA, 1969.

84. Watt W. and Johnson W., Proc. 3rd. Conf. Ind. Carbon Graphite, Soc. Chem. Ind., 1970.

85. Knibbs R.H., J. Microsc., 94, 273, 1971.

86. Butler B.L., Ph.D. Thesis, Rensselaer Poly. Inst., Troy, N.Y., 1969.

87. Larsen J.V. and Smith T.G., NOLTR 71-166, 1971.

87a Wicks BJ and Coyle RA, J. Mat. Sci., 11, 376, 1976

88. LeMaistre C.W. and Diefendorf R.J., SAMPE Quart., 4, 1, 1973.

89. Watt W. and Johnson W., private communication.

90. Johnson D.J., Crawford D. and Jones B.F., J. Mat. Sci., 8, 286, 1973.

91. Jones B.F. and Duncan R.G., ibid., 6, 289, 1971.

92. Johnson J.W., Rose P.G. and Scott G., Proc. 3rd. Conf. Ind. Carbon Graphite, Soc. Chem. Ind., London, 1970.

93. Layden G.K., Carbon, 10, 59, 1972.

94. Fourdeux A., Hérinckx C., Perret R. and Ruland W., Compt. Rend., Sér. C, 269, 1597, 1969.

95. Sharp J.V., Burnay S.G., Matthews J.R. and Harper E.A., Proc. 2nd. Int. Carbon Fibre Conf., Plast. Inst., London, 1974.

96. Bullock R.E., J. Mat. Sci., 7, 964, 1972.

97. Bullock R.E., Gordon D.E. and Deaton B.C., 11, 418, 1973.

98. Wicks B.J., ARL MET Rpt. 93, 1974.

99. Barnet F.R. and Noor M.K., NOLTR 73-154, 1974.

100. Idem., Proc. 2nd. Int. Carbon Fibre Conf., Plast. Inst., London, 1974.

101. Hart G.L. and Pritchard G., Nature, 246, 78, 1973.

102. Idem., Proc. 4th. Conf. Ind. Carbon Graphite, Soc. Chem. Ind., 1974.

103. McKee D.W. and Mimeault V.J., Chem. Phys. Carbon, 8, 151, 1970.

104. Molleyre F. and Bastick M., Proc. 4th. Conf. Ind. Carbon Graphite, Soc. Chem. Ind., 1974.

105. Ehrburger P., Herque J.J. and Donnet J.B., ibid.

106. Bless P. and Lando J.B., Polym. Letters Edn., 13, 153, 1975.

107. Ruland W., Proc. 9th Carbon Conf., Boston, USA, 1969.

108. Reynolds W.N., Proc. 3rd. Conf. Ind. Carbon Graphite, Soc. Chem. Ind., 1970.

109. Henrichsen R.E. and Fishbach D.B., Proc. 4th. Conf. Ind. Carbon Graphite, Soc. Chem. Ind., 1974.

110. Whitney W. and Kimmel R.M., Nature, 237, 93, 1972.

111. USP 3 841 079.

112. Stewart M. and Feughelman M., J. Mat. Sci., 8, 1119, 1973.

113. Reynolds W.N. and Sharp J.V., Carbon, 12, 103, 1974.

114. Seldin E.J. and Nezbeda C.W., J. Appl. Phys., 41, 3389, 1970.

115. Franklin R.E., Acta Cryst., 4, 253, 1951.

116. Hindeleh A.M. and Johnson D.J., J. Phys. D.: Appl. Phys., 4, 259, 1971.

117. Valentine R.C., Adv. Opt. Electron Microsc., 1, 180, 1966.

118. Ergun S., Phys. Rev., B1, 3371, 1970.

119. Thrower P.A. and Nagle D.C., Carbon, 11, 663, 1973.

120. Ruland W. and Tompa H., J. Appl. Cryst., 5, 225, 1972.

121. Johnson D.J. and Crawford D., J. Microsc., 98, Pt. 3, 313, 1973.

122. Oates C., Ph.D. Thesis, Univ. Leeds, 1974.

123. MOD Contract No. AT/2062/047 Mat., Final Rpt., 1974.

124. Mencik Z., Plummer H.K. and Bartosiewicz L., Carbon, 13, 417, 1975.

125. Seldin E.J. and Nezbeda C.W., J. Appl. Phys., 41, 3389, 1970.

126. Johnson W., private communication.

127. Scherzer O., J. Appl. Phys., 20, 20, 1949.

128. Heidenreich R.D., Fundamentals of Transmission Electron Microscopy, John Wiley and Sons, 1964.

129. Zernike F., Phys. Z., 36, 848, 1935.

130. Haine M.E., The Electron Microscope, Spon, London, 1961.

131. Thon F., Electron Microscopy in Materials Science, Ed. by Valdré U., Academic Press, London, 1971.

132. Bennett S.C. and Saville B.P., unpublished results.

133. Crawford D. and Marsh H., Proc. EMAG75, Inst. Phys., Bristol,1975.

134. Höppe W., Acta Cryst., A26, 414, 1970.

135. Crawford D. and Marsh H., Fuel, 55, 251, 1976.

136. Jefferson D., Millward G.R. and Thomas J.M., private communication.

137. Cockayne D.J.H., Parsons J.R. and Hoelke C.W., Phil. Mag., 24, 139, 1971.